Universidade Estadual de Campinas

Faculdade de Engenharia Civil, Arquitetura e Urbanismo

Karolinne Oliveira Coelho

Aproximações localmente conservativas usando o Método dos Elementos Finitos de Contorno Escalado

Locally conservative approximations using the Scaled Boundary Finite Element Method

campinas
2023

Karolinne Oliveira Coelho

Aproximações localmente conservativas usando o Método dos Elementos Finitos de Contorno Escalado

Locally conservative approximations using the Scaled Boundary Finite Element Method

Thesis presented to the School of Civil Engineering, Architecture and Urban Design of the University of Campinas in partial fulfillment of the requirements for the degree of Doctor Civil Engineering - Structures and Geotechnics.

Tese apresentada à Faculdade de Engenharia Civil, Arquitetura e Urbanismo da Universidade Estadual de Campinas como parte dos requisitos exigidos para a obtenção do título de Doutora em Engenharia Civil, na área de Estruturas e Geotécnica.

Supervisor: Philippe Remy Bernard Devloo

Este exemplar corresponde à versão final da tese defendida pela aluna Karolinne Oliveira Coelho, e orientada pelo Prof. Dr. Philippe Remy Bernard Devloo.

Signature

_____

Campinas
2023

Ficha catalográfica
Universidade Estadual de Campinas
Biblioteca da Área de Engenharia e Arquitetura
Rose Meire da Silva - CRB 8/5974

C65L

Coelho, Karolinne Oliveira, 1992-
Locally conservative approximations using the scaled boundary finite element method / Karolinne Oliveira Coelho. – Campinas, SP : [s.n.], 2023.

Orientador: Philippe Remy Bernard Devloo.
Tese (doutorado) – Universidade Estadual de Campinas, Faculdade de Engenharia Civil, Arquitetura e Urbanismo.

1. Método dos elementos finitos. 2. Fluxo de Darcy. 3. Análise numérica. 4. Programação orientada a objetos (Computação). I. Devloo, Philippe Remy Bernard, 1958-. II. Universidade Estadual de Campinas. Faculdade de Engenharia Civil, Arquitetura e Urbanismo. III. Título.

Informações Complementares

Título em outro idioma: Aproximações localmente conservativas usando o método dos elementos finitos de contorno escalado
Palavras-chave em inglês:
Finite element method
Darcy flow
Numerical analysis
Object-oriented programming
Área de concentração: Estruturas e Geotécnica
Titulação: Doutora em Engenharia Civil
Banca examinadora:
Philippe Remy Bernard Devloo [Orientador]
José Maria Campos dos Santos
Sergio Persival Baroncini Proença
Eduardo Gomes Dutra do Carmo
Luiz Carlos Wrobel
Data de defesa: 18-01-2023
Programa de Pós-Graduação: Engenharia Civil

Identificação e informações acadêmicas do(a) aluno(a)
- ORCID do autor: https://orcid.org/0000-0002-3088-9977
- Currículo Lattes do autor: http://lattes.cnpq.br/8153446476609557

UNIVERSIDADE ESTADUAL DE CAMPINAS
FACULDADE DE ENGENHARIA CIVIL, ARQUITETURA E URBANISMO

APROXIMAÇÕES LOCALMENTE CONSERVATIVAS USANDO O MÉTODO DOS ELEMENTOS FINITOS DE CONTORNO ESCALADO

LOCALLY CONSERVATIVE APPROXIMATIONS USING THE SCALED BOUNDARY FINITE ELEMENT METHOD

Karolinne Oliveira Coelho

Tese de Doutorado aprovada pela Banca Examinadora, constituída por:

Prof. Dr. Philippe Remy Bernard Devloo
Presidente e Orientador(a)/FECFAU/UNICAMP

Prof. Dr. José Maria Campos dos Santos
FEM/UNICAMP

Prof. Dr. Sergio Persival Baroncini Proença
Escola de Engenharia de São Carlos/USP

Prof. Dr. Eduardo Gomes Dutra do Carmo
COPPE/UFRJ

Prof. Dr. Luiz Carlos Wrobel
Brunel University

A Ata da defesa com as respectivas assinaturas dos membros encontra-se no SIGA/Sistema de Fluxo de Dissertação/Tese e na Secretaria do Programa da Unidade.

Campinas, 18 de janeiro de 2023

"To this I hold, my hope is only Jesus
All the glory evermore to Him
When the race is complete, still my lips shall repeat
Yet not I, but through Christ in me"

J. Robinson, R. Thompson & M. Farren

Agradecimentos

Primeiramente agradeço a Deus. "*Ó profundidade das riquezas, tanto da sabedoria, como da ciência de Deus! Quão insondáveis são os seus juízos, e quão inescrutáveis os seus caminhos! Por que quem compreendeu a mente do Senhor? ou quem foi seu conselheiro? Ou quem lhe deu primeiro a ele, para que lhe seja recompensado? Porque dele e por ele, e para ele, são todas as coisas; glória, pois, a ele eternamente. Amém.*" (Romanos 11:33-36). Por muitas vezes achei que não seria capaz de concluir, mas Deus me deu a capacidade necessária para a conclusão de mais essa etapa na minha vida.

Aos meus pais, Edilson e Raimunda, obrigada por me ensinar a importância do estudo e da dedicação. Obrigada pelos sacrifícios feitos para que eu pudesse ter educação de qualidade. À minha irmã, Karinne, obrigada por todo o apoio, principalmente nos momentos em que não pude estar presente.

Ao meu orientador, Prof. Philippe Devloo, obrigada pelo conhecimento compartilhado, pelas oportunidades confiadas a mim, pelas exortações e conselhos e por tanto me apoiar nos momentos bons e também nos difíceis. À Prof. Sônia Gomes, que foi essencial no desenvolvimento matemático das formulações aqui propostas. Obrigada por aceitar o desafio e se engajar em um tema fora da zona de conforto, e assim, mudar o rumo dessa tese. Ao Prof. Chongmin Song, pela orientação no período de intercâmbio na Austrália. Aos colegas de LabMeC e da UNSW, em especial a Omar, Pablo, Thiago Quinelato e Natália pela ajuda no aprendizado do NeoPZ e com dúvidas relativas a programação. Ao Prof. Mark Ainsworth por uma conversa quando esteve na UNICAMP, que apesar de breve, trouxe diversas ideias a essa tese.

Agradeço também aos amigos que estiveram ao meu lado durante os períodos que morei em Campinas, Sydney e Maceió.

Ao apoio financeiro da ANP (Agência Nacional do Petróleo, Gás Natural e Biocombustíveis) / FUNCAMP (2014/00090-2) durante os primeiros dois anos dessa tese. À ARC (Australian Research Council), UNSW e Prof. Chongmin Song pelo auxílio financeiro durante o período de intercâmbio.

Abstract

The Scaled Boundary Finite Element Method (SBFEM) is a finite element technique where the approximation space is composed of semi-analytical shape functions. These functions are obtained by approximating a homogeneous partial differential equation (PDE) by a Ricatti ordinary differential equation (ODE) whose analytical solution is known. The SBFEM is applied mainly in singularity problems, infinite domains, and simulations using complex meshes. This thesis aims to extend the SBFEM to simulate mechanical problems where the divergence-free condition is an essential characteristic of the numerical method, such as in incompressible fluid simulation. For that, this work is divided into three steps. First, it is demonstrated that the SBFEM approximation space is a subspace of Duffy's tensorial functions, which are based on the geometry of collapsed elements. Moreover, it is shown that the SBFEM space has intrinsic orthogonality in the energy semi-norm; such property is applied in the proof of a priori error estimates. In the sequence, the second part of the thesis addresses the construction of an SBFEM bubble function space for approximating non-homogeneous PDEs. A priori error estimates demonstrate that the proposed approximation leads to optimal convergence rates. Finally, a locally conservative SBFEM formulation is proposed, based on applying the mixed hybridization technique in a finite-element cell of infinitesimal width, in such a way as to obtain the SBFEM coefficient matrices that represent the Ricatti ODE. All formulations proposed in this thesis were implemented in an object-oriented finite element library. Numerical examples of a Darcy flow in a two-dimensional domain tested the accuracy of the technique. The tests included domains with square-root singularities, depicting the capacity of the method to simulate a flow in a fractured porous media. Optimal convergence rates were observed, including for the flow and high-order approximations.

Keywords: Finite Element Method, Darcy Flow, Numerical analysis, Object-Oriented Programming.

Resumo

O Método dos Elementos Finitos de Contorno Escalado, ou Escalonado no Contorno, (SBFEM) é uma técnica de elementos finitos na qual o espaço de aproximação é composto por funções de forma semi-analíticas. Essas funções são obtidas pela aproximação de uma equação diferencial parcial (EDP) homogênea por uma equação diferencial ordinária (EDO) de Ricatti, cuja a solução analítica é conhecida. O SBFEM é aplicado principalmente em problemas com singularidades, domínios infinitos e simulações usando malhas complexas. Essa tese visa estender o SBFEM para simular problemas mecânicos onde a condição de divergente nulo é uma característica essencial do método numérico, como em simulação de fluidos incompressíveis. Para isso, esse trabalho é dividido em três etapas. Primeiro, é demonstrado que o espaço de aproximação SBFEM é um subespaço do espaço das funções tensoriais de Duffy, que são baseadas na geometria de elementos colapsados. Além disso, é mostrado que o espaço de aproximação SBFEM tem uma ortogonalidade intrínseca na semi-norma de energia; tal propriedade é usada na prova da estimação de erro a priori. Na sequência, a segunda parte da tese aborda a construção de um espaço de funções bolha SBFEM para aproximar EDPs não-homogêneas. Estimadores de erro a priori demonstram que a aproximação proposta leva a ótimas taxas de convergência. Finalmente, uma formulação SBFEM localmente conservativa é proposta, baseada na aplicação da técnica de hibridização mista em uma célula de elemento finito de espessura infinitesimal, de forma a obter as matrizes de coeficiente SBFEM que representam a EDO de Ricatti. Todas formulações propostas nessa tese são implementadas em uma biblioteca de elementos finitos orientada à objeto. Exemplos numéricos de um fluxo de Darcy em um domínio bi-dimensional testaram a acurácia da técnica. Os testes incluíram domínio com singularidade do tipo raiz-quadrada, retratando a capacidade do método para simular um fluxo em um meio poroso fraturado. Ótimas taxas de convergência foram observadas, incluindo para o fluxo e para aproximações de alta ordem.

Palavras-chave: Método dos Elementos Finitos, fluxo de Darcy, análise numérica, programação orientada a objetos.

List of Figures

List of Tables

List of Abbreviations

BDFM Brezzi-Douglas-Fortin-Marini.

BEM Boundary Element Method.

DOF Degree of Freedom.

FE Finite Element.

FEM Finite Element Method.

GMsFEM Generalized Multiscale Finite Element Method.

HHO Hybrid High-Order

HPC High-Performance Computing

LabMeC Computational Mechanics Laboratory.

MHM Multiscale Hybrid Method.

MHM-$H(div)$ Multiscale Hybrid Method using Mixed formulations.

MPI Message Passing Interface.

NURBS Non-Uniform Rational B-Splines.

ODE Ordinary Differential Equation.

PDE Partial Differential Equation.

PU Partition of Unit.

RT Raviart-Thomas.

SBFEM Scaled Boundary Finite Element Method.

SFEM Smooth Finite Element Method.

SIF Stress Intensity Factor´.

VEM Virtual Element Method.

XFEM Extended Finite Element Method.

List of Symbols

In this section the main mathematical symbols, operators and variables are described. In general, the variables and symbols are represented as:

- Scalars: in italic A;
- Vectors: using a underline $\underline{A}$;
- Matrices: using two underlines $\underline{\underline{A}}$.

Functions or variables with a hat symbol are described in the parametric space (ξ, η) for 2D or (ξ, η_1, η_2) for 3D. Omitted cases are described over the thesis.

Chapter 2

Operators

$\frac{\partial}{\partial \underline{x}_i}$ Derivative in x_i-direction.

$\nabla_{\underline{\hat{x}}}$ Gradient operator in the master coordinates.

$\nabla_{\underline{x}}$ **or** ∇ Gradient operator in the deformed coordinates.

$\nabla\times$ Curl operator.

$\nabla\cdot$ Divergence operator.

Δ Laplace operator, $\nabla \cdot (\nabla\cdot)$.

$|\underline{\underline{\cdot}}|$ Determinant of a matrix.

$\langle \cdot, \cdot \rangle$ **or** $\langle \cdot, \cdot \rangle_{L^2}$ L^2 inner-product.

$\langle \cdot, \cdot \rangle_{H^1}$ H^1 inner-product.

$\langle \underline{\cdot}, \underline{\cdot} \rangle_{div}$ $H(div)$ inner-product.

$\langle \cdot, \cdot \rangle_{H^{1/2}(\Gamma^h)\times H^{-1/2}(\Gamma^h)}$ Duality between $H^{1/2}(\Gamma^h)$ and $H^{-1/2}(\Gamma^h)$.

$||\cdot||$ **or** $||\cdot||_{L^2}$ L^2 norm.

$||\cdot||_{H^1}$ H^1 norm.

$||\underline{\cdot}||_{div}$ $H(div)$ norm.

γ Trace operator in H^1 space.

γ_{div} Trace operator in $H(div)$ space.

Π^h L^2 projection-based operator.

$\Pi^h_{H^1}$ H^1 projection-based operator.

Π^h_{div} $H(div)$ projection-based operator.

$[\![\underline{\underline{\sigma}}]\!]$ $\underline{\underline{\sigma}} \cdot \underline{n}$ on Γ^h and $\underline{\underline{\sigma}}^+ \cdot \underline{n}^+ + \underline{\underline{\sigma}}^- \cdot \underline{n}^-$ on Γ^h.

Function spaces

$\mathbb{P}_k$ Space of polynomials of degree $\leq k$.

L^2 Lebesgue space.

H^1 Hilbert space.

$H^{1/2}$ The H^1 trace function space.

$H(div)$ Space of square-integrable divergence.

$H^{-1/2}$ The $H(div)$ trace function space.

$\mathcal{V}^h$ Finite-dimensional H^1 subspace.

$\mathcal{M}^h$ Finite-dimensional space for the Lagrange multipliers $L^2(\mathcal{E}^h)$.

$\mathcal{Z}^h$ Finite-dimensional L^2 subspace.

$\underline{\mathcal{Z}}^h$ Vector-valued finite-dimensional L^2 subspace.

$\underline{\mathcal{Q}}^h$ Finite-dimensional $H(div)$ subspace.

Geometry

$\mathbb{R}^d$ Euclidean space.

d Dimension.

$\underline{x}$ Geometric coordinates in $\mathcal{K}$.

$\underline{\hat{x}}$ Parametric coordinates in $\hat{K}$ composed of $(\hat{\xi}, \hat{\eta})$ for 2D or $(\hat{\xi}, \hat{\eta}_1, \hat{\eta}_2)$ for 3D domains.

$\mathcal{K}$ Bounded domain in $\mathbb{R}^d$ (or geometric element).

$\partial\mathcal{K}$ Boundary of $\mathcal{K}$.

$\hat{K}$ Master element.

Ω Domain in $\mathbb{R}^d$ with sufficiently regular boundary.

$\mathcal{T}^h$ Partition of the domain Ω into subdomains/elements.

Γ Boundary of Ω.

Γ^h Set of boundary edges or facets over Γ.

e_{ij} Interface between the elements $\mathcal{K}_i$ and $\mathcal{K}_j$.

$\mathcal{E}^h$ Skeleton mesh.

F Geometric affine transformation.

P Piola transformation.

$\underline{\underline{J}}$ Jacobian matrix for a geometric map F.

$\underline{n}$ Outward normal vector.

h Characteristic mesh size.

$\hat{I}$ Interval $[-1, 1]$.

$\hat{Pr}$ Prism described by $\{0 \leq \hat{\xi} \leq 1, 0 \leq \hat{\xi} + \hat{\eta}_1 \leq 1, 0 \leq \hat{\eta}_2 \leq 1\}$.

$\hat{Py}$ Parametric pyramid described by $\{-1 \leq \hat{\xi} - \hat{\eta}_2 \leq 1, -1 \leq \hat{\eta}_1 - \hat{\eta}_2 \leq 1, 0 \leq \hat{\eta}_2 \leq 1\}$.

$\hat{He}$ Parametric hexahedron described by $-1 \leq \hat{\xi},\ \hat{\eta}_1,\ \hat{\eta}_2 \leq 1$.

$\hat{Q}$ Parametric quadrilateral $-1 \leq \hat{\xi},\ \hat{\eta} \leq 1$.

$\hat{T}$ Parametric triangle described by $\{0 \leq \hat{\xi} \leq 1, 0 \leq \hat{\xi} + \hat{\eta}_1 \leq 1\}$.

$\hat{Te}$ Parametric tetrahedron described by $\{0 \leq \hat{\xi} \leq 1, 0 \leq \hat{\xi} + \hat{\eta}_1 \leq 1, 0 \leq \hat{\xi} + \hat{\eta}_1 + \hat{\eta}_2 \leq 1\}$.

Finite elements and functions

$\mathcal{F}$ Finite element.

L_i DOF (elements of Σ).

Σ Set of linear forms for a basis of $\mathbb{P}$.

$\hat{\phi}$ Shape function in $\mathcal{V}^h(\hat{K}) \subset H^1(\hat{K})$.

f_n Chebyshev polynomial of n-th order.

$\underline{\hat{\psi}}$ Shape function in $\underline{\mathcal{Q}}^h(\hat{K}) \subset H(div; \hat{K})$.

Scalars, vectors and matrices

u State variable.

$\underline{\sigma}$ Flux variable.

ζ Lagrange multiplier.

u_D Dirichlet value for the state variable.

f Source term of a non-homogeneous PDE.

N_P Dimension of $\mathbb{P}_k$ space.

$\underline{\underline{K}}$ Stiffness matrix.

$\underline{S}$ Vector composed of the multiplier coefficients for $\underline{\sigma}^h \in \underline{\mathcal{Q}}^h$.

$\underline{U}$ Vector composed of the coefficients for $u^h \in \mathcal{Z}^h$ using the Mixed FEM.

$\underline{\mathcal{S}}$ Vector composed of the multiplier coefficients for $\underline{\sigma}^h \in \underline{\mathcal{Z}}^h$.

$\underline{\mathcal{U}}$ Vector composed of the multiplier coefficients for $u^h \in \mathcal{Z}^h$ using the Hybridized-Mixed FEM.

$\underline{G}$ Vector composed of $-\langle u_D, \underline{q}^h \cdot \underline{n} \rangle_{H^{1/2}(\Gamma^h) \times H^{-1/2}(\Gamma^h)}$.

$\underline{F}$ Vector composed of $-\langle f, v^h \rangle$.

$\underline{\mathcal{G}}$ Vector composed of $-\int_{\Gamma^h} u_D [\![\underline{q}^h]\!] ds$.

$\underline{\mathcal{F}}$ Vector composed of $-\langle f, z^h \rangle$.

$\underline{\mathcal{L}}$ Vector composed of the multiplier coefficients for $\underline{\zeta}^h \in \mathcal{M}^h$.

$\underline{\underline{\mathbb{H}}}$ Condensed force vector for the hybridized-mixed method.

$\underline{\underline{A}}$ Matrix composed of the bilinear form $a : \underline{\mathcal{Q}}^h \times \underline{\mathcal{Q}}^h \to \mathbb{R}$.

$\underline{\underline{B}}$ Matrix composed of the bilinear form $b : \mathcal{Z}^h \times \underline{\mathcal{Q}}^h \to \mathbb{R}$.

$\underline{\underline{\mathbb{A}}}$ Hybrid matrix composed of the bilinear form $a : \underline{\mathcal{Z}}^h \times \underline{\mathcal{Z}}^h \to \mathbb{R}$.

$\underline{\underline{\mathbb{B}}}$ Hybrid matrix composed of the bilinear form $b : \mathcal{Z}^h \times \underline{\mathcal{Z}}^h \to \mathbb{R}$.

$\underline{\underline{\mathbb{C}}}$ Hybrid matrix composed of the bilinear form $c : \mathcal{M}^h \times \underline{\mathcal{Z}}^h \to \mathbb{R}$.

$\underline{\underline{\mathbb{E}}}$ Condensed stiffness matrix for the hybridized-mixed method.

Chapter 3

Operators

$\nabla_{\underline{\eta}}$ Gradient operator over the mapped surface $\hat{L}$.

$\underline{\underline{L}}$ Differential operator.

$||_{H^s}$ H^s semi-norm.

$\langle \phi, \psi \rangle_{\nabla, S}$ The inner product between $\nabla\phi$ and $\nabla\psi$.

$\langle \phi, \psi \rangle_{\mathcal{E}, S}$ The inner product between $\underline{\underline{D}}\underline{\epsilon}(\phi)$ and $\underline{\epsilon}(\psi)$.

$\overset{\nabla}{\oplus}$ Gradient inner product orthogonality.

$\mathcal{I}_k^h$ Trace interpolant operator $H^s(\Gamma^h) \to \Lambda_k(\Gamma^h)$.

$\mathcal{F}_k^{h,\Delta}$ Harmonic virtual interpolant operator $H^s(\Gamma^h) \to \mathcal{V}_k^{h,\Delta}(\Gamma^h)$.

$a(\cdot, \cdot)$ Bilinear form $\mathbb{S}_k \times \mathbb{S}_k \to \mathbb{R}$.

$a^E(\cdot, \cdot)$ Bilinear form $\underline{\mathbb{S}}_k \times \underline{\mathbb{S}}_k \to \mathbb{R}$.

Function spaces

$C(\Gamma^S)$ Continuous space in Γ^S.

$C(\Gamma^S, \mathbb{R}^d)$ Continuous space for vector-valued functions in Γ^S.

$\mathcal{D}_k$ Duffy's space.

$\mathcal{D}_k^0(S)$ Duffy's bubble function space in S.

$\underline{\mathcal{D}}_k$ Duffy's space of vector-valued functions.

H^s General Sobolev space, $s \geq 1$.

H_0^1 Sobolev space of all functions that vanish at Γ.

$\mathcal{H}(S)$ Space of harmonic functions in S.

$\mathbb{D}_k^h(S)$ Finite-dimensional Duffy's polynomial space.

$\mathbb{D}_k^{0,h}(S)$ Finite-dimensional Duffy's polynomial bubble space.

$\mathbb{Q}_{k,k}$ Polynomial space of total degree k order in η_1 and η_2 direction.

$\mathcal{V}_k^h$ Polynomial finite-dimensional H^1 subspace up to $k-$-th order.

$\mathcal{V}_k^{h,FE}$ Polynomial finite-dimensional H^1 subspace for a conglomerate mesh $\mathcal{P}^h$.

$\mathcal{V}_k^{h,\Delta}$ Harmonic virtual space.

$\mathbb{S}_k$ SBFEM space for Harmonic problems.

$\underline{\mathbb{S}}_k$ SBFEM space for Elasticity problems with null body loads.

$\mathbb{S}_k^{h,0}$ SBFEM space of functions that vanish at $\partial\Omega$.

Λ_k Trace FE space composed of scalar functions $N_k^S(\underline{x})$.

$\underline{\Lambda}_k$ Trace FE space composed of vector-valued functions $\underline{N}_k^S(\underline{x})$.

Geometry

$\underline{x}_b$ Surface coordinate over $L \subset K$.

ξ Radial coordinate.

$\underline{\mathbf{a}}_i$ Vertices of K.

$\underline{\mathbf{a}}_0$ Collapsed vertex in K.

$\underline{\eta}$ Mapped surface coordinate over $\hat{L} \subset \hat{K}$ composed of (η_1, η_2).

S Star-shaped element or S-element.

∂S Boundary of a S-element.

$\mathbf{O}$ Scaling center of a S-element.

K Duffy element (also collapsed element).

∂K Boundary of K.

F_K Duffy's geometric transformation.

F_L Geometric transformation from $\hat{L}$ to L.

$\underline{\underline{J}}_K$ Jacobian matrix of Duffy's transformation F_K.

L Facet opposed to the collapsed side of K.

$\hat{L}$ Facet in $\hat{K}$ mapped from L in a Duffy element.

N^{Γ^S} Number of facets of a S-element.

$\mathcal{P}^h$ Conglomerate mesh of triangles, tetrahedrons, or pyramids that compose $\mathcal{T}^h$.

$\mathcal{T}^{h,S}$ Partition of a S-element into Duffy's elements.

Finite elements and functions

$\mathcal{N}^S$ Dimension of $\mathbb{S}_k$ space.

$\hat{\phi}$ SBFEM shape function given by $\hat{\phi} = \hat{\rho}(\xi)\hat{\alpha}(\underline{\eta})$.

$\hat{\psi}$ Duffy test function in $\mathcal{D}_k(\hat{K}) \subset H^1(\hat{K})$.

$q_i(\underline{x})$ SBFEM function associated to $\underline{\underline{\hat{Q}}}(\xi)$.

$\Gamma^{h,S}$ Scaled boundary finite element.

$\hat{\alpha}(\underline{\eta})$ Surface function for $\hat{\phi}$ in $\mathcal{V}_k(\hat{L})$.

$\underline{\hat{\alpha}}(\underline{\eta})$ Vector-valued surface function for $\underline{\hat{\phi}}$ in $\mathcal{V}_k(\hat{L})$.

$\hat{\beta}(\underline{\eta})$ Surface function for $\hat{\psi}$ in $\hat{L}$.

$\hat{\rho}(\xi)$ Radial function for $\hat{\phi}$.

$\hat{\tau}(\xi)$ Radial function for $\hat{\psi}$.

$E^h_{L^2}$ L^2 error $\|u - u^h\|_{L^2(\Omega)}$.

$E^h_{H^1}$ H^1 error $|u - u^h|_{H^1(\Omega)}$.

$\underline{\epsilon}(\underline{\phi})$ SBFEM strain vector approximation.

$\hat{N}^l_k(\underline{\eta})$ Shape functions in $\mathcal{V}_k(\hat{L})$.

$\underline{\hat{N}}^l_k(\underline{\eta})$ Vector-valued shape functions in $\mathcal{V}_k(\hat{L}; \mathbb{R}^d)$.

$\underline{N}^S_k(\underline{x}_b)$ Vector composed of the scalar shape functions $N^{n,S}_k(\underline{x}_b) \in \Lambda_k(\Gamma^S)$.

$\underline{\underline{N}}^S_k(\underline{x}_b)$ Matrix composed of the vector-valued shape functions $\underline{N}^{n,S}_k(\underline{x}_b) \in \underline{\Lambda}_k(\Gamma^S)$.

$\underline{\hat{\Phi}}(\xi)$ Product $\underline{a}^T\hat{\rho}(\xi)$.

$\underline{\hat{\Psi}}(\xi)$ Product $\underline{b}^T\hat{\tau}(\xi)$.

$\underline{B}_1(\underline{\eta})$ Column matrix composed of the product of $[\underline{\underline{J}}^{-1}_K(1, \underline{\eta})]^{-T}$ and the vector composed of the shape functions.

$\underline{B}_2(\underline{\eta})$ Column matrix composed of the product of $[\underline{\underline{J}}^{-1}_K(1, \underline{\eta})]^{-T}$ and the vector composed of the gradient of shape functions.

$\underline{\underline{B}}_1(\underline{\eta})$ Matrix composed of the product of $\underline{\underline{b}}_1$ and $\underline{\underline{\hat{N}}}^S_k(\eta)$.

$\underline{\underline{B}}_2(\underline{\eta})$ Matrix composed of the product of $[\underline{\underline{b}}_2 \quad \underline{\underline{b}}_3]$ and $\nabla_{\underline{\eta}}\underline{\underline{\hat{N}}}^S_k(\eta)$.

$\underline{\underline{X}}(\xi)$ Solution of the SBFEM eigenvalue problem.

$\underline{\underline{\hat{\Phi}}}(\xi)$ Matrix composed of $\underline{\hat{\Phi}}_i(\xi) = \underline{A}_{+,i}\xi^{\lambda_{+,i}}$.

$\underline{\underline{\hat{Q}}}(\xi)$ Matrix composed of $\underline{\hat{Q}}_i(\xi) = \underline{A}^q_{+,i}\xi^{\lambda_{+,i}}$.

Scalars, vectors and matrices

E Young modulus.

ν Poisson coefficient.

$\underline{a}$ Vector composed of the multiplier coefficients of $\hat{N}_k^S$ composing $\hat{\alpha}$.

$\underline{b}$ Vector composed of the multiplier coefficients of $\hat{N}_k^S$ composing $\beta(\underline{\eta})$.

$\underline{\underline{\mathbf{b}}}_i$ Matrix composed by multiplying $\underline{\underline{L}}$ and the i-th line of $[\underline{\underline{J}}_K^{-1}(1,\underline{\eta})]^{-T}$.

$\underline{u}$ Displacement.

$\underline{u}_D$ Prescribed displacement in Γ.

$\underline{\lambda}$ Vector composed of the SBFEM eigenvalues for the Poisson problem.

$\underline{\lambda}_+$ Vector composed of only the positive part of $\underline{\lambda}$.

$\underline{c}$ Vector composed of the SBFEM multiplier coefficients, given by $\underline{\underline{A}}^{-1}\underline{u}^S$.

$\underline{f}$ Force vector.

$\underline{u}^S$ Values for $\underline{u}(\xi = 1)$.

$\underline{\underline{A}}$ Matrix composed of the SBFEM eigenvectors associated to $\underline{\hat{\Phi}}(\xi)$ and $\underline{\lambda}$.

$\underline{\underline{A}}_+$ Matrix composed of the SBFEM eigenvectors $\underline{\underline{A}}$ associated to $\underline{\lambda}_+$.

$\underline{\underline{A}}^q$ Matrix composed of the SBFEM eigenvectors associated to $\underline{\hat{Q}}(\xi)$ and $\underline{\lambda}$.

$\underline{\underline{D}}$ Second-order constitutive tensor for Elasticity.

$\underline{\underline{I}}$ Identity matrix.

$\underline{\underline{E}}_0$ SBFEM coefficient matrix composed of $\underline{\underline{B}}_1^T\underline{\underline{B}}_1$ product for the Poisson problem;

$\underline{\underline{E}}_1$ SBFEM coefficient matrix composed of $\underline{\underline{B}}_2^T\underline{\underline{B}}_1$ product for the Poisson problem;

$\underline{\underline{E}}_2$ SBFEM coefficient matrix composed of $\underline{\underline{B}}_2^T\underline{\underline{B}}_2$ product for the Poisson problem;

$\underline{\underline{K}}^S$ SBFEM stiffness matrix.

$\underline{\underline{Z}}$ SBFEM Hamiltonian matrix composed of the SBFEM coefficient matrices for the Poisson problem.

Note: For the Elasticity problem, the SBFEM matrices and functions have a superscript e, for instance: $\underline{a}^e$, $\underline{b}^e$, $\hat{\rho}(\xi)^e$, $\hat{\tau}(\xi)^e$, $\underline{\hat{\Phi}}^e$, $\underline{\hat{\Phi}}^e$, $\underline{\underline{A}}^e$, $\underline{\lambda}^e$, $\underline{\underline{E}}_0^e$, $\underline{\underline{E}}_1^e$, $\underline{\underline{E}}_2^e$, $\underline{\underline{Z}}^e$.

Chapter 4

Operators

$\oplus$ Direct sum of function spaces.

Function spaces

$\mathcal{D}^0_{k,m}$ Space of Duffy polynomial bubbles of degree $\leq k$ in $\underline{\eta}$ and $\leq m$ in ξ-direction.

$\mathcal{D}^0_{k,m}$ Space of Duffy polynomial bubbles of degree $\leq k$ in $\underline{\eta}$ and ξ-direction.

$\mathbb{B}_k$ SBFEM bubble space for the Poisson problem.

$\underline{\mathbb{B}}_k$ SBFEM bubble space for the Elasticity problem.

$\mathbb{V}_k$ SBFEM space for scalar functions composed of $\mathbb{B}_k \oplus \mathbb{S}_k$.

$\underline{\mathbb{V}}_k$ SBFEM space for vector-valued functions composed of $\underline{\mathbb{B}}_k \oplus \underline{\mathbb{V}}_k$.

$\mathbb{V}^{0,h}_k$ Global SBFEM space of scalar functions that vanish at Γ.

$\underline{\mathbb{V}}^{0,h}_k$ Global SBFEM space of vector-valued functions that vanish at Γ.

Geometry

$\mathcal{P}^S$ Conglomerate mesh of triangles, tetrahedrons, or pyramids that compose $\mathcal{T}^{h,S}$.

Finite elements and functions

$\varphi_{m,n}(\underline{x})$ Duffy polynomial bubble of degree $\leq k$ for $\underline{\eta}$ and $\leq m$ for ξ-direction.

$\varphi_i(\underline{x})$ Duffy bubble function composed of the pair of eigenvalues and eigenvectors λ_i and $\underline{A}_i$.

$\underline{\varphi}_{m,n}(\underline{x})$ Vector-valued Duffy polynomial bubble of degree $\leq k$ for $\underline{\eta}$ and $\leq m$ for ξ-direction.

$\underline{\varphi}_i(\underline{x})$ Vector-valued Duffy bubble function composed of the pair of eigenvalues and eigenvectors λ^e_i and $\underline{A}^e_i$.

$\hat{\rho}^b_i(\xi)$ Radial component of $\varphi_i(\underline{x})$.

$\hat{\rho}^b_m(\xi)$ Radial component of $\varphi_{m,n}(\underline{x})$.

$\underline{\hat{\rho}}^b_i(\xi)$ Vector composed of ξ^k and ξ^{λ_i}.

$\underline{\hat{\rho}}^b_m(\xi)$ Vector composed of ξ^m and ξ^{m-1}.

$\underline{\underline{\hat{\rho}}}(\xi)$ Diagonal matrix diag$(\xi^{\underline{\lambda}-0.5(d-2)})$.

$\underline{\underline{\hat{\rho}}}^b(\xi)$ Matrix that gathers $\underline{\hat{\rho}}^b_m(\xi)$ and $\underline{\hat{\rho}}^b_i(\xi)$.

$\underline{\boldsymbol{\phi}}(\underline{x})$ Vector composed of the SBFEM basis function $\phi_i(\underline{x})$ for the Poisson problem.

$\underline{\hat{\boldsymbol{\Phi}}}(\xi)$ Vector composed of $\underline{\boldsymbol{\phi}}\ \underline{\underline{A}}^{-T}$.

$\underline{\hat{\boldsymbol{\Phi}}}^b(\xi)$ Vector composed of $\underline{\boldsymbol{\varphi}}\ \underline{\underline{T}}^T$.

Note: For the Elasticity problem, the SBFEM functions have a superscript e, for instance: $\rho^{b,e}(\xi)$, $\underline{\hat{\boldsymbol{\Phi}}}^e(\xi)$, $\underline{\hat{\boldsymbol{\Phi}}}^{b,e}(\xi)$.

Scalars, vectors and matrices

$\underline{F}$ Force vector for the SBFEM approximations in $\mathbb{V}_k$ or $\underline{\mathbb{V}}_k$.

$\underline{F}^{\partial}$ Force vector for the SBFEM approximations in $\mathbb{S}_k$ or $\underline{\mathbb{S}}_k$.

$\underline{F}^{b}$ Force vector for the SBFEM approximations in $\mathbb{V}_k$ or $\underline{\mathbb{V}}_k$.

$\underline{\underline{K}}^{\partial}$ Usual stiffness matrix for the SBFEM approximations.

$\underline{\underline{K}}^{b}$ Stiffness matrix composed of only SBFEM bubble approximations.

$\underline{\underline{T}}$ Matrix that gathers $\underline{t}$.

Chapter 5

Operators

Function spaces

$\mathbb{P}_{1,k}$ Space of polynomials of degree ≤ 1 in $\hat{\xi}$-direction and $\leq k$ in $\hat{\eta}$-direction.

Geometry

δ Infinitesimal dimensionless width of the FE cell.

C Subpartition of a FE cell.

$\bar{S}$ FE cell.

L_e Exterior facet of a FE cell.

L_i Fictitions interface facet of a FE cell.

F_C Geometric map from $\hat{K}$ to C.

$F_{L_e}(\underline{\hat{\eta}})$ Geometric map of the exterior facet L^e of a FE cell.

$F_{L_i}(\underline{\hat{\eta}})$ Geometric map of the fictitious interface facet L^i of a FE cell.

$F_{L_{int}}(\underline{\hat{\eta}})$ Geometric map of the interior facet L^{int} of a FE cell.

P_C Piola transformation for C.

$\underline{\underline{C}}_{\delta}$ Diagonal matrix composed of δ and $\hat{\xi}$ components of $\underline{\underline{J}}_C$

$\underline{\underline{J}}_C$ Jacobian matrix of the geometric transformation F_C.

$\mathcal{T}^{\bar{S}}$ Partition of the domain Ω into FE cells $\bar{S}$.

$n^{\bar{S}}$ Number of exterior facets of $\bar{S}$.

Finite elements and functions

$\hat{\phi}_i^i$ Shape functions related to the fictitious interface DOF $\underline{u}^i$.

$\hat{\phi}_i^e$ Shape functions related to the external DOF $\underline{u}^e$.

$\hat{\varphi}_i^i$ Shape functions related to the infinitesimal differential pressure.

$\hat{\varphi}_i^e$ Shape functions related to the average infinitesimal pressure.

$\underline{\varphi}$ Vector composed of the functions $\hat{\varphi}_i^i$ and $\hat{\varphi}_i^e$.

$\underline{\psi}^{int}$ Vector-valued shape functions to approximate the internal flux

$\underline{\psi}^i$, $\underline{\psi}^e$ Vector-valued shape functions to approximate the exterior flux.

Scalars, vectors and matrices

$\bar{\underline{u}}$ Infinitesimal average pressure of a FE cell.

$d\bar{\underline{u}}$ Infinitesimal "differential pressure" of a FE cell.

$\underline{u}^e$ Pressure in L^e.

$\underline{u}^i$ Pressure in L^i.

$\underline{\mathcal{L}}^i$ Lagrange multiplier DOF related to the differential external pressure.

$\underline{\mathcal{L}}^e$ Internal Lagrange multiplier DOF related to the external pressure.

$\underline{\underline{K}}^{ii}$ Stiffness matrix computed using φ^i.

$\underline{\underline{K}}^{ie}$ Stiffness matrix computed using φ^i and φ^e.

$\underline{\underline{K}}^{ee}$ Stiffness matrix computed using φ^e.

$\underline{\underline{E}}_0^{div}$, $\underline{\underline{E}}_1^{div}$, $\underline{\underline{E}}_2^{div}$ SBFEM coefficient matrices using the hybridized-mixed approach.

$\underline{\underline{Z}}^{div}$ SBFEM Hamiltonian matrix for the Darcy flow using a hybridized-mixed approach.

$\underline{\underline{\mathcal{X}}}(\xi)$ Matrix composed of $\underline{u}_i^e(\xi)$ and $\underline{q}_i(\xi)$.

$\underline{\underline{\mathbb{A}}}^{int,int}$ Submatrix of $\underline{\underline{\mathbb{A}}}$ using internal vector-valued functions.

$\underline{\underline{\mathbb{A}}}^{int,e}$ Submatrix of $\underline{\underline{\mathbb{A}}}$ using internal and external vector-valued functions.

$\underline{\underline{\mathbb{A}}}^{e,e}$ Submatrix of $\underline{\underline{\mathbb{A}}}$ using external vector-valued functions.

$\underline{\underline{\mathbb{B}}}^{pi,int}$ Submatrix of $\underline{\underline{\mathbb{B}}}$ using internal scalar and vector-valued functions.

$\underline{\underline{\mathbb{B}}}^{pi,e}$ Submatrix of $\underline{\underline{\mathbb{B}}}$ using internal scalar functions and external vector-valued functions.

$\underline{\underline{\mathbb{C}}}^{i,i}$ Submatrix of $\underline{\underline{\mathbb{C}}}$ using internal functions.

$\underline{\underline{\mathbb{C}}}^{e,e}$ Submatrix of $\underline{\underline{\mathbb{C}}}$ using external functions.

Summary

Chapter 1

Introduction

1.1 Motivation

Many physical problems are described through partial differential equations (PDEs) with divergence-free constraints (for instance, for a flux $\nabla \cdot \underline{\sigma} = 0$), such as incompressible Darcy flows, Navier-Stokes equations, and Maxwell equations (MASUD; HUGHES, 2002; COCKBURN; LI; SHU, 2004; XU; ZHANG, 2010; CARVALHO; DEVLOO; GOMES, 2020). For the first two problems, the divergence-free condition is explicitly an essential term of the equation. Neglecting this fact leads to numerical defects (COCKBURN; LI; SHU, 2004), such as nonphysical oscillations and instabilities (JO; KWAK; LEE, 2021). On the other hand, it is impracticable to impose divergence-free conditions employing the usual H^1 finite element (FE) approximations since it leads to non-local conservation flux (ARNOLD, 1990). Moreover, a combined system of transport and elliptic equations often describes these mechanical problems; so, most of the time, predicting the dual variable, such as the velocity or flux, is as important as approximating the primal variable, for instance the pressure.

Several techniques have been developed in the scope of the Finite Element Method (FEM) to compute locally conservative fluxes, such as Mixed FEM (BOFFI; BREZZI; FORTIN, 2013; ARNOLD, 1990), Hybridized-Mixed FEM (COCKBURN; GOPALAKRISHNAN, 2004), Continuous and Discontinuous Galerkin combined with additional post-processing techniques, to name a few (HUGHES et al., 2000; COCKBURN; LI; SHU, 2004; COCKBURN; GOPALAKRISHNAN; WANG, 2007). Among these methods, the Mixed FEM stands out because the divergence-free condition is imposed directly by the approximation space. Moreover, it leads to a straightforward variational formulation that approximates primal and dual variables with optimal convergence rates.

Although the Mixed FEM effectively establishes a locally conservative flux, numerical issues still arise in approximating divergence-free conditions in domains with singularities, such as crack tips, V-notches, re-entrant corners, or dissimilar materials. Performing flow simulations with divergence-free conditions and singularities over the domain is a current area of active research due to the numerical difficulties that emerge in this problem. Some strategies have been developed in the literature in recent years to solve locally conservative problems with singularities. For instance, the Mixed FEM was coupled to the smooth domain method by Belhachmi, Sac-Epée and Sokolowski (2005) for the simulation of cracks in elastic domains. To model dissimilar materials, Devloo et al. (2021) applied the

Multiscale Hybrid Method using Mixed formulations (MHM-$H(div)$) in a heterogeneous media case.

For fluid mechanics, Devloo et al. (2019a) also applied the MHM-$H(div)$ in two-dimensional fracture networks; and Berre et al. (2021) tested several strategies for simulating a single-phase flow in a three-dimensional fractured porous media, including Mixed FEM. Despite the mentioned advances, the formulations often lead to very complex approximations, high DOF, large computational costs, and remeshing techniques. On the other hand, the SBFEM approximates problems with square-root singularities with great accuracy, optimal rates of convergence, low DOFs, and no remeshing techniques are required (CHIONG et al., 2014; SONG; OOI; NATARAJAN, 2018; GUO et al., 2019b; ANKIT, 2021; COELHO; DEVLOO; GOMES, 2021). Thus, developing an SBFEM $H(div)$-compatible space would couple the advantages of SBFEM and Mixed FEM to target the aforementioned problems.

1.2 Justification

FEM is widely used to approximate PDEs due to its robustness and generality. Nonetheless, intrinsic constraints impose obstacles to simulating certain sorts of problems. For instance, FEM has limitations in accurately approximating analytical solutions having square-root singularities and infinite domains. Yet, the meshing procedure uses only simple convex polytopes, such as tetrahedra, pyramids, and hexahedra (3D) or triangles and quadrilaterals (2D).

Different techniques have been introduced in the literature to overcome these issues, such as the Extended Finite Element Method (XFEM), Smoothed Finite Element Methods (SFEM), and Virtual Element Methods (VEM) (NATARAJAN et al., 2014; VEIGA et al., 2013). The XFEM contributes to solving fracture problems but without improving the mesh flexibility. Although SFEM and VEM allow using meshes of generic polyhedra, they struggle to approximate square-root singularities. In a different direction, the Boundary Element Method (BEM) targets both issues and reduces the spatial dimension by one (ALIABADI, 2002), though it leads to a non-symmetric stiffness matrix and demands a fundamental solution often complicated.

As detailed in Table 1.1, the BEM and the SBFEM only require boundary discretization, reducing the spatial dimension for the solution by one and allowing a flexible mesh generation. But differently from BEM, SBFEM does not require any fundamental solution. In the SBFEM, the interior solution is almost analytical based on the interpolated approximation over the element's skeleton. The construction of the semi-analytical shape functions is performed through a simple eigenvalue problem. Although the goal of this thesis is not the simulation of unbounded media, SBFEM can be used to simulate infinite or semi-infinite domains, such as soil-structure interaction. For SBFEM and BEM, the radial condition at infinity is satisfied.

On the other hand, as well as the FEM, the SBFEM leads to sparse symmetric stiffness matrices that are easily invertible. Additionally, the computation of the Stress Intensity Factors (SIF) using SBFEM is straightforward since it is directly based on the approxi-

[1]Based on Mohasseb, S.: Accessed in: https://ethz.ch/content/dam/ethz/special-interest/baug/ibk/structural-mechanics-dam/education/femII/SBFEM1.pdf at Sep 24 2021

Table 1.1: Comparison of advantages and disadvantages of FEM, BEM, and SBFEM.[1]

	FEM	BEM	SBFEM
Only the surface is discretized (Reduction of the spatial dimension by 1)		X	X
No fundamental solution is required	X		X
Interior solution computed analytically using the surface approximation			X
Radiation condition at infinity satisfied for simulation of unbounded media		X	X
No discretization of free and fixed boundaries and interfaces between different materials			X
Straightforward calculation of stress concentrations and intensity factors based on their definition			X
Symmetric sparse stiffness matrix	X		X
Straightforward coupling of bounded and unbounded media	X		X
Straightforward three-dimensional fracture simulation		X	

mated solution. Recently, the SBFEM has been expanded to several applications, such as

- Crack propagation under themo-mechanical loads (IQBAL et al., 2021), cohesive crack propagation (ANKIT, 2021), concrete cracking due to corrosion (DAI; LONG; WANG, 2021) and three-dimensional fracture in brittle materials (ASSAF et al., 2022);
- Contact problems (YA et al., 2021; PRAMOD et al., 2021; WIJESINGHE et al., 2022);
- Image-based mesh generation (EISENTRÄGER et al., 2020; SAPUTRA et al., 2020);
- High-performance computing (HPC) (ZHANG et al., 2022);
- Fluid mechanics (PFEIL et al., 2021), to name a few.

Further details on applications will be addressed in Section 1.5, where a brief literature review is presented.

Despite the aforementioned recent advances in numerical applications, fluid simulations using the SBFEM are still incipient in the literature. Pfeil et al. (2021) simulate only the pressure using the Reynolds equation. In such study, convergence curves are not plotted for velocity and flow analysis is not performed. To the best of our knowledge, convergence analysis for Darcy, Stokes, and Navier-Stokes fluid simulations using the SBFEM is not available in the literature. On the other hand, several other FE techniques approximate compressible and incompressible fluids, such as Mixed FEM, Hybridized Mixed FEM, and Stabilized Methods. Emphasis is given in this thesis to the Mixed and the Hybridized Mixed FEM.

Whereas the classical FEM approximation approximates the Darcy flow in its primal form, which is a second-order PDE, the Mixed FEM involves approximating both pressure and flux through a system of first-order equations. The advantages of using mixed formula-

tions are depicted by Arnold (1990) and Boffi, Brezzi and Fortin (2013). The main asset is that mixed formulations allow imposing the divergence-free condition directly in the approximation space. Hence, the technique is appropriate for incompressible fluid simulation and conservative velocity fields, making it suitable to solve transport equations. For instance, for Stokes problems, methods based on approximating the primal form are usually impractical. The Mixed FEM becomes, therefore, a more straightforward and widely used alternative. In addition, higher accuracy of the primal variable is reported by Castro et al. (2016b), as well as for the dual variable approximation is reported by Castro et al. (2016b) and Arnold (1990).

However, a noticeable disadvantage of the Mixed FEM is that it leads to a saddle point problem; thus, the stiffness matrix is not positive definite. The Hybridized Mixed FEM, as detailed by Cockburn and Gopalakrishnan (2004), was conceived to overcome this issue. The hybridization consists in including Lagrange multipliers to impose the continuity restrictions between the finite elements in a weak form. It leads to a positive symmetric definite matrix, and the DOF can be reduced through a static condensation procedure.

Given the robust mathematical theory for error analysis (BOFFI; BREZZI; FORTIN, 2013; ARNOLD; BREZZI, 1985; ERN; GUERMOND, 2013), the framework of mixed and hybridized-mixed FE can be applied to the SBFEM, in order to obtain locally conservative subspaces. Among other applications, it is expected that the SBFEM-$H(div)$-compatible spaces lower computational cost for fluid simulations in fractured media. Yet, one can take advantage of the flexibility in mesh generation to simulate velocity fields, especially in solid-fluid interaction. Although the SBFEM developments will provide a framework to tackle these mechanical problems, this thesis focuses on the theoretical background of the method, as addressed in the following section.

1.3 Objectives

This thesis aims to develop a locally conservative formulation for the Scaled Boundary Finite Element Method (SBFEM). The proposed formulation is based on approximating a flow in a porous media using a Darcy flow formulation through the Mixed-SBFEM technique. An $H(div)$ compatible function space is constructed to approximate the flux, whereas a discontinuous SBFEM space is applied for the pressure.

The following milestones were accomplished to achieve this goal:

1. To define the SBFEM as a type of tensorial Duffy's approximation space;
2. To prove the mathematical convergence of the SBFEM;
3. To develop an approximation to solve non-homogeneous PDEs using a bubble function approach;
4. To construct an $H(\mathrm{div})$ function space for the SBFEM;
5. To implement the mathematical formulations in a C++ library, the NeoPZ, and perform numerical tests to analyze the convergence rates.

1.4 Outline of the thesis

The remainder of this thesis is organized into five additional chapters. First, introductory FEM concepts are presented. The contributions of this thesis are described from Chapter 3 to Chapter 5. In each chapter, numerical tests were included to verify the convergence rates numerically. Namely, each chapter refers to:

- Chapter 2: Presents the introductory concepts of FEM, such as the partition of the domain and geometry, function spaces, and variational statements of different approaches: Galerkin FEM, Mixed FEM, and Hybridized-Mixed FEM.
- Chapter 3: Presents the classical SBFEM formulation under the framework of Duffy's approximation. Some mathematical properties of the SBFEM spaces are discussed and applied to prove the optimal rates of convergence.
- Chapter 4: Proposes a bubble function space for SBFEM to approximate non-homogeneous PDEs in two and three-dimensional domains. The advantages of the approach are discussed: optimal rates of convergence, good computational cost, and the ease to construct the bubbles.
- Chapter 5: Describes the Mixed-SBFEM formulation and defines the construction process of the SBFEM-$H(div)$ function spaces to compute the flux numerically. It also presents and discusses examples of multiphysics simulation for a Darcy flow for 2D problems, including a problem with square-root singularity.
- Chapter 6: Summarizes the main conclusions of this thesis, as well as the novel contributions this thesis to the SBFEM research field. Suggestions for future research and topics for further investigation are briefly discussed.

1.5 A brief literature review

1.5.1 The Scaled Boundary Finite Element Method

The origin of the SBFEM remounts the method called "the consistent infinitesimal finite-element cell method" in the 1990s (WOLF; SONG, 1996). Initially, the method was conceived to simulate unbounded media and applied in the numerical simulation of soil-structure interaction. Wolf and Song's idea was to discretize only the structure-medium interface and obtain an analytical expression in the radial direction through the limit of an infinitesimal finite-element cell (WOLF; SONG, 1995a; WOLF; SONG, 1995b; SONG; WOLF, 1995).

Later, the Song and Wolf (1997) generalized the method using a Galerkin weighted residual technique to approximate a PDE by an ODE. Such an ODE, named the scaled boundary finite element equation in displacement, has the radial component as the independent variable. This equation is a well-known ODE, the Ricatti equation, in which the analytical solution is known and easy to compute through an eigenvalue problem. In such a work, the name "Scaled Boundary Finite Element method" was used for the first time. Indeed, the method is a FE technique where the discretization occurs only at the element's boundary. The interpolated solution over the element's skeleton is scaled into the domain, which can be either bounded or unbounded.

After these pioneer studies, the SBFEM has been applied to a wide range of applications. For instance, due to the SBFEM intrinsic features, the dynamic analysis of soil-structure interactions is straightforward (WOLF; SONG, 1998). Late in the 1990s, specifically in 1999, Song and Wolf (1999b) applied the SBFEM for a diffusion problem in a bi-material circular plate, where the analytical solution exhibits a singularity at the interface between the two materials. This paper showed that the method is relevant not only for unbounded domains but also to simulate problems that exhibit singularities in the analytic solution, such as cracks, V-notches, and re-entrant corners.

Initially, only problems with null body loads were under the scope of the numerical applications since the technique applied in SBFEM formulations leads to an ODE with a null source term, which is easier to obtain the analytical solution. Later, in 1999, Song and Wolf (1999a) proposed a procedure to compute the approximated solution of a non-homogeneous PDE by solving the resulting non-homogeneous ODE using the technique of variation of parameters. This strategy was applied by Song (2006) to the stress field analysis in multi-material domains under thermal loads and further extended to compute scaled boundary bubble functions (OOI; SONG; NATARAJAN, 2016; OOI; SONG; NATARAJAN, 2017). More recently, mathematical developments have shown the high-order completeness of scaled boundary approximated solution composed of the shape functions of the homogeneous equation and the bubble shape functions (JIA et al., 2020).

After Song and Wolf's publication on SBFEM with body loads (SONG; WOLF, 1999a), several papers focused on applying the method to the numerical analysis of a wide range of mechanical problems with body loads. Wolf and Song (2001) performed the analysis of benchmark problems of elastodynamics analysis, emphasizing that the body loads formulation does not need domain discretization. To simulate fracture mechanics benchmarks, Song and Wolf (2002) evaluated orthotropic materials with a crack and compared the results to reference solutions.

Approximating the SBFEM to the FEM users, Deeks and Wolf (2002a) deduced the Ricatti ODE through the virtual work technique. In addition, the authors verified that the ODE's eigenvalue and eigenvector pairs represent basic displacement modes. The SBFEM eigenvalues are always obtained in conjugate pairs $(\lambda_i, -\lambda_i),\ i = 1, ..., n$ where n is the number of modes. The negative eigenvalues and their respective eigenvectors represent displacement modes for unbounded domains, and the positive eigenvalues describe modes for bounded domains.

Still, in the early 2000s, Deeks and Cheng (2003) applied the SBFEM to potential flow simulations using the 2D Laplace equation for bounded and unbounded domains. For domains with singularities, square cylinders were considered as well as practical examples, such as the SBFEM as applied to compute the tangential velocity of a flow over a symmetric NACA 0012 wing. Expanding the range of applications, Song and Wolf (2002) analyzed stress singularities in anisotropic multi-material domains and Ekevid and Wiberg (2002) used SBFEM to simulate the effects of wave propagation due to high-speed trains. The innovation in this period involved not only practical engineering applications but also applying FE techniques to the SBFEM, such as adaptativity (DEEKS; WOLF, 2002b) and *a posteriori* error estimates (DEEKS; WOLF, 2002c).

From the mid-2000s onwards, the applications of the SBFEM in fracture mechanics had a noticeable increment. Chidgzey and Deeks (2005) showed that the scaled boundary finite element approximated solution converges to the Williams expansion of the asymptotic

field of crack tip in linear elastic. In other words, it means that the stress intensity factor (SIF) and the stress field can be directly represented using the SBFEM shape functions. The SIF and T-stresses are also computed for dynamic cases by Song and Vrcelj (2008), for transient dynamic cases by Yang, Deeks and Hao (2007) and for multi-material cracks and corners by Song (2005). Because of the similarities of the mesh generation in SBFEM and BEM, Yang (2006), Yang and Deeks (2007) and Ooi and Yang (2009) developed fully-automatic modeling of crack propagation combining an efficient remeshing procedure with a propagation criterion for linear and cohesive crack growth.

In addition to the aforementioned research, the modal interpretation of the SBFEM basis functions allowed applications of this method in a wider range of dynamic problems. Gravenkamp, Song and Prager (2012) performed the SBFEM in the dispersion and modal analysis of guided waves in plate structures, with application in structural monitoring. Just a year later, the formulation was extended for 3D waveguides in elastic problems (GRAVENKAMP et al., 2013), and subsequently, the 2D analysis was performed for plates with defects (GRAVENKAMP; BIRK; SONG, 2015). The wave propagation modeling using SBFEM was explored by Birk and Behnke (2012), Chen, Birk and Song (2015) in 3D layered soils considering damping and unbounded domains.

By the end of the 2010s, the flexibility of the SBFEM mesh generation was further explored through quadtree (2D) and octree (3D) meshes. The advantage of using the SBFEM in these cases is that no additional treatment is required due to the hanging nodes. To name a few applications in two-dimensional problems, Guo et al. (2019a) used image-based quadtree meshes to perform concrete fracture modeling at the mesoscale, whilst Pramod et al. (2019) used quadtree meshes to model phase-field brittle fractures. Yet, in 2D problems, the quadtree meshes were also applied to simulate nonlocal damage problems (ZHANG et al., 2019) and transient wave scattering (BAZYAR; SONG, 2017). For 3D cases, Liu et al. (2019) performed 3D image-based analysis using complex octree meshes and Zhang et al. (2018) applied octree meshes to perform 3D damage analysis using the SBFEM.

From 2020 to now: SBFEM as a general FE technique and further developments in numerical applications

Most recent papers further explore octree analysis through adaptative mesh generation, parallel computing, elastoplastic analysis, and composite materials. In addition to the application papers, theoretical studies show that SBFEM can be seen as a FE technique owning a very particular way to compute the shape functions.

Regarding mesh generation and octree meshes, several advances to perform the SBFEM analysis in more efficient ways have been addressed in the literature. An adaptive refinement technique allowed to locally refine octree meshes accordingly to an error indicator (ZHANG et al., 2020b). To take advantage of the growing CPU capacity of clusters, Zhang et al. (2021) developed a parallel explicit solver using MPI (Message Passing Interface) to perform explicit dynamic simulations using octree meshes and SBFEM approximations, obtaining good scalability to problems over a billion DOF. Automatic octree mesh generation was also applied in elastoplastic materials for static and dynamic cases (LIU et al., 2020).

Recent studies in composite materials also explore a wide range of applications. For instance, Dölling et al. (2020) examined the interlaminar failure in composite laminates.

Since these failures are usually triggered by stress concentrations, the SBFEM showed good agreement with experimental results in the literature. Liu et al. (2021) investigated transient dynamic behaviors of functionally graded material sandwich plates using the SBFEM due to the high efficacy and accuracy of the method. The advantages of SBFEM were explored by Zhang et al. (2020a) to simulate the mechanical behavior of fiber-reinforced composite materials, such as 3D specimens of concrete with fibers.

Recent mathematical studies about the SBFEM convergence were explored numerically by Gravenkamp, Saputra and Duczek (2021), theoretically by Jia et al. (2020), Bertrand, Boffi and Diego (2021), and both numerically and theoretically by Coelho, Devloo and Gomes (2021). Gravenkamp, Saputra and Duczek (2021) performed a numerical analysis involving the accuracy and convergence of the SBFEM, comparing different interpolants for the trace space. Lagrange polynomials, hierarchical shape functions, NURBS (Non-Uniform Rational B-Splines), and Fourier shape functions were applied to interpolate the solution at the element's skeleton. The authors observed no significant difference between Lagrange polynomials and hierarchical shape functions, whilst NURBS interpolation only showed relevance in isogeometric analysis. Jia et al. (2020) proved the high-order completeness of the SBFEM function space for two and three-dimensional problems, including curved boundaries and solution of PDEs with a source term. The key to the demonstration was to prove that the SBFEM space has the complete polynomial FE space, i.e. polynomial bases can be always obtained regardless of the shape of the scaled boundary FE.

The convergence analysis was explored by Bertrand, Boffi and Diego (2021), Coelho, Devloo and Gomes (2021) for the Laplace equation. Bertrand, Boffi and Diego (2021) focused their analysis on defining the SBFEM as a space of semi-discrete functions and constructing an interpolation operator onto this space. Likewise, Coelho, Devloo and Gomes (2021) proved the convergence through the definition of the SBFEM space, but the authors analyzed the properties of the SBFEM space in more detail. For instance, Coelho, Devloo and Gomes (2021) verified that the SBFEM basis function is a generic type of Duffy's function - a type of function known in applied mathematics and utilized in spectral methods. Furthermore, these spaces have interesting properties, such as the gradient-orthogonality of these functions and Duffy's bubble functions. This property was useful to prove the convergence and to show that the SBFEM has lower error values than traditional FEM.

As it can be seen, recent studies showed that the SBFEM is a FE technique in which the basis functions that compose the finite space are constructed in a particular way. It means that a wide range of mathematical demonstrations, *a priori*, and *a posteriori* error analysis, and application of this technique in other FE frameworks, such as multiscale methods, and De Rham sequences are still future research to be explored. This thesis aims to contribute to the SBFEM research by developing the method for the application in Mixed and Hibridized-Mixed FEM.

1.5.2 Mixed Finite Element Method

Although this thesis focuses on the SBFEM, it is valuable to highlight later developments and applications of the Mixed FEM. This topic does not intend to be exhaustive, but a summary of relevant research for this thesis is presented.

The Mixed method was initially conceived by engineers. The main focus was to solve incompressible elasticity or any other problem where there is a constraint like $\nabla \cdot \underline{\sigma} = 0$. The idea of writing the variational statement using a different approach is an old subject in the literature, dating from the 1950s (REISSNER, 1953). The author writes the variational statement for the elasticity problem by approximating both displacement and stress through a system of two equations. However, the term "Mixed methods" was only used in the 1960s (ARNOLD, 1990) to describe these sorts of methods where the displacement and the stress variables are approximated as primary variables.

So, in a generic concept, the Mixed FEM is a method to approximate the solution of PDEs by converting the problem from a second-order PDE into a system of first-order equations. It means that instead of approximating only one variable, known as the primal variable (such as pressure or displacement), the Mixed FEM approximates both primal and dual variables (velocity and stress, for instance) using compatible function spaces. For example, in Elasticity analysis, the classical FEM uses the H^1 space to approximate the displacement variable. These shape functions have the continuity property, described mathematically by having a square-integrable gradient. However, to approximate the stress variable using mixed methods, the appropriate choice of the function space for the stress variable is often the $H(div)$ space. Such a space has the feature of the normal vector continuity, mathematically described by basis functions owning square-integrable divergence.

To ease the understanding and focus on the purpose of this study, from this part onwards, the thesis will restrict the analysis of Mixed FEM as the procedure to approximate the dual variable using $H(div)$ spaces. Mathematical details about the formulation can be found in Chapter 5.

The Mixed Galerkin FEM can be applied for several engineering applications, for instance, in the simulation of incompressible elastic materials, Darcy flows, Kirchhoff-Love plate model and the Stokes Flow (ARNOLD, 1990). The latter is rarely used in its primal form, once it involves the inversion of the differential operator $\text{div}(\underline{\underline{C}}\ \underline{\underline{\mathcal{E}}}(\vec{v}))$, where $\mathcal{E}$ is the symmetric part of $\nabla\vec{v}$, with $\vec{v}$ denoting the velocity.

Due to the simplicity of the Darcy flow formulation and its applications in civil, geotechnical, and petroleum engineering, the Mixed FEM has been widely applied in these sorts of simulations. The advantages highlighted in these studies are mainly to overcome the loss of accuracy regarding the flux variable and the difficulties to impose mass conservation when using primal methods. Some other alternatives to tackle both problems (accuracy and mass conservation) can be found in the literature, such as additional post-processing of the velocity proposed by Malta, Loula and Garcia (2000). However, the simplicity of the mixed variational formulation made this method popular in conservative fluid simulations (MASUD; HUGHES, 2002).

To cite a few applications for the Darcy flow, in civil engineering one can find the Mixed FEM to simulate the diffusion of CO_2 in reinforced concrete structures (RADU et al., 2013). In the geotechnical area, Mixed methods have been applied to poroelasticity problems, in which the Darcy flow is coupled to the elasticity problem (TCHONKOVA; PETERS; STURE, 2008). Still based on Darcy flow and Mixed methods, Li, Liu and Lewis (2005) performed a coupled thermo-hydro-mechanical analysis in unsaturated porous media, through a poroplasticity model.

In Petroleum engineering, the simulation of Darcy flows has been performed through mixed methods with application in reservoir simulations. Arbogast and Wheeler (1995) applied the Mixed FEM to the simulation of the Darcy flow equation coupled to the advection-diffusion equation. Still, in the oil & gas area, BERGAMASCHI; MANTICA; MANZINI applied the mixed methods to simulate the black oil model - a compressible model of a reservoir, in which three independent components (oil, gas, and water) compose a three-phase flow (liquid, vapor, and aqua, respectively). Other noteworthy works on the simulation of the black oil model using the Mixed FEM can be found on the literature (WHEELER; WHEELER; YOTOV, 2002; SINGH; WHEELER, 2016; CORREA; MURAD, 2018).

Recently, multiscale methods based on the Mixed FEM have been applied to simulate Darcy flow in heterogeneous media. For instance, He et al. (2021) developed a technique named GMsFEM (Generalized Multiscale Finite Element Method) to simulate a single-phase flow in a 2D fractured porous media. Similarly, Devloo et al. (2019a) analyzed a flow in a 2D discrete fractured network in a porous using the MHM-$H(div)$ (Multiscale Hybrid Method for $H(div)$ compatible spaces). Later, Duran et al. (2021) applied the same method for two-phase flow in 3D domains. It is worth mentioning that the multiscale mixed methods can be also applied to elasticity problems, as it can be found in the studies of Devloo et al. (2021), Gomes, Pereira and Valentin (2020).

Hybridized Mixed Finite Element Method

From a generic point of view, hybrid FEM is any FE technique where Lagrange multipliers are applied to overcome troublesome constraints. Accordingly to Pian (1978), the name "Hybrid Model" was stated in 1968 to describe an alternative procedure to compute the stiffness matrix, based on the Stress Method (PIAN, 1964). Instead of assuming continuous displacement functions, the displacement is imposed as a boundary condition at the element's interface. So, in summary, the variational statement is rewritten to: given prescribed boundary displacements, find the stress distribution over the element. A few years later, in 1970, the hybrid model was applied to generically name the sort of methods in which the variational statement is modified to relax the inter-element continuity constraint (TONG, 1970).

Although hybridization is not a technique recently discovered, this strategy was not fully explored in the early developments. One considerable disadvantage in that period was that weakening the continuity expressively increased the DOF. However, Cockburn and Gopalakrishnan re-addressed the idea at the beginning of the 2000s for two reasons (COCKBURN; GOPALAKRISHNAN, 2004; COCKBURN; GOPALAKRISHNAN; LAZAROV, 2009). First, the surge of computers and increased capacity to compute large problems. Second, they proposed the DOFs reduction just by performing a simple static condensation.

Since the hybridization technique is very generic, it can be applied to any method that requires inter-element continuity. For instance, this technique has been applied in classical FEM (COCKBURN; GOPALAKRISHNAN; WANG, 2007) and Mixed FEM (COCKBURN; GOPALAKRISHNAN, 2004), to name a few. Since this thesis performs a hybridization process in Mixed FEM, the studies presented are restricted to this method.

Cockburn and Gopalakrishnan (2004) list the benefits of hybridizing the Mixed FEM. The main advantage arises in the difficulty to invert the stiffness matrix resulting from

the mixed formulation. The Mixed variational statement leads to a saddle point problem, in which the resulting stiffness matrix is not positive definite; therefore, it requires considerable computational efforts to compute its inverse. Cockburn and Gopalakrishnan (2004) and Arnold and Brezzi (1985) summarized these points as follows:

1. The resulting stiffness matrix is positive definite, which means it is invertible using simple algorithms, such as the conjugate gradient method;
2. By performing a static condensation, the Hybridized Mixed FEM leads to a considerably smaller number of DOF;
3. The Lagrange multipliers can be also applied to provide *a posteriori* error estimates for Mixed and nonconforming methods.

Researches from the Computational Mechanics Laboratory

The Computational Mechanics Laboratory (LabMeC), headed by Prof. Devloo, has been developing research in Mixed and Hybrid FE techniques since 2010, when Siqueira, Devloo and Gomes (2010), Siqueira, Devloo and Gomes (2013) proposed a systematic procedure to construct high-order $H(div)$ and $H(curl)$ shape functions, based on hierarchical H^1 shape functions, initially for 2D problems. Later, in 2016, the 3D hierarchical shape functions were also developed by Castro et al. (2016b). Still, in 2016, Castro et al. (2016a) improved the procedure to compute the hierarchical high-order $H(div)$ shape functions. The authors proposed a procedure to compute the vector functions in the master element, mapped to the deformed element through the Piola transformation, either for linear or curved elements.

In the following years, several studies in $H(div)$ spaces were performed. Farias et al. (2017) proved that enriched versions of the BDFM (Brezzi-Douglas-Fortin-Marini) and RT (Raviart-Thomas) spaces increase the rates of convergence of Mixed FE approximations. Devloo et al. (2018a) applied the enriched spaces for elliptic problems in curved meshes conducted by the fact that the image of the flux space by the divergence operator coincides with the potential space in the master element. Exact sequences based on the De Rham diagram were constructed by Devloo et al. (2019b) for 3D meshes, including pyramids. The accuracy of the $H(div)$ functions in non-affine meshes was the goal of Devloo et al. (2020).

The aforementioned contributions were implemented in the NeoPZ environment, a C++ object-oriented finite element library. The NeoPZ was developed by Prof. Devloo and his co-workers from the Computational Mechanics Laboratory (LabMeC) (DEVLOO, 1997). The library's structure reflects the LabMeC's developments in novel FE techniques for simulating PDEs using a variety of functional spaces such as $H^1(\Omega)$, $H(div)$, discontinuous or $H(curl)$, and several procedures such as adaptativity, Mixed FE, Hybrid FE, Multiscale, and SBFEM.

Using the NeoPZ library, Forti et al. (2016) compared numerically continuous and discontinuous Galerkin, Mixed and Hybrid FEM in problem with smooth solutions, and another exhibiting a square-root singularity in 2D examples, whilst Devloo et al. (2018b) performed a similar analysis for 3D problems. As expected, the mixed formulation using $H(div)$ functions produced a better approximation of the dual variable for the smooth solution. However, 3D Mixed and hybrid problems exhibited, especially the enhanced version, increased the computational cost. For the singular solution, the local conservation

of the $H(div)$ space did not improve the solution. To improve the accuracy, the authors used quarter-point elements and *hp*-adaptativity, increasing the computational cost.

Due to the high level of abstraction of NeoPZ classes and blocks, the FE techniques can be coupled and used together to simulate a variety of problems. For instance, Devloo et al. (2016b), Devloo et al. (2016a) analyzed 2D elliptic PDEs with singular analytical solution through the combination of *hp* adapted mesh and $H(div)$ function spaces, while Devloo et al. (2018a) performed a similar analysis for 3D problems. The Multiscale Hybrid Method for Mixed FEM (MHM-$H(div)$) was also implemented in NeoPZ, combining the framework already existing in the library with upscaling and downscaling algebraic operations for Darcy flows (DURAN et al., 2019).

The NeoPZ is also applied in the simulation of a wide range of engineering problems. The applications mainly involved the oil and gas industry, such as reservoir and wellbore simulations. For instance, Duran et al. (2021) simulated a two-phase flow inside a 3D synthetic reservoir in a heterogeneous porous media using the MHM-$H(div)$. Verification benchmarks also emphasized the accuracy of the NeoPZ in the simulation of a single phase flow in 3D fractured porous media in Berre et al. (2021) studies. Elastoplastic models for petroleum geomechanics analysis were addressed by Duran et al. (2020), Sanei, Forti and Santos (2020), also with application in reservoir simulation.

Yet, in the geomechanics area, a numerical scheme for elastoplasticity was proposed to improve the integration algorithm, with special attention to the modified Cam-Clay criterion. For the wellbore simulation, it is worth mentioning the studies of Cecílio et al. (2019) that perform a stability analysis of excavated wells using an elastoplastic formulation based on the DiMaggio-Sandler model. Uncertainties regarding the heterogeneous media were incorporated into this analysis by Batalha et al. (2020), leading to a robust reliability model based on elastoplastic constitutive laws for vertical and inclined wellbores.

In recent applications, Carvalho, Devloo and Gomes (2020) applied the mixed FEM in computational fluid mechanical problems, namely Brinkman, coupled Stokes-Darcy, and Stokes flow. Still, in fluid mechanics (DEVLOO et al., 2019a), the MHM-$H(div)$ implemented in NeoPZ was applied in 2D flow simulations in fractured porous media. Electromagnetic problems were addressed by Orlandini et al. (2018), Orlandini et al. (2019) making use of the $H(curl)$ function spaces to improve the accuracy of waveguide simulations. The adaptative mesh refinement techniques available in NeoPZ were applied to the simulation of marine ice sheet stability, useful to predict the evolution of ice sheets in a changing climate (SANTOS et al., 2019).

As can be seen through the literature review, the LabMeC expertise in Mixed FEM supports the development of the SBFEM for Mixed FE formulations. Although this thesis focuses on theoretical and convergence studies, the SBFEM-$H(div)$ formulation can be explored for complex simulation, for instance, in conservative flows in domains with singularities, such as discrete fracture networks.

Chapter 2

Introductory Concepts of Finite Element

A classical definition of a finite element was established by Ciarlet (2002) as a triad $\mathcal{F} = (\mathcal{K}, \mathbb{P}, \Sigma)$ where

1. $\mathcal{K}$ denotes a bounded domain in the Euclidean space $\mathbb{R}^d$, where d is the dimension that can be either $d = 0$ a point, $d = 1$ a line, $d = 2$ a triangle or quadrilateral, and $d = 3$ a tetrahedron, a prism, or an hexahedron;
2. $\mathbb{P}$ denotes a space of polynomials on $\mathcal{K}$ of finite dimension $dim(\mathbb{P}) = N_P$;
3. Σ denotes a set of linear forms for a basis of $\mathbb{P}$, i.e. $\Sigma = \{L_1, L_2, ..., L_{N_P}\}$, such that

$$L_i \ : \ \mathbb{P} \rightarrow \mathbb{R}, \ i = 1, 2, ..., N_P,$$

   L_i the elements of Σ are often called DOF.

Each component of the triple is explored briefly in the sequence of this chapter.

2.1 Geometry

As mentioned in the triad definition, the geometry of a FE is defined as a bounded domain in a Euclidean space $\mathcal{K} \subset \mathbb{R}^d$ that can be either:

- $d = 0$: a point;
- $d = 1$: a line;
- $d = 2$: a triangle or a quadrilateral;
- $d = 3$: a tetrahedron, a hexahedron, a pyramid, or a prism.

The most classical family of FE is the affine FEs. For those elements, an affine transformation $F : \underline{x} \rightarrow \underline{\hat{x}}$ maps from the coordinates $\underline{\hat{x}} \in \hat{K}$ in the master element, to coordinates in the deformed element $\underline{x} \in \mathcal{K}$ (see Fig. 2.1 (a)). A most general case, but also classic, are the isoparametric elements, in which the geometric transformation can map from the master element to a deformed element with curved boundaries. Both families are illustrated in Fig. 2.1.

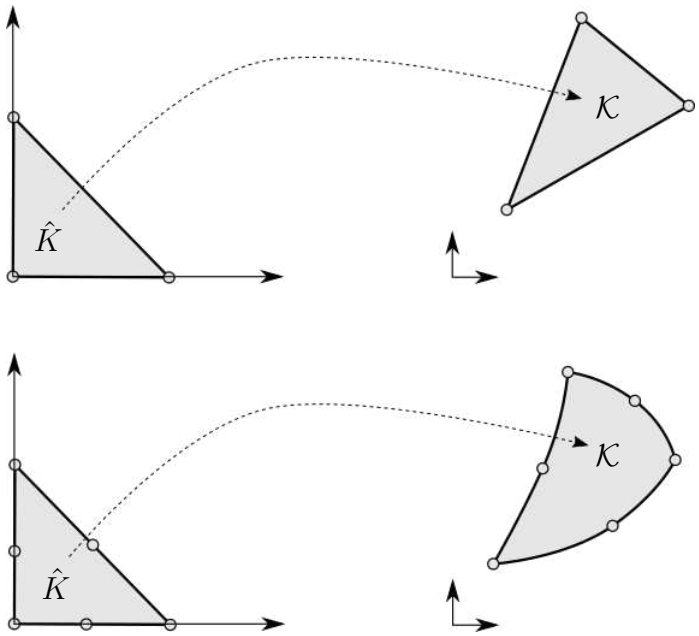

Figure 2.1: Affine and isoparametric map from a master element $\hat{K}$ in the parametric space $(\hat{\xi}, \hat{\eta})$ to a deformed element $\mathcal{K}$ in Cartesian coordinates (x, y).

Let us consider the parametric coordinates $\underline{\hat{x}} \in \mathbb{R}^2 = \left(\hat{\xi}, \hat{\eta}\right)$ and $\underline{\hat{x}} \in \mathbb{R}^3 = \left(\hat{\xi}, \hat{\eta}_1, \hat{\eta}_2\right)$.The master element $\hat{K}$ is the choice of the designer. Therefore, these bounds are commonly used bounds as opposed to "necessary" bounds:

- $d = 1$: a line defined by the interval $\hat{I} = \{\xi \in \mathbb{R} | -1 \leq \hat{\xi} \leq 1\}$;
- $d = 2$:
  - a triangle $\hat{T} = \{(\hat{\xi}, \hat{\eta}) \in \mathbb{R}^2 | 0 \leq \hat{\xi} \leq 1, 0 \leq \hat{\xi} + \hat{\eta} \leq 1\}$, or
  - a quadrilateral $\hat{Q} = \{(\hat{\xi}, \hat{\eta}) \in \mathbb{R}^2 \Big| -1 \leq \hat{\xi}, \hat{\eta} \leq 1\}$;
- $d = 3$:
  - a tetrahedron $\hat{T}e = \{(\hat{\xi}, \hat{\eta}_1, \hat{\eta}_2) \in \mathbb{R}^3 \Big| 0 \leq \hat{\xi} \leq 1, 0 \leq \hat{\xi} + \hat{\eta}_1 \leq 1, 0 \leq \hat{\xi} + \hat{\eta}_1 + \hat{\eta}_2 \leq 1\}$,
  - a pyramid $\hat{P}y = \{(\hat{\xi}, \hat{\eta}_1, \hat{\eta}_2) \in \mathbb{R}^3 \Big| -1 \leq \hat{\xi} - \hat{\eta}_2 \leq 1, -1 \leq \hat{\eta}_1 - \hat{\eta}_2 \leq 1, 0 \leq \hat{\eta}_2 \leq 1\}$,
  - a prism $\hat{P}r = \{(\hat{\xi}, \hat{\eta}_1, \hat{\eta}_2) \in \mathbb{R}^3 \Big| 0 \leq \hat{\xi} \leq 1, 0 \leq \hat{\xi} + \hat{\eta}_2 \leq 1, 0 \leq \hat{\eta}_2 \leq 1\}$, or
  - a hexahedron $\hat{H}e = \{(\hat{\xi}, \hat{\eta}_1, \hat{\eta}_2) \in \mathbb{R}^3 \Big| -1 \leq \hat{\xi}, \hat{\eta}_1, \hat{\eta}_2 \leq 1\}$.

Some properties related to the change of variables are useful for the FE formulations, such as the Jacobian matrix, given by

$$\underline{\underline{J}} := \nabla_{\underline{\hat{x}}} F(\underline{\hat{x}}). \tag{2.1.0}$$

The gradient of $\underline{x}$ in $\mathcal{K}$ can be computed using the geometric map F through the relationship

$$\nabla_{\underline{x}} v(\underline{x}) = \underline{\underline{J}}\ \nabla_{\underline{\hat{x}}} \hat{v}(\underline{\hat{x}}). \tag{2.1.0}$$

This property is especially helpful in H^1 finite element computations since it is easier to compute the gradient in a regular element $\hat{K}$ than in the deformed element $\mathcal{K}$. Another practical relationship is

$$\int_{\mathcal{K}} v \; d\mathcal{K} = \int_{\hat{K}} \hat{v} |\underline{\underline{J}}| \; d\hat{K},$$

where $|\underline{\underline{J}}|$ is the determinant of the Jacobian matrix.

For vector-valued functions, the map from a parametric function $\underline{\hat{q}}(\hat{K}) \in \left[L^2(\hat{K})\right]^d$ to $\underline{q}(\mathcal{K}) \in [L^2(\mathcal{K})]^d$ is defined by Piola transformation $P : [L^2(\hat{K})]^d \rightarrow [L^2(\mathcal{K})]^d$, given by Boffi, Brezzi and Fortin (2013)

$$\underline{q}(\underline{x}) = P(\underline{\hat{q}}(\underline{x})) := \frac{\underline{\underline{J}}}{|\underline{\underline{J}}|} \; \underline{\hat{q}}(\underline{\hat{x}}). \tag{2.1.0}$$

Applying the divergent operator leads to,

$$\nabla \cdot \underline{q}(\underline{x}) = \frac{1}{|\underline{\underline{J}}|} \; \nabla \cdot \underline{\hat{q}}(\underline{\hat{x}}). \tag{2.1.0}$$

Eq. (2.1) shows that it is possible to perform computations in vector-valued functions using only the Jacobian matrix and the vector-valued function $\underline{\hat{q}}$ in the master element $\hat{K}$. As a consequence, the following relationship applies (BOFFI; BREZZI; FORTIN, 2013)

$$\begin{aligned}
\int_{\mathcal{K}} \underline{q} \nabla \cdot v \; d\mathcal{K} &= \int_{\hat{K}} \underline{\hat{q}} \nabla \cdot \hat{v} \; d\hat{K}, \\
\int_{\mathcal{K}} v \left(\nabla \cdot \underline{q} \right) \; d\mathcal{K} &= \int_{\hat{K}} \hat{v} \left(\nabla \cdot \underline{\hat{q}} \right) \; d\hat{K}, \\
\int_{\partial \mathcal{K}} \underline{q} \cdot \underline{n} v \; ds &= \int_{\partial \hat{K}} \underline{\hat{q}} \cdot \underline{n} \hat{v} \; d\hat{s},
\end{aligned}$$

where $\underline{n}$ is the outward normal unit vector over the surface.

2.2 Function spaces

Consider $\Omega \subset \mathbb{R}^d$ a domain with a sufficiently regular boundary. The function spaces are defined as follows:

Lebesgue spaces - $L^2(\Omega)$

The $L^2(\Omega)$ function space, also known as the space of the square-integrable functions is defined as

$$L^2(\Omega) = \left\{ z \; \middle| \int_{\Omega} z^2 \; d\Omega < +\infty \right\}. \tag{2.2.0}$$

This space has the associated inner product

$$\langle z, v \rangle_{L^2} \equiv \langle z, v \rangle := \int_{\Omega} zv \; d\Omega, \tag{2.2.0}$$

and the norm

$$||z||_{L^2} \equiv ||z|| := \sqrt{\langle z, z \rangle}. \tag{2.2.0}$$

A property of interest regarding the L^2 space in FE analysis is that functions in this space do not need to be continuous inter-element.

Hilbert spaces - $H^1(\Omega)$

The Hilbert space $H^1(\Omega)$ is a type of Lebesgue space of square-integrable first derivatives, i.e.

$$H^1(\Omega) := \left\{ v \in L^2(\Omega) \,\middle|\, \frac{\partial v}{\partial x_i} \in L^2(\Omega),\ 1 \leq i \leq d,\ x_i \in \Omega \right\}, \tag{2.2.0}$$

The H^1 inner product is expressed as

$$\langle u, v \rangle_{H^1} = \langle u, v \rangle + \langle \nabla u, \nabla v \rangle. \tag{2.2.0}$$

and its norm is given by

$$||v||_{H^1} = \sqrt{\langle v, v \rangle_{H^1}} = \sqrt{||v||^2 + ||\nabla v||^2}. \tag{2.2.0}$$

Another important space is the $H^1(\Omega)$ trace functions space, defined as $H^{1/2}(\Gamma)$. A trace function is defined as $\gamma v = v|_\Gamma$ where $\Gamma = \partial\Omega$ is the boundary of Ω and γ is the trace operator such that $H^{1/2}(\Gamma) = \gamma(H^1(\Omega))$.

$H(div; \Omega)$ **space**

Another function space of interest is the $H(div; \Omega)$, denoted as

$$H(div; \Omega) := \left\{ \underline{q} \in \left[L^2(\Omega) \right]^d \mid \nabla \cdot \underline{q} \in L^2(\Omega),\ d = 2, 3 \right\}, \tag{2.2.0}$$

where $\nabla\cdot$ is the divergent operator, i.e. this space is composed of vector-valued functions with square-integrable divergence. Such a space has the inner product

$$\langle \underline{q}, \underline{v} \rangle_{div} := \langle \underline{q}, \underline{v} \rangle + \langle \nabla \cdot \underline{q}, \nabla \cdot \underline{v} \rangle, \tag{2.2.0}$$

and $H(div; \Omega)$-norm is computed as

$$||\underline{q}||_{div} = \sqrt{\langle \underline{q}, \underline{q} \rangle_{div}} = \sqrt{||\underline{q}||^2 + ||\nabla \cdot \underline{q}||^2}. \tag{2.2.0}$$

Similarly to $H^1(\Omega)$ space, there is a trace space for the $H(div; \Omega)$ functions, the $H^{-1/2}(\Gamma)$, such that $H^{-1/2}(\Gamma) = \gamma_{div}(H(div; \Omega))$. The $H(div; \Omega)$ trace operator is so as, for a vector-valued function $\underline{q}$, $\gamma_{div}(\underline{q}) = \underline{q} \cdot \underline{n}$.

The $H(div, \Omega)$ space is applied in approximating engineering problems where the local conservation property is required, such as for incompressible fluids. This thesis aims to define scaled boundary $H(div, \Omega)$ subspaces to be applied in the multiphysics simulation of Darcy flows. More details of this subspace are described in Chapter 5.

Properties relative to a partition of Ω

Partitioning the domain Ω into subdomains, more known as elements, is an essential feature of the FEM. Denote $\Omega = \mathcal{T}^h = \cup_{e=1}^n \mathcal{K}_e$ a partition of the domain in $\mathcal{K}_e$ elements that can assume one of the aforementioned geometric entities: triangles or quadrilaterals for 2D domains; and hexahedra, prism or pyramids for 3D ones. The interface of the elements is defined as

$$e_{ij} = \partial\mathcal{K}_i \cap \partial\mathcal{K}_j$$

and

$$\mathcal{E}^h = \bigcup_{ij} e_{ij} \bigcup \Gamma^h = \bigcup_{\mathcal{K}} \partial\mathcal{K}, \tag{2.2.0}$$

where Γ^h is the set of boundary edges or facets over $\Gamma = \partial\Omega$ and the index h denotes the characteristic mesh size. The geometric entities Γ^h and e_{ij} are illustrated in Fig. 2.2, respectively in blue and in red.

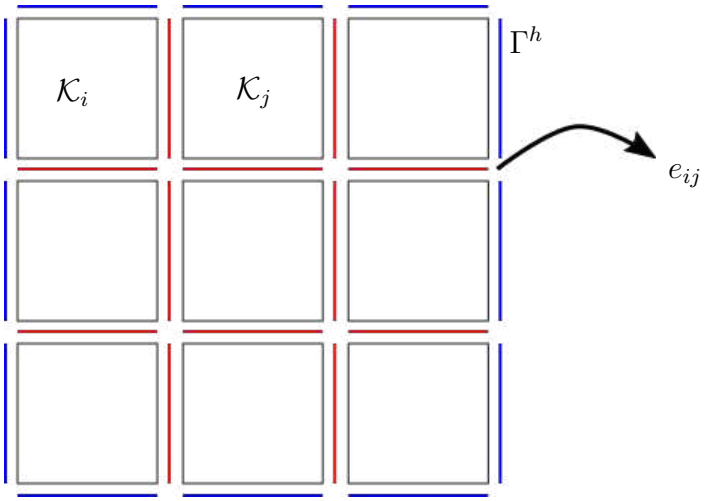

Figure 2.2: Skeleton mesh: Γ^h (in blue) is the discretization over Γ, and e_{ij} is the interface between the finite elements $\mathcal{K}_i$ and $\mathcal{K}_j$.

For the partition $\mathcal{T}^h$, the following subspaces apply

$$\begin{aligned}
\mathcal{V}^h &= \{v \ : \ v \in H^1(\Omega), v|_{\mathcal{K}_e} \in \mathcal{V}^h(\mathcal{K}_e), \ \mathcal{K}_e \in \mathcal{T}^h\}, \\
\underline{\mathcal{Q}}^h &= \{\underline{q} \ : \ \underline{q} \in H(div;\Omega), \underline{q}|_{\mathcal{K}_e} \in \underline{\mathcal{Q}}^h(\mathcal{K}_e), \ \mathcal{K}_e \in \mathcal{T}^h\}, \\
\mathcal{Z}^h &= \{z \ : \ z \in L^2(\Omega), z|_{\mathcal{K}_e} \in \mathcal{Z}^h(\mathcal{K}_e), \ \mathcal{K}_e \in \mathcal{T}^h\}.
\end{aligned}$$

Also, the following conformity requirements apply for $\mathcal{V}^h \subset H^1(\Omega)$ and $\underline{\mathcal{Q}}^h \subset H(div;\Omega)$:

- The trace of $v|_{\mathcal{K}_i}$ and $v|_{\mathcal{K}_j}$ is the same for each common face e_{ij};
- The trace of the normal component $\underline{n} \cdot \underline{q}|_{\mathcal{K}_i}$ and $\underline{n} \cdot \underline{q}|_{\mathcal{K}_j}$ is the same for each common face e_{ij}, where $\underline{n}$ is a unique outward normal vector to e_{ij};
- $\underline{q}|_{\mathcal{K}_i} \in [H^1(\mathcal{K}_e)]^d$ for each $\mathcal{K}_e \in \mathcal{T}^h$.

For $\mathcal{Z}^h$, there are no continuity requirements.

De Rham diagram

The De Rham diagram relates the aforementioned function spaces $L^2(\Omega)$, $H^1(\Omega)$, $H(div;\Omega)$ and its respective finite-dimensional spaces $\mathcal{Z}^h$, $\mathcal{V}^h$, and $\underline{\mathcal{Q}}^h$ employing differential operators. For two-dimensional cases, this diagram is written as

$$\begin{array}{ccccc}
H^1(\Omega) & \xrightarrow{\nabla\times} & H(div;\Omega) & \xrightarrow{\nabla\cdot} & L^2(\Omega) \\
\downarrow \Pi^h_{H^1} & & \downarrow \Pi^h_{div} & & \downarrow \Pi^h \\
\mathcal{V}^h & \xrightarrow{\nabla\times} & \underline{\mathcal{Q}}^h & \xrightarrow{\nabla\cdot} & \mathcal{Z}^h
\end{array}$$

where $\nabla\times$ is the curl operator, $\nabla\cdot$ is the divergence operator and the projection-based operators define the finite-dimensional subspaces

$$\Pi^h_{H^1} : H^1(\Omega) \to \mathcal{V}^h(\Omega), \quad \Pi^h_{div} : H(div,\Omega) \to \underline{\mathcal{Q}}^h(\Omega), \quad \Pi^h : L^2(\Omega) \to \mathcal{Z}^h(\Omega).$$

where k is the polynomial order. The De Rham diagram is a useful tool to create finite-dimensional approximation spaces that lead to formulations with stability properties (SOLIN; SEGETH; DOLEZEL, 2003a). For example for a function in the $H(div)$ space, $\underline{q} \in \underline{\mathcal{Q}}^h$ (ROBERTS; THOMAS, 1991),

$$\nabla \cdot \left(\Pi^h_{div,k}\underline{q}\right) = \Pi^h_{k-1}\left(\nabla \cdot \underline{q}\right).$$

Moreover, as highlighted by Solin, Segeth and Dolezel (2003b) and proved in Gurtin (1982), the operation $\nabla \cdot (\nabla \times u) = 0$.

Demkowicz et al. (2000) point out that the De Rham diagram provides the mathematical basis to prove stability and convergence for the Mixed Methods. These topics will be further addressed in Chapter 4. Moreover, the FE interpreted in a more general sense can be as sequences of scalar and vector-valued elements. Another practical application is that SBFEM-$H(div)$ spaces, or even the full De Rham sequence for two and three-dimensional problems, can be constructed by applying the curl or divergence operator. Since the scope of this thesis is to perform multiphysics simulations in 2D domains only, the author refers to Boffi, Brezzi and Fortin (2013) and Solin, Segeth and Dolezel (2003b) for the three-dimensional diagram.

2.2.1 Shape functions

The subspaces of local basis functions for $H^1(\mathcal{K}_e)$ and $H(div;\mathcal{K}_e)$ spaces are constructed in the master element $\hat{K}_e$ and mapped to $\mathcal{K}_e$ using the geometric map for scalar functions or the Piola transformation for vector-valued functions.

$H^1(\hat{K})$-conforming approximations

The construction of FE of H^1 approximations is well-known in the literature, with several options of Lagrangian and hierarchical shape functions, such as the ones presented by Solin, Segeth and Dolezel (2003a) and the references cited therein. This thesis uses the basis functions conceived by Devloo and co-authors and further detailed in Devloo, Bravo and Rylo (2009). These functions are implemented in NeoPZ and defined for topologies of one, two, and three dimensions in the master element $\hat{K}$ as defined in Section 2.1.

Let us consider $\mathcal{V}^h(\hat{K}) = \text{span}\left\{\hat{\phi}_i\right\} \subset H^1(\hat{K})$. For instance, for a quadrilateral element, the shape functions $\hat{\phi}_i$ are defined as:

1. 4 vertex functions:
   - $\hat{\phi}^{v_0}(\hat{\xi},\hat{\eta}) = \dfrac{1-\hat{\xi}}{2}\dfrac{1-\hat{\eta}}{2}$
   - $\hat{\phi}^{v_1}(\hat{\xi},\hat{\eta}) = \dfrac{1+\hat{\xi}}{2}\dfrac{1-\hat{\eta}}{2}$
   - $\hat{\phi}^{v_2}(\hat{\xi},\hat{\eta}) = \dfrac{1+\hat{\xi}}{2}\dfrac{1+\hat{\eta}}{2}$

- $\hat{\phi}^{v_3}(\hat{\xi},\hat{\eta}) = \dfrac{1-\hat{\xi}}{2}\dfrac{1+\hat{\eta}}{2}$

2. $4(k-1)$ edge functions:
   - $\hat{\phi}_n^{e_0}(\hat{\xi},\hat{\eta}) = \hat{\phi}^{v_0}(\hat{\xi},\hat{\eta})\left[\hat{\phi}^{v_1}(\hat{\xi},\hat{\eta}) + \hat{\phi}^{v_2}(\hat{\xi},\hat{\eta})\right] f_n(\xi)$
   - $\hat{\phi}_n^{e_1}(\hat{\xi},\hat{\eta}) = \hat{\phi}^{v_1}(\hat{\xi},\hat{\eta})\left[\hat{\phi}^{v_2}(\hat{\xi},\hat{\eta}) + \hat{\phi}^{v_3}(\xi,\eta)\right] f_n(\hat{\eta})$
   - $\hat{\phi}_n^{e_2}(\hat{\xi},\hat{\eta}) = \hat{\phi}^{v_2}(\hat{\xi},\hat{\eta})\left[\hat{\phi}^{v_3}(\hat{\xi},\hat{\eta}) + \hat{\phi}^{v_0}(\hat{\xi},\hat{\eta})\right] f_n(-\hat{\xi})$
   - $\hat{\phi}_n^{e_3}(\hat{\xi},\hat{\eta}) = \hat{\phi}^{v_3}(\hat{\xi},\hat{\eta})\left[\hat{\phi}^{v_0}(\hat{\xi},\hat{\eta}) + \hat{\phi}^{v_1}(\hat{\xi},\hat{\eta})\right] f_n(-\hat{\eta})$
3. $(k-1)^2$ internal bubble functions:
   - $\hat{\phi}^b_{n_0,n_1}(\hat{\xi},\hat{\eta}) = \hat{\phi}^{v_0}(\hat{\xi},\hat{\eta})\hat{\phi}^{v_2}(\hat{\xi},\hat{\eta}) f_{n0}(\hat{\xi}) f_{n1}(\hat{\eta})$, where $0 \leq n_0, n_1 \leq k-2$.

$H(div,\hat{K})$ shape functions

The $H(div,\hat{K})$ shape functions applied in this thesis followed the methodology presented by Siqueira, Devloo and Gomes (2013). Define the normal vectors $\underline{n}_0 = (0,-1)$, $\underline{n}_1 = (1,0)$, $\underline{n}_2 = (0,1)$, $\underline{n}_3 = (-1,0)$ for the edges 0 to 3. The approximation space the $\underline{\mathcal{Q}}^h(\hat{K}) = \text{span}\{\underline{\hat{\psi}}_i\} \subset H(div;\hat{K})$ is summarized below for a quadrilateral master element.

1. $4(k+1)$ edge functions;
   - Edge 0: $\underline{\hat{\psi}}_0^{e_0}(\hat{\xi},\hat{\eta}) = \hat{\phi}^{v_0}(\hat{\xi},\hat{\eta})\ \underline{n}_0, \quad \underline{\hat{\psi}}_1^{e_0}(\hat{\xi},\hat{\eta}) = \hat{\phi}^{v_1}(\hat{\xi},\hat{\eta})\ \underline{n}_0;$
   - Edge 1: $\underline{\hat{\psi}}_0^{e_1}(\hat{\xi},\hat{\eta}) = \hat{\phi}^{v_1}(\hat{\xi},\hat{\eta})\ \underline{n}_1, \quad \underline{\hat{\psi}}_1^{e_1}(\hat{\xi},\hat{\eta}) = \hat{\phi}^{v_2}(\hat{\xi},\hat{\eta})\ \underline{n}_1;$
   - Edge 2: $\underline{\hat{\psi}}_0^{e_2}(\hat{\xi},\hat{\eta}) = \hat{\phi}^{v_0}(\hat{\xi},\hat{\eta})\ \underline{n}_2, \quad \underline{\hat{\psi}}_1^{e_2}(\hat{\xi},\hat{\eta}) = \hat{\phi}^{v_1}(\hat{\xi},\hat{\eta})\ \underline{n}_2;$
   - Edge 3: $\underline{\hat{\psi}}_0^{e_3}(\hat{\xi},\hat{\eta}) = \hat{\phi}^{v_0}(\hat{\xi},\hat{\eta})\ \underline{n}_3, \quad \underline{\hat{\psi}}_1^{e_3}(\hat{\xi},\hat{\eta}) = \hat{\phi}^{v_1}(\hat{\xi},\hat{\eta})\ \underline{n}_3;$
2. $2(k-1)^2$ internal functions;
   - $\underline{\hat{\psi}}^{b_1}_{n_0,n_1}(\hat{\xi},\hat{\eta}) = \hat{\phi}^b_{n_0,n_1}(\hat{\xi},\hat{\eta})\ \underline{n}_2, \quad \underline{\hat{\psi}}^{b_2}_{n_0,n_1}(\hat{\xi},\hat{\eta}) = \hat{\phi}^b_{n_0,n_1}(\hat{\xi},\hat{\eta})\ \underline{n}_3$

     $\underline{\hat{\psi}}^{b_n}_{n,i}(\hat{\xi},\hat{\eta}) = \hat{\phi}^{e_i}_n(\hat{\xi},\hat{\eta})\ \underline{n}_{i+1}$

Two edge functions and two internal $H(div;\hat{K})$ functions are plotted in Fig. 2.3 for $k=2$, illustrating the basis functions already implemented in NeoPZ.

2.3 Variational Statement

Consider as the model problem the Poisson equation, for a given force term $f \in L^2(\Omega)$, given by

$$\Delta u = f$$
$$u|_\Gamma = u_D$$

where $\Delta u = \nabla \cdot (\nabla u)$ is the Laplace operator, $u_D \in H^{1/2}(\Gamma)$ and γ the aforementioned trace operator and u_D smooth. The variational statement for this problem is written using

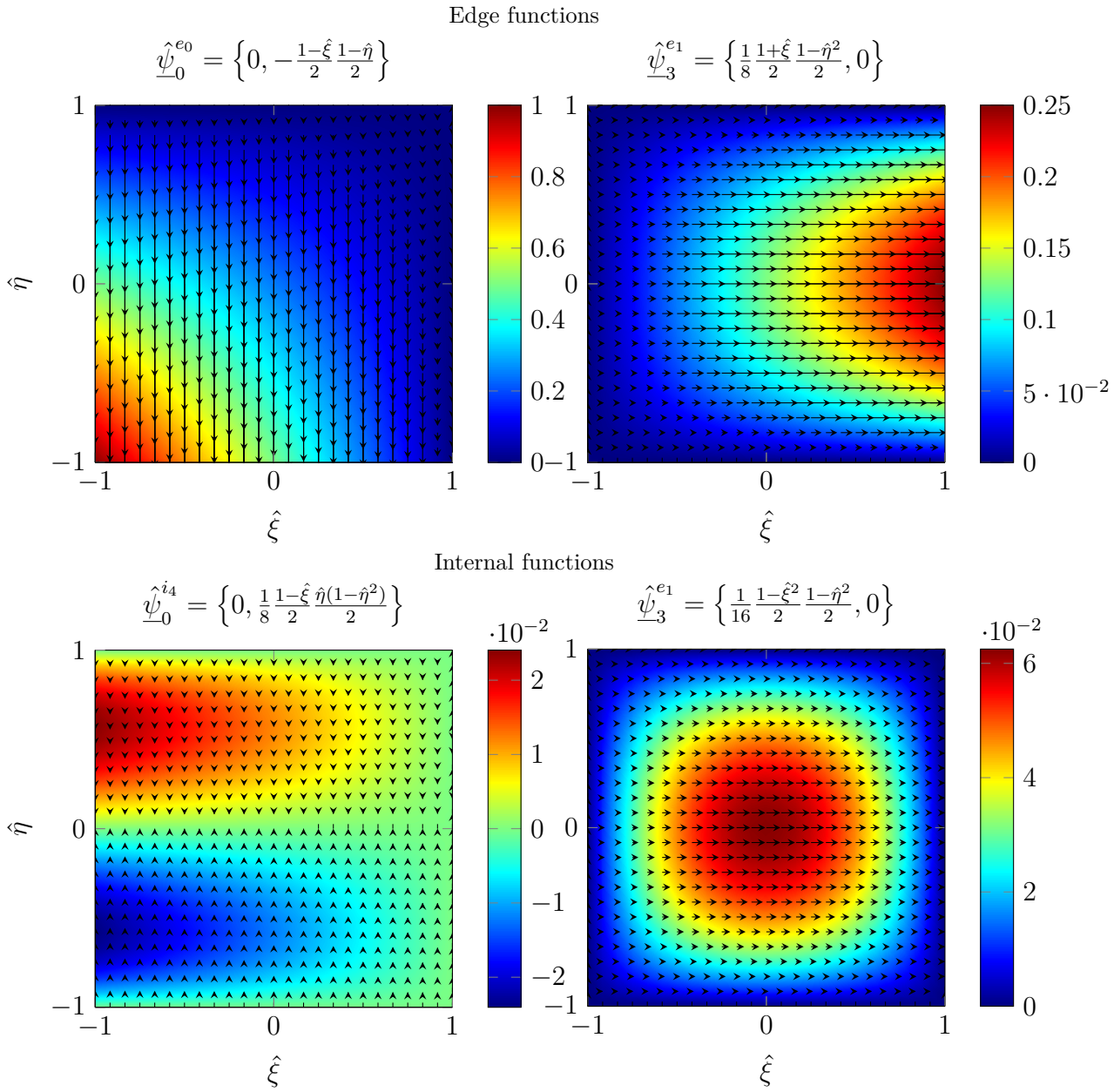

Figure 2.3: Edge and internal $H(div)$ shape functions $\underline{\psi} \in \underline{\mathcal{Q}}^h \subset H(div, \hat{K})$ defined in a parametric quadrilateral element $\hat{K} = \hat{Q}$.

three techniques, namely: the usual Galerkin method, and the Mixed and Hybridized Mixed techniques.

2.3.1 Galerkin Finite Elements

For the Galerkin method, (2.3) is multiplied by a test function $v \in H^1(\Omega)$, and integrated over Ω. Integrating by parts $\int_\Omega (\Delta u)v \; d\Omega$ the variational formulation is given by: Find $u \in H^1(\Omega)$ such that,

$$\int_\Omega \nabla u \cdot \nabla v = \int_\Omega f v \; d\Omega, \;\; \forall \; v \in H_0^1(\Omega)$$
$$u|_\Gamma = u_D.$$

Consider a general partition $\mathcal{T}^h = \{\mathcal{K}\}$ composed of a conglomerate of $\Omega = \bigcup_{\mathcal{K}} \mathcal{K}$, and let $\mathcal{V}^h$ be a finite-dimensional subspace of $H^1(\Omega)$, such that

$$\mathcal{V}^h = \{v^h \in H^1(\Omega) \ : \ \forall \mathcal{K} \in \mathcal{T}^h, \ v^h|_{\mathcal{K}} \in \mathcal{V}^h(\mathcal{K})\}$$

with $\mathcal{V}^h(\mathcal{K})$ defined in .

For $u^h, v^h \in \mathcal{V}^h$ and for all $\mathcal{K} \in \mathcal{T}^h$,

$$\int_\Omega \nabla u^h \cdot \nabla v^h \ d\Omega = \langle f, v^h \rangle \tag{2.3.0}$$

where $\langle f, v^h \rangle$ is the L^2 inner product $\int_\Omega f v^h \ d\Omega$.

2.3.2 Mixed Finite Elements

Mixed FEM was first introduced in the literature in 1967 by Herrmann (1967) for the plate elasticity problem. Generally speaking, a mixed method involves the simultaneous approximation of two or more fields defined in the physical problem (ROBERTS; THOMAS, 1991). More specifically, this thesis focus on the Mixed Dual FEM.

Introducing the vector field flux $\underline{\sigma} = \nabla u$, Eq. (2.3) can be written as a system of equations

$$\begin{aligned} \underline{\sigma} &= \nabla u \\ \nabla \cdot \underline{\sigma} &= f \\ u|_\Gamma &= u_D. \end{aligned}$$

An intuitive consequence of the mixed formulation is that each variable $\underline{\sigma}$ and u is approximated using two different finite element spaces. To have a convergent method, the approximation spaces must be chosen in such a way that $\underline{\sigma} \in H(div; \Omega)$ and $u \in L^2(\Omega)$. More details are addressed in Boffi, Brezzi and Fortin (2013).

To obtain the variational formulation, (2.3.2) is multiplied by a test function $z \in L^2(\Omega)$. Yet, (2.3.2) is multiplied by a test function $\underline{q} \in H(div; \Omega)$ and the divergence theorem is applied, leading to

$$\begin{aligned} \int_\Omega \underline{\sigma} \cdot \underline{q} \ d\Omega - \int_\Omega u \left(\nabla \cdot \underline{q}\right) \ d\Omega &= - \int_\Gamma u_D (\underline{q} \cdot \underline{n}) \ d\Gamma, \\ - \int_\Omega (\nabla \cdot \underline{\sigma}) \ z \ d\Omega &= - \int_\Omega f z \ d\Omega. \end{aligned}$$

Consider again a general partition $\mathcal{T}^h = \{\mathcal{K}\}$. Let $\mathcal{Z}^h = \text{span}\{\phi_i\}$ be a finite-dimensional subspace $L^2(\Omega)$ such that $u^h, z^h \in \mathcal{Z}^h, u|_{\mathcal{K}} \in \mathcal{Z}^h(\mathcal{K})$ and $z^h|_{\mathcal{K}} \in \mathcal{Z}^h(\mathcal{K})$. Also, consider $\underline{\mathcal{Q}}^h = \text{span}\{\underline{\psi}_j\} \subset H(div; \Omega)$ a finite-dimensional space such that $\underline{\sigma}^h, \underline{q}^h \in \underline{\mathcal{Q}}^h, \underline{\sigma}^h|_{\mathcal{K}} \in \underline{\mathcal{Q}}^h(\mathcal{K})$ and $\underline{q}^h|_{\mathcal{K}} \in \underline{\mathcal{Q}}^h(\mathcal{K})$. The discrete form of the variational mixed dual formulation is given by: Find $(\underline{\sigma}^h, u^h) \in \underline{\mathcal{Q}}^h \times \mathcal{Z}^h$

$$\begin{aligned} a(\underline{\sigma}^h, \underline{q}^h) + b(\underline{q}^h, u^h) &= -\langle u_D, \underline{q}^h \cdot \underline{n} \rangle_{H^{1/2}(\Gamma^h) \times H^{-1/2}(\Gamma^h)}, \ \forall \ \underline{q}^h \in \underline{\mathcal{Q}}^h, \\ b(\underline{\sigma}^h, z^h) &= -\langle f, z^h \rangle, \ \forall \ z^h \in \mathcal{Z}^h, \end{aligned}$$

where $a : \underline{\mathcal{Q}}^h \times \underline{\mathcal{Q}}^h \to \mathbb{R}$ and $b : \mathcal{Z}^h \times \underline{\mathcal{Q}}^h \to \mathbb{R}$ are bilinear forms given by, respectively,

$$a(\underline{\sigma}^h, \underline{q}^h) = \int_\Omega \underline{\sigma}^h \cdot \underline{q}^h \; d\Omega,$$
$$b(u^h, \underline{q}^h) = \int_\Omega u^h \left(\nabla \cdot \underline{q}^h\right) \; d\Omega.$$

$\langle f, v^h \rangle$ is the L^2 inner product and

$$\langle u_D, \underline{q}^h \cdot \underline{n} \rangle_{H^{1/2}(\Gamma^h) \times H^{-1/2}(\Gamma^h)} = \int_{\Gamma^h} u_D (\underline{q}^h \cdot \underline{n}) \; d\Gamma$$

is the duality between $H^{1/2}(\Gamma^h)$ and $H^{-1/2}(\Gamma^h)$. The finite element approximation leads to a matrix problem given by

$$\begin{pmatrix} \underline{\underline{A}} & \underline{\underline{B}}^T \\ \underline{\underline{B}} & \underline{\underline{0}} \end{pmatrix} \begin{Bmatrix} \underline{S} \\ \underline{U} \end{Bmatrix} = \begin{Bmatrix} \underline{G} \\ \underline{F} \end{Bmatrix} \tag{2.3.0}$$

The stiffness matrix

$$\underline{\underline{K}} = \begin{pmatrix} \underline{\underline{A}} & \underline{\underline{B}}^T \\ \underline{\underline{B}} & \underline{\underline{0}} \end{pmatrix} \tag{2.3.0}$$

is A and B are respectively an $n \times n$ matrix and an $m \times n$ matrix, $\underline{S}$ and $\underline{U}$ are $n \times 1$ and $m \times 1$ vectors, respectively, composed of the coefficients $\underline{\sigma}^h$ and u^h. Last, $\underline{G}$ and $\underline{F}$ are also $n \times 1$ and $m \times 1$ vectors composed of the linear forms previously described. Boffi, Brezzi and Fortin (2013) prove the solvability and stability of the system (2.3.2).

The inf-sup condition imposed in the mixed formulation leads to a saddle point problem. It implies that the stiffness matrix (2.3.2) is computationally hard to invert since the system is indefinite. A first possibility is to use a direct solver applying Pivot strategies. The second possibility is to eliminate $\underline{S}$ from the equations, which requires inverting $\underline{\underline{A}}$. However, $\underline{\underline{A}}^{-1}$ is a dense matrix, and the computational cost of inverting this matrix is prohibitive. A strategy to overcome this issue is to hybridize the mixed method, leading us to the next topic.

2.3.3 Hybridized-Mixed Finite Elements

The idea of Hybrid methods in general is to relax regularity requirements by introducing a Lagrange multiplier. As shown by Cockburn and Gopalakrishnan (2004), to hybridize the dual mixed formulation, the continuity of the normal flux required by the definition of $H(div; \Omega)$ is relaxed and imposed by using a Lagrange multiplier. Consider the following function spaces

$$\underline{\mathcal{Z}}^h = \left\{ \underline{z}_h \in L^2(\Omega) \times L^2(\Omega) \; : \; \underline{z}_h|_{\mathcal{K}} \in \; \mathbb{P}_k(\mathcal{K}) \times \mathbb{P}_k(\mathcal{K}) + \underline{x}\mathbb{P}_k(\mathcal{K}), \; \forall \mathcal{K} \in \mathcal{T}^h \right\}$$
$$\mathcal{M}^h = \left\{ \mu \in L^2(\mathcal{E}_h) \; : \; \mu_e \in \mathbb{P}_k(e), \; \forall \; e \in \mathcal{E}_h \right\}$$

where $\mathcal{E}^h$ is the skeleton mesh, already defined in (2.2). Thus, instead of defining the variational statement as finding $(\underline{\sigma}^h, \; u^h) \; \in \; \underline{\mathcal{Q}}^h \times \mathcal{Z}^h$, the hybridized-mixed method seeks $(\underline{\sigma}^h, \; u^h, \zeta^h) \; \in \; \underline{\mathcal{Z}}^h \times \mathcal{Z}^h \times \mathcal{M}^h$, where ζ^h are Lagrange multipliers that impose the normal flux continuity in weak form. The hybridized-mixed variational statement of the

model problem is given by: Find $(\underline{\sigma}^h,\ u^h, \zeta^h)\ \in\ \underline{\mathcal{Z}}^h \times \mathcal{Z}^h \times \mathcal{M}^h$ such that

$$\int_\Omega \underline{\sigma}^h \cdot \underline{q}^h\ d\Omega - \sum_{\mathcal{K}\in\mathcal{T}^h} \int_\mathcal{K} u^h \left(\nabla \cdot \underline{q}^h\right)\ d\Omega + \sum_{e\in\mathcal{E}^h} \int_e \zeta^h [\![\underline{q}^h]\!]\ ds = -\int_{\Gamma^h} u_D [\![\underline{q}^h]\!]\ ds,$$
$$-\sum_{\mathcal{K}\in\mathcal{T}^h} \int_\mathcal{K} v^h \nabla\cdot \underline{\sigma}^h\ d\Omega = -\int_\Omega f v^h\ d\Omega,$$
$$\sum_{e\in\mathcal{E}^h} \int_e \mu^h [\![\underline{\sigma}^h]\!] = 0,$$

for all $(\underline{q}^h, v^h, \mu^h) \in \underline{\mathcal{Z}}^h \times \mathcal{Z}^h \times \mathcal{M}^h$ where $[\![\underline{\sigma}^h]\!] = \underline{\sigma}^h \cdot \underline{n}$ on $s \in \Gamma^h$ and $[\![\underline{\sigma}^h]\!] = \underline{\sigma}^{h^+}_e \cdot \underline{n}^+_e + \underline{\sigma}^{h^-}_e \cdot \underline{n}^-_e$ on $e \in \mathcal{E}^h$. It means that the continuity of the normal flux is weakened and imposed by Lagrange multipliers that represent the trace of u^h over the element's skeleton. Written in matricial form, (2.3.3) to (2.3.3) lead to the system

$$\begin{pmatrix} \underline{\underline{\mathbb{A}}} & \underline{\underline{\mathbb{B}}}^T & \underline{\underline{\mathbb{C}}}^T \\ \underline{\underline{\mathbb{B}}} & \underline{\underline{0}} & \underline{\underline{0}} \\ \underline{\underline{\mathbb{C}}} & \underline{\underline{0}} & \underline{\underline{0}} \end{pmatrix} \begin{Bmatrix} \underline{\mathcal{S}} \\ \underline{\mathcal{U}} \\ \underline{\mathcal{L}} \end{Bmatrix} = \begin{Bmatrix} \underline{\mathcal{G}} \\ \underline{\mathcal{F}} \\ \underline{0} \end{Bmatrix}. \tag{2.3.0}$$

where $\mathcal{L}$ groups the multiplier coefficients for the Lagrange multiplier approximation. The approximations for $\underline{\sigma}_h$ and u_h are the same as in the Mixed FEM, which means that $\underline{\mathcal{S}}$ and $\underline{\mathcal{U}}$ remains being the coefficients of $\underline{\sigma}_h$ and u_h, respectively. $\underline{\underline{\mathbb{A}}}$, $\underline{\underline{\mathbb{B}}}$ and $\underline{\underline{\mathbb{C}}}$ in which the components are respectively given by the bilinear forms $a : \underline{\mathcal{Z}}^h \times \underline{\mathcal{Z}}^h \to \mathbb{R}$, $b : \mathcal{Z}^h \times \underline{\mathcal{Z}}^h \to \mathbb{R}$ and $c : \mathcal{M}^h \times \underline{\mathcal{Z}}^h \to \mathbb{R}$.

Although the system of equations increases considerably, the greatest advantage is that $\underline{\underline{\mathbb{A}}}$ is sparse, block diagonal, symmetric, and positive-definite. It is computationally cheaper, then, to compute the inverse $\underline{\underline{\mathbb{A}}}^{-1}$ and condense the DOF $\underline{\mathcal{S}}$ and $\underline{\mathcal{U}}$, leading to the system

$$\underline{\underline{\mathbb{E}}}\ \underline{\mathcal{L}} = \underline{\mathbb{H}} \tag{2.3.0}$$

where

$$\underline{\underline{\mathbb{E}}} = \underline{\underline{\mathbb{C}}}\ \underline{\underline{\mathbb{A}}}^{-1} \left(\underline{\underline{\mathbb{A}}} - \underline{\underline{\mathbb{B}}}^T \left(\underline{\underline{\mathbb{B}}}\ \underline{\underline{\mathbb{A}}}^{-1} \underline{\underline{\mathbb{B}}}^T\right)^{-1} \underline{\underline{\mathbb{B}}}\right) \underline{\underline{\mathbb{A}}}^{-1} \underline{\underline{\mathbb{C}}}^T$$
$$\underline{\mathbb{H}} = \underline{\mathbb{H}}_g + \underline{\mathbb{H}}_f$$
$$\underline{\mathbb{H}}_g = -\underline{\underline{\mathbb{C}}}\ \underline{\underline{\mathbb{A}}}^{-1} \left(\underline{\underline{\mathbb{A}}} - \underline{\underline{\mathbb{B}}}^T \left(\underline{\underline{\mathbb{B}}}\ \underline{\underline{\mathbb{A}}}^{-1} \underline{\underline{\mathbb{B}}}^T\right) \underline{\underline{\mathbb{B}}}\right) \underline{\underline{\mathbb{A}}}^{-1} \underline{\mathcal{G}}$$
$$\underline{\mathbb{H}}_f = -\underline{\underline{\mathbb{C}}}\ \underline{\underline{\mathbb{A}}}^{-1} \underline{\underline{\mathbb{B}}}^T \left(\underline{\underline{\mathbb{B}}}\ \underline{\underline{\mathbb{A}}}^{-1} \underline{\underline{\mathbb{B}}}^T\right) \underline{\mathcal{F}}$$

The local condensed stiffness matrix and nodal force vector are assembled and a smaller global stiffness matrix is obtained. This technique is applied in Chapter 5 to obtain a locally conservative SBFEM approximation.

Chapter 3

The Scaled Boundary Finite Element Method

This chapter introduces the SBFEM in a slightly different way compared to the classical SBFEM literature. From a geometric point of view, the scaled boundary element is a conglomerate of Duffy's elements; thus, from a computational point of view, the SBFEM approximation is a type of Duffy's approximation constructed using a semi-analytical approach instead of using only polynomials. The SBFEM shape functions are semi-analytical because the construction process of the local space involves solving analytically an ODE based on approximating a homogeneous PDE using a trace FE space. Further in this chapter, it is proven that the basis functions of SBFEM are Duffy's functions constructed imposing a gradient-orthogonality constraint. Such a property is important to prove the optimal rate of convergence of SBFEM approximations.

The SBFEM generalizes the FE geometry and the function space. Analogously to Ciarlet, the Scaled Boundary FE is a triple $\Gamma^S = \left(S, \mathbb{S}_k, \Sigma^S\right)$ such that,

1. S denotes a bounded domain in the Euclidean space $\mathbb{R}^d$, where $d = 2, 3$ is the dimension, but the geometry requirements are relaxed: S is a star-shaped element, also known as S-element, enclosing an arbitrary number of facets and vertices, in which the only requirement is that a point inside the S-element, named scaling center, can be seen over the boundary of S, i.e. ∂S;

2. $\mathbb{S}_k$ denotes a space of general functions on ∂S of finite dimension $\dim(\mathbb{S}_k) = \mathcal{N}^S$. The function space $\mathbb{S}_k$ is composed of the tensorial product of polynomial functions defined as a trace space over the boundary of S and radial functions that can have any exponent;

3. $\Sigma^S = \{L_1, L_2, ..., L_{\mathcal{N}^S}\}$ denotes a set of linear forms, such that

$$L_i \ : \ \mathbb{S}_k \to \mathbb{R}, \ i = 1, 2, ..., \mathcal{N}^S.$$

   The L_i elements of Σ^S are called DOFs. Notice that the DOFs are defined only at ∂S.

The function space $\mathbb{S}_k$, in SBFEM, depends on the variational statement. Thus, the SBFEM is a finite element technique that belongs to the class of operator-adapted methods. One can interpret the SBFEM shape functions as semi-analytical functions that

mimic the analytic solution properties inside the element. Two features distinguish SBFEM from the other operator-adapted methods. The first one is related to the partition of the domain, or the geometry of the SBFEM elements. The second attribute remounts the construction process of the SBFEM basis functions.

Regarding the geometric aspects, the SBFEM approximation is based on partitions of the domain Ω into general polygonal/polyhedral subregions S, also called S- elements. These elements obey the star-shaped requirement, which means that any point at ∂S is directly visible from a center point, also named scaling center $\mathbf{O} \in S$. A generic partition of the domain, $\mathcal{T} = \{S\}$, is illustrated in Fig. 3.1.

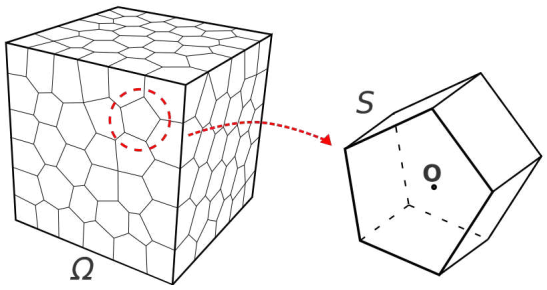

Figure 3.1: A 3D domain partitioned into polyhedral S-elements.

Although the facets shown in Fig. 3.1 are linear planes, curved boundaries can be considered in a blend and b-splines geometries. Moreover, there is no requirement for S to be bounded. It means that S can be an open domain, as illustrated in Fig. 3.2. To ease the demonstrations, this chapter considers only closed affine elements.

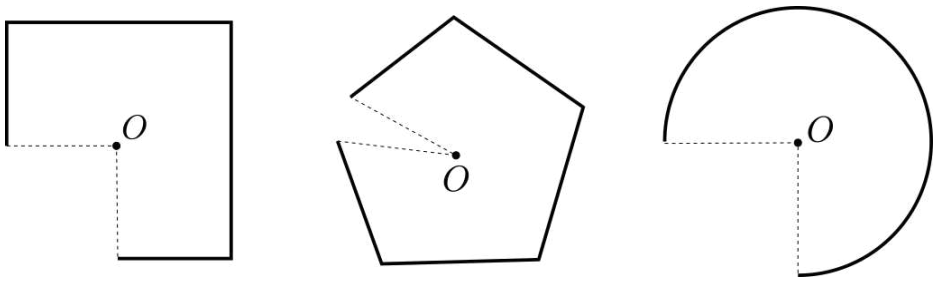

Figure 3.2: General two-dimensional open S-elements.

The second feature is associated with the construction of the approximation space, i.e. the basis functions that will compose the approximated solution. Based on the S-elements geometry, the SBFEM approximation space has two components:

1. A piecewise polynomial space over ∂S: trace finite element (FE) space;
2. A radial extension from the approximation in ∂S into S: a radial function obtained by the local solution of an ordinary differential equation (ODE) eigenvalue problem.

Using tensorial Duffy's basis functions as defined above, the variational statement is written as an ODE eigenvalue problem, whose analytical solution is obtained using the separation of variables technique. Then, the second-order ODE is constructed by rewriting a homogeneous PDE as a function only of the radial function, having the radial variable, ξ as the independent variable.

The first part of this chapter defines Duffy's geometric map. Then, the SBFEM approximation spaces for Poisson problems and Elasticity problems are formally defined. Such a definition allows for highlighting relevant properties of the method. Last, the mathematical properties are applied to define error estimates for the SBFEM and prove that it reaches optimal convergence rates. Numerical tests illustrate the optimal convergence properties of the method to approximate harmonic functions.

The results of this chapter were published in the paper:

COELHO, K. O.; DEVLOO, P. R. B.; GOMES, S. M. Error estimates for the scaled boundary finite element method. *Computer Methods in Applied Mechanics and Engineering*, v. 379, p. 113765, 2021.

3.1 Duffy's Approximation Space

3.1.1 Collapsed element

Duffy's geometric transformations (DUFFY, 1982) are invertible maps of a rectangle, a hexahedron, or a prism to, respectively, a triangle, a pyramid, or a tetrahedron. This geometric map was originally introduced by Duffy to ease the computation of integrals over pyramids with a vertex singularity. In such a map, a facet of the master element (a rectangle, a hexahedron, or a prism) is collapsed to a point - for this reason, this map is also known as a collapsed coordinate system (KARNIADAKIS; SHERWIN, 1999). Applications of Duffy's transformation can be found to define integration quadrature formulae in triangles (LYNESS; COOLS, 1994; BLYTH; POZRIKIDIS, 2006), in the Extended Finite Element Method (XFEM) (MOUSAVI; SUKUMAR, 2010), and the construction of spectral methods on simplices (triangles, tetrahedra) (KARNIADAKIS; SHERWIN, 1999). Collapsed isoparametric elements parametrized by Duffy's transformations also have applications in crack problems (WU, 1993; PU; HUSSAIN; LORENSEN, 1978; RAJU, 1987).

The key aspect of Duffy's transformations is to collapse one facet in $\hat{K}$ on a single vertex of the deformed element K. In the geometric map, described as $F_K : \hat{K} \to K$, the master element has the general form $\hat{K} = [0,1] \times \hat{L} \subset \mathbb{R}^d$, where $\hat{L} \subset \mathbb{R}^{d-1}$, $d = 2, 3$. In the parametric coordinates $\underline{\hat{x}} = (\xi, \underline{\eta}) \in \hat{K}$, ξ is a radial variable, whilst $\underline{\eta}$ plays the role of surface coordinates.

The geometry of the master elements may be one of the following kinds:

- Case 1: Rectangle $\hat{K}$, where $\hat{L} = \hat{I}$ is the interval $\hat{I} = [-1, 1]$.
- Case 2: Hexahedron $\hat{K}$, where $\hat{L} = \hat{Q}$ is the quadrilateral $\hat{Q} = [-1, 1] \times [-1, 1]$.
- Case 3: Prism $\hat{K}$, where $\hat{L} = \hat{T}$ is the triangle $\hat{T} = \{\underline{\eta} = (\eta_1, \eta_2); 0 \leq \eta_i \leq 1, \eta_1 + \eta_2 \leq 1\}$.

Cases 1 to 3 are detailed in the following.

Case 1: From a quadrilateral $\hat{K}$ to triangular K

Let $\hat{K}$ be the rectangular master element with vertices listed in Table 3.1. Also, consider the general triangular element illustrated in Figure 3.3, with vertices $\underline{\mathbf{a}}_0 = F_K(\underline{\hat{\mathbf{a}}}_0)$, $\underline{\mathbf{a}}_1 = F_K(\underline{\hat{\mathbf{a}}}_1)$, and $\underline{\mathbf{a}}_2 = F_K(\underline{\hat{\mathbf{a}}}_2)$. Duffy's geometric map collapses the edge $[\underline{\hat{\mathbf{a}}}_0, \underline{\hat{\mathbf{a}}}_3]$ onto the

vertex $\underline{\mathbf{a}}_0 = F_K(\hat{\underline{\mathbf{a}}}_0) \in K$, whilst $\underline{\mathbf{a}}_1$ and $\underline{\mathbf{a}}_2$ are the vertices of the opposite edge $L = F_K(1,\eta) = F_L(\eta)$.

Table 3.1: Vertices of the quadrilateral master element $\hat{K} = [0,1] \times [-1,1]$.

$\hat{\underline{\mathbf{a}}}_0$	$\hat{\underline{\mathbf{a}}}_1$	$\hat{\underline{\mathbf{a}}}_2$	$\hat{\underline{\mathbf{a}}}_3$
$(0,-1)$	$(1,-1)$	$(1,1)$	$(0,1)$

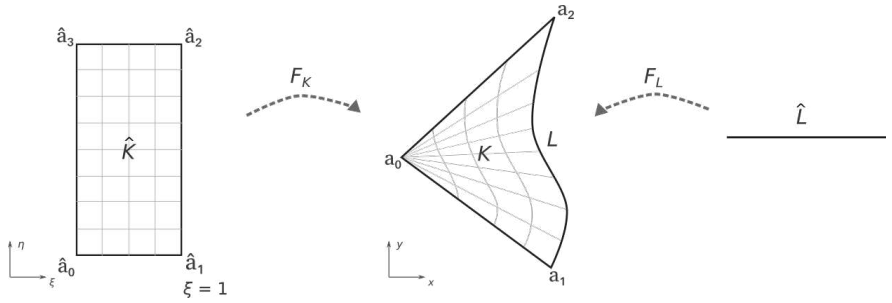

Figure 3.3: Geometric illustration of the transformation F_L as well as Duffy's transformation F_K from a rectangle to a triangle.

Case 2: From a hexahedral $\hat{K}$ to pyramidal K

For the hexahedral master element $\hat{K}$ whose vertices are listed in Table 3.2, Duffy's transformation maps the hexahedron $\hat{K}$ to a pyramid, as illustrated in Fig. 3.4, with vertices $\underline{\mathbf{a}}_i = F_K(\hat{\underline{\mathbf{a}}}_i)$, $i = 0, \cdots 4$, where $\underline{\mathbf{a}}_0$ is the collapsed vertex opposite to the quadrilateral face $L = [\underline{\mathbf{a}}_1, \underline{\mathbf{a}}_2, \underline{\mathbf{a}}_3, \underline{\mathbf{a}}_4]$.

Table 3.2: Vertices of the hexahedral master element $\hat{K} = [0,1] \times \hat{Q}$, where $\hat{Q} = [-1,1] \times [-1,1]$.

$\hat{\underline{\mathbf{a}}}_0$	$\hat{\underline{\mathbf{a}}}_1$	$\hat{\underline{\mathbf{a}}}_2$	$\hat{\underline{\mathbf{a}}}_3$	$\hat{\underline{\mathbf{a}}}_4$	$\hat{\underline{\mathbf{a}}}_5$	$\hat{\underline{\mathbf{a}}}_6$	$\hat{\underline{\mathbf{a}}}_7$
$(0,-1,-1)$	$(1,-1,-1)$	$(1,1,-1)$	$(1,1,1)$	$(1,-1,1)$	$(0,-1,1)$	$(0,1,1)$	$(0,1,-1)$

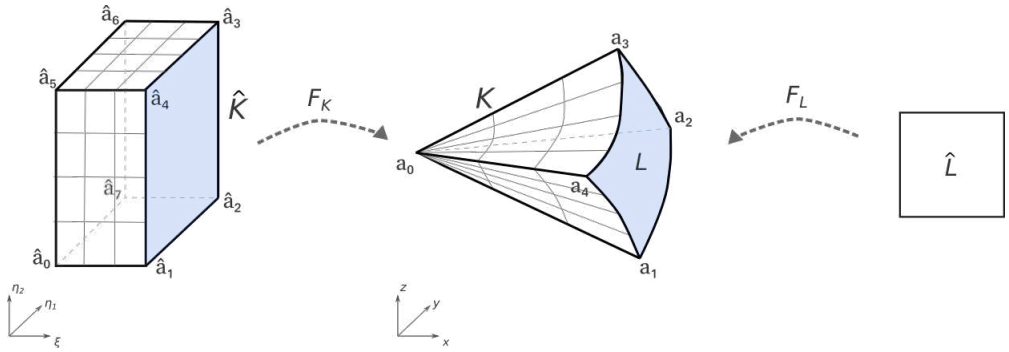

Figure 3.4: Geometric illustration of Duffy's transformation from a hexahedron to a pyramid.

From Fig. 3.4, observe that:

1. The rectangular face $[\hat{\underline{\mathbf{a}}}_0, \hat{\underline{\mathbf{a}}}_5, \hat{\underline{\mathbf{a}}}_6, \hat{\underline{\mathbf{a}}}_7]$ collapses onto $\underline{\mathbf{a}}_0$;
2. The face $[\hat{\underline{\mathbf{a}}}_0, \hat{\underline{\mathbf{a}}}_1, \hat{\underline{\mathbf{a}}}_4, \hat{\underline{\mathbf{a}}}_5]$ is mapped to the triangle $[\underline{\mathbf{a}}_0, \hat{\underline{\mathbf{a}}}_1, \hat{\underline{\mathbf{a}}}_4]$;

3. The face $[\hat{\underline{\mathbf{a}}}_0, \hat{\underline{\mathbf{a}}}_1, \hat{\underline{\mathbf{a}}}_2, \hat{\underline{\mathbf{a}}}_7]$ is mapped to the triangle $[\underline{\mathbf{a}}_0, \hat{\underline{\mathbf{a}}}_1, \hat{\underline{\mathbf{a}}}_2]$;
4. The face $[\hat{\underline{\mathbf{a}}}_2, \hat{\underline{\mathbf{a}}}_3, \hat{\underline{\mathbf{a}}}_6, \hat{\underline{\mathbf{a}}}_7]$ is mapped to the triangle $[\underline{\mathbf{a}}_0, \hat{\underline{\mathbf{a}}}_2, \hat{\underline{\mathbf{a}}}_3]$;
5. The face $[\hat{\underline{\mathbf{a}}}_3, \hat{\underline{\mathbf{a}}}_6, \hat{\underline{\mathbf{a}}}_5, \hat{\underline{\mathbf{a}}}_4]$ is mapped to the triangle $[\underline{\mathbf{a}}_0, \hat{\underline{\mathbf{a}}}_4, \hat{\underline{\mathbf{a}}}_3]$.

Case 3: From a prismatic $\hat{K}$ to tetrahedral K

The last case is a prismatic master element $\hat{K}$ whose vertices are listed in Table 3.3. Fig. 3.5 shows the tetrahedron, whose vertices are $\underline{a}_i = F_K(\hat{\underline{\mathbf{a}}}_i)$, $i = 0, \cdots 3$, with $\underline{\mathbf{a}}_0$ being the collapsed vertex opposed to the face $L = [\underline{\mathbf{a}}_1, \underline{\mathbf{a}}_2, \underline{\mathbf{a}}_3]$.

Table 3.3: Vertices of the prismatic master element $\hat{K} = [0,1] \times \hat{T}$, where $\hat{T} = \{\underline{\eta} = (\eta_1, \eta_2); 0 \leq \eta_1 \leq 1, \eta_1 + \eta_2 \leq 1\}$.

$\hat{\underline{\mathbf{a}}}_0$	$\hat{\underline{\mathbf{a}}}_1$	$\hat{\underline{\mathbf{a}}}_2$	$\hat{\underline{\mathbf{a}}}_3$	$\hat{\underline{\mathbf{a}}}_4$	$\hat{\underline{\mathbf{a}}}_5$
$(0,0,0)$	$(1,1,0)$	$(0,1,0)$	$(0,1,1)$	$(1,0,0)$	$(0,0,1)$

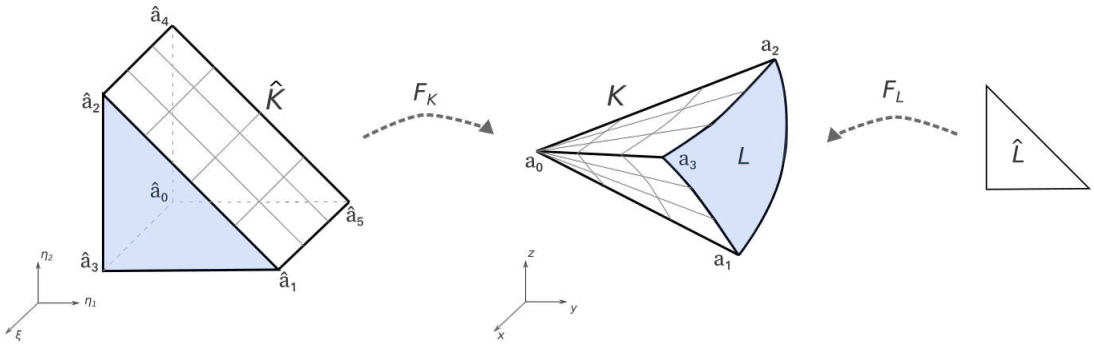

Figure 3.5: Geometric illustration of Duffy's transformation over a prism to a tetrahedron.

Note that:

1. The triangular face $[\hat{\underline{\mathbf{a}}}_0, \hat{\underline{\mathbf{a}}}_4, \hat{\underline{\mathbf{a}}}_5]$ collapses onto the vertex $\underline{a}_0$;
2. The quadrilateral face $[\hat{\underline{\mathbf{a}}}_0, \hat{\underline{\mathbf{a}}}_4, \hat{\underline{\mathbf{a}}}_2, \hat{\underline{\mathbf{a}}}_3]$ collapses onto the triangle $[\underline{\mathbf{a}}_0, \underline{\mathbf{a}}_2, \underline{\mathbf{a}}_3]$;
3. The quadrilateral face $[\hat{\underline{\mathbf{a}}}_0, \hat{\underline{\mathbf{a}}}_3, \hat{\underline{\mathbf{a}}}_1, \hat{\underline{\mathbf{a}}}_5]$ collapses onto the triangle $[\underline{\mathbf{a}}_0, \underline{\mathbf{a}}_1, \underline{\mathbf{a}}_3]$;
4. The quadrilateral face $[\hat{\underline{\mathbf{a}}}_1, \hat{\underline{\mathbf{a}}}_2, \hat{\underline{\mathbf{a}}}_4, \hat{\underline{\mathbf{a}}}_5]$ collapses onto the triangle $[\underline{\mathbf{a}}_0, \underline{\mathbf{a}}_1, \underline{\mathbf{a}}_2]$.

Recall that the tetrahedron Duffy's element can also be derived in two steps: first from a hexahedron to a prism, and then from the prism to tetrahedron (KARNIADAKIS; SHERWIN, 1999).

Generic Duffy's transformation

If $\underline{x} = F_K(\xi, \underline{\eta})$ denotes the Cartesian coordinate in K, the mapped points for the three cases are generically defined by

$$F_K(\xi, \underline{\eta}) = \xi \left(F_L(\underline{\eta}) - \underline{\mathbf{a}}_0 \right) + \underline{\mathbf{a}}_0, \tag{3.1.0}$$

where $\underline{\mathbf{a}}_0$ is the collapsed vertex in K, and $L \subset \partial K$ is the opposite facet to $\underline{\mathbf{a}}_0$, which is mapped by the geometric transformation $F_L : \hat{L} \to L$.

Since the whole facet $\{(0, \underline{\eta}), \underline{\eta} \in \hat{L}\} \subset \hat{K}$ is collapsed over the vertex $\underline{\mathbf{a}}_0 \in K$, Duffy's element K can be regarded as a quadrilateral with two identical vertices, a hexahedron with four equal vertices, or a prism with three identical vertices. From another perspective, the mapping F_K can be seen as a scaling from $F_L(\underline{\eta}) \in L$ to the vertex $\underline{\mathbf{a}}_0$.

The Jacobian matrix $\underline{\underline{J}}_K = \nabla_{\underline{x}} F_K$ of the Duffy's transformation (3.1.1) is

$$\underline{\underline{J}}_K(\xi, \underline{\eta}) = \begin{bmatrix} F_L(\underline{\eta}) - \underline{\mathbf{a}}_0 & \xi \nabla_{\underline{\eta}} F_L(\underline{\eta}) \end{bmatrix} = \underline{\underline{J}}_K(1, \underline{\eta}) \begin{bmatrix} 1 & 0 \\ 0 & \xi \underline{\underline{I}}_{d-1} \end{bmatrix}, \tag{3.1.0}$$

where $\underline{\underline{I}}_{d-1}$ is the $d-1 \times d-1$ identity matrix, and $\underline{\underline{J}}_K(1, \underline{\eta}) = \begin{bmatrix} F_L(\underline{\eta}) - \underline{\mathbf{a}}_0 & \nabla_{\underline{\eta}} F_L(\underline{\eta}) \end{bmatrix}$ is the Jacobian matrix at $F_K(1, \underline{\eta}) = F_L(\underline{\eta})$. Thus, its inverse is given by

$$\underline{\underline{J}}_K^{-1} = \begin{pmatrix} 1 & 0 \\ 0 & \frac{1}{\xi} \underline{\underline{I}}_{d-1} \end{pmatrix} \underline{\underline{J}}_K^{-1}(1, \underline{\eta}).$$

3.1.2 Duffy's approximations

The Duffy's approximation space is composed of basis function $\phi(\underline{x}) = \hat{\phi}(\xi, \underline{\eta})$ referring to functions $\phi = \mathbb{F}_K(\hat{\phi})$ defined for $\underline{x} = F_K(\xi, \underline{\eta}) \in K$, where $\hat{\phi}(\xi, \underline{\eta})$ is defined in $\hat{K}$. Namely, the focus of this thesis is on functions ϕ obtained by separating variables in $\hat{\phi}(\xi, \underline{\eta}) = \hat{\rho}(\xi)\hat{\alpha}(\underline{\eta})$, where $\hat{\rho}(\xi)$ is called the radial component and $\hat{\alpha}(\underline{\eta})$ is the surface component. Generally, the Duffy's approximation space refers to $\mathcal{D}_k(K) = \mathbb{F}_K(\mathcal{D}_k(\hat{K}))$ such that

$$\mathcal{D}_k(\hat{K}) = \left\{ \hat{\phi} = \hat{\rho}(\xi)\hat{\alpha}(\underline{\eta}); \hat{\alpha}(\underline{\eta}) \in \mathcal{V}_k(\hat{L}) \right\} \tag{3.1.0}$$

where $\mathcal{V}_k(\hat{L})$ can be either,

1. Case 1: $\hat{L} = \hat{I} = [-1, 1]$: $\mathcal{V}_k(\hat{L}) = \mathbb{P}_k(\hat{L})$ is the space of the polynomials of total degree not greater than k;
2. Case 2: $\hat{L} = \hat{Q} = [-1, 1] \times [-1, 1]$: $\mathcal{V}_k(\hat{L}) = \mathbb{Q}_{k,k}(\hat{L})$ is the space of the polynomials of total degree not greater than k on each coordinate η_1, η_2, or;
3. Case 3: $\hat{L} = \hat{T} = \{\underline{\eta} = (\eta_1, \eta_2); 0 \leq \eta_i \leq 1, \eta_1 + \eta_2 \leq 1\}$: $\mathcal{V}_k(\hat{L}) = \mathbb{P}_k(\hat{L})$ is the space of the polynomials of total degree not greater than k.

For each case, the surface components $\hat{\alpha}(\underline{\eta}) \in \mathcal{V}_k(\hat{L})$, used to define FE approximation spaces $\mathcal{V}_k(L) = \mathbb{F}_L(\mathcal{V}_k(\hat{L}))$, are finite-dimensional polynomial spaces $\mathcal{V}_k(\hat{L})$.

Gradient operation in $\mathcal{D}_k(K)$

The gradient operator using Duffy's geometric map is given by

$$\nabla_{\underline{x}} = [\underline{\underline{J}}_K(1, \underline{\eta})]^{-T} \begin{Bmatrix} \frac{\partial}{\partial \xi} \\ \frac{1}{\xi} \nabla_{\underline{\eta}} \end{Bmatrix}.$$

where $\nabla_{\underline{\eta}} = \begin{Bmatrix} \dfrac{\partial}{\partial \eta_1} \\ \dfrac{\partial}{\partial \eta_2} \end{Bmatrix}$

If

$$\underline{\underline{J}}_K^{-1}(1,\underline{\eta}) = \begin{pmatrix} j_{11} & j_{12} & j_{13} \\ j_{21} & j_{22} & j_{23} \\ j_{31} & j_{32} & j_{33} \end{pmatrix},$$

the gradient $\nabla_{\underline{x}}$ can be also written as (SONG, 2018)

$$\begin{Bmatrix} \frac{\partial}{\partial x_1} \\ \frac{\partial}{\partial x_2} \\ \frac{\partial}{\partial x_3} \end{Bmatrix} = \begin{Bmatrix} j_{11} \\ j_{21} \\ j_{31} \end{Bmatrix} \frac{\partial}{\partial \xi} + \frac{1}{\xi} \left(\begin{Bmatrix} j_{12} \\ j_{22} \\ j_{32} \end{Bmatrix} \frac{\partial}{\partial \eta_1} + \begin{Bmatrix} j_{13} \\ j_{23} \\ j_{33} \end{Bmatrix} \frac{\partial}{\partial \eta_2} \right).$$

Restricting the study to mapped spaces $\mathcal{D}_k(K) = \mathbb{F}_K(\mathcal{D}_k(\hat{K})) \subset H^1(K)$, where $H^1(K)$ is the local Sobolev space, the chain rule implies that

$$\begin{aligned} \nabla_{\underline{x}}\phi(\underline{x}) &= [\underline{\underline{J}}_K(1,\underline{\eta})]^{-T} \begin{bmatrix} 1 & 0 \\ 0 & \frac{1}{\xi}\underline{\underline{I}}_{d-1} \end{bmatrix} \begin{bmatrix} \hat{\rho}'(\xi)\hat{\alpha}(\underline{\eta}) \\ \hat{\rho}(\xi)\nabla_{\underline{\eta}}\hat{\alpha}(\underline{\eta}) \end{bmatrix} \\ &= [\underline{\underline{J}}_K(1,\underline{\eta})]^{-T} \begin{bmatrix} \hat{\rho}'(\xi)\hat{\alpha}(\underline{\eta}) \\ \frac{1}{\xi}\hat{\rho}(\xi)\nabla_{\underline{\eta}}\hat{\alpha}(\underline{\eta}) \end{bmatrix} \\ &= [\underline{\underline{J}}_K(1,\underline{\eta})]^{-T} \begin{bmatrix} \hat{\alpha}(\underline{\eta}) & 0 \\ 0 & \nabla_{\underline{\eta}}\hat{\alpha}(\underline{\eta}) \end{bmatrix} \begin{bmatrix} \hat{\rho}'(\xi) \\ \frac{1}{\xi}\hat{\rho}(\xi) \end{bmatrix}. \end{aligned}$$

If $\mathcal{V}_k(\hat{L}) = \text{span}\{\hat{N}_k^l\}$ and $\hat{\alpha}(\underline{\eta}) = \sum_l a^l \hat{N}_k^l(\underline{\eta})$ is a linear combination of FE shape functions $\hat{N}_k^l(\underline{\eta})$, then (3.1.2) can be grouped as

$$\nabla_{\underline{x}}\phi(\underline{x}) = \sum_l \begin{bmatrix} \underline{B}_{1l}(\underline{\eta}) & \underline{B}_{2l}(\underline{\eta}) \end{bmatrix} \begin{bmatrix} a^l\hat{\rho}'(\xi) \\ \frac{1}{\xi}a^l\hat{\rho}(\xi) \end{bmatrix}, \tag{3.1.-2}$$

where

$$\underline{B}_{1l}(\underline{\eta}) = [\underline{\underline{J}}_K(1,\underline{\eta})]^{-T} \begin{bmatrix} \hat{N}_k^l(\underline{\eta}) \\ 0 \end{bmatrix}, \text{ and } \underline{B}_{2l}(\underline{\eta}) = [\underline{\underline{J}}_K(1,\underline{\eta})]^{-T} \begin{bmatrix} 0 \\ \nabla_{\underline{\eta}}\hat{N}_k^l(\underline{\eta}) \end{bmatrix}.$$

In the following, Eq. (3.1.2) is applied to deduce the SBFEM approximation space.

3.2 SBFEM approximation spaces

3.2.1 Star-shaped element

The SBFEM considers partitions $\mathcal{T} = \{S\}$ of the domain $\Omega \subset \mathbb{R}^d$ by S-elements that verify the star-shaped geometric requirement (see Fig. 3.6). Star-like scaling requirement imposes that any point on ∂S should be directly visible from a point $\mathbf{O} \in S$, called the scaling center. This chapter shall be restricted to convex polytopal S-elements (polygonal or polyhedral with flat facets $L^e \subset \partial S$). The set $\partial S = \Gamma^{h,S} = \cup_e L^e$, $e = 1, \cdots, N^{\Gamma^S}$ is known as the scaled boundary element, where N^{Γ^S} is the number of facets in S.

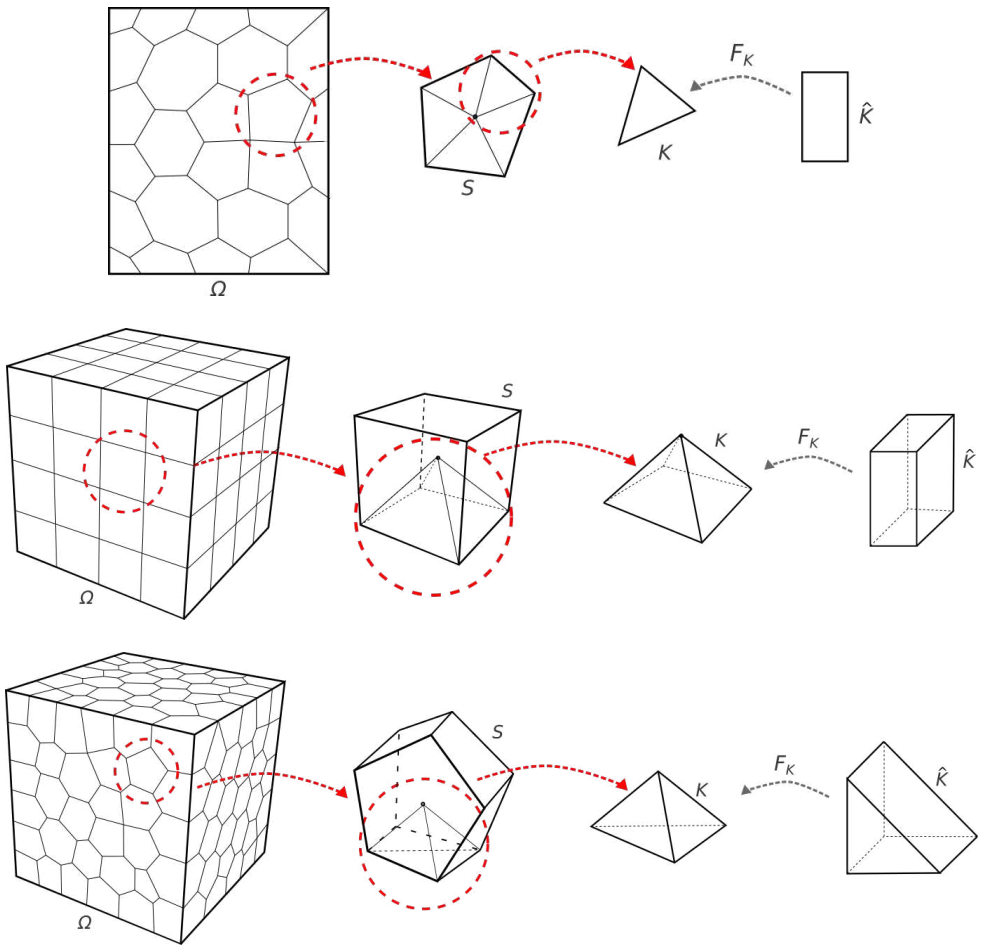

Figure 3.6: Illustration of macro partitions $\mathcal{T} = \{S\}$, with focus on a sector $K \in \mathcal{T}^{h,S}$, with corresponding Duffy's transformation, for triangular, pyramidal and tetrahedral K.

The S-element is a conformal sub-partition $\mathcal{T}^{h,S} = \{K^e\}$ formed by sectors K^e sharing the scaling center $\mathbf{O}$ as one of their vertices. The scaled boundary element $\Gamma^{h,S}$ is composed of facets L^e opposed to the scaling center. As illustrated in Fig. 3.6, the sectors K^e have different geometries according to S: triangular in 2D, pyramidal, or tetrahedral in 3D. The scaled boundary element is a conglomerate of facets L^e being a line segment, a quadrilateral, or a triangular element. Although a generic 3D S-element may also be partitioned by hybrid tetrahedral-pyramidal meshes, this chapter restricts the analysis to partitions $\mathcal{T}^{h,S}$ where all elements K^e have the same geometry.

The geometry of the S-element implies that the points $\underline{x} \in S$ can be uniquely represented by a radial coordinate $0 \leq \xi \leq 1$ and a surface coordinate $\underline{x}_b \in \Gamma^{h,S}$. The radial coordinate points from the scaling center ($\xi = 0$) to a point $\underline{x}_b \in \Gamma^{h,S}$ (where $\xi = 1$). The S-element may also be defined in each sector $K^e \in \mathcal{T}^{h,S}$ using Duffy's geometric map $F_{K^e} : \hat{K} \rightarrow K^e$, as described in the previous section. K^e is a collapsed quadrilateral, hexahedral or prismatic geometric element in which the facet $F_{K^e}(0, \underline{\eta})$ is collapsed to the scaling center $\Gamma^{h,S}$. The points $\underline{x}_b$ in the opposed facet L^e are given by $F_{K^e}(1, \underline{\eta}) = F_{L^e}(\underline{\eta})$, $\underline{\eta} \in \hat{L}$. These maps are also illustrated in Fig. 3.6.

3.2.2 Duffy's spaces in S-elements

Duffy's space for scalar functions

Since S-elements are a conglomerate of Duffy's elements sharing the same collapsed vertex, the approximation space in S can be described using the definitions established in Section 3.1.1. The construction of functions $\phi(\underline{x}) \in \mathcal{D}_k(S) \in H^1(S)$ follows three stages described in the sequence:

1) Define local parametrizations $K^e \subset S$ and $L^e \subset \Gamma^{h,S}$, such that $\underline{x} = F_{K^e}(\xi, \underline{\eta}) \in K^e$ and $\underline{x}_b \in F_{L^e}(\underline{\eta}) \in L^e$.

2) Define a trace FE space over $\Gamma^{h,S}$, given by

$$\Lambda_k(\Gamma^S) = \text{span}\{N_k^{n,S} \subset C(\Gamma^S)\} \tag{3.2.0}$$

where $N_k^{n,S}$ is the assembly of local shape functions $N_k^{\ell}(\underline{x}) = \hat{N}_k^{\ell}(\underline{\eta}),\ \underline{x}_b \in L^e$. Using vector notation, define

$$\alpha(\underline{x}_b) = \underline{N}_k^S \cdot \underline{a} \in \Lambda_k(\Gamma^S) \tag{3.2.0}$$

as the polynomial approximation over Γ^S.

3) Radial extensions of $\alpha(\underline{x}_b) \in \Lambda_k(\Gamma^{h,S})$ to points $\underline{x} = F_{K^e}(\xi, \underline{\eta}) \in S$ using the radial function $\hat{\rho}(\xi)$ to be defined. Notice that for both cases, $\hat{\rho}(\xi)$ is a scalar function that has the same radial component applied to all $K^e \in S$.

In summary, for a S-element,

$$\mathcal{D}_k(S) = \left\{\phi(\underline{x}) \in H^1(S);\ s.t.\ \phi|_{\Gamma^{h,S}} = \alpha(\underline{x}_b) \in \Lambda_k(\Gamma^{h,S}) \text{ and } \hat{\phi}(\xi, \underline{\eta}) = \hat{\alpha}(\underline{\eta})\hat{\rho}(\xi)\right\}, \tag{3.2.0}$$

and $\mathcal{D}_k^0(S) \subset \mathcal{D}_k(S)$ is the space of bubble functions, i.e. $\phi|_{\Gamma^{h,S}} = 0$.

The global space for Ω is defined as follows. Let $\mathcal{T}^h = \{S\}$ be a partition composed of a family of conformal polytopal S-elements, where h is the characteristic size of the S facets. Moreover, define the mesh skeleton Γ^h as the assembly of the S-element's facets $\Gamma^{h,S}$. Then, Duffy's space is defined as

$$\mathcal{D}_k^h = \{w \in H^1(\Omega);\ w|_S \in \mathcal{D}_k(S),\ S \in \mathcal{T}^h\}.$$

The first stage is typical of FE contexts, but for specific scaled S-elements the extension to the interior can be performed in the radial direction.

Gradient in $\mathcal{D}_k(S)$

Let $\phi(\underline{x}),\ \psi(\underline{x}) \in \mathcal{D}_k(S) \subset H^1(S)$ be approximations given by

$$\begin{aligned}
\phi(\underline{x}) = \hat{\phi}(\xi, \underline{\eta}) &= \hat{\alpha}^S(\underline{\eta})\hat{\rho}(\xi) \\
&= \left(\underline{\hat{N}}_k^S(\underline{\eta}) \cdot \underline{a}\right)\hat{\rho}(\xi) \\
\psi(\underline{x}) = \hat{\psi}(\xi, \underline{\eta}) &= \beta^S(\underline{\eta})\hat{\tau}(\xi) \\
&= \left(\underline{\hat{N}}_k^S(\underline{\eta}) \cdot \underline{b}\right)\hat{\tau}(\xi)
\end{aligned}$$

Applying the expression for the gradient obtained for K in Eq. (3.1.2) for the S-element leads to

$$\nabla\phi(\underline{x}) = \left[\begin{array}{cc} \underline{B}_1(\underline{\eta}) & \underline{B}_2(\underline{\eta}) \end{array}\right] \left[\begin{array}{c} \underline{a}^T\hat{\rho}'(\xi) \\ \frac{1}{\xi}\underline{a}^T\hat{\rho}(\xi) \end{array}\right], \text{ and } \nabla\psi(\underline{x}) = \left[\begin{array}{cc} \underline{B}_1(\underline{\eta}) & \underline{B}_2(\underline{\eta}) \end{array}\right] \left[\begin{array}{c} \underline{b}^T\hat{\tau}'(\xi) \\ \frac{1}{\xi}\underline{b}^T\hat{\tau}(\xi) \end{array}\right] \tag{3.2.-2}$$

$$\underline{B}_1(\underline{\eta}) = [\underline{\underline{J}}_K(1,\underline{\eta})]^{-T} \left[\begin{array}{c} \hat{\underline{N}}_k^S(\underline{\eta}) \\ 0 \end{array}\right], \text{ and } \underline{B}_2(\underline{\eta}) = [\underline{\underline{J}}_K(1,\underline{\eta})]^{-T} \left[\begin{array}{c} 0 \\ \nabla_{\underline{\eta}}\hat{\underline{N}}_k^S(\underline{\eta}) \end{array}\right].$$

Moreover, consider

$$\hat{\underline{\Phi}}(\xi) = \underline{a}^T\hat{\rho}(\xi)$$
$$\hat{\underline{\Psi}}(\xi) = \underline{b}^T\hat{\tau}(\xi)$$

Then Eq. (3.2.2) is simplified to

$$\nabla\phi(\underline{x}) = \left[\begin{array}{cc} \underline{B}_1(\underline{\eta}) & \underline{B}_2(\underline{\eta}) \end{array}\right] \left[\begin{array}{c} \hat{\underline{\Phi}}'(\xi) \\ \frac{1}{\xi}\hat{\underline{\Phi}}(\xi) \end{array}\right], \text{ and } \nabla\psi(\underline{x}) = \left[\begin{array}{cc} \underline{B}_1(\underline{\eta}) & \underline{B}_2(\underline{\eta}) \end{array}\right] \left[\begin{array}{c} \hat{\underline{\Psi}}'(\xi) \\ \frac{1}{\xi}\hat{\underline{\Psi}}(\xi) \end{array}\right] \tag{3.2.-2}$$

Duffy's space for vector-valued functions

The three stages for constructing Duffy's approximation space for scalar functions $\mathcal{D}_k(S)$ can be applied to construct a space of Duffy's vector-valued functions $\underline{\mathcal{D}}_k$. In such a case, the radial component of Duffy's basis function $\hat{\rho}(\xi)$ remains scalar to all $K^e \in S$. On the other hand, the surface component is a vector-valued function $\hat{\underline{\alpha}}(\underline{\eta}) \in \mathcal{V}_k(\hat{L};\mathbb{R}^d),\ d = 2,3$. In short, for vector-valued Duffy's functions,

$$\underline{\mathcal{D}}_k(S) = \left\{\underline{\phi}(\underline{x}) \in H^1(S,\mathbb{R}^d);\ s.t.\ \underline{\phi}|_{\Gamma^{h,S}} = \underline{\alpha}(\underline{x}_b) \in \underline{\Lambda}_k(\Gamma^{h,S}) \text{ and } \hat{\underline{\phi}}(\xi,\underline{\eta}) = \hat{\underline{\alpha}}(\underline{\eta})\hat{\rho}(\xi)\right\}. \tag{3.2.-2}$$

where $\underline{\Lambda}_k(\Gamma^{h,S})$ is a vector-valued version of $\Lambda_k(\Gamma^{h,S})$, written, analogously to Eq. (3.2.2), as

$$\underline{\Lambda}_k(\Gamma^{h,S}) = \text{span}\{\underline{N}_k^{n,S} \subset C(\Gamma^{h,S},\mathbb{R}^d)\},\ d = 2,3. \tag{3.2.-2}$$

leading to vector-valued surface functions expressed as

$$\underline{\alpha}(\underline{x}_b) = \underline{\underline{N}}_k^S\underline{a} \tag{3.2.-2}$$

where $\underline{\underline{N}}_k^S = \left[\underline{N}_k^{0,S} \quad \underline{N}_k^{1,S} \quad \dots \quad \underline{N}_k^{\mathcal{N}^S,S}\right]$.

Finally, similarly to Eq. 3.2.2, the global space $\underline{\mathcal{D}}_k^h$ for Ω, where Ω is partitioned into a family of conformal polytopal S-elements $\mathcal{T}^h = \{S\}$, is given by

$$\underline{\mathcal{D}}_k^h = \{\underline{w} \in H^1(\Omega,\mathbb{R}^d);\ \underline{w}|_S \in \underline{\mathcal{D}}_k(S),\ S \in \mathcal{T}^h\}.$$

3.2.3 SBFEM approximations for the Poisson problem

First, the SBFEM space is constructed for a Poisson problem with a null source term, also known as the harmonic problem, written in strong form as

$$\begin{aligned} \Delta u = 0,\ u \in \Omega \\ u|_{\partial\Omega} = u_D \end{aligned}$$

where u_D are prescribed Dirichlet boundary conditions. The variational statement is obtained through the Galerkin method, considering an approximation for u in $H^1(\Omega)$, multiplying Eq. (3.2.3) by a test function $v \in H^1(\Omega)$ and integrating it by parts.

In its discrete form, let Ω be partitioned into S-elements, $\mathcal{T}^h = \{S\}$, where h is the characteristic size of the S-element's facets. The variational statement can be written as: Find $u_h(\underline{x}) \in \mathbb{S}_k^h \subset H^1(\Omega)$ such that

$$\begin{aligned} \int_\Omega \nabla u_h \cdot \nabla v \ d\Omega = 0,\ \forall v \in \mathbb{S}_k^{h,0} \subset H_0^1(\Omega) \\ u_h|_{\partial\Omega} = u_D, \end{aligned}$$

where $H_0^1(\Omega) \subset H^1(\Omega)$ is the Sobolev space of all functions that vanish at $\partial\Omega$, and $\mathbb{S}_k^h \in \mathcal{D}_k^h(S)$ is the SBFEM space for harmonic problems, given by

$$\mathbb{S}_k^h = \left\{ w \in H^1(\Omega);\ w|_S \in \mathbb{S}_k^h(S), S \in T^h \right\}, \tag{3.2.-2}$$

and

$$\mathbb{S}_k(S) = \left\{ \phi \in \mathcal{D}_k(S);\ \int_S \nabla\phi \cdot \nabla\psi \ dS = 0, \forall \psi \in \mathcal{D}_k^0(S),\ \psi(\mathbf{O}) = 0 \right\}. \tag{3.2.-2}$$

It means that the SBFEM seeks an approximated function that imposes weakly the property of harmonic functions directly in the approximation space. Knowing that the gradients $\nabla\phi$ and $\nabla\psi$ were given by Eq. (3.2.2), the SBFEM basis functions will be obtained by expressing $\int_S \nabla\phi \cdot \nabla\psi \ dS$ ad an ODE as follows.

$$\begin{aligned} \int_S \nabla\phi(\underline{x}) \cdot \nabla\psi(\underline{x}) \mathrm{d}S &= \int_0^1 \int_{-1}^1 \begin{bmatrix} \underline{B}_1(\underline{\eta}) & \underline{B}_2(\underline{\eta}) \end{bmatrix} \begin{bmatrix} \hat{\underline{\Phi}}'(\xi) \\ \frac{1}{\xi}\hat{\underline{\Phi}}(\xi) \end{bmatrix} \cdot \begin{bmatrix} \underline{B}_1(\underline{\eta}) & \underline{B}_2(\underline{\eta}) \end{bmatrix} \begin{bmatrix} \hat{\underline{\Psi}}'(\xi) \\ \frac{1}{\xi}\hat{\underline{\Psi}}(\xi) \end{bmatrix} \xi^{d-1} |\underline{\underline{J}}_K(1,\underline{\eta})| \, d\underline{\eta} d\xi \\ &= \int_0^1 \int_{-1}^1 \begin{bmatrix} \hat{\underline{\Phi}}'(\xi) & \frac{1}{\xi}\hat{\underline{\Phi}}(\xi) \end{bmatrix} \cdot \left(\begin{bmatrix} \underline{B}_1^T \\ \underline{B}_2^T \end{bmatrix} \begin{bmatrix} \underline{B}_1 & \underline{B}_2 \end{bmatrix} |\underline{\underline{J}}_K(1,\underline{\eta})| \right) \begin{bmatrix} \hat{\underline{\Psi}}'(\xi) \\ \frac{1}{\xi}\hat{\underline{\Psi}}(\xi) \end{bmatrix} \xi^{d-1} \, d\underline{\eta} d\xi \\ &= \int_0^1 \begin{bmatrix} \hat{\underline{\Phi}}'(\xi) & \frac{1}{\xi}\hat{\underline{\Phi}}(\xi) \end{bmatrix} \cdot \begin{bmatrix} \underline{\underline{E}}_0 & \underline{\underline{E}}_1^T \\ \underline{\underline{E}}_1 & \underline{\underline{E}}_2 \end{bmatrix} \begin{bmatrix} \hat{\underline{\Psi}}'(\xi) \\ \frac{1}{\xi}\hat{\underline{\Psi}}(\xi) \end{bmatrix} \xi^{d-1} d\xi, \end{aligned}$$

where $\underline{\underline{E}}_i,\ i = 0, 1, 2$ are the SBFEM coefficient matrices (SONG, 2018)

$$\begin{aligned} \underline{\underline{E}}_0 &= \int_{-1}^1 \underline{B}_1^T \underline{B}_1 |\underline{\underline{J}}_K(1,\underline{\eta})| \ \mathrm{d}\underline{\eta} \\ \underline{\underline{E}}_1 &= \int_{-1}^1 \underline{B}_2^T \underline{B}_1 |\underline{\underline{J}}_K(1,\underline{\eta})| \ \mathrm{d}\underline{\eta} \\ \underline{\underline{E}}_2 &= \int_{-1}^1 \underline{B}_2^T \underline{B}_2 |\underline{\underline{J}}_K(1,\underline{\eta})| \mathrm{d}\underline{\eta}. \end{aligned}$$

Recall that $\underline{B}_1$ is related to $\underline{N}_k^S(\underline{\eta})$ and $\underline{B}_2$ to the gradient $\nabla\underline{N}_k^S(\underline{\eta})$. The SBFEM coefficient matrices are arranged in such a way that $\underline{\underline{E}}_0$ is related to the components of the derivative in ξ and constant in $\underline{\eta}$, $\underline{\underline{E}}_2$ is composed of the gradients $\nabla\underline{N}_k^S(\underline{\eta})$. Finally, $\underline{\underline{E}}_1$ is composed of both $\underline{N}_k^S(\underline{\eta})$ and its gradient $\nabla\underline{N}_k^S(\underline{\eta})$.

The gradient-inner product (3.2.3) is now only an expression of ξ, that can be expanded as

$$\int_S \nabla\phi(\underline{x})\cdot\nabla\psi(\underline{x}),\mathrm{d}S = \int_0^1 \hat{\underline{\Psi}}^{'}(\xi)\cdot\left[\xi^{d-1}\underline{\underline{E}}_0\hat{\underline{\Phi}}^{'}(\xi)+\xi^{d-2}\underline{\underline{E}}_1\hat{\underline{\Phi}}(\xi)\right]+ \hat{\underline{\Psi}}(\xi)\cdot\left[\xi^{d-2}\underline{\underline{E}}_1^T\hat{\underline{\Phi}}^{'}(\xi)+\xi^{d-3}\underline{\underline{E}}_2\hat{\underline{\Phi}}(\xi)\right]d\xi.$$

Consider

$$\hat{\underline{Q}}(\xi) = \xi^{d-1}\underline{\underline{E}}_0\hat{\underline{\Phi}}^{'}(\xi)+\xi^{d-2}\underline{\underline{E}}_1\hat{\underline{\Phi}}(\xi) \tag{3.2.-5}$$

and apply integration by parts in ξ, one obtains

$$\int_0^1 \hat{\underline{\Psi}}^{'}(\xi)\cdot\hat{\underline{Q}}(\xi)d\xi = \hat{\underline{\Psi}}\cdot\ \hat{\underline{Q}}\Big]_0^1 - \int_0^1 \hat{\underline{\Psi}}(\xi)\cdot\hat{\underline{Q}}^{'}(\xi)\,d\xi.$$

where

$$\hat{\underline{Q}}^{'}(\xi) = \underline{\underline{E}}_0\left(\xi^{d-1}\hat{\underline{\Phi}}^{''}(\xi)+(d-1)\xi^{d-2}\hat{\underline{\Phi}}^{'}(\xi)\right)+\underline{\underline{E}}_1\left(\xi^{d-2}\hat{\underline{\Phi}}^{'}(\xi)+(d-2)\xi^{d-3}\hat{\underline{\Phi}}(\xi)\right). \tag{3.2.-5}$$

Substituting Eq (3.2.3) in (3.2.3) yields

$$\int_S \nabla\Phi(\underline{x})\cdot\nabla\Psi(\underline{x})\mathrm{d}S = \hat{\underline{\Psi}}(\xi)\cdot\underline{\hat{Q}}_i\Big|_0^1 - \int_0^1 \hat{\underline{\Psi}}(\xi)\cdot\left[\xi^{d-1}\underline{\underline{E}}_0\hat{\underline{\Phi}}^{''}(\xi)+\left[(d-1)\underline{\underline{E}}_0-\underline{\underline{E}}_1^T+\underline{\underline{E}}_1\right]\xi^{d-2}\hat{\underline{\Phi}}^{'}(\xi) + \left[(d-2)\underline{\underline{E}}_1-\underline{\underline{E}}_2\right]\xi^{d-3}\hat{\underline{\Phi}}(\xi)\right]\,d\xi.$$

If $\hat{\underline{\Psi}}(\xi)$ zeroes the Ricatti equation, orthogonality property $\int_S\nabla\phi(\underline{x})\cdot\nabla\psi(\underline{x})\mathrm{d}S = 0$ holds. In other words, for all functions $\psi\in\mathcal{D}_k^0(S)$ and $\psi(\mathbf{O})=0$, i.e., vanishing on Γ^S, $\underline{\hat{\psi}}(\xi=1)=0$, but also vanishing on the scaling center, $\underline{\hat{\psi}}(\xi=1)=0$, Eq. (3.2.3) zeroes. These constraints on ψ cancel the boundary term in (3.2.3). On the other hand, the condition for vanishing the integral term in (3.2.3) for all $\underline{\hat{\psi}}(\xi)$ is equivalent to say that $\underline{\hat{\phi}}(\xi)$ must solve the following equation

$$\xi^{d-1}\underline{\underline{E}}_0\hat{\underline{\Phi}}^{''}(\xi)+\left[(d-1)\underline{\underline{E}}_0-\underline{\underline{E}}_1^T+\underline{\underline{E}}_1\right]\xi^{d-2}\hat{\underline{\Phi}}^{'}(\xi)+\left[(d-2)\underline{\underline{E}}_1-\underline{\underline{E}}_2\right]\xi^{d-3}\hat{\underline{\Phi}}(\xi)=0. \tag{3.2.-6}$$

Notice that this is the usual scaled boundary equation for the SBFEM shape functions, as documented in Song and Wolf (1997), Wolf (2003) and Song (2018) and other classical SBFEM references. The resolution of (3.2.3) is well documented in the SBFEM literature, and it involves an auxiliary eigenvalue problem for an ODE system in terms of both $\hat{\underline{\Phi}}(\xi)$ and $\hat{\underline{Q}}(\xi)$.

The second-order ODE problem (3.2.3) can be solved using standard methods through a system of first-order differential equations directly from Eqs. (3.2.3) and (3.2.3) as described by Song (2018). By isolating $\xi\underline{\Phi}'(\xi)$ from (3.2.3), the first equation of the system is written as,

$$\xi\hat{\underline{\Phi}}^{'}(\xi) = \left(-\underline{\underline{E}}_0^{-1}\underline{\underline{E}}_1+0.5(d-2)\underline{\underline{I}}\right)\hat{\underline{\Phi}}(\xi)+\underline{\underline{E}}_0^{-1}\hat{\underline{Q}}(\xi). \tag{3.2.-6}$$

The second equation is obtained from Eq. (3.2.3) by eliminating $\xi\hat{\underline{\underline{\Phi}}}'(\xi)$:

$$\xi\hat{\underline{\underline{Q}}}'(\xi) = \left(-\underline{\underline{E}}_1\underline{\underline{E}}_0^{-1}\underline{\underline{E}}_1^T + \underline{\underline{E}}_2\right)\hat{\underline{\underline{\Phi}}}(\xi) + \left(\underline{\underline{E}}_0\underline{\underline{E}}_1^{-1} - 0.5(d-2)\underline{\underline{I}}\right)\hat{\underline{\underline{Q}}}(\xi).$$

The ODE system formed by (3.2.3) and (3.2.3) can be grouped in a matrix form as

$$\xi\underline{\underline{X}}'(\xi) = -\underline{\underline{Z}}\,\underline{\underline{X}}(\xi), \tag{3.2.-6}$$

where $\underline{\underline{X}}(\xi) = \begin{bmatrix}\hat{\underline{\underline{\Phi}}}(\xi)\\ \hat{\underline{\underline{Q}}}(\xi)\end{bmatrix}$ and $\underline{\underline{Z}}$ is the matrix,

$$\underline{\underline{Z}} = \begin{bmatrix}\left(\underline{\underline{E}}_0^{-1}\underline{\underline{E}}_1^T - 0.5(d-2)\underline{\underline{I}}\right) & -\underline{\underline{E}}_0^{-1}\\ -\underline{\underline{E}}_2 + \underline{\underline{E}}_1^T\underline{\underline{E}}_0^{-1}\underline{\underline{E}}_1 & \left(-\underline{\underline{E}}_1\underline{\underline{E}}_0^{-1} + 0.5(d-2)\underline{\underline{I}}\right)\end{bmatrix}. \tag{3.2.-6}$$

Notice that Eq. (3.2.3) is an eigenvalue problem. If $\begin{bmatrix}\underline{\underline{A}}\\ \underline{\underline{A}}^q\end{bmatrix}$ are the linearly independent eigenvectors of $\underline{\underline{Z}}$, and $\underline{\lambda}$ the respective eigenvalues, then the function $\underline{\underline{X}}(\xi) = \begin{bmatrix}\underline{\underline{A}}\\ \underline{\underline{A}}^q\end{bmatrix}\xi^{\underline{\lambda}}$ solves (3.2.3).

One property of the matrix $\underline{\underline{Z}}$ is that it is a Hamiltonian matrix, which means that (SONG, 2018)

$$\underline{\underline{Z}}^T\begin{pmatrix}\underline{\underline{0}} & \underline{\underline{I}}\\ -\underline{\underline{I}} & \underline{\underline{0}}\end{pmatrix}^T = \begin{pmatrix}\underline{\underline{0}} & \underline{\underline{I}}\\ -\underline{\underline{I}} & \underline{\underline{0}}\end{pmatrix}\underline{\underline{Z}}. \tag{3.2.-6}$$

$\underline{\underline{I}}$ being the Identity tensor of dimension $n \times n$. For these type of matrices, the eigenvalues occur in pairs $(+\lambda_i,\ -\lambda_i)$ and the complex eigenvalues occur in conjugate pairs $(\mathrm{Re}(\lambda_i) + \mathrm{Im}(\lambda_i), \mathrm{Re}(\lambda_i) - \mathrm{Im}(\lambda_i))$.

The functions $\xi^{\underline{\lambda}}$ corresponding to eigenvalues having negative real parts are unbounded for $\xi \to 0$, and are unsuited to describe solutions at the interior of the S-element. Indeed, the SBFEM can be also applied to the simulation of unbounded domains. In the origin of SBFEM, the method was often applied for the dynamic simulation of soil-structure problems (WOLF; SONG, 2002). Therefore, the eigenvalues can be grouped as follows:

1. $\mathcal{N}^S - 1$ eigenvalues with positive real parts - $\mathrm{Re}(\lambda_i > 0)$: $\xi^{\lambda_i - 0.5(d-2)} = 0$ applies for $\xi = 0$.
2. 1 eigenvalue such that $\mathrm{Re}(\lambda_i - 0.5(d-2)) = 0$: $\xi^{\lambda_i} = 1$ apply. This eigenvalue represents the translational rigid motion. The corresponding $\underline{A}_i^q$ is a null vector since rigid motions do not produce forces.
3. 1 eigenvalue such that $\mathrm{Re}(\lambda_i + 0.5(d-2)) = 0$: $\xi^{\lambda_i} = 1$ apply. This eigenvalue represents the translational rigid motion for an unbounded domain. The corresponding $\underline{A}_i^q$ is also a null vector.
4. $\mathcal{N}^S - 1$ eigenvalues with negative real parts - $\mathrm{Re}(\lambda_i < 0)$: in this group, $\xi^{\lambda_i + 0.5(d-2)} \to \infty$, for $\xi = 0$. These eigenvalues apply to unbounded domains.

Since the scope of this thesis is only bounded domains, only positive real parts of $\underline{\lambda}$, jointly with the null eigenvalue, are taken as the solution. Thus, the desired solutions of the system (3.2.3)-(3.2.3) are taken as

$$\hat{\underline{\underline{\Phi}}}(\xi) = \underline{\underline{A}}_+\mathrm{diag}(\xi^{\underline{\lambda}_+}), \quad \hat{\underline{\underline{Q}}}(\xi) = \underline{\underline{A}}_+^q\mathrm{diag}(\xi^{\underline{\lambda}_+}),$$

where $\underline{\lambda}_+ \in \mathbb{R}^N$ represents the positive real part of $\underline{\lambda}$, $\underline{\underline{A}}_+ = [\underline{A}_{+i}]$ and $\underline{\underline{A}}^q_+ = [\underline{A}^q_{+i}]$ are the associated eigenvector components. For simplicity, the index + is dropped in the sequence of this thesis.

Finally, the SBFEM basis functions are then composed of pairs of eigenvalues and eigenvectors λ_i, $\underline{A} = \begin{bmatrix} \underline{A}_i \\ \underline{A}^q_i \end{bmatrix}$, respectively, expressed as (SONG, 2018)

$$\phi_i(\underline{x}) = \hat{\phi}_i(\xi, \underline{\eta}) = \xi^{\lambda_i - 0.5(d-2)} \sum_l A^l_i \hat{N}^{S,l}_k(\underline{\eta}),$$
$$q_i(\underline{x}) = \hat{q}_i(\xi, \underline{\eta}) = \xi^{\lambda_i + 0.5(d-2)} \sum_l A^{q,l}_i \hat{N}^{S,l}_k(\underline{\eta}).$$

For a quadratic element ($k = 2$) considering a Poisson problem, the SBFEM basis function ϕ_i are plotted in Fig. 3.7. For this example, the positive eigenvalues are equal to

$$\underline{\lambda} = \{0, 1, 1, 2, 2, 3.26599, 3.26599, 4.3589\}.$$

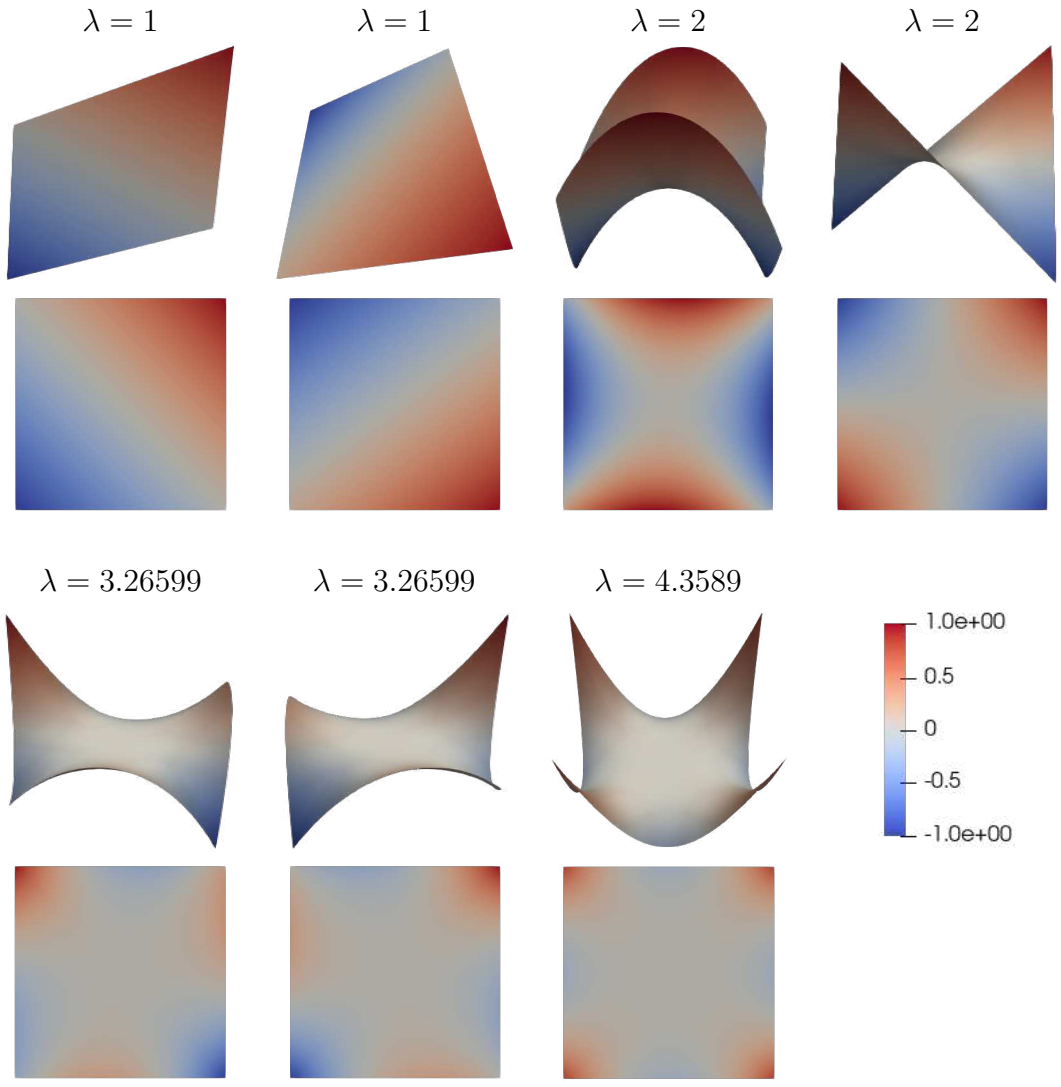

Figure 3.7: Illustrations of some SBFEM basis functions ϕ_i in $\mathbb{S}_2(S)$ for a quadrilateral $\Gamma^{h,S}$.

The SBFEM space is formed by span$\{\phi_i\}$. Grouping the functions in vectorial form and composing the solutions u and q locally for a S-element leads to

$$u(\underline{x}) = \underline{\hat{\phi}}(\xi,\underline{\eta})\cdot\underline{c} = \text{diag}\left(\xi^{\underline{\underline{\lambda_+}}-0.5(d-2)}\right)\underline{\underline{A}}\underline{\hat{N}}_k^S(\underline{\eta})\cdot\underline{c},$$
$$q(\underline{x}) = \underline{\hat{q}}(\xi,\underline{\eta})\cdot\underline{c} = \text{diag}\left(\xi^{\underline{\underline{\lambda_+}}-0.5(d-2)}\right)\underline{\underline{A}}^q\underline{\hat{N}}_k^S(\underline{\eta})\cdot\underline{c}.$$

where $\underline{\hat{\phi}}$ and $\underline{\hat{q}}$ are vectors composed of span$\{\phi_i\}$ and span$\{q_i\}$, respectively, $i = 1, ..., \mathcal{N}^S$, $\mathcal{N}^S$ the DOF for an element. Isolating $\underline{c}$ from (3.2.3) and replacing in (3.2.3) leads to

$$\underline{\underline{A}}^q\ \underline{\underline{A}}^{-1}\underline{u}(\xi) = \underline{q}(\xi). \tag{3.2.-6}$$

For $\xi = 1$, (3.2.3) is written as

$$\underline{\underline{K}}^S\underline{u}^S = \underline{f}. \tag{3.2.-6}$$

where $\underline{\underline{K}}^S$ is the stiffness matrix given by

$$\underline{\underline{K}}^S = \underline{\underline{A}}^q\underline{\underline{A}}^{-1}. \tag{3.2.-6}$$

and u^S is the Dirichlet data in $\Gamma^{h,S}$ and $\underline{f}$ is the force vector.

The solution is composed by the linear combination of the SBFEM basis functions $u_0(\underline{x}) = \hat{u}_0(\xi,\underline{\eta}) = \underline{\hat{\phi}}_l(\xi,\underline{\eta})\cdot\underline{c}$, where $\underline{c} = \underline{\underline{A}}^{-1}\underline{u}^S$. For instance, for a polygonal element, one can construct functions as in Fig. 3.8 by setting 1 on a DOF and null in the others, for example.

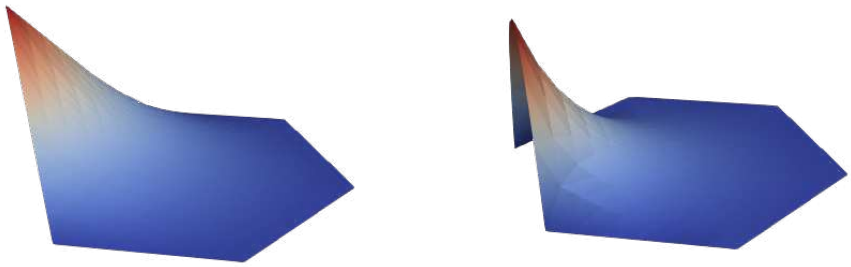

Figure 3.8: SBFEM functions composed by setting $u_i^S = 1$ and the other inputs equal to zero.

3.2.4 SBFEM approximations for the Elasticity problem

For linear elasticity, consider a simple static problem with isotropic material and null body loads, in which the weak statement in matricial form is given by: Find $\underline{u}_h \in \underline{\mathbb{S}}_k^h$ such that

$$\int_\Omega \underline{\underline{D}}\underline{\epsilon}(\underline{u}_h)\cdot\underline{\epsilon}(\underline{v})\ d\Omega = 0,\ \forall\underline{v} \in \underline{\mathbb{S}}_k^{0,h}$$
$$\underline{u}_h|_{\partial\Omega} = \underline{u}_D.$$

where $\underline{\underline{D}}$ is the constitutive tensor, and $\underline{\epsilon}$ is the strain vector, respectively given by, for 3D problems,

$$\underline{\underline{D}} = \frac{E}{(1+\nu)(1-2\nu)}\begin{pmatrix} 1-\nu & \nu & \nu & 0 & 0 & 0 \\ \nu & 1-\nu & \nu & 0 & 0 & 0 \\ \nu & \nu & 1-\nu & 0 & 0 & 0 \\ 0 & 0 & 0 & \frac{1-2\nu}{2} & 0 & 0 \\ 0 & 0 & 0 & 0 & \frac{1-2\nu}{2} & 0 \\ 0 & 0 & 0 & 0 & 0 & \frac{1-2\nu}{2} \end{pmatrix},\quad \underline{\epsilon} = \begin{Bmatrix} \epsilon_{11} \\ \epsilon_{22} \\ \epsilon_{33} \\ 2\epsilon_{12} \\ 2\epsilon_{23} \\ 2\epsilon_{13} \end{Bmatrix}.$$

where E and ν are respectively the Young modulus and the Poisson coefficient and,

$$\epsilon_{ij} = \frac{1}{2}\left(\frac{\partial u_i}{\partial x_j} + \frac{\partial u_j}{\partial x_i}\right).$$

Recall the vector-valued Duffy's space $\underline{D}_k(S)$ defined in (3.2.2). The SBFEM space for Elasticity $\underline{\mathbb{S}}_k^h \in \underline{D}_k^h(S)$ is given by

$$\underline{\mathbb{S}}_k^h = \left\{\underline{w} \in H^1(\Omega;\mathbb{R}^d);\ \underline{w}|_S \in \underline{\mathbb{S}}_k^h(S), S \in \mathcal{T}^h\right\} \tag{3.2.-6}$$

where,

$$\underline{\mathbb{S}}_k(S) = \left\{\underline{\phi} \in \underline{\mathcal{D}}_k(S);\ \int_S \underline{\underline{D}}\ \underline{\epsilon}(\underline{\phi}) \cdot \underline{\epsilon}(\underline{\psi})\ dS = 0, \forall \underline{\psi} \in \underline{\mathcal{D}}_k^0(S),\ \underline{\psi}(\mathbf{O}) = \underline{0}\right\}. \tag{3.2.-6}$$

Notice that now $\underline{\phi}$, $\underline{\psi}$ are vectors with d components, written as

$$\begin{aligned}
\underline{\phi}(\underline{x}) = \underline{\hat{\phi}}(\xi,\underline{\eta}) &= \underline{\hat{\alpha}}(\underline{\eta})\hat{\rho}(\xi) \\
&= \left(\underline{\underline{\hat{N}}}_k^S(\underline{\eta})\underline{a}^e\right)\hat{\rho}^e(\xi) \\
\underline{\psi}(\underline{x}) = \underline{\hat{\psi}}(\xi,\underline{\eta}) &= \underline{\hat{\beta}}(\underline{\eta})\hat{\tau}(\xi) \\
&= \left(\underline{\underline{\hat{N}}}_k^S(\underline{\eta})\underline{b}^e\right)\hat{\tau}^e(\xi).
\end{aligned}$$

To obtain the Ricatti equation, first write the strain vector as $\underline{\epsilon}(\underline{\phi})$ as (SONG, 2018)

$$\underline{\epsilon}(\underline{\phi}) = \underline{\underline{L}}\ \underline{\phi} \tag{3.2.-6}$$

where $\underline{\underline{L}}$ is the differential operator, given by

$$\underline{\underline{L}} = \begin{pmatrix}
\frac{\partial}{\partial x_1} & 0 & 0 \\
0 & \frac{\partial}{\partial x_2} & 0 \\
0 & 0 & \frac{\partial}{\partial x_3} \\
0 & \frac{\partial}{\partial x_3} & \frac{\partial}{\partial x_2} \\
\frac{\partial}{\partial x_3} & 0 & \frac{\partial}{\partial x_1} \\
\frac{\partial}{\partial x_2} & \frac{\partial}{\partial x_1} & 0
\end{pmatrix}.$$

Based on Wolf (2003), the strain vector $\underline{\epsilon}$ is written as a function of $\underline{\underline{B}}_1$ and $\underline{\underline{B}}_2$ in order to write the Riccati ODE for the Elasticity problem using a similar procedure as performed for the Poisson problem. Using Duffy's geometric map, recall that the derivatives are given by

$$\begin{Bmatrix} \frac{\partial}{\partial x_1} \\ \frac{\partial}{\partial x_2} \\ \frac{\partial}{\partial x_3} \end{Bmatrix} = \begin{Bmatrix} j_{11} \\ j_{21} \\ j_{31} \end{Bmatrix} \frac{\partial}{\partial \xi} + \frac{1}{\xi}\left(\begin{Bmatrix} j_{12} \\ j_{22} \\ j_{32} \end{Bmatrix} \frac{\partial}{\partial \eta_1} + \begin{Bmatrix} j_{13} \\ j_{23} \\ j_{33} \end{Bmatrix} \frac{\partial}{\partial \eta_2}\right).$$

Then, $\underline{\underline{L}}$ is rewritten as (WOLF, 2003),

$$\begin{aligned}
\underline{\underline{L}} &= \begin{pmatrix} \underline{\underline{\mathbf{b}}}_1 & \underline{\underline{\mathbf{b}}}_2 & \underline{\underline{\mathbf{b}}}_3 \end{pmatrix} \begin{Bmatrix} \frac{\partial}{\partial \xi} \\ \frac{1}{\xi}\frac{\partial}{\partial \eta_1} \\ \frac{1}{\xi}\frac{\partial}{\partial \eta_2} \end{Bmatrix} \\
&= \underline{\underline{\mathbf{b}}}_1 \frac{\partial}{\partial \xi} + \frac{1}{\xi}\left(\underline{\underline{\mathbf{b}}}_2 \frac{\partial}{\partial \eta_1} + \underline{\underline{\mathbf{b}}}_3 \frac{\partial}{\partial \eta_2}\right)
\end{aligned}$$

where

$$\underline{\underline{\mathbf{b}}}_1 = \begin{pmatrix} j_{11} & 0 & 0 \\ 0 & j_{21} & 0 \\ 0 & 0 & j_{31} \\ 0 & j_{31} & j_{21} \\ j_{31} & 0 & j_{11} \\ j_{21} & j_{11} & 0 \end{pmatrix}, \quad \underline{\underline{\mathbf{b}}}_2 = \begin{pmatrix} j_{12} & 0 & 0 \\ 0 & j_{22} & 0 \\ 0 & 0 & j_{32} \\ 0 & j_{32} & j_{22} \\ j_{32} & 0 & j_{12} \\ j_{22} & j_{12} & 0 \end{pmatrix}, \quad \underline{\underline{\mathbf{b}}}_3 \begin{pmatrix} j_{13} & 0 & 0 \\ 0 & j_{23} & 0 \\ 0 & 0 & j_{33} \\ 0 & j_{33} & j_{23} \\ j_{13} & 0 & j_{13} \\ j_{23} & j_{33} & 0 \end{pmatrix}.$$

Then, the strain $\underline{\epsilon}(\phi) = \underline{\underline{L}}\ \underline{\phi}$ is written as

$$\underline{\epsilon} = \underline{\underline{\mathbf{b}}}_1 \underline{\underline{N}}_k^S(\underline{\eta}) \underline{a}^e \rho^{e\prime}(\xi) + \frac{1}{\xi}\left(\underline{\underline{\mathbf{b}}}_2 \frac{\partial \underline{\underline{N}}_k^S(\underline{\eta})}{\partial \eta_1} \underline{a}^e \rho^e(\xi) + \underline{\underline{\mathbf{b}}}_3 \frac{\partial \underline{\underline{N}}_k^S(\underline{\eta})}{\partial \eta_2} \underline{a}^e \rho^e(\xi) \right)$$

Consider $\hat{\underline{\Phi}}^e(\xi) = \underline{a}^e \hat{\rho}^e(\xi)$, Eq. (3.2.4) is rearranged as

$$\underline{\epsilon} = \begin{pmatrix} \underline{\underline{\mathbf{b}}}_1 \underline{\underline{N}}_k^S(\underline{\eta}) & \underline{\underline{\mathbf{b}}}_2 \dfrac{\partial \underline{\underline{N}}_k^S(\underline{\eta})}{\partial \eta_1} + \underline{\underline{\mathbf{b}}}_3 \dfrac{\partial \underline{\underline{N}}_k^S(\underline{\eta})}{\partial \eta_2} \end{pmatrix} \begin{Bmatrix} \hat{\underline{\Phi}}^{e\prime}(\xi) \\ (1/\xi)\hat{\underline{\Phi}}^e(\xi) \end{Bmatrix}$$

The $\underline{\underline{B}}_1$ and $\underline{\underline{B}}_2$ matrices are introduced as follows

$$\underline{\underline{B}}_1 = \underline{\underline{\mathbf{b}}}_1 \hat{\underline{\underline{N}}}_k^S(\underline{\eta})$$
$$\underline{\underline{B}}_2 = \begin{bmatrix} \underline{\underline{\mathbf{b}}}_2 & \underline{\underline{\mathbf{b}}}_3 \end{bmatrix} \left[\nabla_{\underline{\eta}} \hat{\underline{\underline{N}}}_k^S(\underline{\eta}) \right]^T,$$

where $\nabla_{\underline{\eta}} \hat{\underline{\underline{N}}}_k^S(\underline{\eta})$ is the gradient of $\hat{\underline{\underline{N}}}_k^S$ in the parametric surface coordinates $\underline{\eta} = (\eta_1, \eta_2)$, of dimension $6 \times \mathcal{N}^S$. Performing the multiplications in (3.2.4) and (3.2.4), it is verified that $\underline{\underline{B}}_1$ and $\underline{\underline{B}}_2$ matrices have dimensions $6 \times \mathcal{N}^S$. Thus, the strain vector is simplified to

$$\underline{\epsilon}(\phi) = \begin{bmatrix} \underline{\underline{B}}_1 & \underline{\underline{B}}_2 \end{bmatrix} \begin{bmatrix} \underline{\Phi}^{e\prime}(\xi) \\ (1/\xi)\underline{\Phi}^e(\xi) \end{bmatrix} \tag{3.2.-6}$$

Analogously, $\underline{\epsilon}(\psi)$ is given by

$$\underline{\epsilon}(\psi) = \begin{bmatrix} \underline{\underline{B}}_1 & \underline{\underline{B}}_2 \end{bmatrix} \begin{bmatrix} \underline{\Psi}^{e\prime}(\xi) \\ (1/\xi)\underline{\Psi}^e(\xi) \end{bmatrix} \tag{3.2.-6}$$

Table 3.4 shows that there is a similarity between the expressions of the gradient $\nabla\phi$ for the Poisson problem and the strain $\epsilon(\phi)$ for the Elasticity problem, as well as the approximation space condition. In both cases, the approximation space is constructed based on the semi-norm of the energy for a homogeneous PDE.

Poisson problem		Elasticity problem	
$\nabla\phi$	$\nabla\phi = \begin{bmatrix} \underline{B}_1 & \underline{B}_2 \end{bmatrix} \begin{bmatrix} \underline{\Phi}'(\xi) \\ (1/\xi)\underline{\Phi}(\xi) \end{bmatrix}$	$\epsilon(\phi)$	$\underline{\epsilon}(\phi) = \begin{bmatrix} \underline{\underline{B}}_1 & \underline{\underline{B}}_2 \end{bmatrix} \begin{bmatrix} \underline{\Phi}^{e\prime}(\xi) \\ (1/\xi)\underline{\Phi}^e(\xi) \end{bmatrix}$
Condition imposed for $\mathbb{S}_k$	$\nabla\phi \cdot \nabla\psi = 0$	Condition imposed for $\underline{\mathbb{S}}_k$	$\underline{\underline{D}}\ \underline{\epsilon}(\underline{\phi}) \cdot \underline{\epsilon}(\underline{\psi}) = 0$

Table 3.4: Comparison between expressions using the SBFEM

It means that one can write the internal dot product $\underline{\underline{D\epsilon}}(\phi) \cdot \underline{\epsilon}(\psi)$ as

$$\int_S \underline{\underline{D\epsilon}}(\underline{\phi}) \cdot \underline{\epsilon}(\underline{\psi})\, dS = \int_0^1 \hat{\underline{\Psi}}^{e\prime}(\xi) \cdot \left[\xi^{d-1}\underline{\underline{E}}_0^e \hat{\underline{\Phi}}^{e\prime}(\xi) + \xi^{d-2}\underline{\underline{E}}_1^e \hat{\underline{\Phi}}^{e}(\xi)\right] + \hat{\underline{\Psi}}^{e}(\xi) \cdot \left[\xi^{d-2}\underline{\underline{E}}_1^{eT} \hat{\underline{\Phi}}^{e\prime}(\xi) + \xi^{d-3}\underline{\underline{E}}_2^e \hat{\underline{\Phi}}^{e}(\xi)\right]\, d\xi.$$

where the SBFEM coefficient matrices are given by

$$\underline{\underline{E}}_0^e = \int_{\partial S} \underline{\underline{B}}_1^T \underline{\underline{DB}}_1 |\underline{\underline{J}}_K(1,\eta)| d\underline{\eta}, \tag{3.2.-7}$$

$$\underline{\underline{E}}_1^e = \int_{\partial S} \underline{\underline{B}}_2^T \underline{\underline{DB}}_1 |\underline{\underline{J}}_K(1,\eta)| d\underline{\eta}, \tag{3.2.-7}$$

$$\underline{\underline{E}}_2^e = \int_{\partial S} \underline{\underline{B}}_2^T \underline{\underline{DB}}_2 |\underline{\underline{J}}_K(1,\eta)| d\underline{\eta}. \tag{3.2.-7}$$

The same procedure described by Coelho, Devloo and Gomes (2021) to deduce the Riccati equation is also applied here, leading to a very similar ODE

$$\xi^{d-1}\underline{\underline{E}}_0 \hat{\underline{\Phi}}^{e\prime\prime}(\xi) + \xi^{d-2}\left[(d-1)\underline{\underline{E}}_0^e - [\underline{\underline{E}}_1^e]^T + \underline{\underline{E}}_1\right]\hat{\underline{\Phi}}^{e\prime}(\xi) + \xi^{d-3}\left[(d-2)\underline{\underline{E}}_1 - \underline{\underline{E}}_2\right]\hat{\underline{\Phi}}^{e}(\xi) = 0. \tag{3.2.-7}$$

where the solution is analogously expressed as

$$\underline{\phi}_i(\underline{x}) = \hat{\underline{\phi}}_i(\xi,\underline{\eta}) = \xi^{\lambda_i^e - 0.5(d-2)} \sum_l A_i^{e,l} \hat{\underline{N}}_k^{S,l}(\underline{\eta}),\ \forall \underline{\phi}_i \in \mathbb{S}_k^h(S)$$

$$\underline{q}_i(\underline{x}) = \hat{\underline{\phi}}_i(\xi,\underline{\eta}) = \xi^{\lambda_i^e - 0.5(d-2)} \sum_l A_i^{e,q,l} \hat{\underline{N}}_k^{S,l}(\underline{\eta}),\ \forall \underline{q}_i \in \mathbb{S}_k^h(S).$$

where λ_i^e is the eigenvalue for the Elasticity problem and $\underline{A}_i^e$ and $\underline{A}_i^{e,q}$ are the eigenvectors corresponding to the displacement and force modes. The pairs of eigenvalues/eigenvectors are obtained through the solution of the eigenvalue problem using the same procedure already described previously for the Poisson problem.

3.3 A priori error estimates

Based on the FE theory of Duffy's spaces and the gradient-orthogonality property inherent to the SBFEM spaces, it is proven in this section that the SBFEM approximation spaces have convergence rate of order k, where k is the polynomial approximation for the energy semi-norm. Moreover, for the SBFEM approximations, the rate of convergence is governed by the trace approximation, which means that optimal convergence rates are obtained even for problems with square root singularity.

A priori error estimates for SBFEM in the H1 norm are demonstrated using the orthogonality property shown in definition of the SBFEM space (Section 3.2) followed by traditional FEM interpolation results. Finally, the error analysis for the Galerkin SBFEM approximations is presented. All analyses in this section are based on the harmonic problem, but they can be extended for Elasticity problems as well.

3.3.1 Orthogonality properties of the SBFEM spaces

The SBFEM approximation spaces hold an orthogonality property, subdivided in this thesis into two types: intrinsic and extended orthogonality.

Intrinsic orthogonality property for the SBFEM local spaces

The construction of SBFEM shape functions is based on the determination of analytic eigenfunctions for the SBFEM equation - (3.2.3) for the Poisson problem and (3.2.4) for the Elasticity problem. The resulting ODE for both mechanical problems is constructed by imposing an orthogonal condition that is not well recognized in the SBFEM literature. For instance, taking the Poisson problem as a reference: for a function $\phi \in \mathbb{S}_k(S) \subset \mathcal{D}_k(S)$ the gradient orthogonality constraint

$$\langle \phi, \psi \rangle_{\nabla,S} = \langle \nabla\phi, \nabla\psi \rangle_{L^2(S)} = \int_S \nabla\phi(\underline{x}) \cdot \nabla\psi(\underline{x})\, dS = 0 \tag{3.3.0}$$

holds for all $\psi \in \mathcal{D}_k^0(S)$, with $\psi(\mathbf{O}) = 0$. In such case, then ϕ solves equation (3.2.3). Notice that this orthogonal condition is imposed directly in the construction of the SBFEM space in (3.2.3). Analogous reasoning can be established in the SBFEM space for Elasticity problems as

$$\langle \underline{\phi}, \underline{\psi} \rangle_{\mathcal{E},S} = \langle \underline{\underline{D}}\ \underline{\epsilon}(\underline{\phi}(\underline{x})), \underline{\epsilon}(\underline{\psi}(\underline{x})) \rangle_{L^2(S)} = \int_S \underline{\underline{D}}\ \underline{\epsilon}(\underline{\phi}(\underline{x})) \cdot \underline{\epsilon}(\underline{\psi}(\underline{x}))\, dS = 0 \tag{3.3.0}$$

for all $\underline{\phi} \in \underline{\mathbb{S}}_k(S)$ and $\underline{\psi} \in \underline{\mathcal{D}}_k^0(S)$ with $\underline{\psi}(\mathbf{O}) = 0$.

Extended orthogonality property for the SBFEM local spaces

The SBFEM orthogonality resulting from the approximation space definition, described in Eq. (3.3.1) for the Poisson problem, is now extended to a wider space for ψ. Let $\mathcal{H}(S)$ denote the space of harmonic functions in S. Then, $\langle \phi, \psi \rangle_{\nabla,S} = 0$ for all $\phi \in \mathcal{H}(S)$ and $\psi \in H_0^1(S)$, giving the decomposition

$$H^1(S) = \mathcal{H}(S) \overset{\nabla}{\oplus} H_0^1(S), \tag{3.3.0}$$

where the symbol $\overset{\nabla}{\oplus}$ denotes the orthogonality relation with respect to the gradient inner product $\langle \cdot, \cdot \rangle_{\nabla,S}$. In other words, the $H^1(S)$ can be decomposed in $\mathcal{H}(S)$ and $H_0^1(S)$ with respect to their gradients.

A similar relation to (3.3.1) for Duffy's spaces $\mathcal{D}_k(S) \subset H^1(S)$, $\mathbb{S}_k(S)$ playing the role of the harmonic functions. For that, the gradient orthogonality property (3.3.1) is extended to functions $\psi \in \mathcal{D}_k^0(S)$.

Define the finite-dimensional Duffy's space as

$$\mathbb{D}_k^h(S) = \text{span}\{N_m^S(\underline{\eta})\xi^n\} \subset \mathcal{D}_k(S) \tag{3.3.0}$$

A finite-dimensional Duffy's bubble space $\mathbb{D}_k^{0,h}(S) \subset \mathcal{D}_k(S)$ can be constructed as

$$\mathbb{D}_k^{0,h}(S) = \text{span}\{N_m^S(\underline{\eta})(\xi^{n-1} - \xi^n)\} \subset \mathcal{D}_k^0(S). \tag{3.3.0}$$

Proposition 3.3.1. *The orthogonality property*

$$\langle \phi, \psi \rangle_{\nabla,S} = 0, \quad \forall \phi \in \mathbb{S}_k(S) \ \ \textit{and}\ \psi \in \mathbb{D}_k^0(S) \tag{3.3.0}$$

is valid. Thus,

$$\mathbb{D}_k(S) = \mathbb{S}_k(S) \overset{\nabla}{\oplus} \mathbb{D}_k^0(S). \tag{3.3.0}$$

Proof. A crucial step in the derivation of the SBFEM ODE (3.2.3) is the formula for the gradient inner product $\langle \phi, \psi \rangle_{\nabla,S}$ given in (3.2.3) and replaced here to ease the understanding

$$\int_0^1 \hat{\underline{\Psi}}'(\xi) \cdot \hat{\underline{Q}}(\xi) d\xi = \hat{\underline{\Psi}} \cdot \hat{\underline{Q}} \Big]_0^1 - \int_0^1 \hat{\underline{\Psi}}(\xi) \cdot \hat{\underline{Q}}'(\xi)\, d\xi.$$

Two terms enter into play: a boundary term $\hat{\underline{\Psi}} \cdot \hat{\underline{Q}} \Big]_0^1$ where

$$\hat{\underline{Q}}(\xi) = \xi^{d-1} \underline{\underline{E}}_0 \hat{\underline{\Phi}}'(\xi) + \xi^{d-2} \underline{\underline{E}}_1 \hat{\underline{\Phi}}(\xi)$$

and an integral term $\int_0^1 \hat{\underline{\Psi}}(\xi) \cdot \hat{\underline{Q}}'(\xi)\, d\xi$. The constraints $\psi \in \mathcal{D}_k^0(S)$ and $\Psi(\mathbf{O}) = 0$ make the boundary term to be zero, and the second-order ODE equation (3.2.3) derives from the assumption (3.3.1). It means that the orthogonality remains for any function $\psi \in \text{span}\{N_m^S(\underline{\eta})(\xi^{n-1} - \xi^n)\} \subset \mathcal{D}_k^0(S), \quad n = 2, ..., k..$ The demonstration lacks proving the orthogonality for the linear bubble function $\psi = 1 - \xi$, known as a hat function.

The property $\langle \phi, \psi \rangle_{\nabla,S} = 0$ holds for $\phi \equiv 1$ (i.e. $\lambda_i = 0$) because in such a case $\hat{\underline{Q}}(\xi) = \xi^{d-1} \underline{\underline{E}}_0 \hat{\underline{\Phi}}'(\xi) + \xi^{d-2} \underline{\underline{E}}_1 \hat{\underline{\Phi}}(\xi) = 0$ since

$$\underline{\underline{E}}_1 = \int_{-1}^{+1} \underline{B}_2^T \underline{B}_1 |\underline{\underline{J}}_K(1, \underline{\eta})|\, d\underline{\eta} = 0 \tag{3.3.0}$$

because

$$\underline{B}_2(\underline{\eta}) = \left[\underline{\underline{J}}_K(1, \underline{\eta})\right]^{-T} \begin{bmatrix} \underline{0} \\ \nabla_{\underline{\eta}} \hat{\underline{N}}_k^S(\underline{\eta}) \end{bmatrix} = \underline{0} \tag{3.3.0}$$

for $\nabla_{\underline{\eta}} \hat{\underline{N}}_k^S(\underline{\eta}) = \underline{0}$ for a constant function.

Thus, it is sufficient to verify it for all shape functions $\phi = \phi_i$ associated with eigenvalues $\lambda_1 = 1$, or, more generically $\lambda_i \neq 0$.

The desired orthogonality property (3.3.1) is valid for $\psi(\underline{x}) \in \mathcal{D}_k^0(S)$, with $\psi(\underline{x}) = \hat{\psi}(\xi, \underline{\eta}) = C\hat{\sigma}(\xi)$, if and only if it holds for functions $\varphi = \hat{\psi}(\xi) - C\hat{\sigma}(1) \in \mathcal{D}_0^0(S)$, i.e., for the cases where

$$\hat{\varphi}(\xi) = C(\hat{\sigma}(\xi) - \hat{\sigma}(1)),$$

with $\hat{\varphi}(1) = 0$. For them, apply equation (3.2.3), valid for all shape functions $\phi_i \in \mathbb{S}_k(S)$, to reduce the equation (3.3.1) to

$$\langle \phi_i, \varphi \rangle_{\nabla,S} = \hat{\varphi}(1) \sum_n \hat{\underline{Q}}_{in}(1) - \hat{\varphi}(0) \sum_n \hat{\underline{Q}}_{in}(0).$$

Thus, since $\hat{\varphi}(1) = 0$ and $\hat{\underline{Q}}_{in}(0) = 0$, the orthogonality property is obtained (3.3.1). □

3.3.2 Interpolants

When a Galerkin method is used to approximate a boundary value problem, one of the most important choices is the family of approximation spaces. For elliptic problems, the achievable approximation error is equal to the error obtained by approximating the solution of the partial differential equation directly from the trial space. The accuracy is accessed *a priori* by bounds computed in terms of interpolant errors using the approximation space. In the context of piecewise-defined approximations over subregions (elements) of the computational domain, as is the case of FE methods, the interpolants usually show the following characteristics:

- Locality: in each subregion, a polynomial trace interpolant over the boundary is extended to the interior (a process also called lifting).
- Global conformity: it follows directly from the hypothesis that the trace interpolants depend exclusively on the function restriction over subregion boundaries.
- Optimality: optimal interpolation error estimates are achieved with respect to the discretization parameters: mesh width and polynomial order.

In this direction, the plan is to construct interpolants in Duffy trial spaces and explore them to evaluate the potential of SBFEM approximations. Firstly, new notation and auxiliary results already known in other contexts are introduced in the following.

Define:

1. Conformal polytopal partitions $\mathcal{T}^h = \{S\}$: partition of Ω by S-elements as already described in Section 3.2.1.
2. Mesh skeleton $\Gamma^h = \cup_{L\in\mathcal{E}^h} L$: the assembly of all facets (edges of faces) in $\mathcal{E}^h = \{L \subset \Gamma^{h,S}, S \in \mathcal{T}^h\}$. The parameter h refers to the characteristic size of the facets in Γ^h.
3. Conglomerate partitions $\mathcal{P}^h = \cup_{S\in\mathcal{T}^h}\mathcal{T}^{h,S}$ of Ω. Recall that the elements $K \in \mathcal{T}^{h,S}$ may be affine triangles, pyramids, or tetrahedra inheriting the conformal property from $\mathcal{T}^h$. In principle, the shape regularity of $\mathcal{P}^h$ is not a granted property.

Based on the partitions Γ^h, $\mathcal{T}^h$ or $\mathcal{P}^h$, consider the following approximation spaces.

- FE trace spaces: $\Lambda_k(\Gamma^h) = C(\Gamma^h)\cap\prod_{L\in\mathcal{E}^h}\mathcal{V}_k(L)$, piecewise polynomial spaces, where $\mathcal{V}_k(L) = \mathbb{P}_k(L)$, for 1D edges and triangular facets L, and $\mathcal{V}_k(L) = \mathbb{Q}_{k,k}(L)$, for quadrilateral facets L.
- Duffy's spaces $\mathcal{D}_k^h \subset H^1(\Omega)$: given the local Duffy's spaces $\mathcal{D}_k^h(S), S \in \mathcal{T}^h$ defined in Section 3.1.2, set

$$\mathcal{D}_k^h = \{w \in H^1(\Omega); w|_S \in \mathcal{D}_k^h(S), S \in \mathcal{T}^h\},$$
$$\mathcal{D}_k^{0,h} = \{w \in H^1(\Omega); w|_S \in \mathcal{D}_k^0(S), S \in \mathcal{T}^h\}$$

  Notice that $\mathcal{D}_k^{0,h} \subset \mathcal{D}_k^h, \forall k \geq 0$.
- SBFEM spaces $\mathbb{S}_k^h \subset H^1(\Omega)$: given local SBFEM spaces $\mathbb{S}_k^h(S) \subset \mathcal{D}_k^h(S), S \in \mathcal{T}^h$, described in Section 3.2.3, define

$$\mathbb{S}_k^h = \{w \in H^1(\Omega); w|_S \in \mathbb{S}_k^h(S), S \in \mathcal{T}^h\},$$

  and set $\mathbb{S}_{k,0}^h = \mathbb{S}_k^h \cap H_0^1(\Omega)$.
- FE spaces $\mathcal{V}_k^{h,FE} \subset H^1(\Omega)$: Consider the following FE spaces based on the conglomerated meshes $\mathcal{P}^h$.

  1. Triangular (2D) and tetrahedral (3D) meshes $\mathcal{P}^h$:

$$\mathcal{V}_k^{h,FE} := \mathbb{P}_k(\mathcal{P}^h) \cap H^1(\Omega), \tag{3.3.0}$$

     where $\mathbb{P}_k(\mathcal{P}^h)$ stands for functions piecewise-defined by polynomials in $\mathbb{P}_k(K)$, $K \in \mathcal{P}^h$, of degree not greater than k.

2. Pyramidal (3D) meshes $\mathcal{P}^h$: let us consider

$$\mathcal{V}_k^{h,FE} := \mathcal{U}^{(0),k}(\mathcal{T}^h) \cap H^1(\Omega), \tag{3.3.0}$$

piecewise-defined by a class of rational polynomials $\mathcal{U}^{(0),k}(K)$, for $K \in \mathcal{P}^h$ (NIGAM; PHILLIPS, 2012). Traces of functions in $\mathcal{U}^{(0),k}(K)$ are in $\mathbb{P}_k(L)$ for triangular faces, and in $\mathbb{Q}_{k,k}(L)$ if L is quadrilateral. Moreover, $\mathbb{P}_k(K) \subset \mathcal{U}^{(0),k}(K)$.

Proposition 3.3.2. *For the mesh skeleton Γ_h and the conglomerate partition $\mathcal{P}_h$, the following inclusions are valid:*

i) For a function in a FE space $w \in \mathcal{V}_k^{h,FE}$ (Eqs. (1) and (2)), its trace is included in the FE trace space of Γ_h, i.e. $w|_{\Gamma^h} \in \Lambda_k(\Gamma^h)$.

ii) A polynomial space in $\mathcal{P}^h$ is included in the FE space of $\mathcal{P}^h$, which is included in the polynomial Duffy's space - i.e. $\mathbb{P}_k(\mathcal{P}^h) \subset \mathcal{V}_k^{h,FE} \subset \mathcal{D}_k^h$.

Proof. The trace property (i) is already known, as discussed in Boffi, Brezzi and Fortin (2013, Page 5 - Eq. (1.2.7.)). Also, for a partition $\Omega = \mathcal{P}^h$, the polynomial inclusion (ii) $\mathbb{P}_k(\mathcal{P}^h) \subset \mathcal{V}_k^{h,FE}$ comes from the definition of $\mathcal{V}_k^{h,FE}$ and from the definition of $H^1(\mathcal{P}^h)$. Since $\mathbb{P}_k(\mathcal{P}^h) \subset H^1(\mathcal{P}^h)$, from Eqs. (1) and (2), $\mathbb{P}_k(\mathcal{P}^h) \subset \mathcal{V}_k^{h,FE}$.

To prove the second embedding property in (ii) $\mathcal{V}_k^{h,FE} \subset \mathcal{D}_k^h$, start by considering three particular collapsed triangular, pyramidal, and tetrahedral reference elements.

- *A triangular reference element K*:

  Let K be the reference triangle, with collapsed vertex $\underline{\mathbf{a}}_0 = (0, 0)$, and the opposed edge $L = [\underline{\mathbf{a}}_1, \underline{\mathbf{a}}_2]$, where $\underline{\mathbf{a}}_1 = (1, 0)$ and $\underline{\mathbf{a}}_2 = (1, 1)$, as shown in Fig. 3.9.

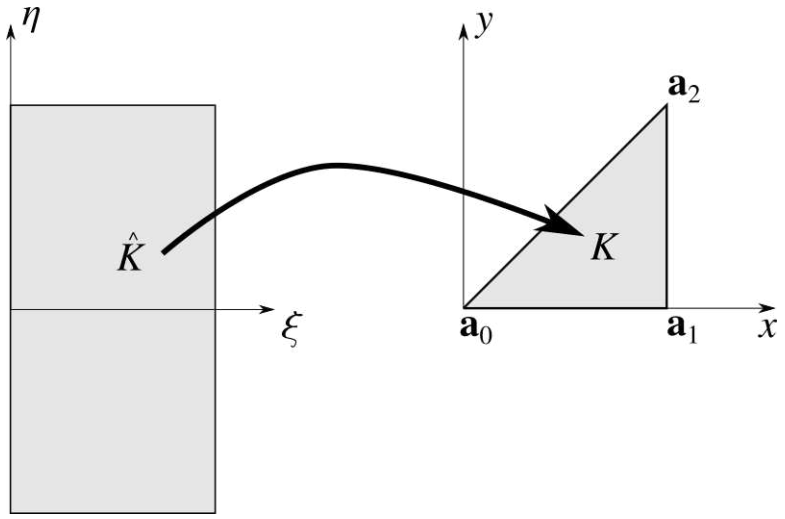

Figure 3.9: The triangular reference element for the proof of Proposition 3.3.2.

  Taking the mapping $F_L : \hat{L} \to L$, defined as $F_L(\underline{\eta}) = \left(\frac{1+\underline{\eta}}{2}, \frac{1-\underline{\eta}}{2}\right)$, Duffy's transformation from $\hat{K}$ over K becomes $x = \frac{\xi}{2}(1 + \underline{\eta})$, $y = \frac{\xi}{2}(1 - \underline{\eta})$, whose inversion is $\xi = x + y$, $\underline{\eta} = \frac{x-y}{x+y}$.

Let $\psi \in \mathcal{D}_k(K)$ be the pullback of functions $\mathbb{F}_K(\hat{\psi}) \in \mathcal{D}_k(\hat{K})$, where $\hat{\psi}(\xi, \underline{\eta}) = \xi^k \hat{\alpha}(\underline{\eta})$, so that $\psi(x, y) = (x + y)^k \hat{\alpha}(\frac{x-y}{x+y})$. By varying $\hat{\alpha} \in \mathbb{P}_k(\hat{L})$, the rational term $\frac{x-y}{x+y}$ cancels with $(x + y)^k$. Thus, all functions $\psi(x, y) \in \mathbb{P}_k(K)$ can be recovered in $\mathcal{D}_k(K)$.

- *A tetrahedral reference element K*:

  Suppose K is the reference tetrahedron with collapsed vertex $\underline{\mathbf{a}}_0 = (0, 0, 0)$, and opposed triangular face $L = [\underline{\mathbf{a}}_1, \underline{\mathbf{a}}_2, \underline{\mathbf{a}}_3]$, with $\underline{\mathbf{a}}_1 = (1, 0, 1)$, $\underline{\mathbf{a}}_2 = (1, 0, 0)$ and $\underline{\mathbf{a}}_3 = (1, 1, 0)$, as shown in Fig. 3.10.

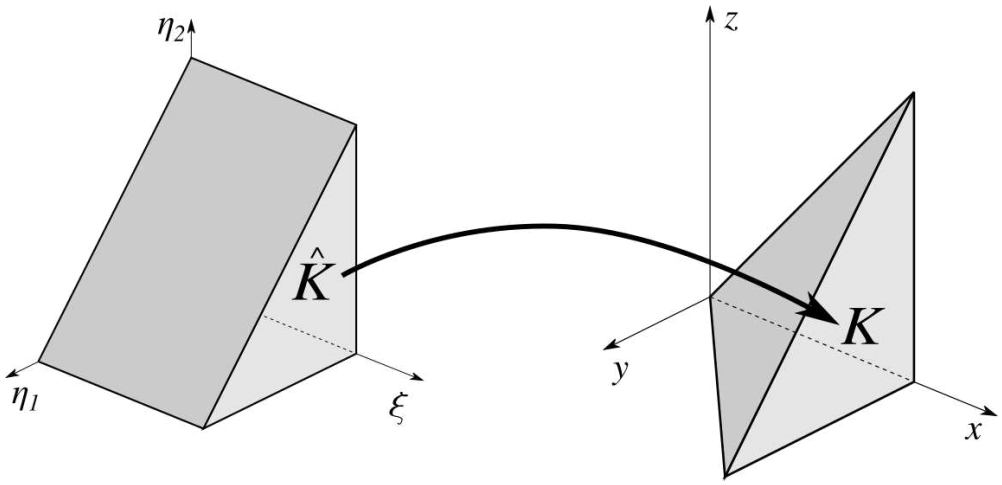

Figure 3.10: The tetrahedral reference element for the proof of Proposition 3.3.2.

  Notice that L can be mapped by $\underline{x} = F_L(\underline{\eta})$, where $x = 1 - \eta_1 - \eta_2$, $y = \eta_1$, and $z = \eta_2$. Then, the Duffy's transformation is $F_K(\xi, \underline{\eta}) = \xi F_L(\underline{\eta})$, whose inverse is $\xi = x + y + z, \quad \eta_1 = \frac{y}{x+y+z}, \quad \eta_2 = \frac{z}{x+y+z}$

  Let $\psi = \mathbb{F}_K(\hat{\psi}) \in \mathcal{D}_k(K)$, with $\hat{\psi}(\xi, \underline{\eta}) = \xi^k \hat{\alpha}(\underline{\eta})$, and $\hat{\alpha} \in \mathbb{P}_k(\hat{L})$. Thus, the functions $\psi(x, y, z) = (x + y + z)^k \hat{\alpha}(\frac{y}{x+y+z}, \frac{z}{x+y+z})$ recover all functions in $\mathbb{P}_k(K)$ because all rational components are canceled by $(x + y + z)^k$. Thus, all functions $\psi(x, y, z) \in \mathbb{P}_k(K)$ can be recovered in $\mathcal{D}_k(K)$.

- *A pyramidal reference element*:

  To prove that $\mathcal{V}_k^{h,FE}$ is included in Duffy's approximation space, is not as straightforward as for the tetrahedron and the triangle cases. For this example, it is used the proof demonstrated in Nigam and Phillips (2012).

  Suppose K is a pyramid with vertex $\underline{\mathbf{a}}_0 = (0, 0, 1)$, and opposed face $L = [\underline{\mathbf{a}}_1, \underline{\mathbf{a}}_2, \underline{\mathbf{a}}_3, \underline{\mathbf{a}}_4]$, with vertices $\underline{\mathbf{a}}_1 = (0, 0, 0)$, $\underline{\mathbf{a}}_2 = (1, 0, 0)$, $\underline{\mathbf{a}}_3 = (1, 1, 0)$, and $\underline{\mathbf{a}}_4 = (0, 1, 0)$. The FE space $\mathcal{U}^{(0),k}(K) \subset H^1(K)$ proposed in Nigam and Phillips (2012), by Nigam and Phillips, is the first space of an exact sequence $\mathcal{U}^{(s),k}(K)$ verifying the De Rham commuting property. Their definition considers the geometric transformation $S_\infty : K_\infty \to K$ of the "infinite pyramid" $K_\infty = \{(x, y, z) \in \mathbb{R}^3; x, y, z \geq 0, x \leq 1, y \leq 1\} \cup \{\infty\}$, given by $S_\infty(x, y, z) = \left(\frac{x}{1+z}, \frac{y}{1+z}, \frac{z}{1+z}\right)$, $S_\infty(\infty) = \underline{\mathbf{a}}_0$. The functions $w \in \mathcal{U}^{(0),k}(K)$ are obtained by the pullback $\mathbb{S}_\infty(u)$ of functions u in a properly chosen subspace of the rational functions $Q_k^{k,k,k}(\hat{K}_\infty) = \{\frac{q}{1+z}; q \in \mathbb{Q}_{k,k,k}(K_\infty)\}$.

Using an analogous idea, the goal is to show that $\mathcal{U}^{(0),k}(K)$ can also be interpreted in the context of Duffy's space $\mathcal{D}_k(K)$. For that, consider the hexahedron $H = [0,1]\times[0,1]\times[0,1]$, with the coordinate system (μ_1, μ_2, ξ), with $(\mu_1, \mu_2) \in [0,1]\times[0,1]$ and $0 \leq \xi \leq 1$. Observe that the geometric transformation $F_\infty : H \to K_\infty$, $F_\infty(\mu_1, \mu_2, \xi) = (\mu_1, \mu_2, \frac{\xi}{1-\xi})$ collapses the face $\xi = 1$ in H onto ∞, leading to the same "infinite pyramid" as in Nigam and Phillips (2012).

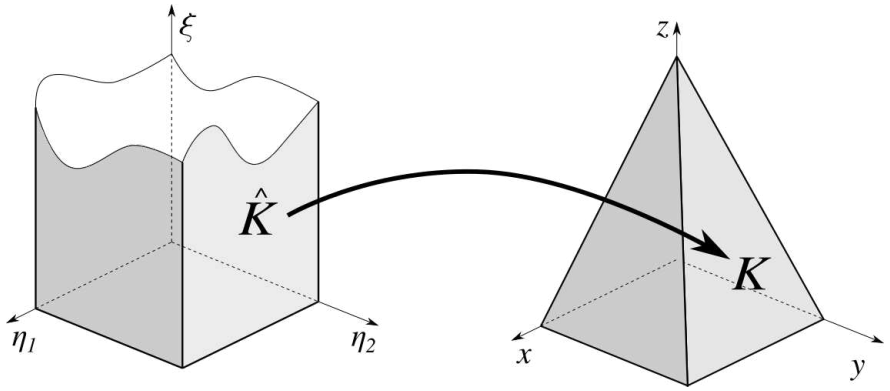

Figure 3.11: The pyramidal reference element for the proof of Proposition 3.3.2.

Moreover, $Q_k^{k,k,k}(\hat{K}_\infty) = \mathbb{F}_\infty(\mathbb{Q}_{k,k,k}(H))$. Consequently,

$$\mathcal{U}^{(0),k}(K) \subset \mathbb{S}_\infty(Q_k^{k,k,k}(\hat{K}_\infty)) = \mathbb{S}_\infty(\mathbb{F}_\infty(\mathbb{Q}_{k,k,k}(H)). \tag{3.3.0}$$

On the other hand, the transformation $F_K : H \to K$, defined by the composition $\underline{x} = F_K(\eta_1, \eta_2, \xi) = S_\infty(F_\infty(\eta_1, \eta_2, \xi))$ results to be a Duffy's transformation collapsing the face $\xi = 1$ in H on top of the vertex $\underline{\mathbf{a}}_0 \in K$. Consequently, $\mathbb{F}_K(\mathbb{Q}_{k,k,k}(H)) \subset \mathcal{D}_k(K)$. Thus, using (3.3.2) results in $\mathcal{U}^{(0),k}(K) \subset \mathcal{D}_k(K)$ - which means that all functions $\psi(x, y, z) \in \mathbb{P}_k(K)$ can be recovered in $\mathcal{D}_k(K)$.

Now consider a general element $K^e \in \mathcal{P}^h$, with collapsed vertex $\mathbf{O}$, and opposed face L^e with vertices $\underline{\mathbf{a}}_l^e$. Notice that K^e can be seen as a geometric affine transformation of one of the reference elements K described above, i.e., $K^e = T^e(K)$, such that $\mathbf{O} = T^e(\underline{\mathbf{a}}_0)$, $\underline{\mathbf{a}}_l^e = T^e(\underline{\mathbf{a}}_l)$, and thus $L^e = T^e(L)$). Since the polynomials $\mathbb{P}_k(K)$, for triangles and tetrahedra, and rational polynomials $\mathcal{U}^{(0),k}(K))$, for pyramids, are preserved by affine transformations, concluding that $\mathcal{V}_k^{h,FE} \subset \mathcal{D}_k^h$. □

3.3.3 FE interpolants

Interpolant operators $\mathcal{F}_k^{h,FE} : H^s(\Omega) \to \mathcal{V}_k^{h,FE}$ have being designed as useful tools for functions in general Sobolev spaces $H^s(\Omega), s \geq 1$. As already mentioned, they are constructed by first defining a piecewise polynomial trace interpolant over the facets $L \subset \partial K$ of each element $K \in \mathcal{P}^h$, and then by extending this trace interpolant to the interior of K. Recall some examples and error estimates already available in the literature. For them, assume the affine conglomerate triangular, pyramidal, or tetrahedral partitions $\mathcal{P}^h$ are regular (e.g. quasi-uniform and shape regular, with parameters independent of h). Under these circumstances, the following estimates hold.

- There are interpolants $\mathcal{F}_k^{h,FE} w$ over FE spaces $\mathcal{V}_k^{h,FE} = \mathbb{P}_k(\mathcal{P}^h) \cap H^1(\Omega)$ defined in Babuška and Suri (1987) for triangles and in Muñoz-Sola (1997) for tetrahedra.

Suppose $w \in H^s(\Omega)$, $s > \frac{3}{2}$ in 2D, and $s > 2$ in 3D, then the estimate

$$|w - \mathcal{F}_k^{h,FE} w|_{H^1(\Omega)} \lesssim \frac{h^{\mu-1}}{k^{d-2}} \quad \|w\|_{H^s(\Omega)}$$

holds for $\mu = \min(k+1, s)$, where the leading constant on the right side is independent of w, h, and k (but depends on s and regularity parameters of $\mathcal{P}^h$).

- There are also the projection-based interpolants, proposed by L. Demkowicz and coworkers, as expounded in Demkowicz (2008) and Demkowicz et al. (2007). They admit a general form, without requiring any specific geometric aspect, and have the flexibility to treat general local spaces, not necessarily polynomials. Note that such constructions may require additional regularity assumptions beyond the minimal H^1-conformity. Indeed, the trace interpolants may require interpolation at element vertices, requiring the regularity H^{1+s} with $s > 1/2$ in 3D FE settings. For FE spaces $\mathcal{V}_k^{h,FE} = \mathbb{P}_k(\mathcal{P}^h) \cap H^1(\Omega)$ based on tetrahedra, the error estimates stated in Demkowicz et al. (2007, Theorem 2.2) for projection-based interpolants $\mathcal{F}_k^{h,FE} w$ have the non-optimal form

$$|w - \mathcal{F}_k^{h,FE} w|_{H^1(\Omega)} \lesssim (\ln k)^2 \left(\frac{h}{k}\right)^{d-2} |w|_{H^s}, \ s > 3/2.$$

  The suboptimal logarithmic factor appearing in (3.3.3) can be dropped in the k-version under the more stringent regularity assumption $s \geq 2$ (MELENK; ROJIK, 2020, Corollary 2.12).

- For pyramidal partitions $\mathcal{P}^h$, projection-based interpolants $\mathcal{F}_k^{h,FE} w$ over the FE spaces $\mathcal{U}^{(0),k}(\mathcal{T}^h)$ are defined in Nigam and Phillips (2012). However, to the best of our knowledge, error estimates are still missing for them, but optimal h-convergence rates have been observed in numerical experiments presented in Bergot, Cohen and Duriflé (2010).

SBFEM interpolant

As for the cases of FE spaces, construct interpolant operators $\Pi_k^h : H^s(\Omega) \to \mathbb{S}_k^h$, for sufficiently smooth functions $w \in H^s(\Omega)$, following three steps: a trace interpolant $\mathcal{I}_k^h : H^s(\Gamma^h) \to \Lambda_k(\Gamma^h)$, local projections $\Pi_k^{h,S} : H^s(S) \to \mathbb{S}_k(S)$ extending trace functions to the interior of the element, and assembly of local interpolants.

1. Trace interpolant $\mathcal{I}_k^h : H^s(\Omega) \to \Lambda_k(\Gamma^h)$ - it is piecewise defined on the facets $L \in \mathcal{E}^h$, following any of the interpolation strategies used so far for the FE spaces $\mathcal{V}_k^{h,FE}$.
2. Local projections $\Pi_k^{h,S} : H^{k+1}(S) \to \mathbb{S}_k(S)$: $\Pi_k^{h,S} w \in \mathcal{D}_k^{h,S}$ solves the problem

$$\begin{aligned} \langle \Pi_k^{h,S} w, v \rangle_{\nabla,S} &= 0 \quad \forall v \in \mathcal{D}_0^0(S), \\ \Pi_k^{h,S} w|_{\Gamma^S} &= \mathcal{I}_k^h w|_{\Gamma^S}. \end{aligned}$$

  Notice that equation (2) ensures that $\Pi_k^{h,S} w \in \mathbb{S}_k(S)$ and the relation (2) enforces the trace constraint matching $\Pi_k^{h,S} w$ to the trace interpolant of w. It is clear from these equations the interpretation of $\Pi_k^{h,S}$ as "radial harmonic extension" of the trace interpolant $\mathcal{I}_k^h w$ to the interior of S.

Let $\underline{\omega}^S$ be the coefficients in the expansion $\mathcal{I}_k^h\, w(\underline{x}_b) = \sum_{n=1}^{\mathcal{N}^S} \omega^{n,S} N_k^{n,S}(\underline{x}_b)$, $\underline{x}_b \in \Gamma^S$. We seek for coefficients $\underline{c} = [c_i]$ such that $\Pi_k^{h,S}\, w = \sum_i c_i \phi_i^S \in \mathbb{S}_k^h(S)$. According to the definition of the local spaces $\mathbb{S}_k^h(S)$, the solution is $\underline{c} = \underline{\underline{A}}^{-1}\underline{\omega}^S$, where $\underline{\underline{A}} = \underline{\underline{A}}^S$ is the eigenvector matrix associated to the traces of the SBFEM shape-functions ϕ_i^S over Γ^S.

3. Assembly - Define $\Pi_k^h\, w$ by assembling the local contributions $\Pi_k^h\, w|_S = \Pi_k^{h,S}\, w$. It is clear that $\Pi_k^{h,S}\, w|_L = \Pi_k^{h,S}\, w|_L$ over an interface $L = S \cap S'$ shared by two S-elements. Thus, the conformity property $\Pi_k^h\, w \in H^1(\Omega)$ holds.

Notice that an analogous procedure can be applied to define the SBFEM interpolants for the Elasticity problem.

Remarks

(1) In the same manner as FE interpolants $\mathcal{F}_k^{h,FE}\, w$, the SBFEM interpolant Π_k^h satisfies the two fundamental properties: locality and global conformity. However, they differ in the way the trace interpolant is extended to the interior of the S-elements by their local projections. Recall that the "radial harmonic extension" adopted in the SBFEM context is possible due to the particular scaled geometry of the S-elements. Moreover, when the SBFEM interpolant shares the trace interpolant of $\mathcal{F}_k^{h,FE}\, w$, then it is clear that

$$\Pi_k^h\, w = \Pi_k^h\, \mathcal{F}_k^{h,FE}\, w. \tag{3.3.0}$$

(2) Since $\mathcal{I}_k^h\, w = w|_{\Gamma^h}$ for functions $w \in \mathcal{D}_k^h$, the trace constraint (2) means that $w - \Pi_k^h\, w \in \mathcal{D}_k^{0,h}$ for all functions w in the Duffy's space $\mathcal{D}_k^h$. Consequently, Proposition 3.3.1 implies the orthogonality property

$$\langle w - \Pi_k^h\, w, v\rangle_\nabla = \sum_{S\in\mathcal{T}^h} \langle w - \Pi_k^{h,S}\, w, v\rangle_{\nabla,S} = 0, \quad \forall w \in \mathcal{D}_k^h, \quad \forall v \in \mathbb{S}_k^h. \tag{3.3.0}$$

SBFEM interpolation errors

Unlike general-purpose FE techniques, SBFEM approximations are constructed to be applied to a specific type of problem. Thus, for Laplace's model, there is no interest in accessing the accuracy of SBFEM interpolants $\Pi_k^h\, w$ when applied to other than for harmonic functions $w \in \mathcal{H}(\Omega)$. For them, the sources of SBFEM interpolation errors are two-fold:

(i) the polynomial discretization of traces $w|_{\Gamma^h} \approx \mathcal{I}_k^h\, w \in \Lambda_k^h$.

(ii) the deviation of $\Pi_k^{h,S}\, w \in \mathbb{S}_k^h$ of being an harmonic function.

For Elasticity problems, the traces are vector-valued functions $\underline{w}|_{\Gamma^h} \approx \underline{\mathcal{I}}_k^h\, \underline{w} \in \underline{\Lambda}_k^h$, whilst (ii) measures the deviation of the radial extension in ξ direction of a Elastic problem with null body loads.

For the harmonic problem, consider the subspace

$$\mathcal{V}_k^{h,\Delta} = \{w \in \mathcal{H}(\Omega); w|_{\Gamma^h} \in \Lambda_k(\Gamma^h)\},$$

where only trace discretization takes place. Denoted by harmonic virtual spaces, they have been used in the context of the operator-adapted virtual FE method proposed in Chernov

and Mascotto (2019), and designed to solve two-dimensional harmonic problems. The term "virtual" emphasizes that functions in $\mathcal{V}_k^{h,\Delta}$ are not known explicitly in the interior of each subregion $S \in \mathcal{T}^h$.

The finite-dimensional spaces $\mathcal{V}_k^{h,\Delta}$ have close similarities with the SBFEM spaces $\mathbb{S}_k^h$. In both cases, the trace functions are in $\Lambda_k(\Gamma^h)$, which are extended to the interior of the S-elements by solving local Dirichlet Laplace's problems: whilst the functions in the local spaces $V_k^\Delta(S) = \mathcal{V}_k^{h,\Delta}|_S$ are strongly harmonic in S, the ones in $\mathbb{S}_k(S)$ are harmonic in a weaker sense. However, unlike for the harmonic subspaces $V_k^\Delta(S)$, it is possible to explore the radial Duffy's structure of $\mathbb{S}_k^h(S)$ to explicitly compute shape functions for them, as described in the previous section.

Consider the harmonic virtual interpolant $\mathcal{F}_k^{h,\Delta} : H^s(\Omega) \to \mathcal{V}_k^{h,\Delta}$ by solving the local Laplace's problems

$$\begin{aligned} \langle \mathcal{F}_k^{h,\Delta} w, v\rangle_{\nabla,S} &= 0 \quad \forall v \in H_0^1(S), \\ \mathcal{F}_k^{h,\Delta} w|_{\Gamma^S} &= \mathcal{I}_k^h w|_{\Gamma^S}, \end{aligned}$$

where the trace interpolant $\mathcal{I}_k^h w$ is the one adopted in $\Pi_k^h w$. Note that this is an analytic recovery problem for it is not directly accessible for computation, whilst the SBFEM interpolant $\Pi_k^h w$ is a computable recovery problem.

For an harmonic function $u \in \mathcal{H}(\Omega)$, consider the decomposition

$$u - \Pi_k^h u = (u - \mathcal{F}_k^{h,\Delta} u) + (\mathcal{F}_k^{h,\Delta} u - \Pi_k^h u) = (i) + (ii).$$

The first term $(i) = u - \mathcal{F}_k^{h,\Delta} u$ compares two harmonic functions differing on the skeleton Γ^h by the trace interpolation error $u - \mathcal{I}_k^h u$, meaning that only the interface errors require to be estimated. In fact, the application of Neumann trace inequality ((SCHWAB, 1998, Theorem A.33)) in each S-element $S \in \mathcal{T}^h$ gives

$$|u - \mathcal{F}_k^{h,\Delta} u|_{H^1(S)} \lesssim \|u - \mathcal{I}_k^h u\|_{H^{\frac{1}{2}}(\partial S)}.$$

We refer to Chernov and Mascotto (2019, Lemma 4.4, Lemma 4.5) for estimates of (3.3.3) in the particular Gauss-Lobatto trace interpolation case, and under some specific graded polygonal mesh circumstances.

On the other hand, since

$$\Pi_k^h u = \Pi_k^h \mathcal{F}_k^{h,FE} u, \tag{3.3.0}$$

the second term becomes $(ii) = \mathcal{F}_k^{h,\Delta} u - \Pi_k^h u = \mathcal{F}_k^{h,\Delta} u - \Pi_k^h \mathcal{F}_k^{h,\Delta} u$, representing the SBFEM interpolation error for the harmonic virtual function $\mathcal{F}_k^{h,\Delta} u \in \mathcal{V}_k^{h,\Delta}$. Consequently, according to (2) and (3.3.3),

$$\langle \mathcal{F}_k^{h,\Delta} u - \Pi_k^h \mathcal{F}_k^{h,\Delta} u, v\rangle_{\nabla,S} = \sum_{S\in\mathcal{T}^h} \langle \mathcal{F}_k^{h,\Delta} u - \Pi_k^h \mathcal{F}_k^{h,\Delta} u, v\rangle_{\nabla,S} = 0, \quad \forall v \in \mathcal{D}_k^{0,h}.$$

In other words, the second term $(ii) = \mathcal{F}_k^{h,\Delta} u - \Pi_k^h u$, which vanishes in Γ^h, is orthogonal to $\mathcal{D}_k^{0,h}$ with respect to the gradient inner product. Thus its energy norm is a measure of the deviation of $\Pi_k^h \mathcal{F}_k^{h,\Delta} u$ of being a harmonic function. Since $\mathbb{P}_m(\mathcal{T}^S) \cap H_0^1(S) \subset \mathcal{D}_k^0(S)$, for polynomials of arbitrary degree $m \geq 1$, the energy norm of the second term (ii) is expected to decay exponentially, and it is eventually dominated by the energy norm of the trace interpolation error represented by the first term (i).

3.3.4 Galerkin SBFEM approximations

Poisson problem

Consider the Poisson model problem

$$\begin{aligned}\Delta u &= 0, \text{ in } \Omega,\\ \gamma_0(u) &= u_D, \text{on } \Gamma,\end{aligned}$$

where $u_D \in H^{1/2}(\Gamma)$, and $\gamma : H^1(\Omega) \to H^{1/2}(\Gamma)$ is the usual trace operator. We assume that u_D is sufficiently smooth for the definition of the trace interpolant.

Let $\mathbb{S}_k^h$ be the trial SBFEM approximation spaces based on geometric partitions $\mathcal{T}^h = \{S\}$ of Ω by S-elements, $\Pi_k^h : H^s(\Omega) \to \mathbb{S}_k^h$ being the corresponding interpolant operators, as defined in the previous section. The Galerkin SBFEM for problem (3.3.4) searches approximate solutions $u^h \in \mathbb{S}_k^h$ satisfying:

$$\begin{aligned}a(u_h, v) &= 0 \quad \forall v \in \mathbb{S}_{k,0}^h,\\ u_h|_\Gamma &= \mathcal{I}_k^h\, u_D|_\Gamma,\end{aligned}$$

where $a(w, v) := \int_\Omega \nabla u \cdot \nabla v \, \mathrm{d}\Omega$ is the usual bounded symmetric bilinear form for $u, w \in H^1(\Omega)$. The bilinear form a is well known to be coercive, meaning there exists $\nu > 0$ such that $a(v, v) \geq \nu \|v\|_{H^1}^2$, $\forall v \in H_0^1(\Omega)$. Thus, problem (3.3.4)-(3.3.4) is well-posed (see Ern and Guermond (2013, Proposition 3.26)). Well-posedness is a property relative to the engineering expectation that a unique solution to a problem must exist and changes slightly if the initial conditions are slightly changed.

Elasticity problem

Consider the Elasticity model problem, with null body loads given by

$$\begin{aligned}\underline{\underline{D}}\, \underline{\epsilon}(u) &= 0, \text{ in } \Omega,\\ \underline{\gamma}_0(\underline{u}) &= \underline{u}_D, \text{on } \Gamma,\end{aligned}$$

where $\underline{u}_D \in H^{1/2}(\Gamma, \mathbb{R}^d)$, and $\underline{\gamma} : H^1(\Omega, \mathbb{R}^d) \to H^{1/2}(\Gamma, \mathbb{R}^d)$ is the usual trace operator for vector-valued functions. The Dirichlet displacement $\underline{u}_D$ is sufficiently smooth for the definition of the trace interpolant.

Again, let $\underline{\mathbb{S}}_k^h$ be the trial vector-valued SBFEM approximation spaces for Elastic problems with null body loads, based on geometric partitions $\mathcal{T}^h = \{S\}$ of Ω by S-elements. The corresponding interpolant operator is given by $\underline{\Pi}_k^h : H^s(\Omega, \mathbb{R}^d) \to \underline{\mathbb{S}}_k^h$, as aforementioned defined in (3.2.4). The Galerkin SBFEM for problem (3.3.4) is expressed as: Seek approximate solutions $\underline{u}^h \in \underline{\mathbb{S}}_k^h$ satisfying:

$$\begin{aligned}a^E(\underline{u}_h, \underline{v}) &= 0 \quad \forall \underline{v} \in \underline{\mathbb{S}}_{k,0}^h,\\ \underline{u}_h|_\Gamma &= \underline{\mathcal{I}}_k^h\, \underline{u}_D|_\Gamma,\end{aligned}$$

where $a^e(\underline{u}, \underline{v}) := \int_\Omega \underline{\underline{D}}\, \underline{\epsilon}(\underline{u}) \cdot \underline{\epsilon}(\underline{v}) \, \mathrm{d}\Omega$ is the usual bounded symmetric bilinear form for $\underline{u}, \underline{w} \in H^1(\Omega, \mathbb{R}^d)$. As well as for the Poisson problem, the bilinear form a^E for the Elasticity problem is also well known to be coercive. Therefore, problem (3.3.4)-(3.3.4) is well-posed as demonstrated in Romano, Rosati and Diaco (1999, Definition 3.1.).

Error analysis for the SBFEM

For the error analysis of the Galerkin SBFEM discretization (3.3.4)-(3.3.4) and (3.3.4)-(3.3.4) for the Poisson and the Elasticity problem, respectively, the purpose is to explore the properties of orthogonality (3.3.3) and interpolation (3.3.3) to estimate energy errors $|u-u^h|_{H^1}$ in approximating the harmonic exact solution u from the projection errors $|u-\mathcal{F}_k^{h,FE}\,u|_{H^1}$ on the FE spaces $\mathcal{V}_k^{h,FE}$, or $|u-\mathcal{F}_k^{h,\nabla}\,u|_{H^1}$ on the virtual harmonic spaces $\mathcal{V}_k^{h,\Delta}$. Recall that the FE interpolant errors are available in Babuška and Suri (1987), Muñoz-Sola (1997), Demkowicz et al. (2007), Melenk and Rojik (2020) for general functions in Sobolev spaces, whilst interpolant errors $|u-\mathcal{F}_k^{h,\Delta}\,u|_{H^1}$ are accessed in Chernov and Mascotto (2019) for harmonic functions for general the virtual harmonic spaces.

Theorem 3.3.1. *Let $\mathcal{T}^h=\{S\}$ be a family of polytopal S-elements partitions of Ω, $\mathbb{S}_k^h$ be the SBFEM space based on $\mathcal{T}^h$, and $\mathcal{V}_k^{h,FE}$ the FE spaces based on the conglomerate meshes $\mathcal{P}^h$. Suppose the same trace interpolant is used in the definitions of Π_k^h and $\mathcal{F}_k^{h,\Delta}$, and the exact solution $u\in H^1$ of the model problem* (3.3.4) *is sufficiently regular for them to make sense. If $u_h\in\mathbb{S}_k^h$ is the associated Galerkin SBFEM approximation, then*

$$|u-u_h|_{H^1(\Omega)}\leq|u-\mathcal{F}_k^{h,FE}\,u|_{H^1(\Omega)}.$$

Proof. Firstly, observe two orthogonality relations.

1. As for any Galerkin approximation, the SBFEM solution verifies the orthogonality property $a(u-u_h,v)=0\quad\forall v\in\mathbb{S}_{k,0}^h$, which is paramount for error estimates for such methods.
2. Proposition 3.3.2 (i.e., $\mathcal{F}_k^{h,FE}\,u\in\mathcal{V}_k^{h,FE}\subset\mathcal{D}_k^h$), combined with properties (3.3.3) and (3.3.3), implies that

$$a(u_h,\Pi_k^h\,u-\mathcal{F}_k^{h,FE}\,u)=0. \tag{3.3.-2}$$

These two orthogonality relations imply the Pythagorean equality

$$|u-\mathcal{F}_k^{h,FE}\,u|_{H^1(\Omega)}^2=|u-u_h|_{H^1}^2+|u_h-\mathcal{F}_k^{h,FE}\,u|_{H^1(\Omega)}^2.$$

Consequently, the estimate (3.3.1) holds. □

Theorem 3.3.2. *Consider again a partition of polytopal S-elements partitions of Ω, $\mathcal{T}^h=\{S\}$. Let $\underline{\mathbb{S}}_k^h$ is be the SBFEM space for the Elasticity problem with null body loads based on $\mathcal{T}^h$, and $\underline{\mathcal{V}}_k^{h,FE}$ is the FE space based on the conglomerate meshes $\mathcal{P}^h$ for vector-valued functions. Moreover, define the same trace interpolant in the definitions of $\underline{\Pi}_k^h$ and $\underline{\mathcal{F}}_k^{h,\Delta}$. If the exact solution $\underline{u}\in H^1(\Omega;\mathbb{R}^d)$ of the model problem* (3.3.4) *is sufficiently regular and the Galerkin SBFEM approximation $\underline{u}_h\in\underline{\mathbb{S}}_k^h$ is the associated Galerkin SBFEM approximation, then*

$$|\underline{u}-\underline{u}_h|_{H^1(\Omega)}\leq|\underline{u}-\underline{\mathcal{F}}_k^{h,FE}\,\underline{u}|_{H^1(\Omega)}.$$

Proof. The proof of (3.3.2) is analogous to the previous theorem. □

Theorems 3.3.1 and 3.3.2 show that the SBFEM has a lower error value than the Virtual Element Method, which, in turn, has lower errors compared to traditional FEM. This fact was already expected since the SBFEM computes the approximation "analytically" inside a S-element.

Theorem 3.3.3. *Let $\mathcal{T}^h = \{S\}$ be a family of polytopal S-elements partitions of Ω, $\mathbb{S}_k^h$ and $\mathcal{V}_k^{h,\Delta}$ be the SBFEM and virtual spaces based on $\mathcal{T}^h$. Suppose the same trace interpolant is used in the definitions of Π_k^h and $\mathcal{F}_k^{h,\Delta}$, and the exact solution $u \in H^1$ of the model problem* (3.3.4) *is sufficiently regular for them to make sense. If $u_h \in \mathbb{S}_k^h$ is the associated Galerkin SBFEM approximation, then*

$$|u - u_h|_{H^1(\Omega)} \leq |u - \mathcal{F}_k^{h,\Delta} u|_{H^1(\Omega)} + |\mathcal{F}_k^{h,\Delta} u - \Pi_k^h \mathcal{F}_k^{h,\Delta} u|_{H^1(\Omega)}.$$

Proof. The result is a consequence of Galerkin orthogonality property

$$|u - u^h|_{H^1(\Omega)} = \inf_{v \in \mathbb{S}_k^h} |u - v|_{H^1(\Omega)} \leq |u - \Pi_k^h u|_{H^1(\Omega)},$$

the error decomposition (3.3.3), and the property $\Pi_k^h u = \Pi_k^h \mathcal{F}_k^{h,\Delta} u$ remarked in (3.3.3). □

Knowing that the error component $|u - \mathcal{F}_k^{h,\Delta} u|_{H^1(\Omega)}$ is higher than $|\mathcal{F}_k^{h,\Delta} u - \Pi_k^h \mathcal{F}_k^{h,\Delta} u|_{H^1(\Omega)}$, and the first one has rate of convergence k, the convergence in the semi-energy norm is bounded by k. Intuitive analysis of the SBFEM convergence rates is that they are bounded by the approximation convergence rates of the trace approximation since the interior is "almost" analytical. The tests presented in the following section explore these aspects from a numerical point of view.

3.4 Numerical tests

In this section, selected tests for Poisson and Elasticity problems numerically verify the predicted theoretical convergence results. The tests include two and three-dimensional problems. Mesh discretizations for 2D examples are based on quadrilateral or polygonal S-elements, each one subdivided into collapsed triangles. Next, three-dimensional tests explore SBFEM approximations based on uniform hexahedral and polyhedral S-elements, both subdivided into pyramids. Irregular partitions are also considered in the context of polyhedral S-elements subdivided by collapsed tetrahedra. For comparison, results obtained by H^1-conforming FEM based on the meshes of the corresponding triangles, pyramids, and tetrahedra partitions of the S-elements are also presented.

To evaluate the SBFEM performance in problems with a point-singularity, simulations of pure SBFEM mesh and a coupled FEM+SBFEM formulation are applied for a harmonic singular function. For the FEM-SBFEM mesh, a traditional finite element formulation is modified by a scaled boundary element in the vicinity of the singularity. For a Steklov problem, the convergence is evaluated for high-order approximations. A plane crack is also analyzed using the SBFEM for a linear elastic problem. In addition to the optimal convergence rates, the stress intensity factors (SIF) are directly obtained from the SBFEM approximations.

The contribution of this chapter is the mathematical analysis of the SBFEM errors. The computational code for the numerical simulations of homogeneous problems using the SBFEM was already implemented in the computational framework NeoPZ[1]. The NeoPZ, the computational tool applied in the following simulations, is an open-source FE library

[1]NeoPZ open-source platform: http://github.com/labmec/neopz

that facilitates the development of innovative technology in FEM simulations (DEVLOO, 1997). For general FEM simulations, the NeoPZ allows using a varied class of element geometries, mesh refinements, and high-order approximations. Moreover, the FE library allows approximating PDEs using different function spaces - H^1, $H(\text{div})$, $H(\text{curl})$ and discontinuous -, as well as mixed and hybrid finite elements and multiscale simulations. Since the NeoPZ uses object-oriented concepts, such as abstract classes, templates, and small blocks, it is possible to implement a general coding of SBFEM simulations by taking advantage of pre-implemented FEM code. Moreover, the concept of element neighbors associated with geometric entities was useful for constructing Duffy's elements and the definition of the S-elements.

3.4.1 Poisson problem

Example 1 - Smooth solution in 2D - Single S-element

In the region $\Omega = S = [-1, 1] \times [-1, 1]$ consider the harmonic function

$$u(x, y) = \exp(\pi x) \sin(\pi y), \tag{3.4.0}$$

and interpret S as regions of $4n$ facets, $n = 2, 4$ and 8, as illustrated in Fig. 3.12. In other words, only a single element was used, whilst the refinement was performed at the element's skeleton two times.

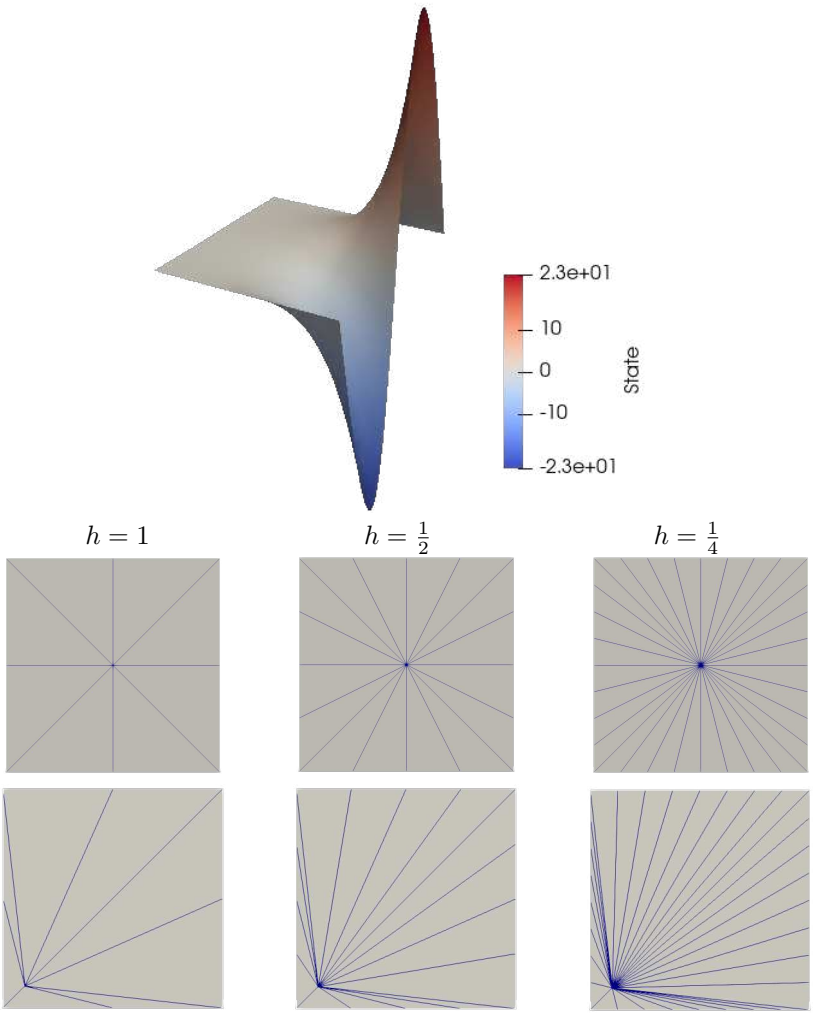

Figure 3.12: Example 1 - Harmonic function $u(x, y)$ and meshes of a single S-element of width $h = \frac{2}{n}$, $n = 2, 4$ and 8, composed of triangular partitions with facets: central scaling centers (top) and dislocated scaling centers and distorted sub-partitions (bottom).

The scaled boundary elements $\Gamma^{h,S}$ are obtained by subdividing each side of ∂S into n subintervals of width $h = \frac{2}{n}$. In other words, S is formed by $4n$ triangles K^e sharing the scaling center point as a vertex and having one edge in $\Gamma^{h,S}$ as an opposite facet. The triangles K^e are mapped by Duffy's geometric transformations described in Section 3.1.1. Two different partitions are analyzed. The first one is a regular uniform partition of collapsed triangles, in which the scaling center is located at the center of the S-element. The second family of meshes is composed of distorted sub-partitions, where the scaling center was dislocated to a region close to the S-boundary, namely with coordinates $(-0.8, -0.8)$. Both cases share the same scaled boundary elements $\Gamma^{h,S}$.

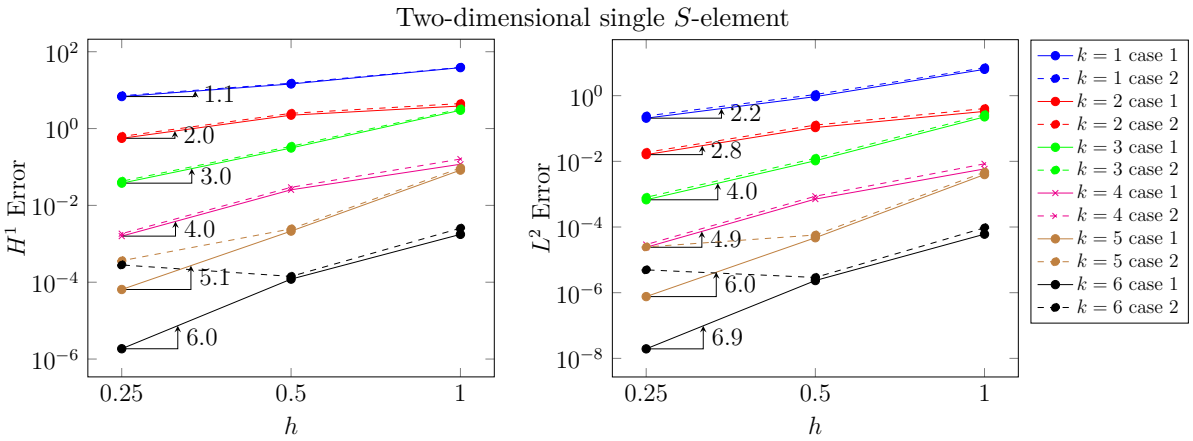

Figure 3.13: Example 1 - Energy and L^2 SBFEM errors versus h: case 1 - uniform (solid lines) subpartitions of S, and case 2 - distorted (dashed lines) subpartitions based on Fig. 2.6, and approximation of degree $k = 1, \cdots, 6$.

For the scaled geometry illustrated in Fig. 3.12, it is considered the SBFEM space $\mathbb{S}_k^{h,S}$ varying the polynomial approximation $k = 1, \ldots, 6$ and computing the interpolants $\Pi_k^{h,S} u$. The corresponding error histories versus the scaled boundary mesh width h are plotted in Figure 3.13, reflecting the usual convergence behavior governed by the FE trace discretizations $\mathcal{I}_k^h u$ over ∂S, of order k in the energy norm, and order $k+1$ in the L^2-norm. The convergence data is summarized in Table A.1 in Appendix A.

The same convergence behavior for the distorted sub-partitions, up to $k = 4$ (see Fig. 3.13). When increasing the polynomial order, the numerical solution starts to diverge at the most refined level ($h = \frac{1}{4}$), for the size of the eigenvalue problem increases significantly and then some numerical difficulties to extend the boundary solution to the domain in very narrow and distorted elements appear. When the scaling center is moved far from the center of the polygon, the conditioning of the problem corresponding to the scaled ODE system (3.2.3) gets worse, affecting the precision of the eigenvalues and eigenvectors.

Example 2 - Smooth solution in 2D - Quadrilateral and polygonal mesh refining the domain

The analytical solution (3.4.1) for Laplace's equation is approximated on the same domain $\Omega = [-1; 1] \times [-1; 1]$; but instead of partitioning the skeleton, the domain is partitioned into meshes of quadrilateral and polygonal elements, as illustrated in Fig. 3.14.

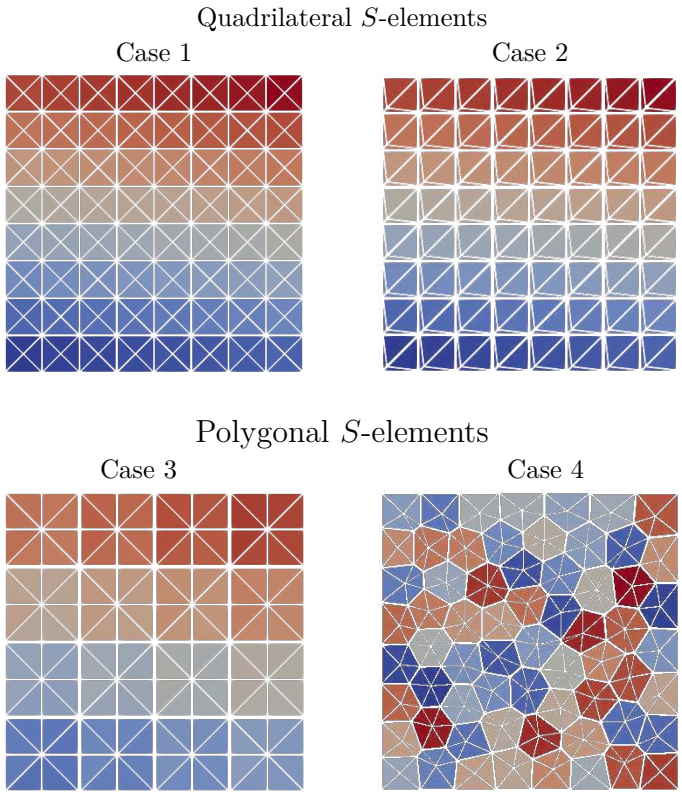

Figure 3.14: Example 2 - Uniform quadrilateral and polygonal partitions $\mathcal{T}^h$, $h = \frac{1}{4}$: S-element distinguished by different colors and subdivided into scaled triangles.

Eq. (3.4.1) is approximated using the Galerkin SBFEM in sequences of partitions $\mathcal{T}^h$ of S-elements, with refinement levels $h = 2^{-\ell}$, $\ell = 1, \cdots 4$, where h is the characteristic width given by the higher distance between two vertices of ∂S. The solutions are searched in SBFEM space $\mathbb{S}_k^h$, using polynomial orders $1 \leq k \leq 6$, which are based on uniform quadrilateral S-elements (with uniform or distorted sub-partitions) and two cases of polygonal S-elements. Figure 3.14 illustrates the particular partitions for $h = \frac{1}{4}$.

The adopted partitions follow one of the cases:

Case 1. Uniform $n \times n$ - quadrilateral S-elements, $n = 2^{\ell+1}$, each one having Γ^S formed by its 4 edges, and uniform collapsed triangular sub-partitions, with scaling center coinciding with the S-element's centroid;

Case 2. The same uniform $n \times n$-quadrilateral S-elements, but with distorted sub-partitions resulted from moving the scaling centers closer to the scaled boundary elements (following the same pattern of the previous example, the scaling center is $(-0.8, 0.8)$);

Case 3. Polygons with 8 edges (case 1) obtained from uniform quadrilaterals whose sides are subdivided once, and

Case 4. Unstructured irregular polygonal S-elements (case 2) constructed using the mesh generator software PolyMesher (TALISCHI et al., 2012), by giving as input the number of elements in x and y axes. For this sequence, the scaled boundaries have average characteristic width close to the adopted in the uniform contexts.

The numerical results described in Table A.2 and the convergence curves plotted in Fig. 3.15 for Cases 1 and 2 are following the predicted rates of order k for energy errors.

Optimal rates of order $k+1$ are also observed for the errors measured by the L^2-norm. These optimal rates of convergence occur even for sub-partitions of distorted triangular Duffy's elements. Indeed, the error values for this configuration are virtually similar to the ones obtained using uniform Duffy's triangular elements. In this direction, Theorem 5.2 appears to be useful to guide the error analysis in the presence of deformed Duffy's sub-elements occurring when the scaling centers are dislocated towards the scaled boundary elements while keeping a regular partition of the scaled boundary $\Gamma^{h,S}$. The same behavior is observed for Case 3 (regular polygons) in Fig. 3.16.

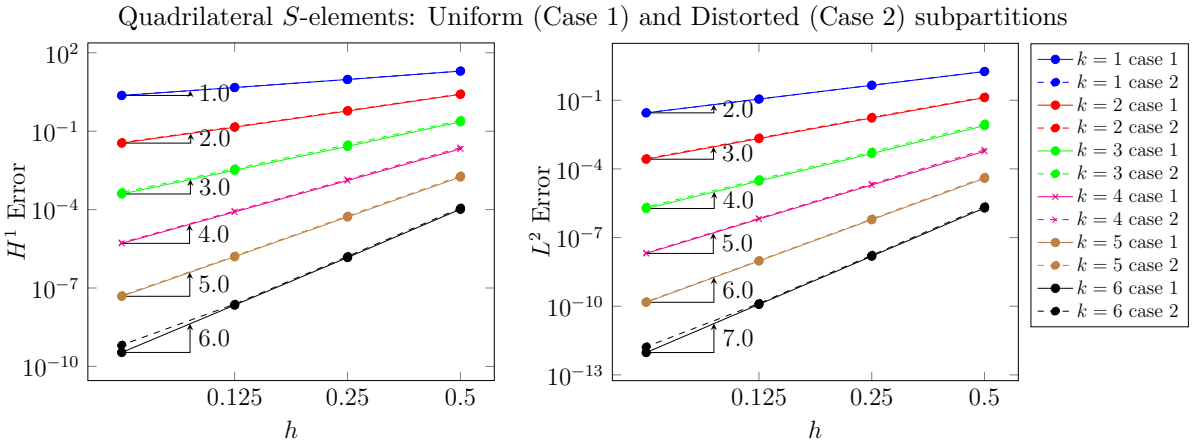

Figure 3.15: Example 2 - Energy and L^2 SBFEM interpolation errors versus h: Case 1 - uniform (solid lines) subpartitions of S, and Case 2 - distorted (dashed lines) subpartitions based on Fig. 3.14, and approximation degree $k = 1, \cdots, 6$.

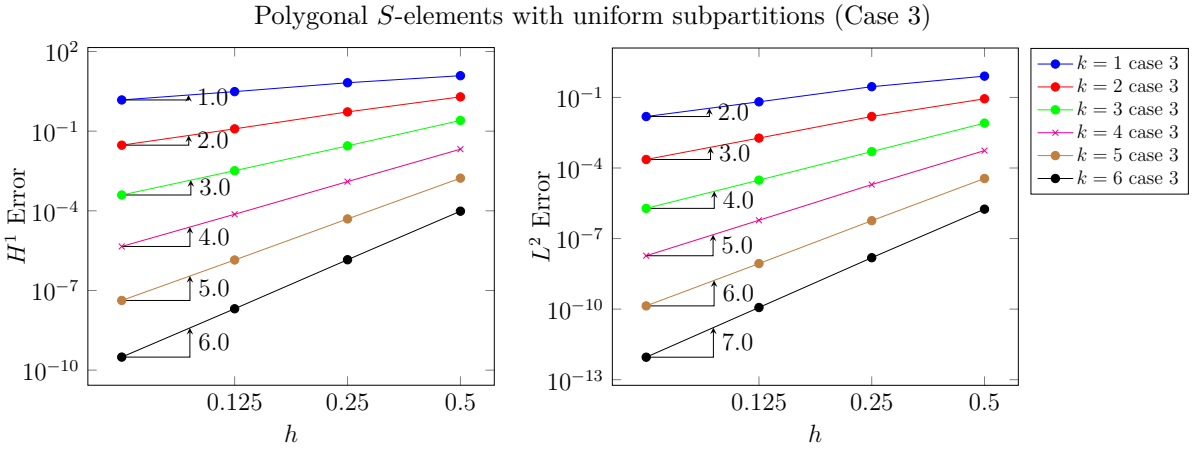

Figure 3.16: Example 2 - Energy and L^2 SBFEM interpolation errors versus h: Case 3 - uniform subpartitions of a polygonal mesh based on Fig. 3.14, and approximation degree $k = 1, \cdots, 6$.

In Figure 3.17, the energy and L^2 errors are plotted versus the number of DOF for Galerkin SBFEM solutions in $\mathbb{S}_k^h$ based on the irregular polygonal meshes of Case 4 (Fig. 3.14) and polynomial approximation order of $k = 2, 4$, and 6. For comparison, the Galerkin FEM method was applied and solutions are also shown. These solutions were constructed using $\mathcal{V}_k^{h,FE}$ for the FEM mesh using the conglomerate partition $\mathcal{P}^h$ composed of the triangular elements that form each S-element. The error comparison reveals comparable accuracy in both methods, but with less DOF in SBFEM simulations.

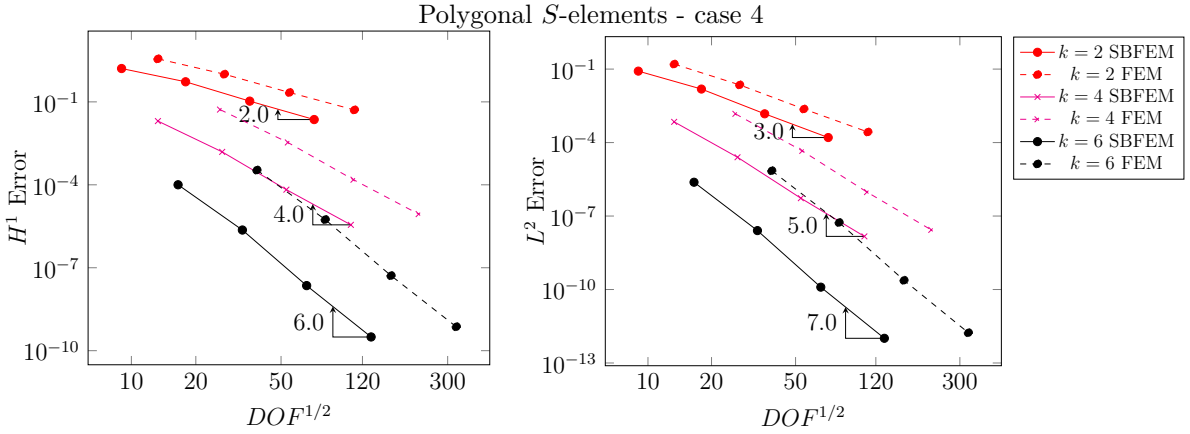

Figure 3.17: Example 2 - Energy and L^2 errors versus DOF for the Galerkin SBFEM solutions in $\mathbb{S}_k^h$, based on the irregular polygonal S-elements of case 4, and for the Galerkin FE solutions in $\mathcal{V}_k^{h,FE}$ based on the associated conglomerate triangular partitions $\mathcal{P}^h$, for $k = 2, 4$ and 6.

Recall that SBFEM shape functions are determined by the traces over scaled boundary elements, whilst FE spaces are also populated with shape functions connected with triangular DOF other than the edge ones opposed to the scaling center. One also observes that their error curves approach the possible optimal slopes $-k$ and $-(k+1)$ when measured by energy or L^2 norms. This experiment illustrates the SBFEM flexibility with respect to mesh generation for numerical simulations without convergence deterioration. More details of the error values are compiled in Table A.4, in Appendix A.

Plots illustrating SBFEM k-convergence histories in the energy norm versus the square root of the DOF are shown in Figs. 3.18 and 3.19, with $k = 1, \cdots, 6$, and for S-elements with fixed boundary mesh size $h = \frac{1}{4}$. The plots on Fig. 3.18 are for the SBFEM interpolation in the single S-element (see Example 1 - Fig. 3.12) and for the Galerkin SBFEM experiment for the uniform quadrilateral partition $\mathcal{T}^h$ of Figure 3.14. For both cases, the error decay as k increases shows a typical exponential convergence, but the interpolation experiment, by just refining the boundary of a single element, requires less DOF for a given accuracy threshold. Additionally, for comparison, k-convergence plots for three H^1-conforming FE methods are also included in Fig. 3.18: using $\mathbb{P}_k(K)$ polynomials in the triangles K of the conglomerate partitions $\mathcal{P}^h$ (FE-triangles), $\mathbb{Q}_{k,k}(K)$ polynomials in the quadrilateral S-elements (FE-quadrilaterals), and for Duffy's spaces $\mathcal{D}_{k,k}^h(S)$ (Duffy's FE).

Notice that for the lowest order case $k = 1$ and this particular case of quadrilateral S-elements, SBFEM and FEM coincide. Errors for SBFEM and Duffy's spaces are comparable, but the latter has much more equations to be solved. With respect to the results of the usual FE methods for triangles and quadrilaterals, both having comparable accuracy, their errors are superior in magnitude to the ones provided by SBFEM. For the FEM based on the conglomerate triangular mesh, this comparison is in accordance with the prediction by Theorem 3.3.1 because the energy FE errors are bounded by FE interpolation errors. Moreover, the most noticeable aspect of these plots is that SBFEM requires less DOF to reach a given accuracy than these FE methods, the key property expected to be held for an operator-adapted method, as the SBFEM. It is worth mentioning that this notable reduction in the DOF for the SBFEM has the cost of solving an eigenvalue problem. And for the single S-element, the matrix for the eigenvalue problem grows,

increasing the challenge of solving it numerically, as already discussed in Example 1.

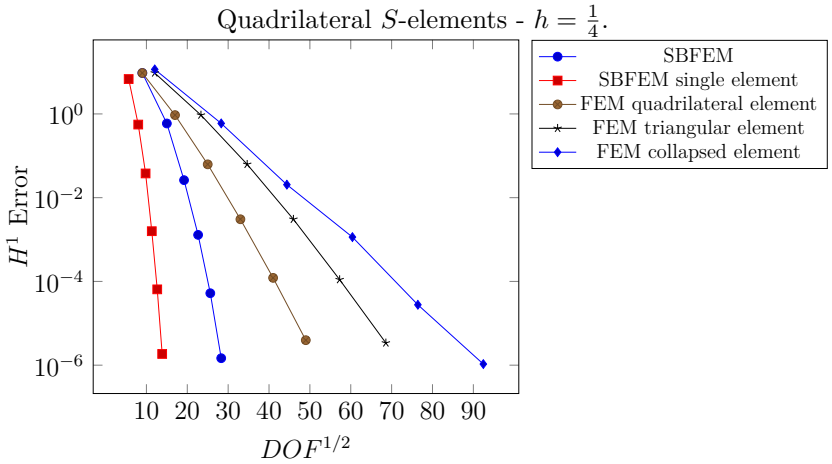

Figure 3.18: Example 2 - k-convergence histories versus the number of DOF, for $k = 1, \cdots, 6$ - Experiment based on uniform quadrilateral S-elements: Single S-element based on the scaled partition of Fig. 3.12, Galerkin SBFEM refining the domain for $\mathbb{S}_k^h$, Duffy's FE for $\mathcal{D}_{k,k}^h$, both based on the uniform quadrilateral partition $\mathcal{T}^h$ of S-elements of Figure 3.14, and FE method for $\mathcal{V}_k^{h,FE}$ based on the associated conglomerate triangular partition $\mathcal{P}^h$, as well as for polynomials $\mathbb{Q}_{k,k}(S), S \in \mathcal{T}^h$.

.

Comparing the k-convergence properties in Fig. 3.19 of the Galerkin SBFEM for spaces based on $\mathcal{T}^h$ of the uniform quadrilateral and irregular polygonal S-elements (Case 1 and Case 3, respectively) of Fig. 3.14, it is observed the uniform polygonal mesh of Case 3 requires fewer equations to be solved for a given target error. On the other hand, similarly to the observations in Fig. 3.18, a bigger eigenvalue system has to be solved for each S-element. This kind of polygonal mesh can be seen as a combination of refining both the boundary and inside the subdomains. Due to this flexibility, the SBFEM can generate octree (3D) or quadtree (2D) meshes (CHEN et al., 2018; SAPUTRA et al., 2020), giving high accuracy, without any additional techniques.

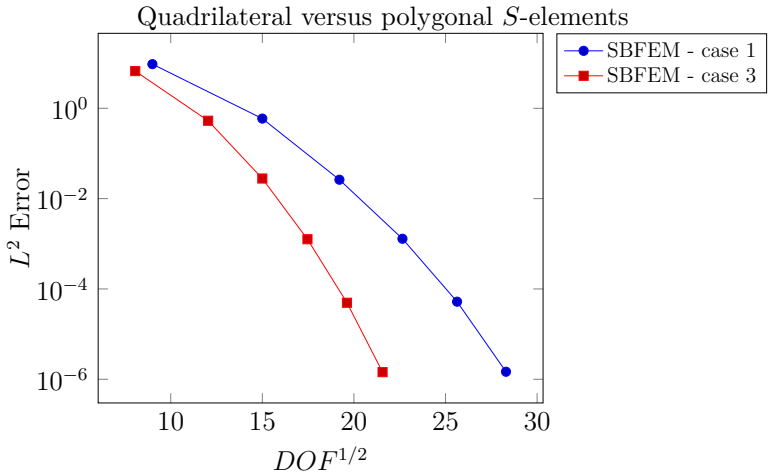

Figure 3.19: Example 2 - k-convergence histories versus the number of DOF, for $k = 1, \cdots, 6$ - Galerkin SBFEM solutions in $\mathbb{S}_k^h$ using the uniform blue quadrilateral S-elements (Case 1), and polygonal S-elements (Case 3), shown in Fig. 3.14. All cases are for $h = \frac{1}{4}$, and uniform triangular sub-partitions.

Example 3 - Smooth solution in 3D - Single S-element

The third example is the three-dimensional harmonic function

$$u(x,y,z) = 4\left(\exp\left(\frac{\pi x}{4}\right)\sin\left(\frac{\pi y}{4}\right) + \exp\left(\frac{\pi y}{4}\right)\sin\left(\frac{\pi z}{4}\right)\right)$$

defined in the region $\Omega = [0,1]\times[0,1]\times[0,1]$.

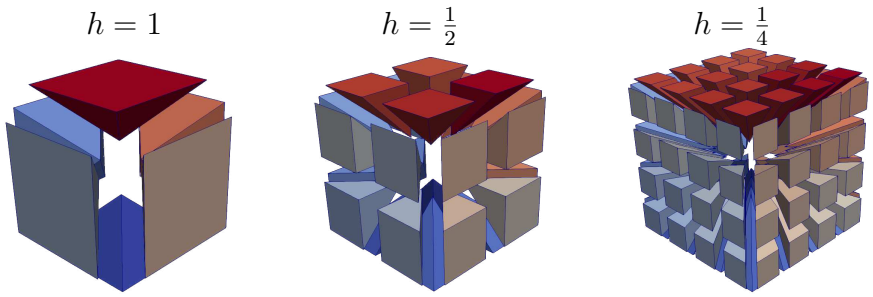

Figure 3.20: Example 3 - Scaled pyramidal partitions $\mathcal{T}^{h,S}$ of $S = [0,1]\times[0,1]\times[0,1]$ with scaled boundary $\Gamma^{h,S}$ formed by $6n^2$ uniform quadrilateral facets of characteristic width $h = \frac{1}{n}$, $n = 1, 2$ and 4.

The mesh is composed of a single S-element $\Omega = S$, where a boundary refinement is performed. The mesh refinement leads to a polyhedral region with $6n^2$ facets, as illustrated in Fig. 3.22. In summary, the scaled boundaries $\Gamma^{h,S}$ are formed by subdividing each face in ∂S into $n \times n$ quadrilaterals, with characteristic size $h = \frac{1}{n}$. Thus, the partitions $\mathcal{T}^{h,S}$ are composed of $6n^2$ pyramids K^e sharing the scaling center point as a vertex. The pyramids are mapped by Duffy's geometric transformations of the reference hexahedron, as described in Section 3.1.1.

The analytical solution u (3.4.1) is approximated by the SBFEM interpolants $\Pi_k^{h,S}u$ for $k = 1, ..., 4$, and the interpolation error curves are plotted in Fig. 3.21 , revealing the typical optimal convergence rates of order k in energy norm, and order $k+1$ in the L^2 norm of the trace interpolant as well as already observed for a single element two-dimensional example. The convergence rates are summarized in Appendix A - Table A.5.

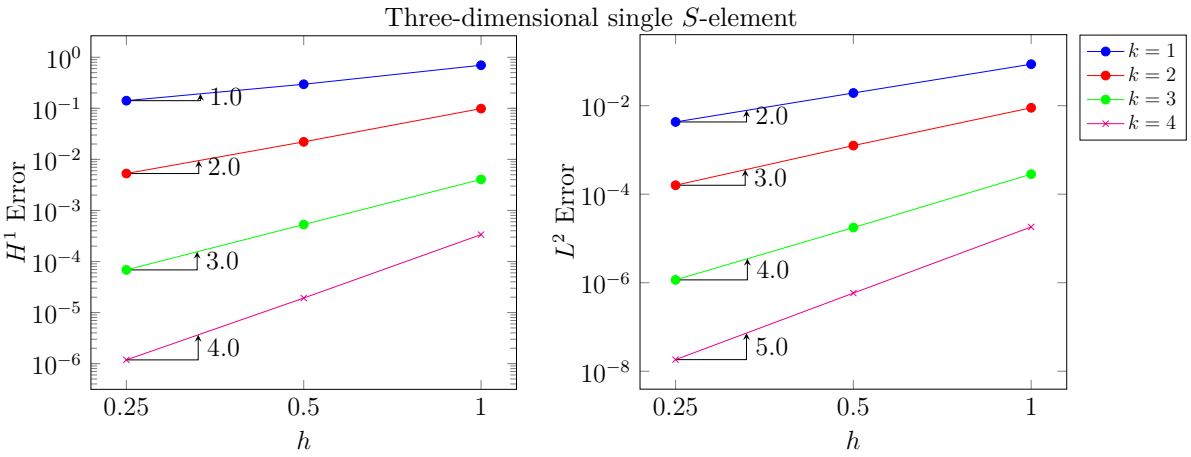

Figure 3.21: Example 3 - Energy and L^2 SBFEM interpolation errors versus h: $\mathbb{S}_k^h(S)$ based on the scaled pyramidal partitions $\mathcal{T}^{h,S}$ of Figure 3.20, and trace spaces $\Lambda_k^{h,S}$ of degree $k = 1, \cdots, 4$.

Example 4 - Smooth solution in a 3D domain - Hexahedral and polytopal mesh

The fourth example refers to approximating the analytical solution of the previous example (3.4.1) for Laplace's equation on a 3D domain $\Omega = [0,1] \times [0,1] \times [0,1]$, but refining the domain instead. Three types of geometry for $\mathcal{T}^h$ are considered, each one with refinement levels $h = 2^{-\ell}$, $\ell = 1, 2$, and 3. The illustrations in Fig. 3.22 are for $h = \frac{1}{4}$ for the following cases

Case 1. $n \times n \times n$ uniform hexahedral partitions, $n = 2^{\ell}$, where each S-element is decomposed into six pyramids.

Case 2. Polygons constructed by subdividing once each square face of uniform hexahedral partitions (Case 1) into four uniform squares (for this configuration, each S-element is a polyhedron with 24 quadrilateral facets, and composed by 24 scaled pyramids).

Case 3. General polyhedral partitions constructed by the software package Neper (QUEY; DAWSON; BARBE, 2011), by giving the number n of S-elements in x, y, and z directions. For each $S \in \mathcal{T}^h$, the finite element mesh generator gmsh (GEUZAINE; REMACLE, 2009) is applied for the construction of the internal tetrahedral subpartitions $\mathcal{T}^{h,S}$.

The average edge characteristic sizes of the scaled boundary elements of the irregular partitions resulted to be comparable to the parameter h of the uniform contexts. The pyramids and tetrahedra forming S are mapped by Duffy's transformations from the reference hexahedron or prism, respectively.

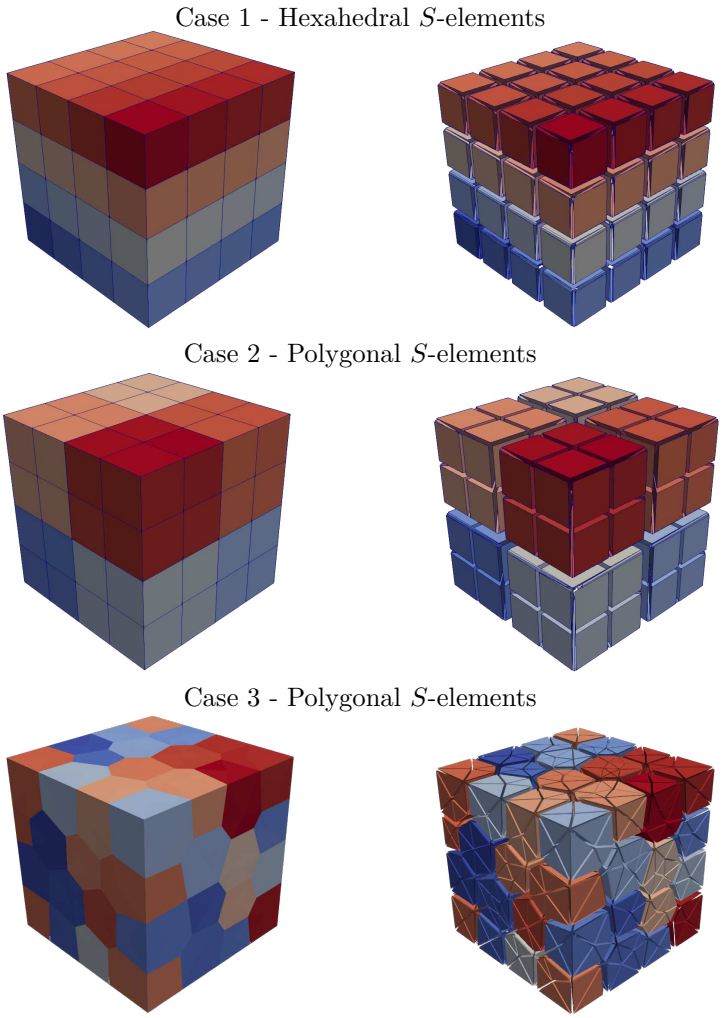

Figure 3.22: Example 4 - Hexahedral and polyhedral partitions $\mathcal{T}^h$, $h = \frac{1}{4}$: $\mathcal{T}^{h,S}$ composed by scaled pyramids (top), and by scaled tetrahedra (bottom).

The results for the Galerkin SBFEM solutions in $\mathbb{S}_k^h$ are plotted in Fig. 3.23 and documented in Appendix A - Table A.6 for the mesh based on the uniform hexahedral S-elements subdivided into regular pyramids (Case 1 - see Fig. 3.22). For this example, the polynomial trace approximation adopted is $k = 1, \cdots, 4$. Optimal accuracy of order k for energy norm and $k+1$ for the L^2-norm occur. Similar results were obtained for the regular polyhedral mesh described in Case 2, where error values have the same magnitude as the errors obtained in Case 1. As detailed in Appendix A - Table A.6, the error for both L^2 and energy norms are slightly lower, but in Case 2, lower DOF are required.

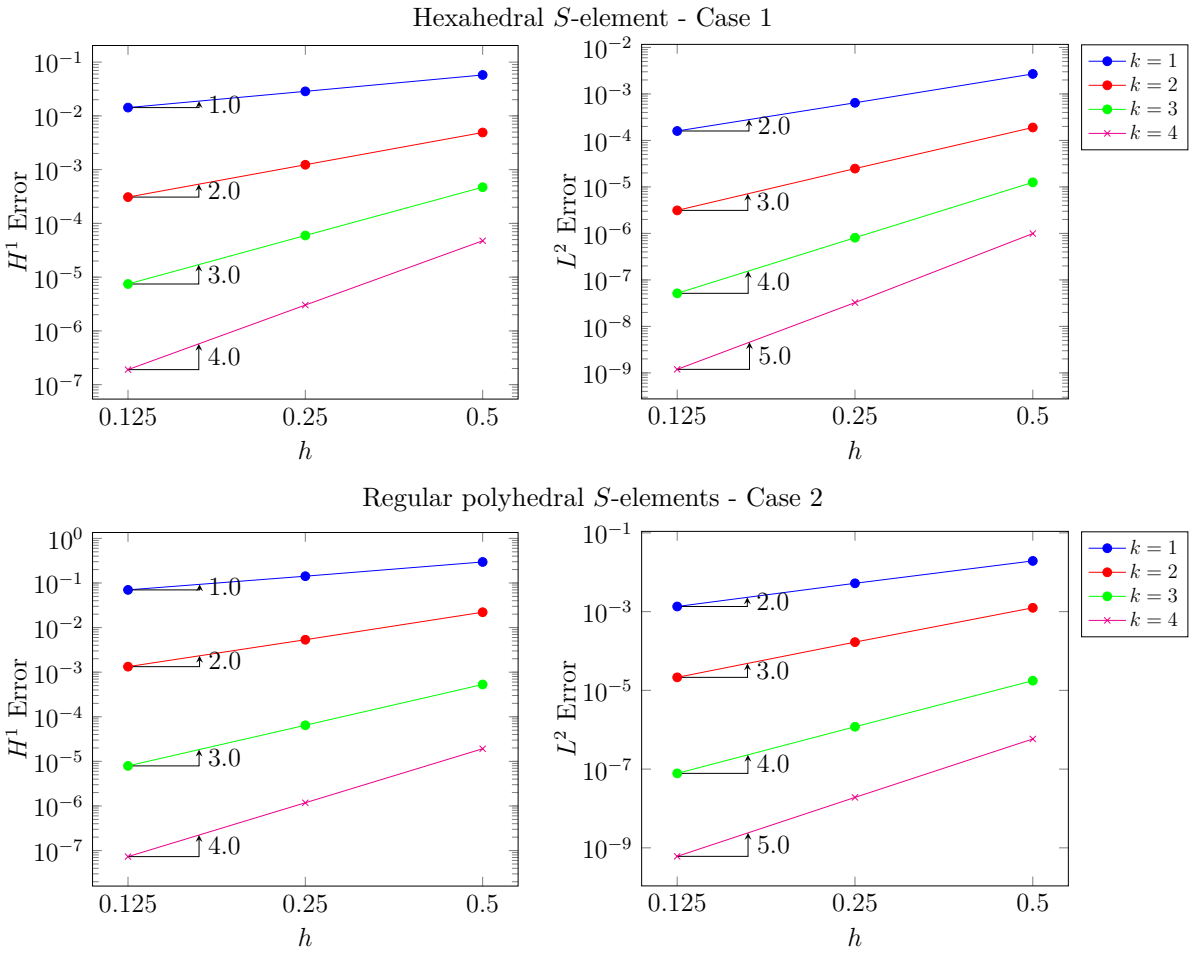

Figure 3.23: Example 4 - Energy and L^2 SBFEM interpolation errors versus h: $\mathbb{S}_k^h(S)$ based on the scaled pyramidal partitions $\mathcal{T}^{h,S}$ of Figure 3.20, and trace spaces $\Lambda_k^{h,S}$ of degree $k = 1, \cdots, 4$.

Energy and L^2 errors obtained with the irregular polyhedral partitions of case 3 versus the DOF are plotted in Fig. 3.24. For comparison, the Galerkin FE solutions in the space $\mathcal{V}_k^{h,FE}$ based on the associated scaled tetrahedral partitions $\mathcal{P}^h$ are also shown. Similar conclusions hold as for the experiment in Example 2 that compares FEM and SBFEM approximated solutions based on triangular and scaled boundary partitions, respectively (see Fig. 3.17). One can also observe that both Galerkin SBFEM and FE approximation errors have similar magnitude, but with less DOF in the SBFEM systems. Their error curves measured with energy and L^2 norms also approach the possible optimal slopes $-k$ and $-(k+1)$, respectively. It is worth mentioning that the reduction of DOF in the SBFEM is at the expense of solving local ODEs. The error values for both SBFEM and FEM approximations are summarized in Table A.6.

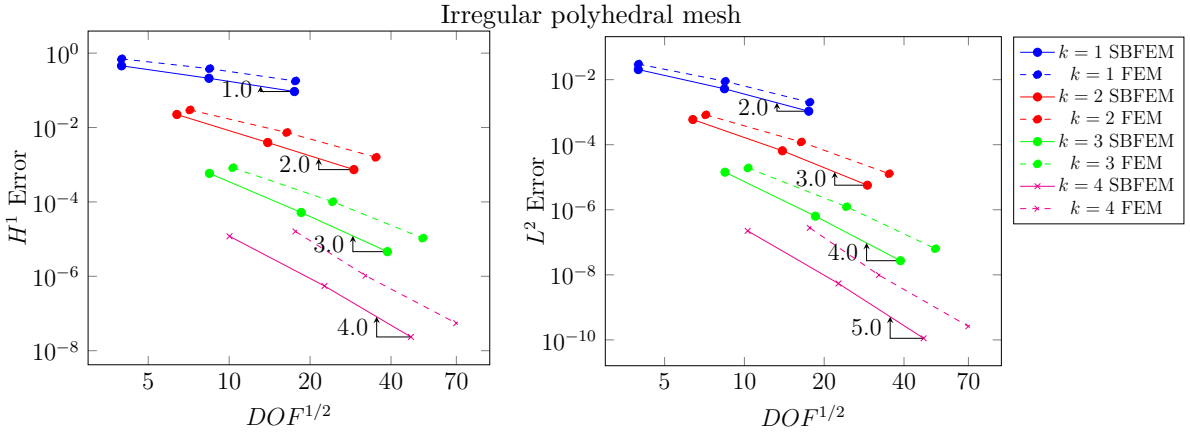

Figure 3.24: Example 4 - Energy and L^2 errors versus DOF for the Galerkin SBFEM solution in $\mathbb{S}_k^h$, for $k = 1, \cdots, 4$, based on the irregular polyhedral S-elements of Case 3.

Fig. 3.25 compares the SBFEM k-convergence using the fixed uniform hexahedral partition at the refinement level $h = \frac{1}{4}$, shown in Fig. 3.22, with equivalent results for the FE method using the spaces $\mathcal{V}_k^{h,FE} \subset H^1(\Omega)$ based on the associated pyramidal partition $\mathcal{P}^h$. FE results for the hexahedral partition are also plotted, recalling that for $k = 1$ this corresponds to SBFEM. Notice that both FE simulations have comparable accuracy, but with less DOF when the mesh is hexahedral. The approximations by SBFEM lead to lower error values as compared with the FE methods and using linear systems with a reduced number of equations. For the case of FE simulations based on the conglomerate pyramidal mesh, this is a result predicted by Theorem 3.3.1. The error curve of the interpolation experiment illustrated in Figure 3.21 is also included.

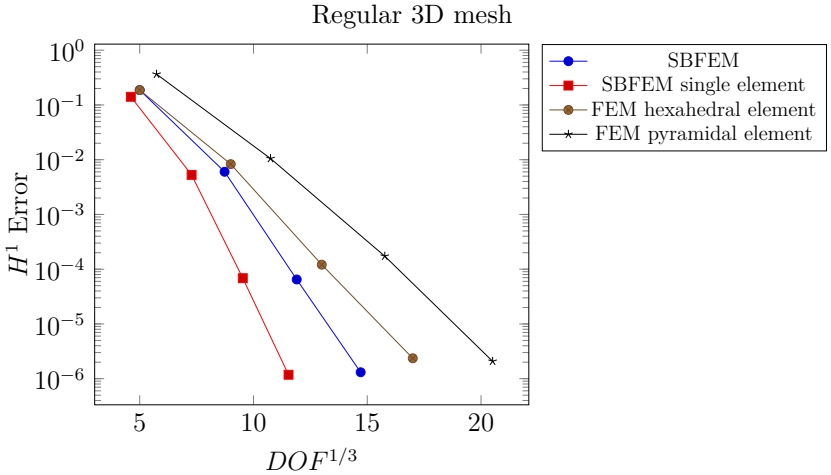

Figure 3.25: Example 4 - k-convergence histories as function of the DOF, for $k = 1, \cdots, 4$: SBFEM using a single S-element (see Fig. 3.20), Galerkin SBFEM based on uniform hexahedral partition $\mathcal{T}^h$, FE method for $\mathcal{V}_k^{h,FE}$ based on the conglomerated pyramidal partition $\mathcal{P}^h$, and FE spaces $\mathbb{Q}_{k,k,k}(S), S \in \mathcal{T}^h$.

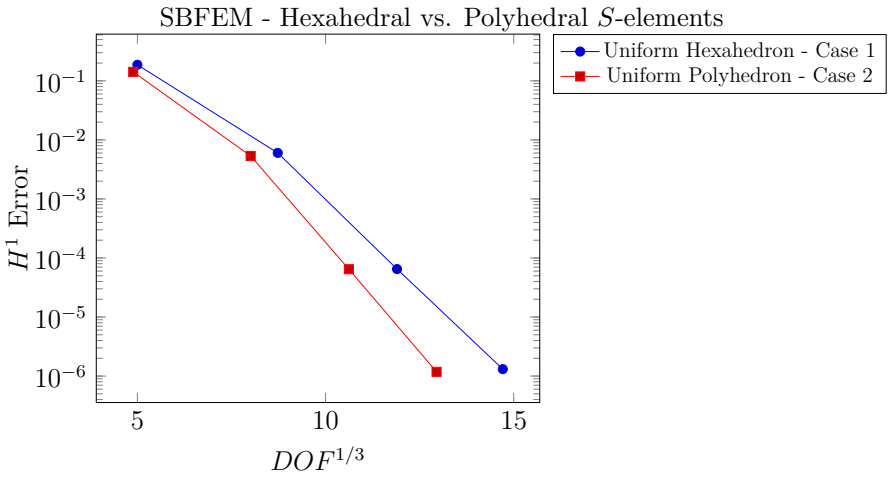

Figure 3.26: Example 4 - Galerkin SBFEM for $\mathbb{S}_k^h$ based on hexahedral and polyhedral S-elements of case 1. In all the experiments, $h = \frac{1}{4}$.

The plots on Fig. 3.26 compare the the k-convergence of the two SBFEM solutions in $\mathbb{S}_k^h$ based on the uniform hexahedral partition illustrated in Fig. 3.22 - Case 1, and on the polyhedral partition of Case 2, also shown in Fig. 3.22, both with $h = \frac{1}{4}$. Similarly to the comparison experiment of the previous example, shown in Fig. 3.19 for the two-dimensional example (see Example 2), these convergence histories also show that the use of polygonal mesh requires fewer equations to be solved for a given target error, but reminding that it requires bigger eigenvalue systems to be solved for the computation of SBFEM shape functions in the S-elements.

Example 5 - Singular harmonic function - Single S-element

In the region $S = [-1, 1] \times [0, 1]$ define the harmonic function

$$u(x, y) = 2^{-1/4}\sqrt{x + \sqrt{x^2 + y^2}} = 2^{1/4}\sqrt{r}\cos(\frac{\theta}{2}), \tag{3.4.0}$$

shown in Fig. 3.27, with a radial square root singularity at the boundary point $\mathbf{O} = (0, 0)$ ($r = 0$), caused by boundary condition change from Dirichlet $u(x, 0) = 0$, for $x < 0$, to Neumann $\partial u/\partial y(x, 0) = 0$, for $x > 0$. This function belongs to $H^{\frac{3}{2}-\epsilon}(\Omega)$, for all $\epsilon > 0$.

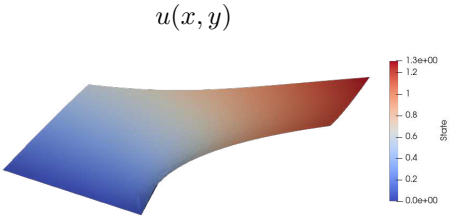

Figure 3.27: Example 5 - Singular harmonic function $u(x, y)$ (3.4.1) in a domain $S = [-1, 1] \times [0, 1]$.

The scaling center is located at the origin and the S-element is taken as an open scaled boundary $\Gamma^{h,S}$ over the two vertical and the top horizontal sides of S, which are uniformly subdivided: n uniform intervals for the vertical edges, and $2n$ for the top edge, for $n = 1, 2$

and 4. This way, in each refinement level, S is composed of internal triangular partition $\mathcal{T}^{h,S}$ formed by $4n$ triangles sharing the scaling center as collapsed vertex, and opposite facet width $h = \frac{1}{n}$.

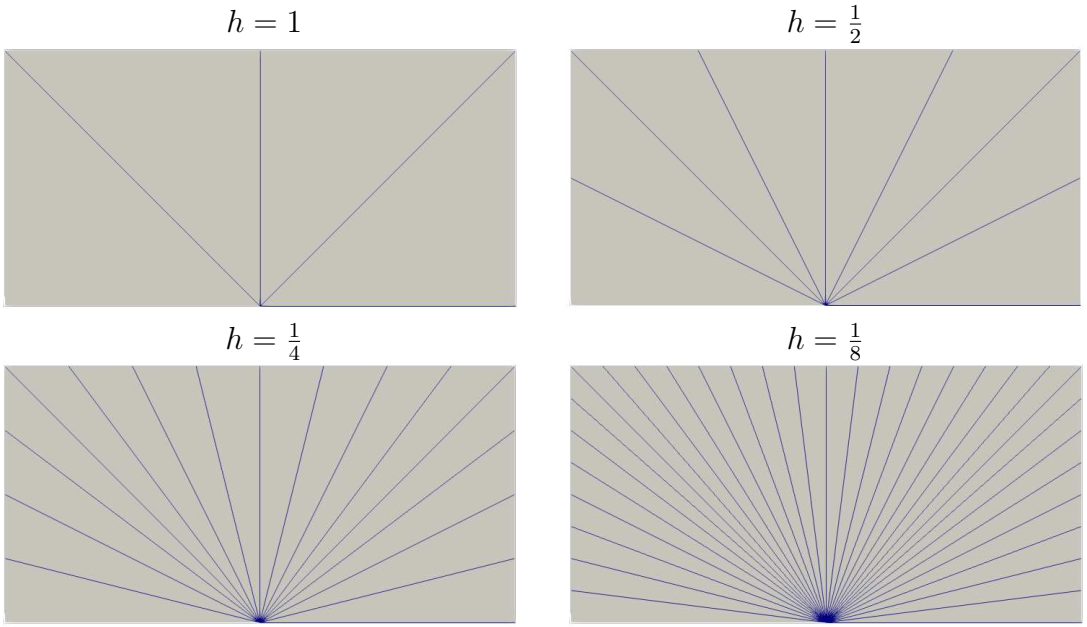

Figure 3.28: Example 5 - Singular harmonic function $u(x, y)$ and scaled triangular partitions $\mathcal{T}^{h,S}$ of $S = [-1, 1] \times [0, 1]$, with open scaled boundary $\Gamma^{h,S}$, with $4n$ uniform facets, $h = \frac{1}{n}$, $n = 1, 2, 4$ and 8.

SBFEM interpolation errors for this singular example are plotted in Figure 3.29 and detailed in Appendix A - Table A.7, revealing usual optimal convergence rates known for trace interpolations by piecewise polynomials, even using in only one element. These results reflect the role of the SBFEM error decomposition in two terms as highlighted in Section 3.3.3, Eq. (3.3.3) and rewritten as follow to ease the reading

$$u - \Pi_k^h u = (u - \mathcal{F}_k^{h,\Delta} u) + (\mathcal{F}_k^{h,\Delta} u - \Pi_k^h u) = (i) + (ii). \tag{3.4.0}$$

In this case, the dominant contribution is expected to come from the virtual interpolant error, determined exclusively by the trace interpolant (term (i)), which is not affected by eventual function singularity not interacting with the scaled boundary $\Gamma^{h,S}$.

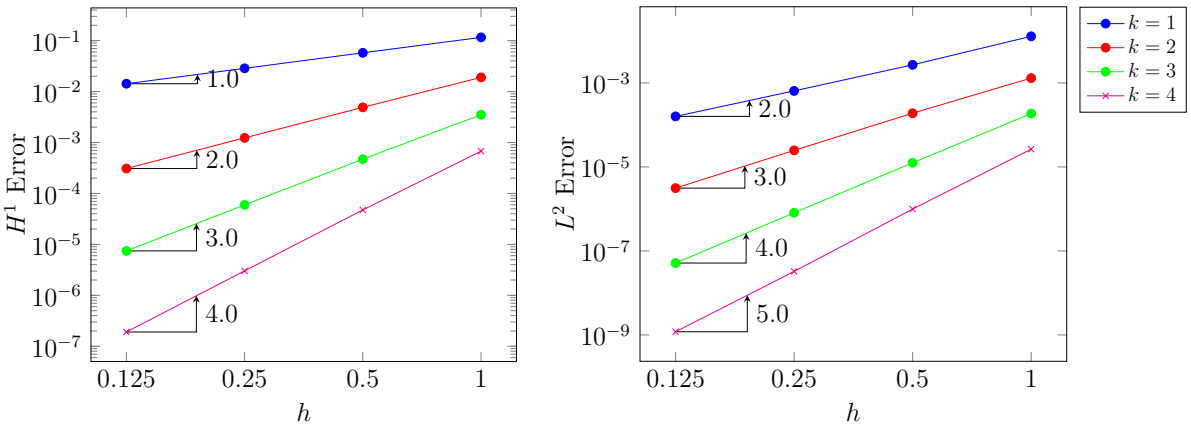

Figure 3.29: Example 5 - Energy and L^2 SBFEM errors versus h for the singular equation (3.4.1) based on the scaled triangular partitions $\mathcal{T}^{h,S}$ of Figure 3.27, and trace spaces $\Lambda_k^{h,S}$ of degree $k = 1, \cdots, 4$.

Because $\Gamma^{h,S}$ is not a closed curve, some care had to be taken in the construction of the SBFEM space $\mathbb{S}^h_k(S)$ in order to incorporate boundary data for u on the bottom boundary side of S. This is accomplished by enforcing in the second order SBFEM ODE system a vanishing Dirichlet boundary condition on one side (associated with vanishing trace value at $\underline{x}_b = (-1, 0)$), whilst a vanishing Neumann condition is assumed on the opposite side (associated with vanishing normal trace at $\underline{x}_b = (1, 0)$). These boundary data are radially extended over the sectors $[-1, 0)$ and $[0, 1]$.

Enforcing Dirichlet boundary condition on $(x, 0)$, $x < 0$, and Neumann boundary condition elsewhere. Due to the lack of regularity of $u \in H^{\frac{3}{2}-\epsilon}(\Omega)$, the error estimates of Theorem 3.3.1 in terms of FE interpolant error based on regular partitions are restricted in theory to order $h^{\frac{1}{2}-\epsilon}$. This problem was considered by Siqueira et al. (2020) to evaluate the efficiency of the mixed FE method when quarter-point elements are used in the vicinity of the origin $\mathbf{O} = (0, 0)$ (singular point), showing dramatic accuracy improvement. Recall that the specific 6-noded quarter-point element is also of Duffy's type, obtained by collapsing a reference quadrilateral element on triangles.

Example 6 - Singular harmonic function - Coupled mesh FEM/SBFEM

The last Poisson example is a formulation composed of SBFEM approximations in a single element $S = [-0.5, 0.5] \times [0, 0.5]$ and FE approximations elsewhere, in the region where the solution is smooth. Similarly to the previous interpolation experiment the space $\mathbb{S}^h_k(S)$ is conceived in such a way that the scaling center is located on the singularity point, which means that an open scaled boundary element is applied. The vertical and top-horizontal edges of S are uniformly subdivided to form an interface partition $\Gamma^{h,S}$. Elsewhere, a uniform quadrilateral mesh matching $\Gamma^{h,S}$ is adopted, as illustrated in Fig 3.30 for $h = \frac{1}{2}$ and $h = \frac{1}{16}$. The coupling between FE and SBFEM approximations is straightforward since SBFEM uses compatible FE spaces at the interface. Four mesh sizes $h = 2^{-\ell}$, $\ell = 1, \cdots, 4$, and polynomials of degree $k = 1, \cdots, 4$ are performed.

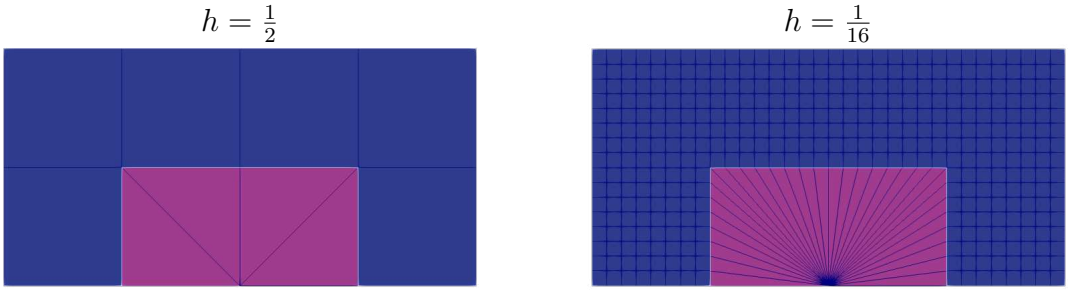

Figure 3.30: Example 5 - Meshes for the coupled FE-SBFEM formulation: FE (blue) in the smooth region and SBFEM (magenta) close to the singularity point.

The corresponding results are documented in Appendix A - Table A.8 and plotted in Fig. 3.31. As for regular problems with smooth solutions, optimal rates of convergence of order k and $k+1$ for energy and L^2 errors hold for this singular problem, without any adaptivity, i.e. uniform degree k is used over the domain and no h-adaptivity is applied as well.

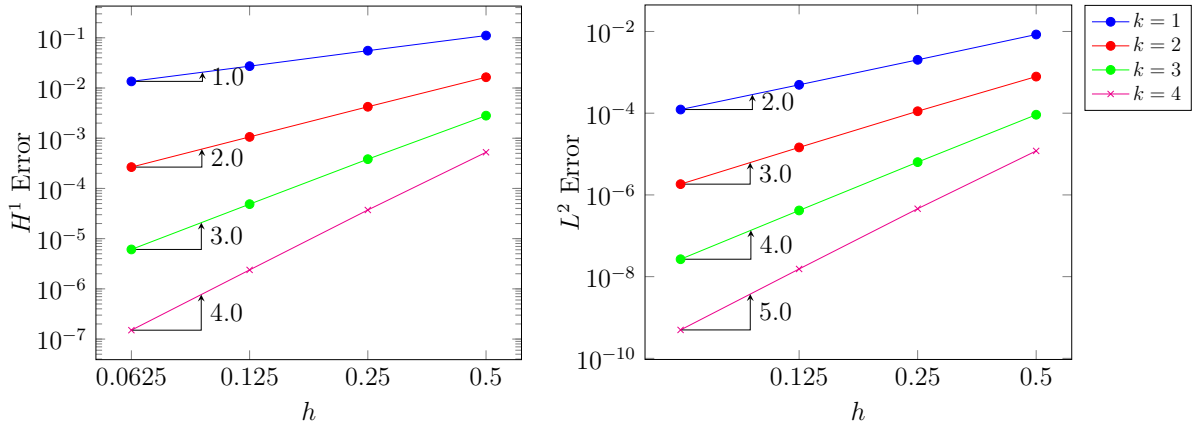

Figure 3.31: Example 5 - Energy and L^2 SBFEM interpolation errors versus h: $\mathbb{S}_k^h(S)$ based on the scaled triangular partitions $\mathcal{T}^{h,S}$ of Figure 3.27, and trace spaces $\Lambda_k^{h,S}$ of degree $k = 1, \cdots, 4$.

For comparison, two k-convergence histories as a function of the number of DOF are shown in Fig. 3.32 for fixed partitions of the domain Ω: one for the SBFEM interpolation errors computed in Example 5 and the other for the combined Galerkin FE-SBFEM method. The partitions used in these experiments are illustrated in Figure 3.32, noticing that they coincide within the region S around the singularity, but the FE partition in the smooth region is more refined. Whilst SBFEM interpolation in the single element Ω requires much less DOF, both experiments reach very close error values, because the error in this problem is governed by the singularity, modeled using SBFEM in both experiments. However, the results of Fig 3.32 could be deceiving. It should be emphasized that global SBFEM interpolation in the whole domain Ω was feasible in this particular test problem, but this is not the case in practical singular problems, for which coupled FE+SBFEM simulations reveal to be a simple and efficient option.

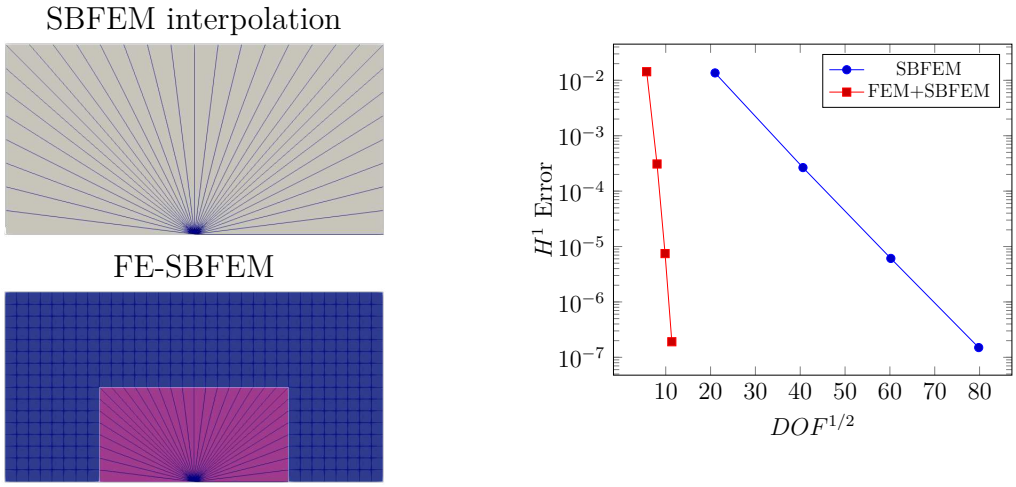

Figure 3.32: Example 6 - Partitions and k-convergence histories versus the number of DOF, with $k = 1, \cdots, 4$, of Example 5 and Galerkin FE-SBFEM solutions.

3.4.2 Elasticity problem

The last set of examples is regarding the convergence analysis of two and three-dimensional Elasticity problems. In the last example, a single crack in a plate is analyzed using

a coupled mesh SBFEM+FEM, showing numerically the error analysis demonstrated theoretically that the error is bounded by the trace interpolation approximation.

Example 7 - Two-dimensional loaded beam

The first Elasticity example is a 2D beam in $\Omega = [-1;-1] \times [1;1]$, under plane stress mode, subjected to a bending moment at its extremity and with the analytical solution

$$\underline{u}(x,y) = \begin{Bmatrix} 5\left(\frac{y}{2G} + \frac{x^2 y}{2E} - \frac{y^3}{6G} + \frac{\nu y^3}{6E}\right) \\ 5\left(-\frac{x^3}{6E} + \frac{\nu x y^2}{2E}\right) \end{Bmatrix}, \tag{3.4.0}$$

where

$$G = \frac{E}{2(1+\nu)},$$

and $E = 10GPa$ and $\nu = 0.3$ are, respectively, the Young Modulus and the Poisson coefficient. Notice that the analytical solution is obtained considering a $k = 3$, showing that the SBFEM approximation contains the full polynomial space up to the order k.

It considered the same uniform mesh refinement with quadrilateral S-elements as in Example 1, illustrated in Fig. 3.12, for the case of a single S-element and skeleton refinement; Example 2, shown in Fig. 3.14 - Case 1 for the domain refinement. In both cases, the scaling center is positioned at the centroid of the quadrilateral S-element, and the quadrilateral is subdivided into uniform four triangles. For the skeleton refinement, the S-element's skeleton is refined two times, as already shown in Fig. 3.14, where the characteristic size is given by $h = 2^{\ell-1},\ \ell = 0,1,2$. For the domain's refinement, one more refinement is performed, leading to a characteristic size of $h = 2^{\ell-1},\ \ell = 0,...,3$. As well as the previous examples, the characteristic size is given by the skeleton's width. The post-processed solution for the stress in x-direction σ_x is plotted in Fig. 3.33 at the left side, and the shear τ_{xy} in the same Figure at the right side, for $k = 3$, that gives the analytical solution.

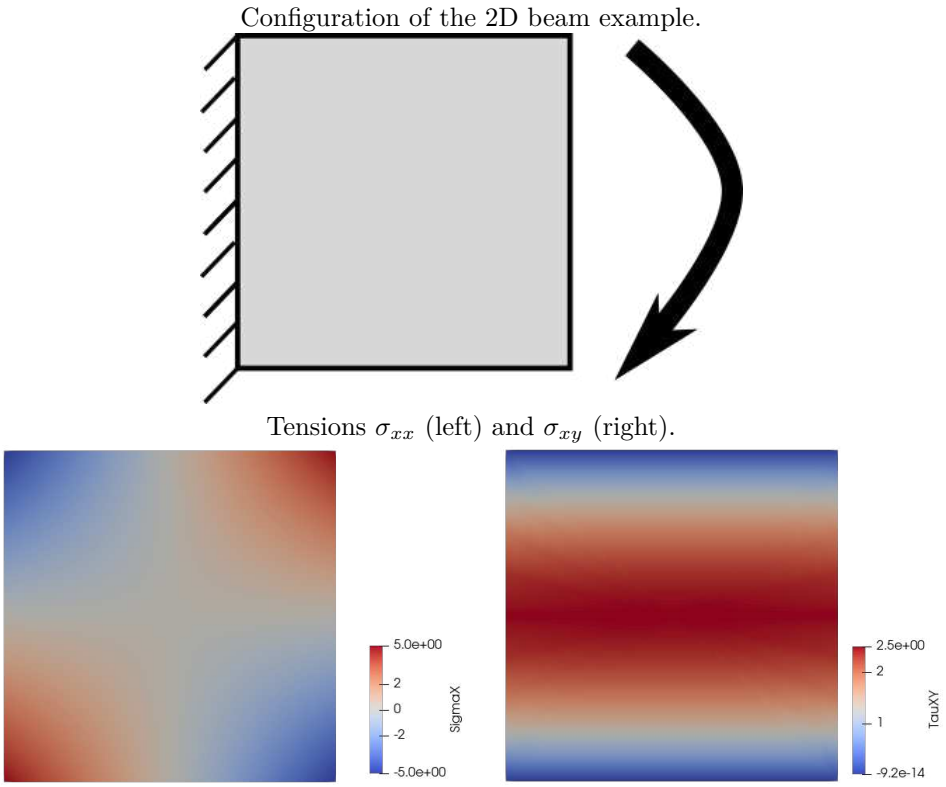

Figure 3.33: Example 7 - Beam with a bending moment applied at the extremity.

The convergence curves for the skeleton and domain refinement are plotted, respectively, in Figure 3.34 and 3.35 for $k = 1, 2$, and 3. Notice that $k = 3$ is numerically equal to the analytical solution, whilst for $k = 1$ and 2 the rates of convergence are equal to $k + 1$ for the L^2 norm and k for the energy norm. Details of the error values can be seen in Appendix A - Table A.9.

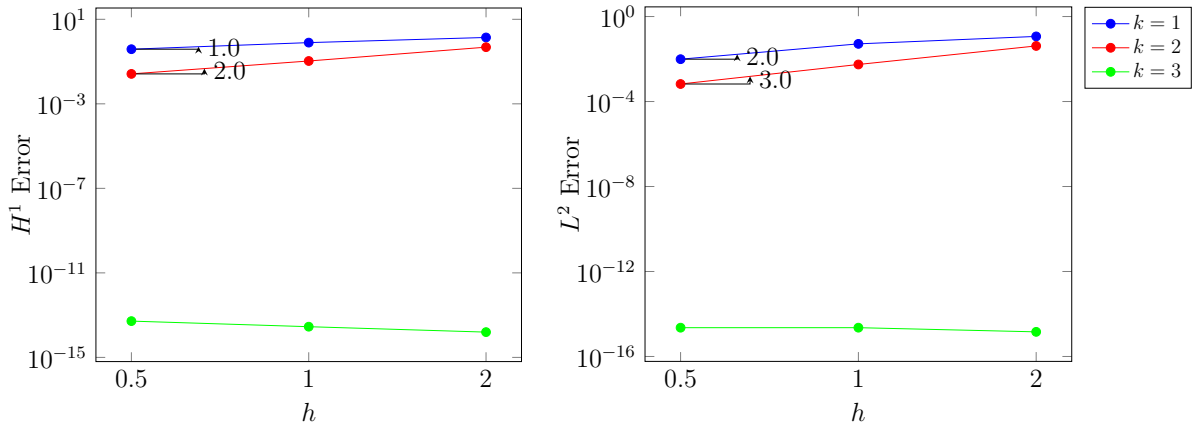

Figure 3.34: Example 7 - Energy and L^2 errors for the two-dimensional Elasticity problem using a single S-element, for $k = 1, 2, 3$ and $h = 2^{1-\ell}$, $\ell = 0, 1, 2$.

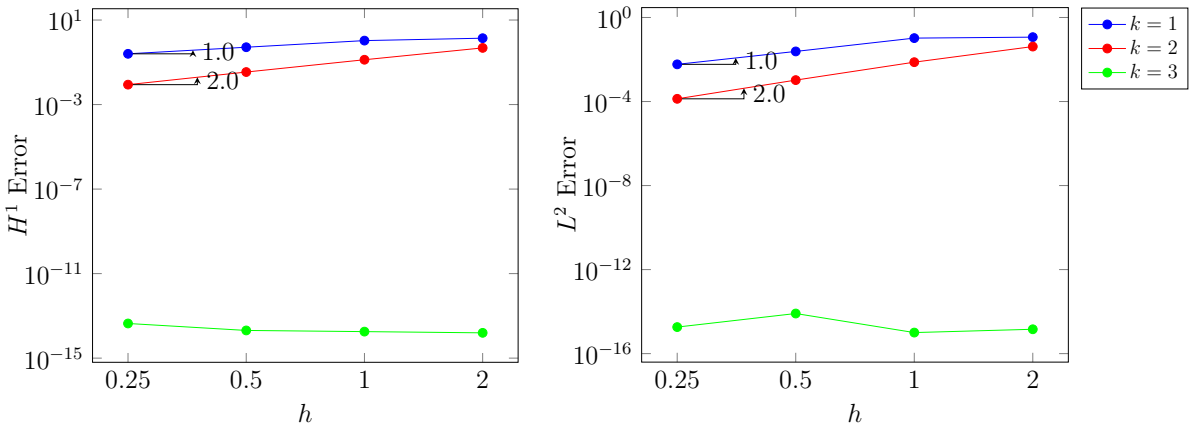

Figure 3.35: Example 7 - Energy and L^2 errors for the two-dimensional Elasticity problem using $n \times n$ S-elements, for $k = 1, 2, 3$ and $h = 2/n$, $n = 2^{\ell}$ and $\ell = 0, ..., 3$.

Example 8 - Three-dimensional cantilever beam

This example is a cantilever beam subjected to an end-shear force F. The beam configuration is shown in Fig. 3.36, in which $a = 0.5$, $b = 0.5$, $L = 5$. The analytical solution is given by Bishop (2014) for a beam that is oriented in the z direction and loaded in the negative y direction. As well as in Bishop (2014), it is considered a force $F = 1$, and an isotropic material with Young modulus of $E = 1$ and Poisson coefficient $\nu = 0.3$.

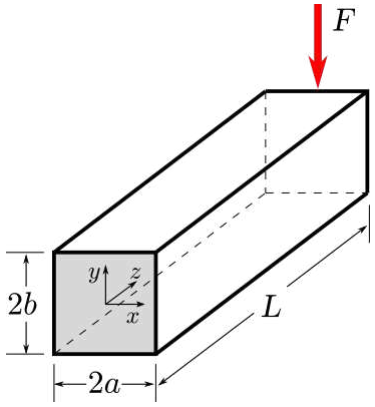

Figure 3.36: Example 8 - Configuration of the 3D cantilever beam.

The mesh is composed of hexahedral S-elements, where each S-element is subpartitioned into six pyramids, as well as in the uniform mesh of the 3D example in Section 3.4.1 (Fig. 3.22 - Hehahedral S-elements). The coarsest mesh ($h = 1$) and the most refined mesh ($h = 0.0625$) are shown in Fig 3.37. A total of four refinement steps are applied, in which the characteristic size of each mesh is $h = 2^{-\ell}$, $\ell = 0, ..., 4$.

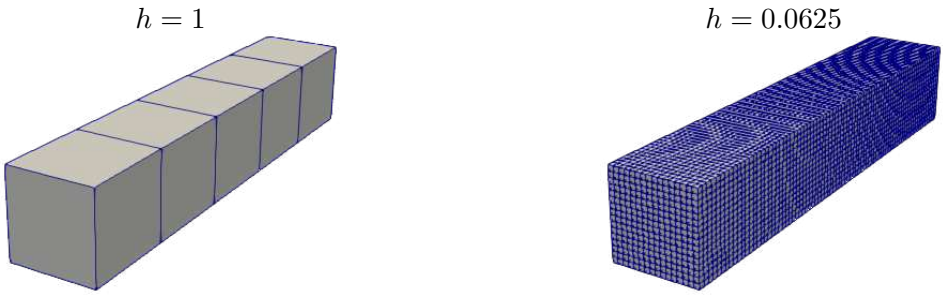

Figure 3.37: Example 2 - 3D cantilever beam: coarsest mesh for $h = 1$ (left), refined mesh with $h = 0.0625$ and four refinement steps (right).

The post-processed displacement solution, for the most refined mesh ($h = 0.0625$) and considering a trace FE approximation of $k = 4$, is plotted in Fig. 3.38 in the beam's deformed configuration.

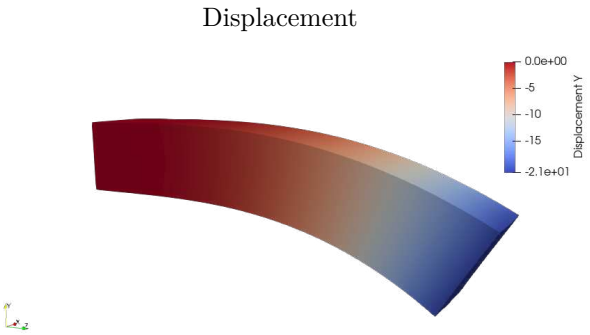

Figure 3.38: Example 2 - 3D cantilever beam: post-processed stress (left) and displacement (right) for $k = 4$ and $h = 0.0625$.

According to Bishop (2014), the stress state of the beam is equal to:

$$\sigma_{xx} = \sigma_{yx} = \sigma_{yy} = 0$$
$$\sigma_{zz} = \frac{F}{I} yz$$
$$\sigma_{zx} = \frac{F}{I} \frac{2a^2}{\pi^2} \frac{\nu}{1+\nu} \Sigma_{n=1}^{\infty} \frac{(-1)^n}{n^2} \sin(n\pi x) \frac{\sinh(n\pi y)}{\cosh(n\pi)}$$
$$\sigma_{zy} = \frac{F}{I} \frac{b^2 - y^2}{2} + \frac{F}{I} \frac{\nu}{1+\nu} \left[\frac{3x^2 - a^2}{6} - \frac{2a^2}{\pi^2} \Sigma_{n=1}^{\infty} \frac{(-1)^n}{n^2} \cos(n\pi x/a) \frac{\cosh(n\pi y/a)}{\cosh(n\pi b/a)} \right]$$

and the corresponding displacement field is equal to:

$$u_x = \frac{-F\nu}{EI} xyz$$
$$u_y = \frac{F}{EI} \left[\frac{\nu}{2}(x^2 - y^2)z - \frac{1}{6} z^3 \right]$$
$$u_z = \frac{F}{EI} \left[\frac{1}{2} y(\nu x^2 + z^2) + \frac{1}{6} \nu y^3 + (1+\nu)(b^2 y - \frac{1}{3} y^3) - \frac{1}{3} a^2 \nu y \right.$$
$$\left. - \frac{4a^3 \nu}{\pi^3} \Sigma_{n=1}^{\infty} \frac{(-1)^n}{n^3} \cos(n\pi x/a) \frac{\sinh(n\pi y/a)}{\cosh(n\pi b/a)} \right]$$

For this experiment, the series is bounded for $n = 5$.

In the convergence analysis, as already predicted theoretically and numerically observed in the previous examples, the SBFEM approximation leads to optimal rates of convergence - $k + 1$ for the L^2 norm and k for the energy norm. The curves are plotted in Fig. 3.39 and summarized in Table A.10 in Appendix 1. The error values for $k = 5$ were computed although not plotted because the error for $h = 0.0625$ could not be computed due to the lack of RAM memory - this configuration results in a system of 3 million DOF.

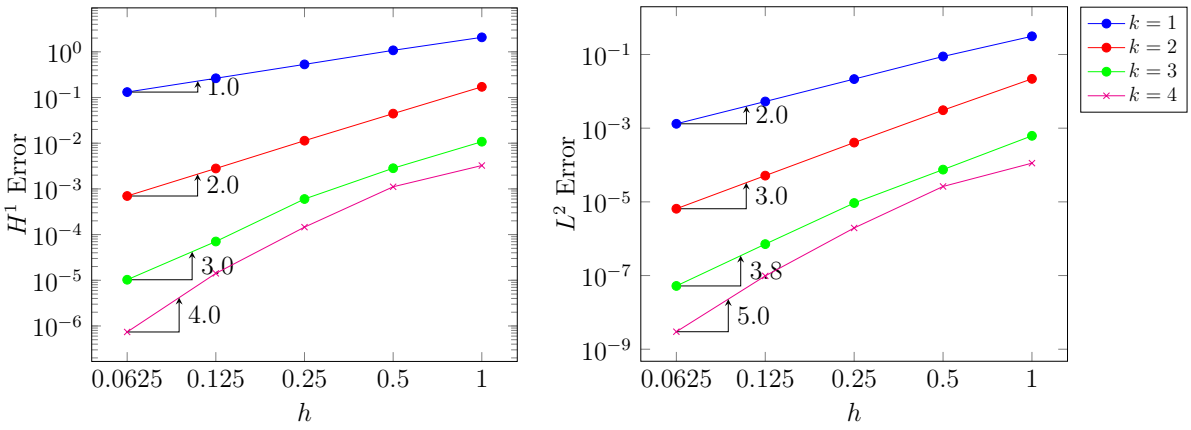

Figure 3.39: Example 1 - Energy and L^2 errors for the three-dimensional Elasticity problem using $n \times n \times 5n$ S-elements, for $k = 1, ..., 4$ and $h = 2/n$, $n = 2^\ell$ and $\ell = 0, ..., 4$.

Example 9 - Lateral crack

In this example, a isotropic plate under plane stress conditions of dimensions $\Omega = [-1; -1] \times [1; 1]$, with a lateral crack, is evaluated. The analytical solution is given by,

$$\underline{u}(x, y) = \begin{Bmatrix} \dfrac{K_I}{2G}\sqrt{\dfrac{r}{2\pi}}\cos\dfrac{\theta}{2}\left(\kappa - 1 + 2\sin^2\dfrac{\theta}{2}\right) \\ \dfrac{K_I}{2G}\sqrt{\dfrac{r}{2\pi}}\sin\dfrac{\theta}{2}\left(\kappa + 1 - 2\cos^2\dfrac{\theta}{2}\right) \end{Bmatrix} \tag{3.4.-1}$$

where

$$G = \frac{E}{2(1+\nu)}, \quad \kappa = \frac{3-\nu}{1+\nu},$$

and E is the Young Modulus and ν the Poisson coefficient, equal to 10 GPa and 0.3, respectively, and the stress intensity factor $K_I = 1$. Chiong et al. (2014) and Song (2018) show that the SIF can be obtained directly from the SBFEM approximated solution through the expression

$$\begin{Bmatrix} K_I \\ K_{II} \end{Bmatrix} = \frac{G}{\kappa + 1}\sqrt{\frac{2\pi}{r_0}} \begin{Bmatrix} u_{A_y}(\xi = 1) - u_{B_y}(\xi = 1) \\ u_{A_x}(\xi = 1) - u_{B_x}(\xi = 1) \end{Bmatrix} \tag{3.4.-1}$$

where u_A and u_B are the displacement values at the points A and B shown in Fig. 3.40 and r_0 is the crack length. Notice that, in this example, to approximate the singularity, the scaling center must be positioned at the crack tip.

First, a mesh composed of a single polygonal S-element is considered. The S-element is a open polygon refined three times, leading to characteristic mesh width of $h = 2^{-\ell}$,

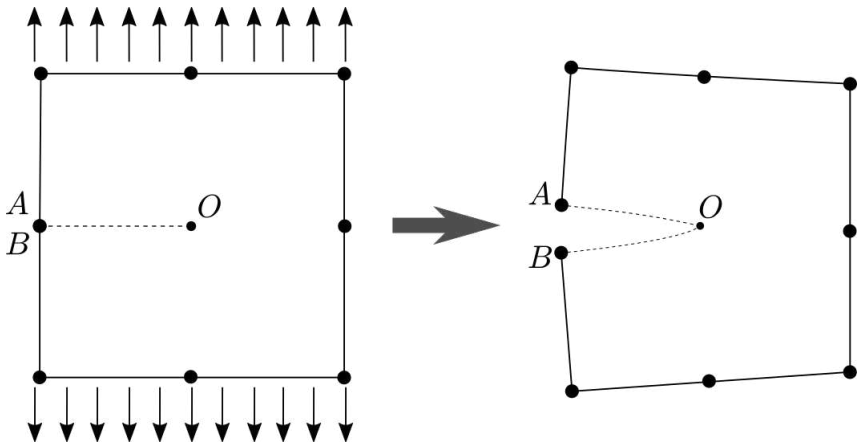

Figure 3.40: Mesh configuration with DOFs for $k = 2$ and a single polygon S-element, with scaling center in O and open in A, B - left: master element configuration, right: deformed element.

$\ell = 0, ..., 3$ the subpartitions illustrated in Fig. 3.41. The post-processed solution for $k = 4$ and $h = \frac{1}{8}$ is plotted in Fig. 3.42. In such a configuration, the error values for the displacement and for the stress are respectively 8.32E-10 and 1.52E-07.

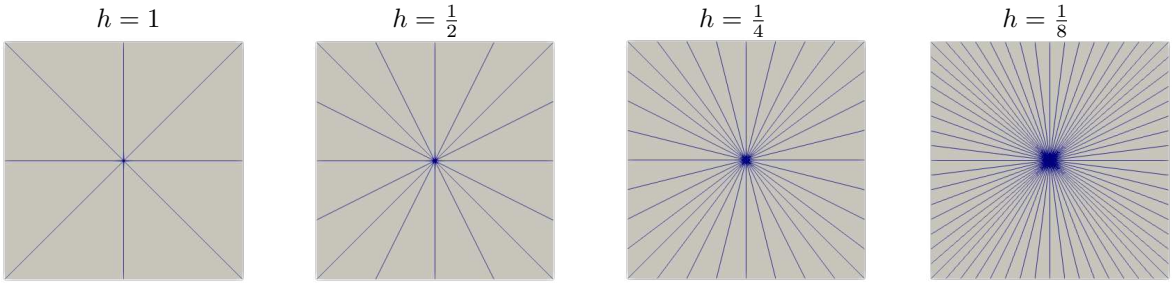

Figure 3.41: Example 9 - Single S-element refined two times for the lateral crack problem.

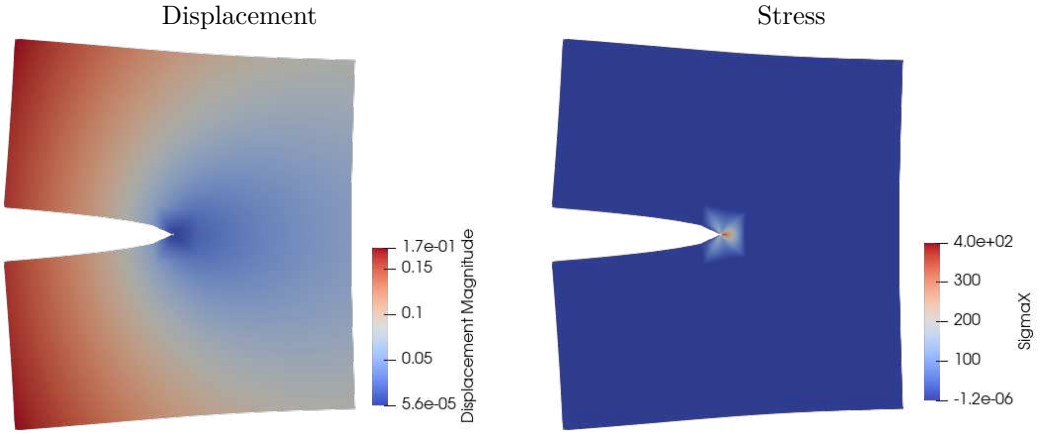

Figure 3.42: Example 9 - SBFEM approximation for displacement magnitude (left) and stress in x-direction for a single S-element and $h = \frac{1}{8}$ (see Fig. 3.41).

Next, a coupled mesh SBFEM+FEM is considered, as shown in Fig. 3.43. As well as the previous mesh configuration, the singularity at the crack tip is approximated using a single S-element, but the smooth part of the solution is approximated with regular FE.

For this configuration, two mesh refinements are performed leading to the characteristic mesh width $h = 2^{-\ell}$, $\ell = 1, 2, 3$, as illustrated in Fig. 3.43. The S-element is an open polygon embedded in the FEM mesh. For the FEM mesh, the FE elements along the crack are disconnected in the mesh generation process.

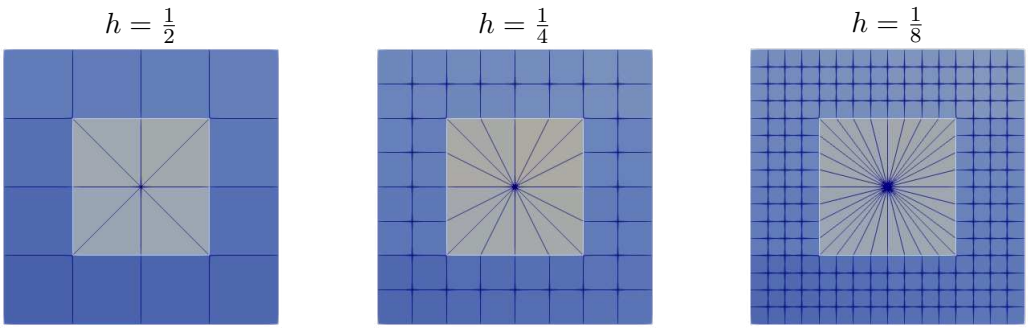

Figure 3.43: Combined FEM+SBFEM mesh: FE - dark blue elements around the crack tip; and Scaled Boundary FE - single element in the middle.

Optimal rates of convergence were obtained, namely $k+1$ for the L^2 norm, and k for the semi-norm of energy. The numerical results are summarized in Appendix A - Table A.11. Therefore, for FEM meshes, in which the computation of the solution near the singularity can be computationally demanding, using only one scaled boundary element recovers optimal rates of convergence. Coupled meshes SBFEM+FEM for fracture mechanics is not a novel topic, but it was explored by Yang and Deeks (2007) and Ooi and Yang (2010). Yet, the numerical results emphasize the novel theoretical results proven in this chapter.

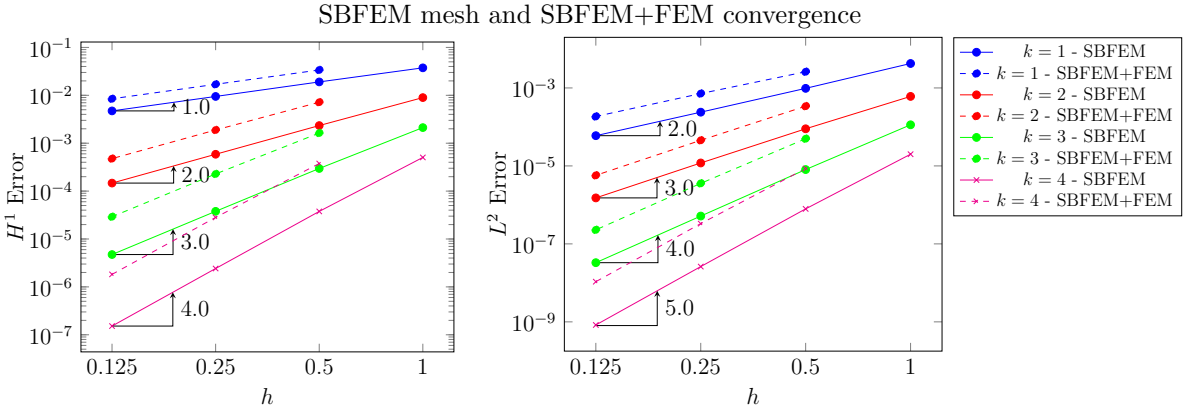

Figure 3.44: Example 5 - Energy and L^2 errors for the SBFEM mesh.

Higher error values were obtained for the coupled mesh SBFEM+FEM. Yet, using SBFEM in the crack tips of a FE mesh recovers the optimal rates of convergence for FEM simulations. It is worth mentioning that the couple between the SBFEM and FEM meshes is straightforward since the SBFEM boundary approximation is a FE trace approximation. It means that the scaled boundary element is seen by the FEM mesh as a FE boundary element, which is usual in FE simulations to impose boundary conditions. It is worth mentioning that the SIF can be computed directly from the SBFEM solution using the procedure presented by Chiong et al. (2014).

The approximated values for SIFs using the SBFEM were computed through Eq. 3.4.2. The summary of the values for K_I and the error values are displayed in Table 3.5. The

lowest error value for K_I was achieved for $k = 3$, of order $\approx 10^{-7}$, using the two more refined meshes, showing that not only the SBFEM provides an easier procedure to compute the SIF but also accurate value. It is worth mentioning that, for the load configuration displayed in Fig. 3.40, the mode $K_{II} = 0$.

Table 3.5: SBFEM approximation for the SIF and error values $||K_I^{SB} - K_I||$ where K_I^{SB} is the SBFEM approximation for the SIF $K_I = 1$, characteristic width of $h = 2/2^{\ell}$, $\ell = 0, ..., 3$, and $k = 1, ..., 4$.

	$k=1$		$k=2$	
ℓ	K_I^{SB}	Error	K_I^{SB}	Error
0	0.995106	4.8936E-3	1.00288	2.8831E-3
1	1.00187	1.8742E-3	1.00031	3.1391E-4
2	1.00041	4.1411E-4	1.00003	3.1908E-5
3	1.0001	1.0082E-4	1.000001	5.3291E-7
	$k=3$		$k=4$	
ℓ	K_I^{SB}	Error	K_I^{SB}	Error
0	1.00026	2.5751E-4	0.999894	1.060E-4
1	0.999969	3.0749E-5	0.999994	5.7238E-6
2	0.999994	5.7236E-6	1.0000005	5.3266E-7
3	1.000001	5.3291E-7	1.0000005	5.3266E-7

3.5 Concluding remarks

This chapter introduces the SBFEM approximations as a subspace of a conglomerate Duffy's approximation space. The mathematical description of the SBFEM space allowed the definition of a priori error estimates for the SBFEM for the energy norm. The approximation error using the SBFEM is divided into two portions: the error regarding the trace approximation and due to the radial extension of the trace data into the interior of a S-element. It is observed that even for problems with square root singularities, the SBFEM reaches optimal rates of convergence since the SBFEM error is bounded by the error of the FE trace space over the scaled boundary element $\Gamma^{h,S}$.

The formal definition of the SBFEM local space, interpreted as a type of Duffy's approximation space as well as the error estimation are outstanding topics in the literature, contribution of this thesis and published in the paper: **COELHO, K. O.**; DEVLOO, P. R. B.; GOMES, S. M. Error estimates for the scaled boundary finite element method. *Computer Methods in Applied Mechanics and Engineering*, v. 379, p. 113765, 2021.

As it is going to be developed in this thesis, the definition of the SBFEM space subspace of Duffy's approximation space allows using the mathematical apparatus already existing in the literature to extend the SBFEM formulation to approximate a variety of problems. For instance, such a definition is the key to solving non-homogeneous PDEs with optimal rates of convergence, as it is going to be explored in Chapter 4.

Chapter 4

A bubble function approach to approximate non-homogeneous PDE with the SBFEM

As highlighted in the previous chapter, in the SBFEM, the polynomial approximation exists only at ∂S. The approximation inside S is constructed by solving local Dirichlet problems with vanishing force terms. Since the approximated solution is obtained through the analytical solution of a homogeneous ODE computed based on the Dirichlet data and a trace polynomial space, the SBFEM is considered a semi-analytical approach (SONG; WOLF, 1997; SONG; WOLF, 1998; WOLF; SONG, 2000). For instance, as demonstrated in the previous chapter for Laplace's equation, the SBFEM approach approximates the analytical solution inside S-elements by radial harmonic extensions of surface components (COELHO; DEVLOO; GOMES, 2021).

Constructing the SBFEM space under a framework of homogeneous PDEs imposes limitations to approximate equations with a force term. To overcome this issue, strategies to solve non-homogeneous PDEs using SBFEM are available in the literature. The earliest SBFEM formulation derived the approximation using the variation of parameters technique (SONG; WOLF, 1999a). Next, Song (2006) applied the framework described in Song and Wolf (1999a) to represent the particular solution of thermal analysis, using the SBFEM, as a power function of the radial coordinate. Later, Ooi and co-authors (see Ooi, Song and Natarajan (2017) and Ooi, Song and Natarajan (2016)) developed a procedure to solve the non-homogeneous term through the addition of bubbles to the standard SBFEM functions. However, the construction of these bubbles is complex and increases the computational cost of simulation considerably. Moreover, the authors did not verify the convergence for 3D simulations. Recently, Gravenkamp, Song and Zhang (2020) applied a very simple quadratic bubble and obtained similar results as the previous authors. However, in this paper considered only a simple force term. For complex body loads, poor rates of convergence are expected.

This chapter proposes a novel procedure to approximate non-homogeneous PDEs using an SBFEM-bubble function approach. This enrichment allows recovering the optimal rates of convergence for non-homogeneous PDEs using SBFEM. Some improvements as compared to the already existing bubble function formulation are addressed. First, in this paper, the convergence analysis of bubble functions is extended to 3D domains, in contrast to the

data in the literature that include only 2D problems (OOI; SONG; NATARAJAN, 2016; OOI; SONG; NATARAJAN, 2017). Second, the advantage of the orthogonality property proven in Coelho, Devloo and Gomes (2021), in which the SBFEM space is orthogonal to a generic bubble approximation space in S, is explored to define a priori error estimates.

In addition, the orthogonality allows the partition of the SBFEM stiffness matrix for static problems into submatrices associated with the boundary functions and internal functions, thus reducing the computational cost. This construction process of the bubbles is straightforward since it is a simple linear combination of the SBFEM basis functions. The integration of stiffness associated with the bubble functions can be done semi-analytically similarly to the stiffness matrix associated with the boundary shape functions. The approach presented also demonstrates that SBFEM computations lead to optimal boundary values and that internal functions can be computed selectively, in regions of interest.

As already proven in the previous chapter, the SBFEM reaches optimal rates of convergence for homogeneous PDEs, even for problems with square-root singularity. However, the mathematical description of physical problems often leads to the presence of a force term. In this case, using SBFEM without any enrichment or modification leads to a loss of convergence since SBFEM is an operator-adapted method that constructs basis functions without considering the force term, as previously shown in this thesis. The numerical results showing the loss of convergence are illustrated in Section 4.5 - Numerical tests, Example 1.

4.1 Model problem: Composing the full SBFEM space

As well as in the previous chapter, two model problems are presented, namely: the Poisson equation and the Elasticity problem. Later, the full approximation space is composed by adding bubble functions. Before introducing the problem, some definitions are useful.

Let a domain $\Omega \subset \mathbb{R}^d,\ d = 2, 3$ be partitioned into geometric S-elements $\mathcal{T}^h = \{S\}$. If h is the characteristic mesh size, given by the size of the $\Gamma^{h,S}$ facets. Again, the S-element can have an arbitrary number of facets, and each S-element is subdivided into Duffy's elements (see Chapter 3 - Fig. 3.6). For such a geometric partition, define:

- $\mathbb{B}_k(S)$: local scalar SBFEM bubble function space for a Poisson problem. This approximation space is a subspace of the scalar Duffy's bubble space $\mathcal{D}_k^0(S) = \{w \in \mathcal{D}_k(S)\ s.t.\ w|_{\partial S} = 0, S \in \mathcal{T}^h\}$, and

$$\mathbb{B}_k^h = \{w \in H^1(\Omega);\ w|_S \in \mathbb{B}_k^h(S),\ S \in \mathcal{T}^h\};$$

- $\underline{\mathbb{B}}_k(S)$: local vector-valued SBFEM bubble function space for an Elasticity problem. $\underline{\mathbb{B}}_k(S)$ is a subspace of the scalar Duffy's bubble space $\underline{\mathcal{D}}_k^0(S) = \{\underline{w} \in \underline{\mathcal{D}}_k(S)\ s.t.\ \underline{w}|_{\partial S} = 0, S \in \mathcal{T}^h\}$ and

$$\underline{\mathbb{B}}_k^h = \{\underline{w} \in H^1(\Omega, \mathbb{R}^d);\ \underline{w}|_S \in \underline{\mathbb{B}}_k^h(S),\ S \in \mathcal{T}^h\};$$

- $\mathbb{V}_k(S)$: scalar SBFEM function space for a Poisson problem, composed of the direct sum of the bubble-free and bubble function spaces, i.e. $\mathbb{S}_k(S) \oplus \mathbb{B}_k(S)$, where $\mathbb{S}_k(S)$ is the bubble-free SBFEM space for harmonic problems, defined in Chapter 3 - (3.2.3) and

$$\mathbb{V}_k^h = \{v \in H^1(\Omega);\ v|_S \in \mathbb{V}_k^h(S),\ S \in \mathcal{T}^h\};$$

- $\underline{\mathbb{V}}_k(S)$: vector-valued SBFEM function space for Elasticity, composed of the direct sum of vector-valued bubble-free and bubble approximation spaces $\underline{\mathbb{S}}_k(S) \oplus \underline{\mathbb{B}}_k(S)$, where $\underline{\mathbb{S}}_k(S)$ is the vector-valued bubble-free SBFEM space for Elasticity defined in Chapter 3 - (3.2.4) and

$$\underline{\mathbb{V}}_k^h = \{\underline{w} \in H^1(\Omega;\mathbb{R}^d);\ \underline{w}|_S \in \underline{\mathbb{V}}_k^h(S),\ S \in \mathcal{T}^h\}.$$

These spaces will be formally defined in this chapter.

A brief overview of $\mathbb{V}_k^h$ and $\underline{\mathbb{V}}_k^h$ properties

The components of the bubble-enriched scalar $\mathbb{V}_k^h$ and vector-valued $\underline{\mathbb{V}}_k^h$ SBFEM approximation spaces has an intrinsic orthogonality, explored in Chapter 3 (Proposition 3.3.1). Namely, $\mathbb{V}_k^h$ and $\underline{\mathbb{V}}_k^h$ has energy-orthogonality properties: $\mathbb{B}_k^h$ is orthogonal to $\mathbb{S}_k^h$ and $\underline{\mathbb{B}}_k^h$ is orthogonal to $\underline{\mathbb{S}}_k^h$, both in the energy norm. As shall be clarified later, these properties are crucial and have two main advantages

1. Recovery of optimal convergence rates measured with energy-norm, as proved for SBFEM solutions of harmonic and Elastic problems (respectively Theorem 3.3.1 and 3.3.2) in Chapter 3. This proof is extended to both models with non-vanishing force terms in this chapter.

2. It is possible to decouple the problems into two kinds of approximations: of skeleton type, for bubble-free shape functions, and of interior type, otherwise. Namely, the stiffness matrix can be generically written as

$$\underline{\underline{K}} = \begin{pmatrix} \underline{\underline{K}}^{\partial} & \underline{\underline{0}} \\ \underline{\underline{0}} & \underline{\underline{K}}^{b} \end{pmatrix}. \tag{4.1.0}$$

   In other words, any static stiffness matrix using $\mathbb{V}_k^h$ and $\underline{\mathbb{V}}_k^h$ has a block decomposition, where $\underline{\underline{K}}^{\partial}$ refers to the usual stiffness matrix for the SBFEM approximations ((3.2.3) - Chapter 3) computed using $\mathbb{S}_k^h$ for the Poisson and $\underline{\mathbb{S}}_k^h$ for Elasticity problems. The block matrix $\underline{\underline{K}}^{b}$ is computed through the extra bubble functions in the spaces $\mathbb{B}_k^h$ for Poisson and $\underline{\mathbb{B}}_k^h$ for Elasticity problems.

4.1.1 Poisson problem

Let a Poisson problem be written as

$$\Delta u = f,\ u \in \Omega$$
$$\gamma(u) = u_D,\ \text{on } \partial\Omega$$

where f is the source term, $u_D \in H^{1/2}(\partial\Omega)$ is the Dirichlet boundary conditions and $\gamma : H^1(\Omega) \to H^{1/2}(\partial\Omega)$ is the usual trace operator. The variational formulation is written in an analogous procedure to Chapter 3 and defines the discrete form as the following.

The variational statement is expressed as: find $u_h(\underline{x}) \in \mathbb{V}_k^h \in H^1(\Omega)$.

$$\int_\Omega \nabla u_h \cdot \nabla v_h\ d\Omega = \int_\Omega f v_h\ d\Omega,\ \forall\ v_h \in \mathbb{V}_k^{h,0}$$
$$u_h|_{\partial\Omega} = \mathcal{I}_k^h u_D$$

where $\mathbb{V}_k^{h,0} = \mathbb{V}_k^h \cap H_0^1(\Omega)$.

4.1.2 Elasticity problem

Considering an isotropic material, the symmetry of the stress and strain tensor, the second model problem is the elasticity problem given by

$$\begin{aligned} -\underline{\nabla} \cdot \underline{\underline{\sigma}} &= \underline{f}, \text{ in } \Omega \\ \underline{\underline{\sigma}} &= \underline{\underline{D}}\ \underline{\underline{\epsilon}}(\underline{u}), \text{ in } \Omega \\ \underline{\gamma}(\underline{u}) &= \underline{u}_D, \text{ on } \Gamma. \end{aligned}$$

where $\underline{\underline{D}}$ is the second-order constitutive tensor, $\underline{\underline{\sigma}}$ and $\underline{\underline{\epsilon}}(\underline{u})$ are the usual stress and strain tensors defining the constitutive equation, $f \in [L^2(\Omega)]^2$ is the body force, $u_D \in \left[H^{1/2}(\Gamma)\right]^d$ is the Dirichlet boundary input, and $\underline{\gamma}(\underline{u})$ stating for the vector version of the trace operator in $[H^1(\Omega)]^d$. Moreover, $\underline{u}_D$ is assumed to be sufficiently smooth for the definition of the trace interpolant $\mathcal{I}_k^h \underline{u}_D$.

The strain vector is given by $\underline{\epsilon} = \{\epsilon_{11}, \epsilon_{22}, \epsilon_{33}, 2\epsilon_{12}, 2\epsilon_{23}, 2\epsilon_{13}\}^T$ where

$$\epsilon_{ij} = \frac{1}{2}\left(\frac{\partial u_i}{\partial x_j} + \frac{\partial u_j}{\partial x_i}\right),\ i, j = 1, ..., 3$$

and´

$$\underline{\underline{D}} = E(1+\nu)(1-2\nu)\begin{pmatrix} 1-\nu & \nu & \nu & 0 & 0 & 0 \\ \nu & 1-\nu & \nu & 0 & 0 & 0 \\ \nu & \nu & 1-\nu & 0 & 0 & 0 \\ 0 & 0 & 0 & \frac{1-2\nu}{2} & 0 & 0 \\ 0 & 0 & 0 & 0 & \frac{1-2\nu}{2} & 0 \\ 0 & 0 & 0 & 0 & 0 & \frac{1-2\nu}{2} \end{pmatrix},$$

For simplicity, only Dirichlet boundary conditions $u|_\Gamma = u_D$ are considered. The weak statement is obtained by replacing (4.1.2) in (4.1.2), multiplying it by a test function v, and applying the Divergence theorem. Thus, the variational statement is written as: Find $u_h \in \underline{\mathbb{V}}_k^h$ such that

$$\begin{aligned} \int_\Omega \underline{\underline{D}}\ \underline{\underline{\epsilon}}(\underline{u}_h) \cdot \underline{\underline{\epsilon}}(\underline{v}_h)\ d\Omega &= \int_\Omega \underline{f}\ \underline{v}_h\ d\Omega,\ \forall\ \underline{v} \in \underline{\mathbb{V}}_k^{0,h} \\ \underline{u}|_\Gamma &= \underline{\mathcal{I}}_k^h \underline{u}_D \end{aligned}$$

where $\underline{\mathbb{V}}_k^{0,h} = \underline{\mathbb{V}}_k^h \cap H_0^1(\Omega, \mathbb{R}^d)$.

4.2 SBFEM bubble spaces

4.2.1 Scalar bubble function space $\mathbb{B}_k^h(S)$

As remarked in the previous chapter, Duffy's functions $\phi \in \mathcal{D}_k(S)$ are represented by the expression

$$\phi(\underline{x}) = \hat{\rho}(\xi)\underline{N}_k^S(\underline{x}_b) \cdot \underline{a}, \tag{4.2.0}$$

in each sector $K \in \mathcal{P}^S$, where $\mathcal{P}^S = \cup_{K \in \mathcal{T}^S}$ is the conglomerate partitions $\mathcal{T}^S$ of S. These functions are represented in terms the local parametrizations $\underline{x}_b = F_L(\underline{\eta}) \in L$, and $\underline{x} = F_K(\xi, \underline{\eta}) \in K$.

Bubble functions in $\mathcal{D}_k^0(S)$ occur by taking radial components verifying $\hat{\rho}(\xi = 1) = 0$. For the current thesis, define subspaces $\mathbb{B}_k^h(S) \subset \mathcal{D}_k^0(S)$ by taking the following bubble functions:

1. Bubble shape functions $\varphi_{m,n} \in \mathcal{D}_{k,m}^{0,h}(S)$

$$\varphi_{m,n}(\underline{x}) = \hat{\rho}_m^b(\xi)\hat{N}_k^{n,S}(\underline{\eta}) \tag{4.2.0}$$

with polynomial radial components

$$\hat{\rho}_m^b(\xi) = \xi^{m-1} - \xi^m. \tag{4.2.0}$$

The space $\mathcal{D}_{k,m}^{0,h}(S)$ is a finite-dimensional subspace of bubble functions in $\mathcal{D}_{k,k}^h(S)$ (i.e. $\mathcal{D}_{k,m}^{0,h}(S) \subset \mathcal{D}_{k,k}^h(S)$). Thus, we have a finite-dimensional subspace

$$\text{span}\{\varphi_{m,n}; 0 \leq n < \mathcal{N}^S, 1 \leq m \leq k\} \quad \text{for all } k > 1 \tag{4.2.0}$$

For $k = 1$ the bubble function is a simple hat function given by $\varphi_{1,0} = (1 - \xi) \in \mathcal{D}_{k,m}^{0,h}(S)$.

Examples: Some examples of bubble functions in $\mathcal{D}_{k,m}^{0,h}(S)$ using polynomial radial components are illustrated in Fig. 4.1 for a square S-element subdivided into four triangles meeting at the center. The plots are for different polynomial degrees (b, r) used over the scaled boundary $b \leq 2$ and for the radial component $0 \leq r \leq 2$ are indicated.

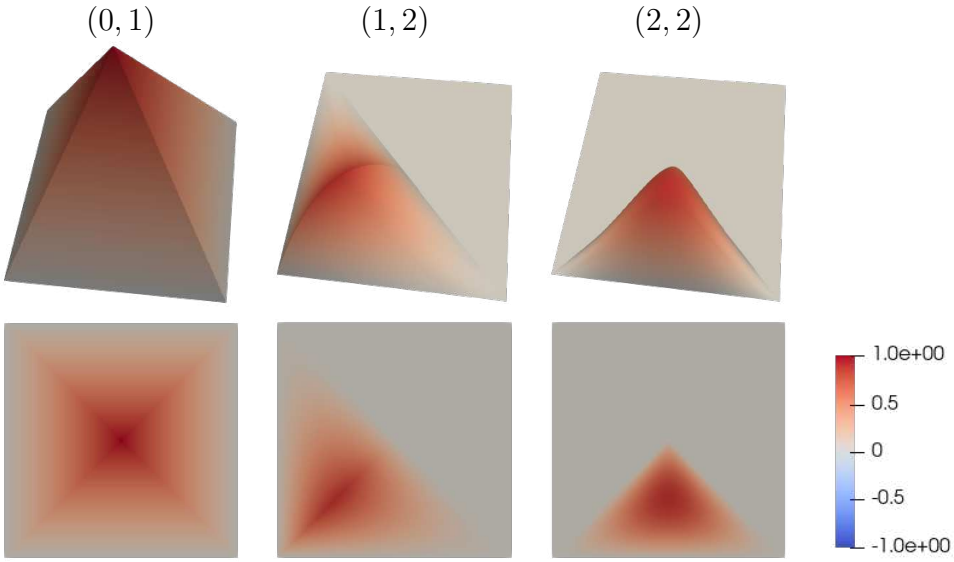

Figure 4.1: Quadrilateral S-element subdivided into four triangles meeting at the center: illustrations of bubble functions in $\mathbb{B}_2^h(S)$ with polynomial radial components; (b, r) indicates the polynomial degrees used over the scaled boundary b and for the radial component r.

2. Bubble shape functions $\varphi_i \in \mathcal{D}_k^{0,h}(S)$:

$$\varphi_i^b(\underline{x}) = \hat{\rho}_i^b(\xi)\underline{\hat{N}}_k^S(\underline{\eta}) \cdot \underline{A}_i, \tag{4.2.0}$$

where

$$\hat{\rho}_i^b(\xi) = \left(\xi^k - \xi^{\lambda_i - 0.5(d-2)}\right), \tag{4.2.0}$$

$\lambda_i, \underline{A}_i$ being pairs of eigenvalues and eigenvectors associated to the bubble-free SBFEM shape functions $\phi_i \in \mathbb{S}^h_k(S)$, for non-integer $\lambda_i - 0.5(d-2)$ exponents and integer exponents such that $\lambda_i - 0.5(d-2) > k$.

The idea is to add bubble shape functions in which the exponents ξ^{λ_i} are not included in $\mathcal{D}^{0,h}_{k,k}(S)$, and then compose the full approximation space.

Examples: Again, for the same square S-element subdivided into four triangles meeting at the center, bubble functions in $\mathbb{B}^h_2(S)$ associated to the non-integer eigenvalues $\lambda = 3.26599$ and $\lambda = 4.3589$ are plotted in Fig. 4.2. The associated SBFEM basis function in $\mathbb{S}^h_k(S)$ were plotted in Chapter 3 - Fig. 3.8.

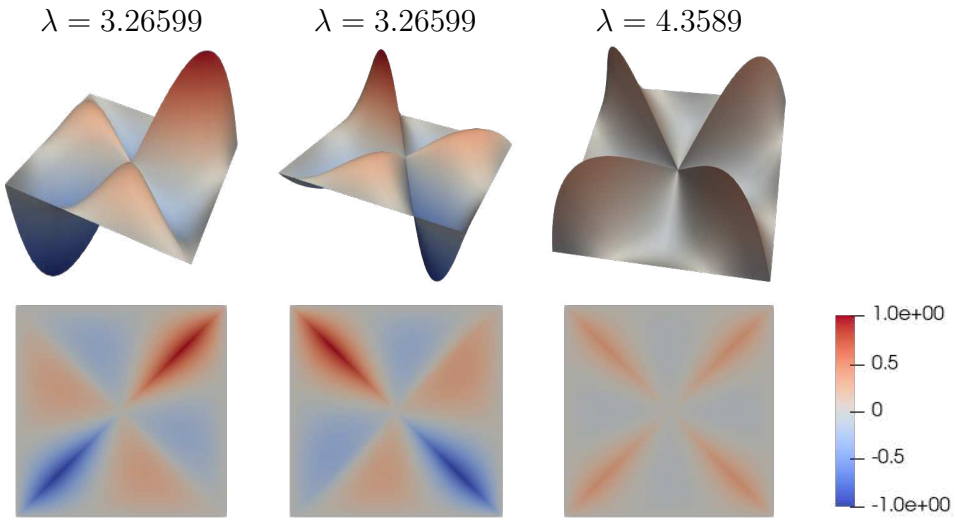

Figure 4.2: Quadrilateral S-element subdivided into four triangles: illustrations of some bubble scaling functions in $\mathbb{B}_2(S)$ associated to the non-integer eigenvalues $\lambda = 3.26599$ and $\lambda = 4.3589$.

4.2.2 Vector-valued bubble function space $\underline{\mathbb{B}}^h_k(S)$

Similar definitions hold for the vector-valued bubble spaces $\underline{\mathbb{B}}^h_k(S)$, recalling that now the boundary components should be spanned by vector-valued trace shape functions $\underline{\underline{N}}^S_k(\underline{x}_b)$. As highlighted in the previous chapter, vector-valued Duffy's functions $\underline{\phi} \in \underline{\mathcal{D}}_k(S)$ are such that

$$\underline{\phi}(\underline{x}) = \hat{\rho}(\xi)\underline{\underline{\hat{N}}}^S_k(\underline{\eta}) \cdot \underline{a}^e$$

We keep in $\underline{\mathbb{B}}^h_k(S)$ the functions in $\underline{\mathcal{D}}^0_k(S)$ with the radial polynomial components $\hat{\rho}_m$ as shown in Eqs. (1) and (2). So the following bubble functions $\varphi \in \underline{\mathbb{B}}^h_k \subset \underline{\mathcal{D}}_k(S)$ apply:

1. Bubble shape functions $\underline{\varphi}_{m,n} \in \underline{\mathcal{D}}^{0,h}_{k,m}(S)$

$$\underline{\varphi}_{m,n}(\underline{x}) = \hat{\rho}^b_m(\xi)\underline{\hat{N}}^{n,S}_k(\underline{\eta}) \tag{4.2.0}$$

with polynomial radial components where $\hat{\rho}^b_m(\xi) = \xi^{m-1} - \xi^m$ is the same of Eq. 2. Analogously to Eq. (1), we have a finite dimensional subspace $\text{span}\{\underline{\varphi}_{m,n}; 0 \le n < \mathcal{N}^{S^e}, 1 \le m \le k\}$ for $k > 1$. For $k = 1$ the bubble function is a hat function given by $\varphi_{1,0} = (1-\xi)\underline{\hat{N}}^S_0(\underline{\eta}) \in \underline{\mathcal{D}}^{0,h}_{k,m}(S)$.

2. Bubble shape functions $\underline{\varphi}_i \in \underline{\mathcal{D}}_k^{0,h}(S)$:

$$\underline{\varphi}_i(\underline{x}) = \hat{\rho}_i^{e,b}(\xi)\underline{\underline{N}}_k^S(\underline{x}_b) \cdot \underline{A}_i^e, \tag{4.2.0}$$

where

$$\hat{\rho}_i^{e,b}(\xi) = \left(\xi^k - \xi^{\lambda_i^e - 0.5(d-2)}\right), \tag{4.2.0}$$

$\lambda_i^e, \underline{A}_i^e$ being pairs of eigenvalues and eigenvectors associated to the bubble-free SBFEM shape functions $\phi_i \in \mathbb{S}_k^h(S)$, for non-integer $\lambda_i^e - 0.5(d-2)$ exponents and integer exponents such that $\lambda_i^e - 0.5(d-2) > k$. It is important to highlight that now the eigenvalues and eigenvectors $\lambda_i^e, \underline{A}_i^e$ refer to those obtained for the construction of vector-valued SBFEM shape functions of $\underline{\mathbb{S}}_k^h(S)$ used for elasticity problems.

4.3 Convergence analysis

The proof the optimal convergence rates of the proposed approximation is based on the premises:

i) $\mathcal{D}_{k,k}(S)$ is convergent;

ii) Duffy polynomial space $\mathcal{D}_{k,k}(S)$ is included in $\mathbb{V}_k(S)$.

Thus, $\mathbb{V}_k(S)$ is also convergent.

Premise i) is already proven in Chapter 3 - Proposition 3.3.2. This Chapter, it remains to prove the inclusion of premise ii).

Proposition 4.3.1. *Duffy's finite-dimensional space of scalar functions is included in the full SBFEM space* $\mathbb{V}_k^h(S)$. *In other words,* $\mathcal{D}_{k,k}^h(S) \subset \mathbb{V}_k^h(S)$, *where* $\mathbb{V}_k^h(S) = \mathbb{B}_k^h(S) \oplus \mathbb{S}_k^h(S)$.

Proof. It is clear that $\mathcal{D}_{k,k}^h(S) = \mathcal{D}_{k,k}^{\partial,h}(S) \oplus \mathcal{D}_{k,k}^{0,h}(S)$, where $\mathcal{D}_{k,k}^{\partial,h}(S) \subset \mathcal{D}_{k,k}^h(S)$ denotes the subspace with non-vanishing traces over the scaled boundary ∂S. As aforementioned $\mathcal{D}_{k,k}^{0,h}(S) = \text{span } \{\varphi_{m,n}; 1 \leq n \leq \mathcal{N}^S,\ 0 \leq m \leq k\} \subset \mathbb{V}_k^h(S)$. Thus, it remains to show that $\mathcal{D}_{k,k}^{\partial,h}(S) \subset \mathbb{V}_k^h(S)$ as well. In fact, since the eigenvectors $\underline{A}_i$ form a set of $\mathcal{N}^S$ linearly independent vectors, then

$$\mathcal{D}_{k,k}^{\partial,h}(S) = \text{span } \{\psi_{m,i}; 1 \leq i \leq \mathcal{N}^S,\ 0 \leq m \leq k\},$$

with basis functions of the form $\psi_{m,i} = \xi^m\, \underline{A}_i \cdot \underline{N}_k^S(\underline{x}_b)$. Let $\phi_i \in \mathbb{S}_k^h(S)$ be a bubble-free shape function associated to a pair of eigenvalues and eigenvectors λ_i and A_i such that $\lambda_i - 0.5(d-2) \leq k$ is non-integer or $\lambda_i - 0.5(d-2) > k$. Thus, $\psi_{m,i}$ is represented in the form

$$\begin{aligned}
\psi_{m,i} &= (\xi^m - \xi^k)\underline{A}_i \cdot \underline{N}_k^S(\underline{x}_b) + \phi_i - \phi_i \\
&= \left[(\xi^m - \xi^k)\underline{A}_i \cdot \underline{N}_k^S(\underline{x}_b) + \phi_i\right] + (\xi^k - \xi^{\lambda_i - 0.5(d-2)})\underline{A}_i \cdot \underline{N}_k^S(\underline{x}_b) \\
&= \left[(\xi^m - \xi^k)\underline{A}_i \cdot \underline{N}_k^S(\underline{x}_b) + \phi_i\right] + \varphi_i.
\end{aligned}$$

Consequently, $\psi_{m,i} \in \left[\mathcal{D}_{k,k}^{0,h}(S) + \mathbb{S}_k^h(S)\right] + \mathbb{B}_k^h(S) \subset \mathbb{V}_k^h(S)$. □

Proposition 4.3.2. *The finite-dimensional Duffy's space $\underline{\mathcal{D}}^h_{k,k}(S)$ is included in the SBFEM space $\underline{\mathbb{V}}^h_k(S)$. In other words, $\underline{\mathcal{D}}^h_{k,k}(S) \subset \underline{\mathbb{V}}^h_k(S)$, where $\underline{\mathbb{V}}^h_k(S) = \underline{\mathbb{B}}^h_k(S) \oplus \underline{\mathbb{S}}^h_k(S)$.*

Proof. The proof is analogous to Proposition 4.3.1. □

Theorem 4.3.1. *Let $\mathcal{T}^h = \{S\}$ be a family of polytopal S-elements partitions of Ω, $\mathbb{V}^h_k$ and $\mathcal{D}^h_{k,k}$ be the SBFEM and Duffy's polynomial spaces based on $\mathcal{T}^h$. Also, consider the projection-based interpolant $\Pi^1_k : H^1(S) \to \mathcal{D}^h_{k,k}$. Suppose the same trace interpolant is used in the definitions of $u^h \in \mathbb{V}^h_k$ and $\Pi^1_k(u) \in \mathcal{D}^h_{k,k}$, and the exact solution $u \in H^1$ of the model problem* (4.1.1) *is sufficiently regular for them to make sense. If $u^h \in \mathbb{V}^h_k$ is the associated Galerkin SBFEM approximation, then*

$$||u - u^h||_{H^1(\Omega)} \leq ||u - \Pi^1_k(u)||_{H^1(\Omega)} \leq ch^k|u|_{H^2},$$
$$||u - u^h||_{L^2(\Omega)} \leq ||u - \Pi^1_k(u)||_{L^2(\Omega)} \leq ch^{k+1}|u|_{H^2}.$$

Proof. Chapter 3 - Proposition 3.3.2, $\mathbb{P}_{k,k}(\mathcal{P}^h) \subset \mathcal{D}^h_{k,k}(\mathcal{P}^h) \subset H^1(\mathcal{P}^h)$. From Ern and Guermond (2013, Proposition 1.134), there exists a constant c such that

$$||u - \Pi^1_k(u)||_{H^1} \leq ch^k|u|_{H^2},$$

For the L^2-estimate, (ERN; GUERMOND, 2013, Theorem 3.18),

$$||u - \Pi^1_k(u)|| \leq ch^{k+1}|u|_{H^2}.$$

Using Propositions 4.3.1 and 4.3.2, i.e. $\mathcal{D}^h_{k,k} \subset \mathbb{V}^h_k$, and Galerkin orthogonality,

$$||u - u^h||_{H^1(\Omega)} \leq ||u - \Pi^1_k(u)||_{H^1(\Omega)},$$
$$||u - u^h||_{L^2(\Omega)} \leq ||u - \Pi^1_k(u)||_{L^2(\Omega)},$$

leading to (4.3.1) and (4.3.1). □

4.4 Computational implementation aspects

The algorithm to approximate PDEs using bubble functions requires just a small addition compared to a usual SBFEM code, such as the algorithm provided by Song (2018). The stiffness matrix related to the bubble functions, $\underline{\underline{K}}^b$ should be computed only if the source term does not vanish (see Algorithm 1) and its respective additional term u_b be considered in the post-processed solution. It means that the code structure does not need to be modified and the bubbles are incorporated in a separate method. This section shows how $\underline{\underline{K}}^b$ and $\underline{F}$ are computed.

Algorithm 1 SBFEM local problem

1: **for all** S in $\mathcal{T}^h$ **do**
2: Compute $\underline{\underline{E}}_0$, $\underline{\underline{E}}_1$, $\underline{\underline{E}}_2$ and solve the eigenvalue problem;
3: Compute $\underline{\underline{K}}^{\partial} = \underline{\underline{Q}}\ \underline{\underline{A}}^{-1}$;
4: **if** $f \neq 0$ **then**
Compute $\underline{\underline{K}}^b$ and $\underline{F}$;
5: **end if**
6: **end for**

The methods to compute $\underline{\underline{K}}^b$ and $\underline{F}$, as well as the post-processing was implemented in an open-source finite element library, NeoPZ[1] (DEVLOO, 1997). The high abstraction and its implementation in small blocks allowed reusability through inheritance and templates. NeoPZ was already performing simulations to approximate homogeneous PDEs using SBFEM. The code was extended to include the bubble functions without any modification of the "standard" code. Since the code is scalable due to the orthogonality, parallelization techniques can be implemented. For this thesis, local static condensations per element are performed to reduce the global DOF.

4.4.1 Stiffness matrix and force vector

Poisson Problem

Although the stiffness matrix for the SBFEM approximation is usually computed as $\underline{\underline{K}}^{\partial} = \underline{\underline{Q}}\ \underline{\underline{A}}^{-1}$, Chiong (2014) presents a different procedure to compute it. Let $\phi_i \in \mathbb{S}^h_k(S)$ be the SBFEM shape functions for a harmonic problem as defined in (4.2.1) and grouped in the vector form $\underline{\boldsymbol{\phi}} = [\phi_i]$ such that

$$\underline{\hat{\boldsymbol{\phi}}} = \underline{\hat{N}}^S_k(\underline{\eta})\underline{\underline{A}}\ \mathrm{diag}(\xi^{\underline{\lambda}-0.5(d-2)}),$$

in which $\underline{\lambda} = [\lambda_i]$ and $\mathrm{diag}(\xi^{\underline{\lambda}-0.5(d-2)})$ is a diagonal matrix. If $\underline{u}^S$ is the Dirichlet values of u over $\Gamma^{h,S}$, the approximate solution for a Poisson problem with null source term is given by $u = \underline{\boldsymbol{\phi}} \cdot \underline{c}$, where $\underline{c} = \underline{u}^S\underline{\underline{A}}^{-1}$, then

$$u = \underline{\hat{N}}^S_k(\underline{\eta})\underline{\underline{A}}\ \mathrm{diag}(\xi^{\underline{\lambda}-0.5(d-2)})\underline{\underline{A}}^{-T} \cdot \underline{u}^S$$

or also $u = \underline{\boldsymbol{\Phi}} \cdot \underline{u}^S$, where

$$\underline{\hat{\boldsymbol{\Phi}}} = \underline{\hat{N}}^S_k(\underline{\eta})\underline{\underline{A}}\ \mathrm{diag}(\xi^{\underline{\lambda}-0.5(d-2)})\underline{\underline{A}}^{-T} \tag{4.4.0}$$

The stiffness matrix of a Poisson problem is computed through the relationship

$$\underline{\underline{K}}^{\partial} = \int_S \nabla\underline{\hat{\boldsymbol{\Phi}}}_i^T \nabla\underline{\hat{\boldsymbol{\Phi}}}_j\ dS \tag{4.4.0}$$

Chiong (2014) expanded the integral above, obtaining a relationship for $\underline{\underline{K}}^{\partial}$ as

$$\underline{\underline{K}}^{\partial} = \underline{\underline{A}}^{-1}\underline{\underline{K}}^{\partial,0}\underline{\underline{A}}_j^{-T} \tag{4.4.0}$$

where

$$\begin{aligned}\underline{\underline{K}}^{\partial,0} = \int_0^1\ & \xi^{d-1}\underline{\underline{\hat{\rho}}}'(\xi)\underline{\underline{A}}^T\underline{\underline{E}}_0\underline{\underline{A}}\ \underline{\underline{\hat{\rho}}}'(\xi) + \xi^{d-2}\underline{\underline{\hat{\rho}}}'(\xi)\underline{\underline{A}}^T\underline{\underline{E}}_1\ \underline{\underline{A}}\ \underline{\underline{\hat{\rho}}}(\xi) \\ +\ & \xi^{d-2}\underline{\underline{\hat{\rho}}}(\xi)\underline{\underline{A}}^T\underline{\underline{E}}_1^T\underline{\underline{A}}\ \underline{\underline{\hat{\rho}}}'(\xi) + \xi^{d-3}\underline{\underline{\hat{\rho}}}(\xi)\underline{\underline{A}}^T\underline{\underline{E}}_2\ \underline{\underline{A}}\ \underline{\underline{\hat{\rho}}}(\xi)\ d\xi.\end{aligned}$$

and $\underline{\underline{\hat{\rho}}}(\xi) = \mathrm{diag}(\xi^{\underline{\lambda}-0.5(d-2)})$. Our goal is to write an equation to compute the stiffness matrix for the bubble function, K^b_{ij}, similar to (3.2.3).

[1] https://github.com/labmec/neopz

The bubble functions can be written in a similar way to the usual SBFEM basis functions $\phi(\underline{x}) = \hat{\rho}(\xi)\underline{N}_k^S(\underline{x}_b) \cdot \underline{A}_i$, as follows

$$\varphi(\underline{x}) = \underline{\hat{N}}_k^S(\underline{\eta})\hat{\rho}^b(\xi) \cdot \underline{A}^b$$

where $\hat{\rho}^b(\xi)$ can be either

$$\begin{aligned}\hat{\rho}_m^b(\xi) &= \xi^m - \xi^{m-1},\ \forall\ 1 < m \leq k,\ \text{or,}\\ \hat{\rho}_i^b(\xi) &= \xi^k - \xi^{\lambda_i - 0.5(d-2)},\end{aligned}$$

for all non-integer $\lambda_i - 0.5(d-2)$ or integer exponents such that $\lambda_i - 0.5(d-2) > k$. $\underline{A}^b$ is a vector of multiplier coefficients of $\underline{\hat{N}}_k^S(\underline{\eta})$ such that $\underline{\varphi}$ can be either Eqs. (1) or (2). In other words, $\underline{A}^b = \underline{A}_i$ when $\hat{\rho}^b(\xi) = \hat{\rho}_i^b(\xi)$ and $\underline{A}^b$ is such that $\underline{A}^b \cdot \underline{\hat{N}}_k^S(\underline{\eta}) = \hat{N}_{k,i}^S(\underline{\eta})$ for $\hat{\rho}^b(\xi) = \hat{\rho}_m^b(\xi)$.

Notice that $\hat{\rho}^b(\xi)$ can be written as an inner product of two vectors as

$$\hat{\rho}_m^b(\xi) = \begin{pmatrix}\xi^m & \xi^{m-1}\end{pmatrix}\begin{pmatrix}1\\-1\end{pmatrix}, \quad \hat{\rho}_i^b(\xi) = \begin{pmatrix}\xi^k & \xi^{\lambda_i - 0.5(d-2)}\end{pmatrix}\begin{pmatrix}1\\-1\end{pmatrix},$$

Finally, grouping all bubble functions in a vector leads to

$$\underline{\hat{\mathbf{\Phi}}}^b(\xi) = \underline{\hat{N}}_k^S(\underline{\eta})\underline{\underline{A}}^b\ \underline{\underline{\hat{\rho}}}^b(\xi)\ \underline{\underline{T}}^T, \tag{4.4.-1}$$

where $\underline{\underline{A}}^b$, $\underline{\underline{\hat{\rho}}}^b(\xi)$, and $\underline{\underline{T}}$ gathers respectively $\underline{A}^b$, $\underline{\hat{\rho}}^b(\xi)$, and $\underline{t}$.

Similarly to Eq. (3.2.3), the components of the matrix $\underline{\underline{K}}^b$ for a S-element through the relationship are computed

$$\underline{\underline{K}}^b = \int_S \nabla\underline{\mathbf{\Phi}}_i^{bT}\nabla\underline{\mathbf{\Phi}}_j^b\ dS.$$

Taking advantage of the similarity between the SBFEM basis functions Eq. (3.2.3) and the bubble functions, one can write

$$\underline{\underline{K}}^b = \underline{\underline{T}}\ \underline{\underline{K}}_0^b\ \underline{\underline{T}}^T$$

where

$$\begin{aligned}\underline{\underline{K}}_0^b = \int_0^1\ &\xi^{d-1}\underline{\underline{\hat{\rho}}}^{b\prime}(\xi)\underline{\underline{A}}_b^T\underline{\underline{E}}_0\underline{\underline{A}}_b\ \underline{\underline{\hat{\rho}}}^{b\prime}(\xi) + \xi^{d-2}\underline{\underline{\hat{\rho}}}^{b\prime}(\xi)\underline{\underline{A}}_b^T\underline{\underline{E}}_1\ \underline{\underline{A}}_b\ \underline{\underline{\hat{\rho}}}^b(\xi)\\ +\ &\xi^{d-2}\underline{\underline{\hat{\rho}}}^b(\xi)\underline{\underline{A}}_b^T\underline{\underline{E}}_1^T\underline{\underline{A}}_b\ \underline{\underline{\hat{\rho}}}^{b\prime}(\xi) + \xi^{d-3}\underline{\underline{\hat{\rho}}}^b(\xi)\underline{\underline{A}}_b^T\underline{\underline{E}}_2\ \underline{\underline{A}}_b\ \underline{\underline{\hat{\rho}}}^b(\xi)\ d\xi.\end{aligned}$$

Instead of performing integration by parts, the integral Eq. (3.2.3) is solved analytically.

The force vector is computed numerically accordingly to the expression

$$\underline{F}^\partial = \int_S f\underline{\mathbf{\Phi}}_i\ dS, \quad \underline{F}^b = \int_S f\underline{\mathbf{\Phi}}_i^b\ dS,$$

where $\underline{F}^\partial$ is the contribution of the SBFEM basis functions and $\underline{F}^b$ is composed of the bubble functions, then,

$$\underline{F} = \begin{Bmatrix}\underline{F}^\partial\\ \underline{F}^b\end{Bmatrix}. \tag{4.4.-2}$$

Elasticity

This procedure can be easily extended for Elasticity problems since similar equations are obtained. The approximated solution for null body loads is given by

$$\underline{u}^{\partial} = \underline{\underline{\mathbf{\Phi}}}^{e} \cdot \underline{u}^{S} \tag{4.4.-2}$$

where

$$\underline{\underline{\hat{\mathbf{\Phi}}}}^{e} = \underline{\underline{\hat{N}}}_{k}^{S}(\underline{\eta})\underline{\underline{A}}^{e}\mathrm{diag}(\xi^{\underline{\lambda}^{e}-0.5(d-2)})\underline{\underline{A}}^{-T} \tag{4.4.-2}$$

and the component of the approximation involving the bubble function

$$\underline{u}^{b} = \underline{\underline{\mathbf{\Phi}}}^{b,e} \cdot \underline{u}^{S} \tag{4.4.-2}$$

where

$$\underline{\underline{\hat{\mathbf{\Phi}}}}^{b,e} = \underline{\underline{\hat{N}}}_{k}^{S}(\underline{\eta})\underline{\underline{A}}^{b,e}\underline{\underline{\hat{\rho}}}^{b,e}(\xi)\underline{\underline{T}}^{e-T} \tag{4.4.-2}$$

The main differences between $\underline{\underline{\mathbf{\Phi}}}^{b,e}$ and $\underline{\mathbf{\Phi}}^{b}$ (Eqs. (3.2.3) and (3.2.3)) is the eigenvalues and eigenvectors utilized to compose the bubbles and the dimension of the function space.

Knowing that the stiffness matrix for the isotropic Elastic problem is given by

$$\underline{\underline{K}}^{\partial} = \int_{S} \left[\underline{\underline{D}}\underline{\epsilon}(\underline{\underline{\mathbf{\Phi}}}_{i}^{e})\right]^{T} \underline{\epsilon}(\underline{\underline{\mathbf{\Phi}}}_{j}^{e})\ dS$$
$$\underline{\underline{K}}^{b} = \int_{S} \left[\underline{\underline{D}}\underline{\epsilon}(\underline{\underline{\mathbf{\Phi}}}_{i}^{b,e})\right]^{T} \underline{\epsilon}(\underline{\underline{\mathbf{\Phi}}}_{j}^{b,e})\ dS$$

Taking advantage of the similarities between the expressions for $\underline{\epsilon}(\underline{\underline{\mathbf{\Phi}}}_{i}^{e})$ and $\nabla\underline{\mathbf{\Phi}}_{i}$ (see Table 3.4 in Chapter 3), the stiffness matrix can be written in an analogous way to (3.2.3) as

$$\underline{\underline{K}}^{b,e} = \underline{\underline{T}}^{e}\underline{\underline{K}}_{0}^{b,e}\underline{\underline{T}}^{eT} \tag{4.4.-2}$$

where

$$\begin{aligned}\underline{\underline{K}}_{0}^{b,e} = \int_{0}^{1}\ & \xi^{d-1}\underline{\underline{\hat{\rho}}}^{b'}(\xi)\underline{\underline{A}}_{b}^{eT}\underline{\underline{E}}_{0}^{e}\underline{\underline{A}}_{b}^{e}\ \underline{\underline{\hat{\rho}}}^{b'}(\xi) + \xi^{d-2}\underline{\underline{\hat{\rho}}}^{b'}(\xi)\underline{\underline{A}}_{b}^{eT}\underline{\underline{E}}_{1}^{e}\ \underline{\underline{A}}_{b}^{e}\ \underline{\underline{\hat{\rho}}}^{b}(\xi) \\ +\ & \xi^{d-2}\underline{\underline{\hat{\rho}}}^{b}(\xi)\underline{\underline{A}}_{b}^{eT}\underline{\underline{E}}_{1}^{eT}\underline{\underline{A}}_{b}^{e}\ \underline{\underline{\hat{\rho}}}^{b'}(\xi) + \xi^{d-3}\underline{\underline{\hat{\rho}}}^{b}(\xi)\underline{\underline{A}}_{b}^{eT}\underline{\underline{E}}_{2}\underline{\underline{A}}_{b}^{e}\ \underline{\underline{\hat{\rho}}}^{b}(\xi)\ d\xi.\end{aligned}$$

The force vector is computed numerically accordingly to the expression

$$\underline{F}^{\partial} = \int_{S} \underline{\underline{\mathbf{\Phi}}}_{i}^{e}\underline{f}\ dS, \quad \underline{F}^{b} = \int_{S} \underline{\underline{\mathbf{\Phi}}}_{i}^{b^{b,e}}\underline{f}\ dS,$$

where $\underline{F}^{\partial}$ is the contribution of the SBFEM basis functions and $\underline{F}^{b}$ is composed of the bubble functions, then,

$$\underline{F} = \begin{Bmatrix}\underline{F}^{\partial} \\ \underline{F}^{b}\end{Bmatrix}. \tag{4.4.-3}$$

4.4.2 Remark: High-order problems

In a few situations, the eigenvalue decomposition shown in Chapter 3, Section 3.2.2., imposes numerical challenges. As already documented by Song (2018), the eigenvalue decomposition will lead to loss of precision when repeated eigenvalues and nearly parallel eigenvectors exist, and the matrix is not diagonalizable. In practical cases, this issue

happens when the number of DOF of an S-element is large, such as in high-order analysis or 3D examples.

As an alternative to overcome this issue, Song (2018) suggests using Schur decomposition to write the SBFEM basis functions. However, this chapter presents a different approach. For high-order 2D analysis and 3D analysis in Galerkin SBFEM approximations, very small imaginary parts of eigenvalues ($\approx 10^{-12}$) are observed, and for these cases, the following procedure can be applied.

Proposition 4.4.1. *Denote $\underline{A}_i + i\underline{A}_{i,I}$ as the complex eigenvector and $\lambda_i = \gamma + i\zeta$ as the complex eigenvalue, and consider also its conjugate pair ($\underline{A}_i - i\underline{A}_{i,I}$ and $\gamma - i\zeta$). If ζ is sufficiently small (abs$(\zeta) \leq 10^{-12}$), the bubble functions are written as*

$$\psi_0 = (\xi^\gamma - \xi^k)\underline{A}_i$$
$$\psi_1 = (\xi^\gamma - \xi^k)\underline{A}_{i,I}.$$

Proof. The basis function for this eigenvalue can be written as

$$\begin{aligned}\left(\underline{A}_i + i\underline{A}_{i,I}\right)\xi^{\gamma+i\zeta} &= \left(\underline{v}_i + i\underline{A}_{i,I}\right)\xi^\gamma\xi^{i\zeta} \\ &= (\underline{A}_i + i\underline{A}_{i,I})\xi^\gamma e^{i\zeta\ln\xi} \\ &= (\underline{A}_i + i\underline{A}_{i,I})\xi^\gamma(\cos(\zeta\ln\xi) + i\sin(\zeta\ln\xi)) \\ &= \xi^\gamma(\underline{A}_i\cos(\zeta\ln\xi) - \underline{A}_{i,I}\sin(\zeta\ln\xi)) + i\xi^\gamma(\underline{A}_i\sin(\zeta\ln\xi) + \underline{A}_{i,I}\cos(\zeta\ln\xi))\end{aligned}$$

Analogously,

$$\left(\underline{A}_i - i\underline{A}_{i,I}\right)\xi^{\gamma-i\zeta} = \xi^\gamma(\underline{A}_i\cos(\zeta\ln\xi) - \underline{A}_{i,I}\sin(\zeta\ln\xi)) - i\xi^\gamma(\underline{A}_i\sin(\zeta\ln\xi) + \underline{A}_{i,I}\cos(\zeta\ln\xi))$$

If we want to match both vectors to real vector-values on the boundary (i.e. $\xi \equiv 1$) and imaginary values sufficiently small (i.e. $\zeta \approx 0$), it follows that the real basis functions are $\xi^\gamma(\underline{A}_i\cos(\beta\ln\xi) - \underline{A}_{i,I}\sin(\beta\ln\xi)) = \underline{A}_i$ and $\xi^\gamma(\underline{A}_i\sin\zeta + \underline{A}_{i,I}\cos\zeta) = \underline{A}_{i,I}$. □

4.5 Numerical tests

In this section, four numerical tests illustrate numerically the optimal rates of convergence obtained using the enrichment proposed in this paper. The first numerical example is a verification test in a 2D domain, followed by the simulation of a heat flow and a 3D Poisson problem. The last two examples are Elasticity problems - 2D and 3D.

4.5.1 Poisson problem

Example 1 - Two-dimensional single element

The first test is a 2D Poisson problem given by

$$\Delta u = 2x + 2x^2 + 20x^3 + 2y + 2y^2 + 20y^3$$

with Dirichlet boundary conditions in a domain $\Omega = [-1, 1] \times [-1, 1]$. The analytical solution is expressed as

$$u(\underline{x}) = x^5 + y^5 + x^2y^2 + x^2y + xy^2 + 1, \tag{4.5.0}$$

For a polynomial source term, it would be intuitive to enrich the bubble-free space $\mathbb{S}_k^h$ with only polynomial bubbles. The goal of this test is to show that if only functions of Duffy's bubble subspace enrich the bubble-free space $\mathbb{S}_k^h$, suboptimal rates of convergence are obtained. Additionally, knowing that the solution can be divided into a boundary term and a domain term, this test aims to verify the influence of each error component (the error related to the boundary approximation and the error associated with the bubbles functions) and analyze how they affect the rate of convergence.

To illustrate numerically the lack of convergence when the SBFEM bubble-free space is enriched with only polynomial bubbles, two approximations are compared:

1. Using polynomial bubble enrichment: $\mathbb{S}_k^h + \mathcal{D}_{k,k}^{0,h}(S)$

2. Using the full bubble space: $\mathbb{S}_k^h + \mathbb{B}_k^h(S)$

For this first example, only a skeleton refinement is performed over a single S-element (see Fig. 4.3 (i)). The domain is composed of a single element S-element refined three times over $\Gamma^{h,S}$, dividing the skeleton into $n = 2^\ell,\ \ell = 0, ..., 3$ elements of characteristic width $h = 2/2^\ell$.

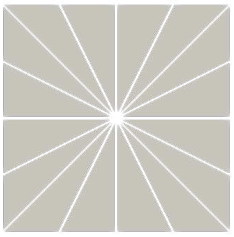

Figure 4.3: Example 1: Partition of the domain using a single S-element - $\mathcal{T}^h = \{S\}$, and a skeleton refinement for $h = 2/2^n,\ n = 2$.

The first sequence of plots considers an enrichment using only polynomial bubbles $\mathbb{S}_k^h(S) \oplus \mathcal{D}_{k,k_b}^0(S)$. The trace polynomial order varies from $k = 1$ to $k = 5$. For each trace approximation, two internal polynomial orders were adopted, namely $k_b = 5, 6$. Fig. 4.4 illustrates graphically the energy and L^2 error histories for the $\mathbb{S}_k^h(S) \oplus \mathcal{D}_{k_b}^{0,h}(S)$, for $k_b = 5, 6$, versus $h = 2/2^\ell,\ \ell = 0, ..., 3$, where ℓ is the refinement level at the element's skeleton. For an internal approximation order equal to the order of the analytical solution $u(\underline{x})$, i.e. $k_b = 5$, no convergence was found and the analytical solution was not recovered for $k = k_b = 5$. The lack of convergence occurs because the eigenvalue bubbles are required to compensate the radial extensions ξ^{λ_i} from the SBFEM bubble-free approximation and then compose a polynomial approximation. Even increasing the internal polynomial order to $k_b = 6$, there is no improvement in the error values. In both cases, the approximation error stagnates at only 1.3E-1 for the energy and 5.9E-3 for the L^2-norm.

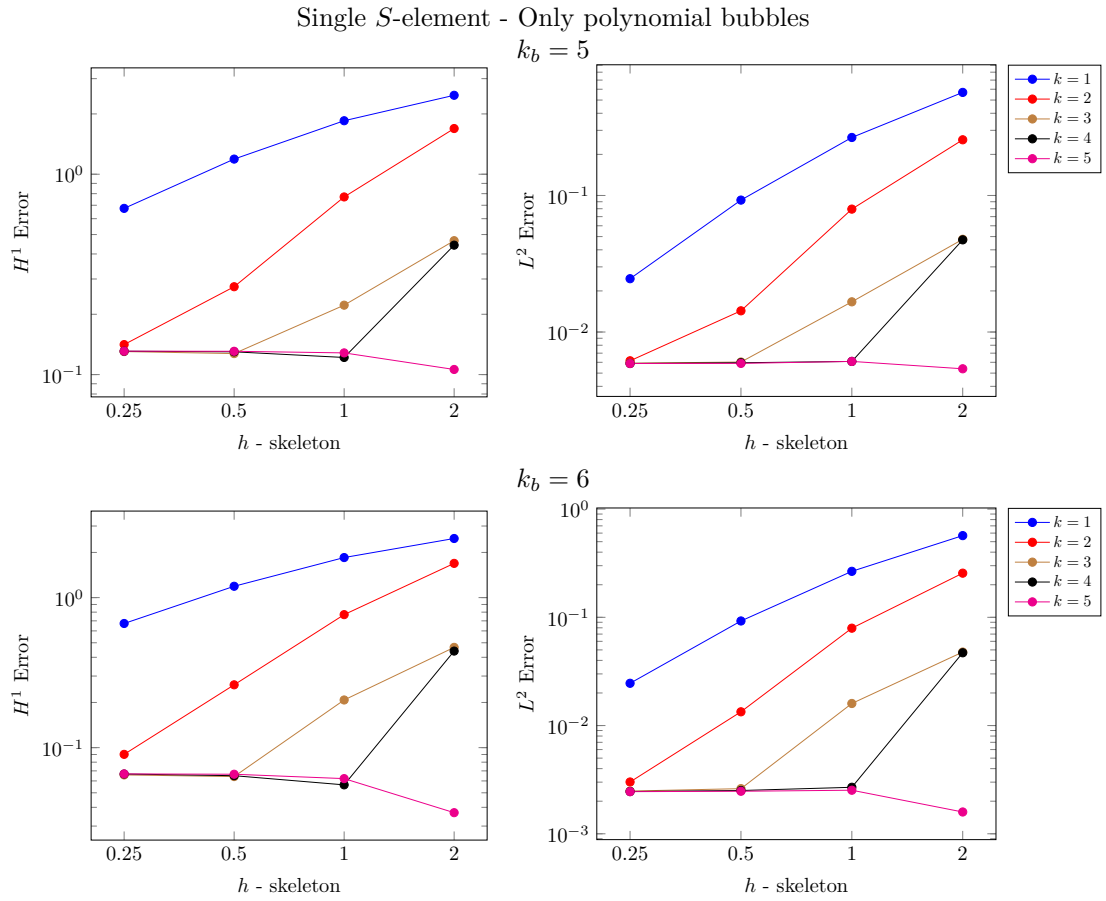

Figure 4.4: Verification Test - Energy and L^2 SBFEM interpolation errors based in a single S-element for $\mathcal{D}^{0,h}_{k,k_b}(S)$, $k = 1, ..., 5$, and $k_b = 5$ (top) and $k_b = 6$ (bottom) versus $h = 2/2^n,\ n = 0, ..., 3$.

In the next sequence of plots, shown in Fig. 4.5, the SBFEM bubble space $\mathbb{B}^h_{k_b}(S)$ approximates the analytical solution using for three different bubble polynomial orders $k_b = 4, 5, 6$. Recall that not only polynomial bubbles up to $k_b = 6$ are applied but also the bubbles based on the eigenvalues and eigenvectors of the harmonic problem. No convergence is found for $k_b = 4$, whilst optimal rates of convergence and the analytical solution are recovered for $k_b = 5, 6$, and , as illustrated in Fig 4.5. It means that the error is bounded by the bubble interpolation when a poor internal approximation is used, i.e. lower than the approximation of the analytical solution. In this case, the error stagnates in 3.8E-2 and 2.8E-3 for the energy and L^2-norm, respectively - just a little lower than the previous test using only polynomial bubbles.

The optimal rates of convergence are recovered if the internal polynomial order is kept at least equal to the polynomial order of the analytical solution. Notice that, even increasing the internal polynomial order to $k_b = 6$, the numerical result does not change. In these cases, the error is bounded by the skeleton's trace space, which has FE convergence properties. For $k = 5$ and either $k_b = 5$ or 6, the last two points present numerical instabilities due to the growth of the eigenvalue problem, which leads to complex eigenvalues that start to affect the approximated solution with bubbles. Song (2018) documented these numerical issues and suggests using the Schur decomposition instead of the usual eigenvalue decomposition to recover only real pairs of eigenvalues/eigenvectors. These graphs show that, for a single element, the bubble function approximation must be chosen as high as necessary to make the error be bounded by the skeleton's approximation.

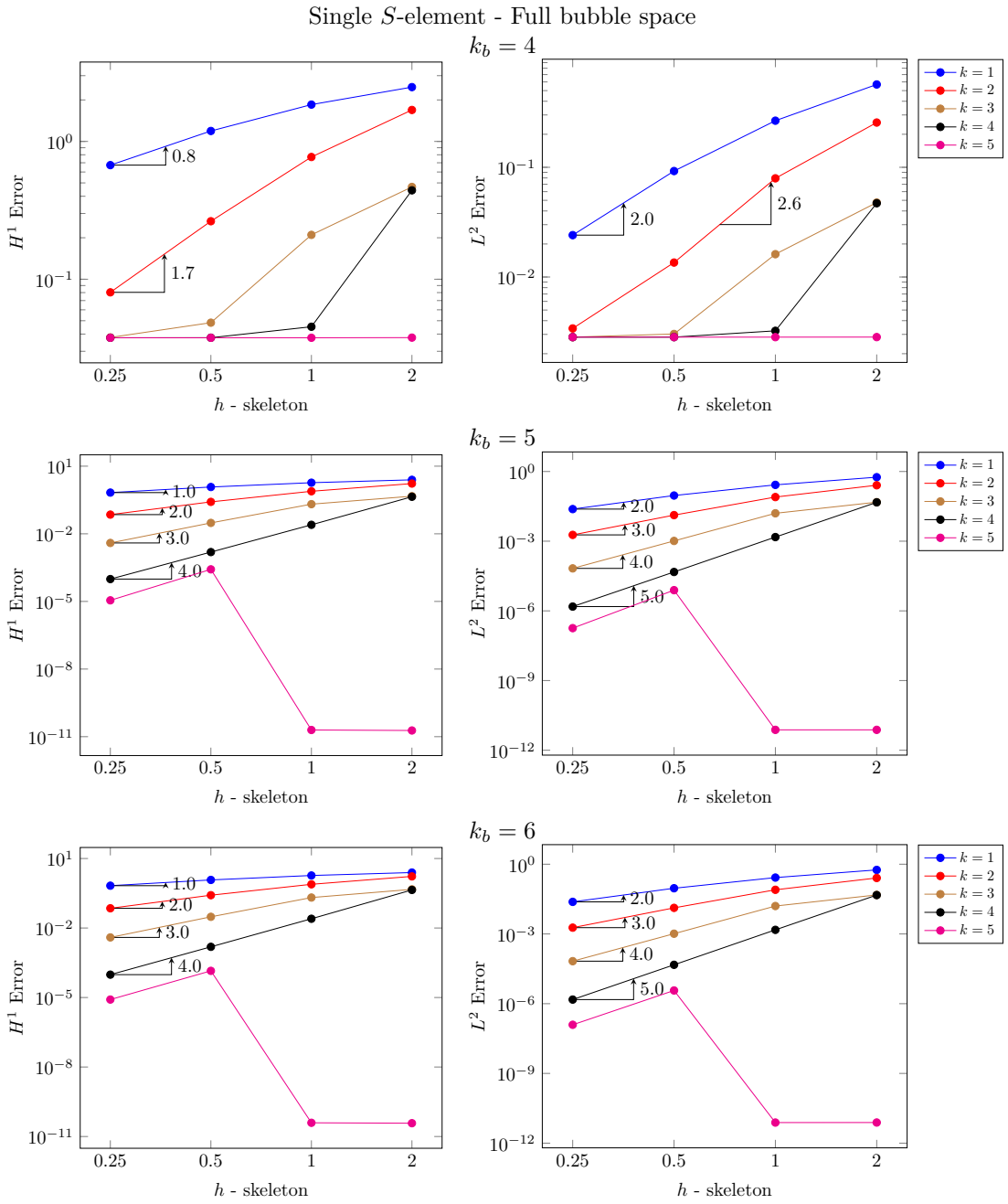

Figure 4.5: Verification Test - Energy and L^2 SBFEM interpolation errors based in a single S element for the full SBFEM bubble space $\mathbb{B}^h_{k_b}(S)$ considering $k_b = 4, 5$, and 6, and a trace space $\Lambda^{h,S}_k$, for $h = 2/2^\ell$, $\ell = 0, 1, 2$ and $k = 1, ..., 5$.

Example 2: Two-dimensional domain refinement

The analytical solution of the previous two-dimensional Poisson problem (Eq. (1)) is approximated, but now a domain refinement is performed instead, as illustrated in Fig. 4.6. The domain $\Omega = [-1, 1] \times [-1, 1]$ is discretized with $n \times n$ S-elements, $n = 2/2^\ell$, refined three times, i.e. $\ell = 0, ..., 3$. The approximated solution is composed of shape functions in the following approximation spaces:

1. $\mathbb{S}^h_k(S) \oplus \mathcal{D}^{0,h}_{k_b}(S)$, for $k = k_b = 1, ..., 5$, and
2. $\mathbb{S}^h_k(S) \oplus \mathbb{B}^h_k(S)$, for $k = k_b = 1, ..., 5$.

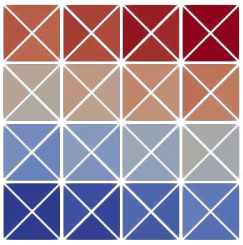

Figure 4.6: Example 1: Partition of the domain using a $n \times n$ S-element and characteristic width $h = 2/2^n,\ n = 2$.

The energy and L^2 errors are plotted versus the characteristic size h, in Fig. 4.7, for the Galerkin SBFEM solutions using $\mathcal{D}^{0,h}_{k,k}(S)$ and $\mathbb{B}^k_h(S)$. As already expected, using only the polynomial Duffy bubble functions, the resulting approximation space leads to sub-optimal rates of convergence - equal to 1 for the energy norm and 2 for the L^2 one, regardless of the approximation order considered. On the other hand, using the SBFEM bubble space, optimal rates of convergence are obtained as predicted theoretically, and numerically null error values are achieved for $k = 5$, the same polynomial order of the analytical solution. Notice that, using the SBFEM Galerkin approximation, optimal rates of convergence are recovered just by keeping the internal polynomial order equal to the external one instead of fixing $k_b = 5$. Moreover, instead of solving one big eigenvalue system, as in the skeleton's refinement, several small eigenvalue problems are solved, avoiding numerical instabilities.

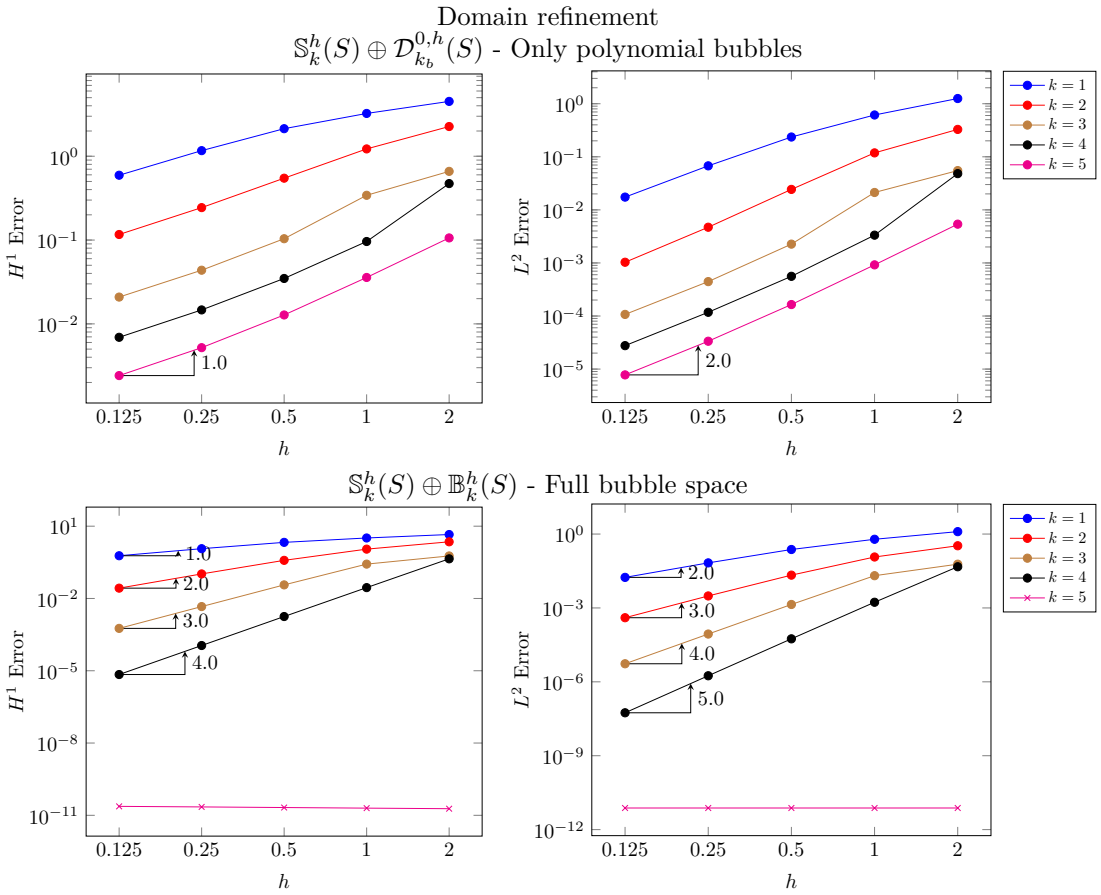

Figure 4.7: Verification test - Energy and L^2 errors versus $h = 2/2^\ell,\ \ell = 0, ..., 4$ for $k = k_b = 1, ..., 5$ using the uniform mesh of square S-elements $2^\ell \times 2^\ell,\ \ell = 0, ..., 4$ for $\mathcal{D}^{0,h}_{k,k}(S)$ and $\mathbb{B}^h_k$.

Example 3: A heat flow

Consider a parabolic PDE, for instance a heat flow, in a domain $\Omega = [-1,1] \times [-1,1]$ with null Dirichlet boundary conditions, given by

$$\begin{aligned} \frac{\partial u}{\partial t} - \Delta u &= 0 \quad \underline{x} \in \Omega \\ u(\underline{x}, t=0) &= \sin(\pi x_1)\sin(\pi x_2) \\ u(\underline{x} = \mathbf{s}, t) &= 0, \ \mathbf{s} \in \partial\Omega, \end{aligned}$$

The analytical solution of this equation is given by:

$$u(\underline{x}, t) = \sin(\pi x_1)\sin(\pi x_2)e^{-2\pi^2 t}.$$

We perform this simulation using a very small timestep, $\Delta t = 10^{-4}$ from $t = 0s$ to $t = 1s$, and evaluate three configurations, namely: without bubbles $\mathbb{S}_k^h$, with polynomial bubbles $\mathbb{S}_k^h \oplus \mathcal{D}_k^{0,h}$, and with the full bubble space $\mathbb{S}_k^h + \mathbb{B}_k^h$. For the simulation without bubbles, the mass matrix is computed and updated for each time step. The domain is partitioned in uniform meshes of quadrilateral S-elements with four refinement levels and $h = 2^{-\ell}, \ell = 1, ..., 4$ as well as in Example 2 (see Fig. 4.6), using polynomial orders $1 \leq k \leq 3$.

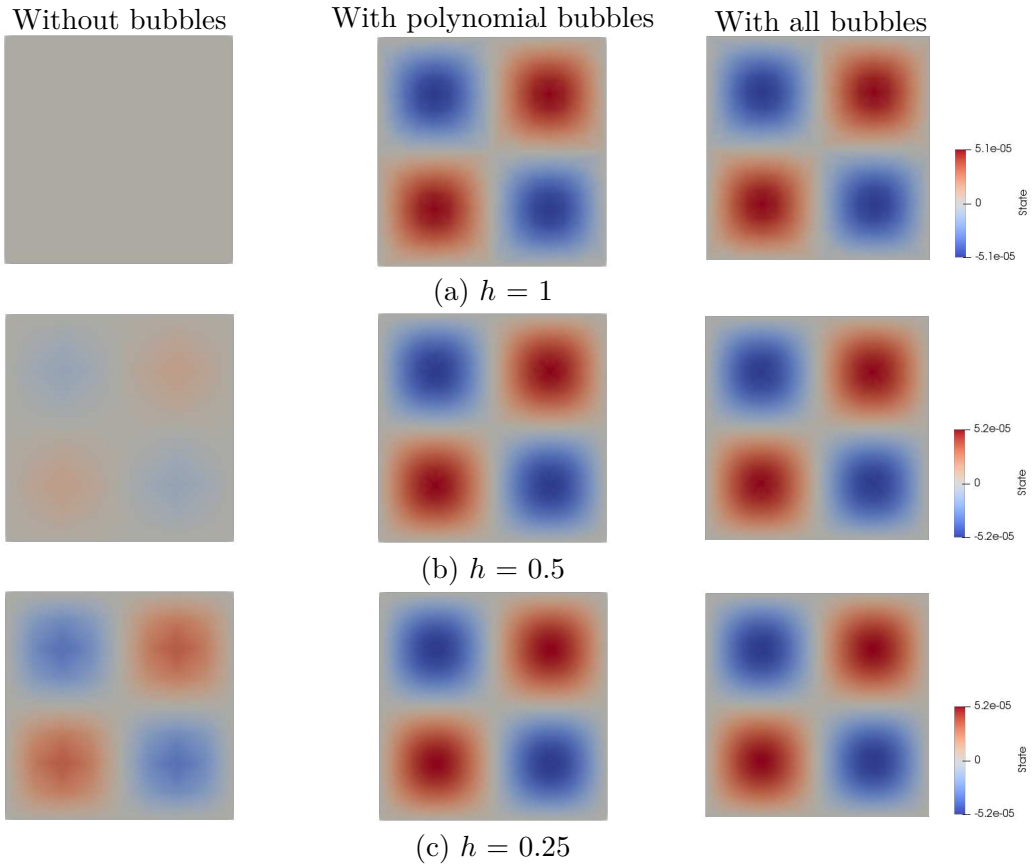

Figure 4.8: Example 3 - Post-processing comparison between Garlekin SBFEM approximations: without bubbles (left), with polynomial bubbles (middle), and with the full bubble space (right) - in uniform partitions $\mathcal{T}^{h,S} = \{S\}$ of quadrilateral S-elements using three refinement steps: $h = 2^{1-\ell}$, $\ell = 1, 2, 3$, for $k = k_b = 3$ and $t = 0.5s$.

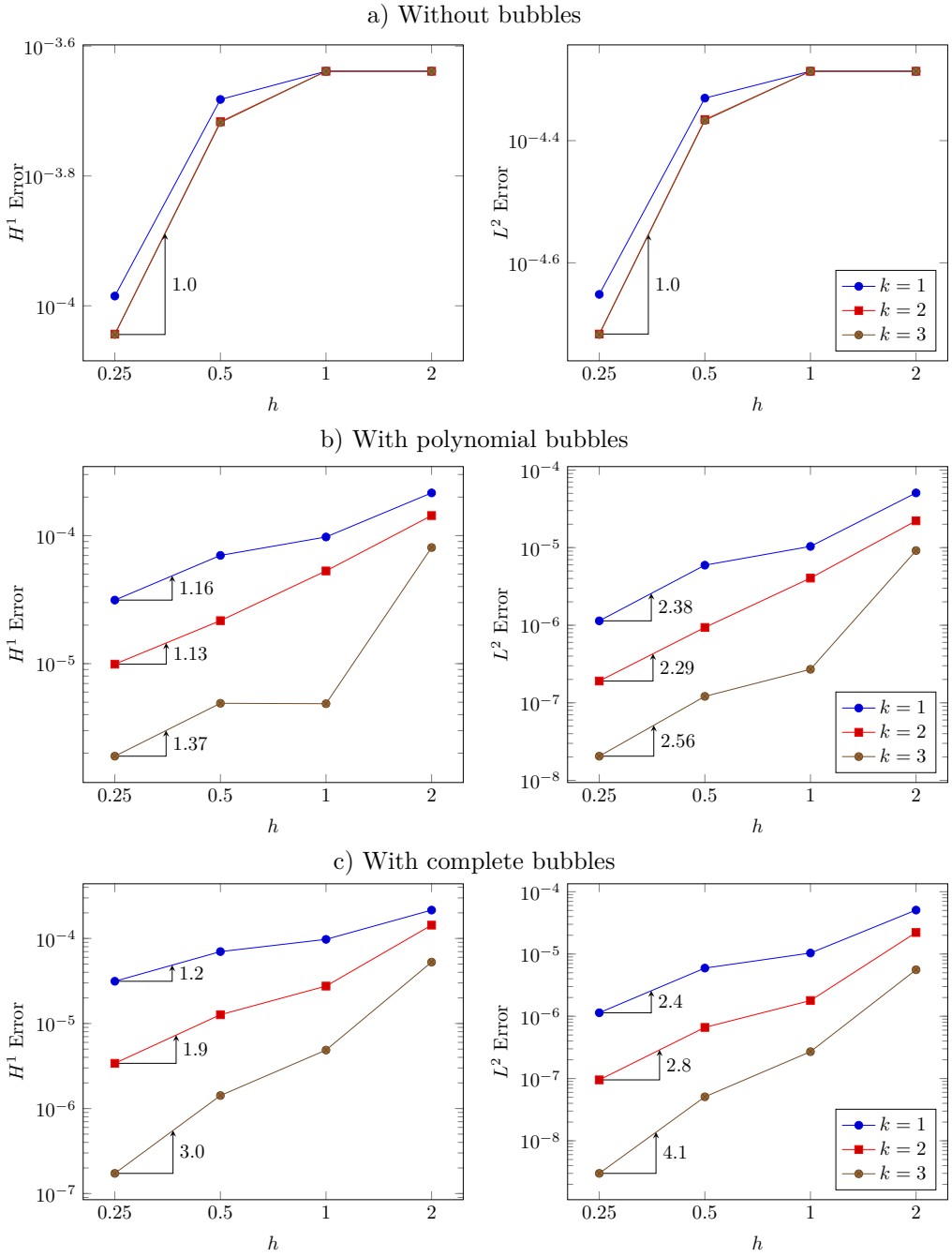

Figure 4.9: Example 3 - Energy and L^2 errors versus $h = 2^{1-\ell}$, $\ell = 0, ..., 3$ using uniform partitions of quadrilateral S-elements for the Galerkin-SBFEM: a) without bubbles (top), b) with polynomial bubbles (middle), c) with all bubble functions (bottom); for $k = k_b = 1, 2, 3$.

Comparing the post-processing of the three schemes, it can be seen that SBFEM without any bubble leads to an inaccurate solution for coarse meshes. As already mentioned in the theory, this fact is related to the definition of the SBFEM approximate spaces, constructed to approximate homogeneous PDEs. Virtually, the approximations with the polynomial and the full bubble space (integer and non-integer bubble functions) are very similar. However, as observed in Fig. 4.9, the absence of the non-integer bubble functions leads to suboptimal rates of convergence.

The convergence curves for $t = 0.5s$ and the rates of convergence are presented in Fig.

4.9. Optimal rates of convergence of $k+1$ for L^2-norm and predicted rates of k for the energy norm only occur when the full bubble function space is considered. On the other hand, if only polynomial bubbles are applied to approximate the force term, the rate of convergence does not improve when the polynomial order k increases, although the error values decrease. More details of the error values for each point is summarized in Table A.16 in A.

Example 4: Three-dimensional single element

The three-dimensional Poisson example is defined in the region $\Omega = [-1,1] \times [-1,1] \times [-1,1]$ with the analytical solution given by

$$u(\underline{x}) = \cos\left(\frac{\pi}{2}x\right)\cos\left(\frac{\pi}{2}y\right)\cos\left(\frac{\pi}{2}z\right). \tag{4.5.-2}$$

such that $u_D = 0$ and source term $f = -\frac{3\pi^2}{4}\cos\frac{\pi x}{2}\cos\frac{\pi y}{2}\cos\frac{\pi z}{2}$. Approximate solutions are constructed for a single S-element, $S = \Omega$, whose boundary facets are subdivided two times. Consequently, subpartitions of S are composed of $6n^2$ pyramids, where $n = 1, 2, 3$ (see Fig. 4.10). In this example, two different configurations for the bubble space are tested:

1. The internal polynomial order is equal to the external one (i.e. $k_b = k$);
2. The internal polynomial order increases with the skeleton's refinement (i.e. $k_b = k + \ell$).

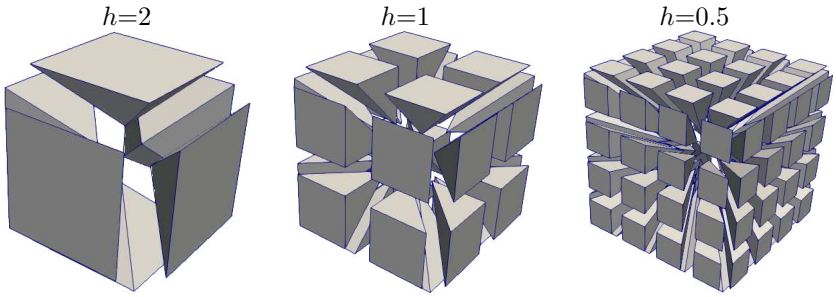

Figure 4.10: Example 4 - collapsed Duffy's partitions $T_{h,S}$ of $S = [-1,1] \times [-1,1] \times [-1,1]$ composed of $6n^2, n = 1, 2, 3$ uniform pyramids of characteristic width $h = 2/2^\ell, \ell = 0, 1, 2$.

In the second mesh configuration, the size of the eigenvalue problem increases considerably. For instance, for the cubic approximation, the size of the eigenvalue problem increases from a 209×209 matrix to a 3349×3349 one - 16 times greater. For this specific configuration, when the scaled boundary and internal approximation are equal, suboptimal rates of convergence are obtained. The optimal rates of convergence are recovered by increasing the internal polynomial order according to the skeleton's refinement. However, the increment in the boundary and internal DOF imposes numerical challenges. For $k = 2$, the rate of convergence in the L^2-norm was 2.6, instead of the expected rate of 3. These results are illustrated in the convergence curves in Fig. 4.11, and summarized in Table A.17.

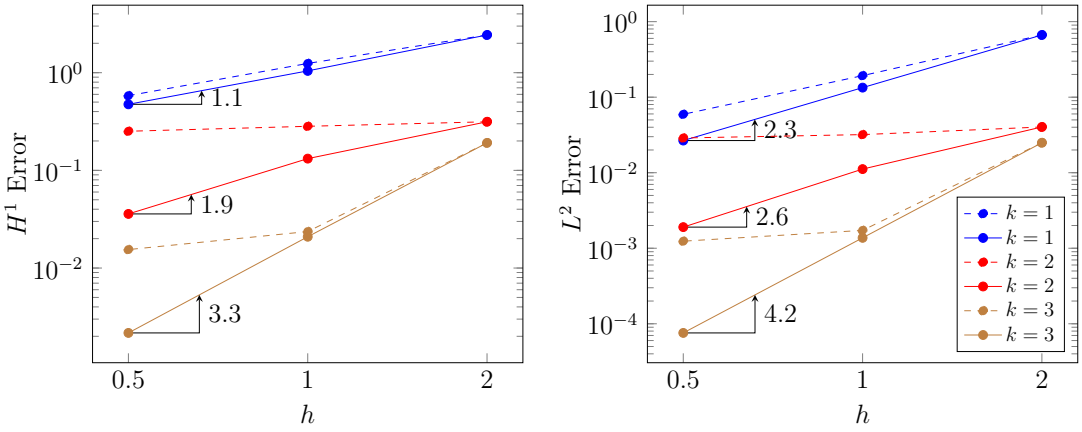

Figure 4.11: Example 4 - Energy and L^2 errors versus $h = 2/2^\ell$, $\ell = 0, 1, 2$ for $k = 1, 2, 3$ for a single S-element, refining the boundary (see Fig. 4.10), and the approximations: (a) dashed line - $k_b = k$; (b) solid line - $k_b = k + \ell$.

Example 5: Three-dimensional uniform refinement by hexahedral S-elements

The last Poisson example consists in approximating the previous equation, Eq. (4), using partitions $\mathcal{T}^h$ of Ω of uniform hexahedral S-elements, each one subdivided into six pyramids, as visualized in Fig. 4.12. Four refinement levels are taken, with $n \times n \times n$ hexahedra, $n = 2^\ell$, $\ell = 0, ..., 3$, having facet mesh sizes $h = 2/n$. The approximations correspond to trace spaces of degree $k = 1, ..., 3$.

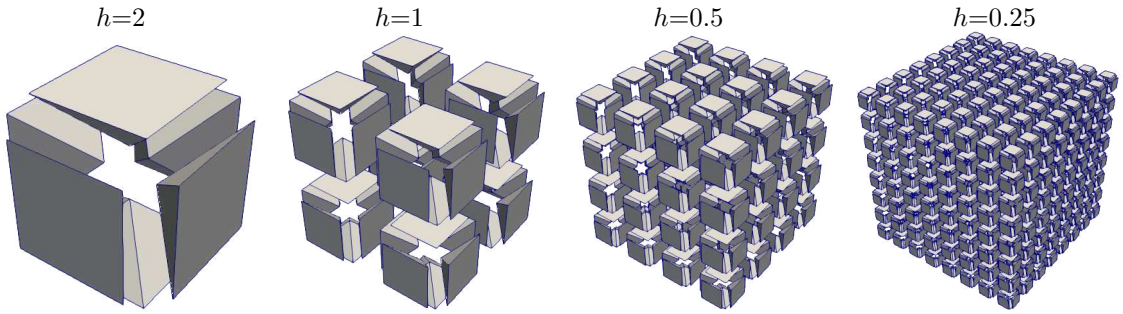

Figure 4.12: Example 5 - Partitions of the 3D domain Ω into uniform hexahedral S-elements, subdivided into regular pyramids of characteristic facet width $h = 2/2^\ell, \ell = 0, ..., 3$.

The Galerkin-SBFEM convergence results for these space configurations are graphically visualized in Fig. 4.13. Optimal rates of convergence are obtained of order $k + 1$ for L^2-norm and order k for the energy semi-norm. It is worth mentioning that the polynomial order for the internal and the boundary approximations are the same. To reduce the computational cost, the internal DOFs were condensed into the external ones for each element leading to a reduced size of the global stiffness matrix and improving the computational cost. The details regarding the error values are summarized in Table A.18.

4.5.2 Elasticity

Example 6: Elasticity problem in 2D

The two-dimensional Elasticity test is a plane strain state (i.e. $u_z = 0$) in a domain $\Omega = [-1, 1] \times [-1, 1]$, with Young Modulus $E = 10$ GPa and Poisson coefficient $\nu = 0.3$.

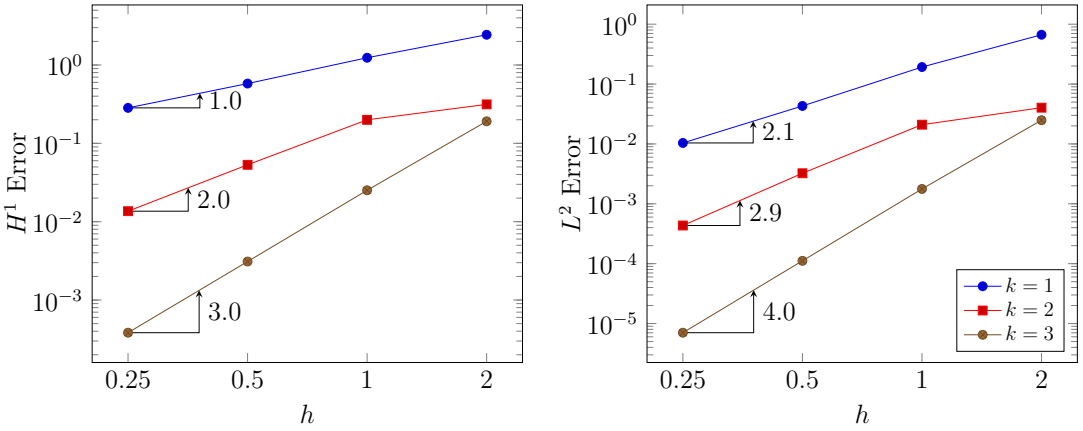

Figure 4.13: Example 5 - Energy and L^2 errors versus $h = 2/2^\ell$, $\ell = 0, ..., 3$, for $k = k_b = 1, 2, 3$ using the uniform hexahedral partitions (see Fig. 4.12).

The body load is

$$\underline{f} = \begin{Bmatrix} 4\pi^2(\lambda + 2\mu)\cos\pi x \sin\pi y \\ 4\pi^2(\lambda + 2\mu)\sin\pi x \cos\pi y \end{Bmatrix},$$

and $\underline{u}_D = 0$, such that the analytical solution, visualized in Fig. 4.14, is

$$\underline{u} = \begin{Bmatrix} 2\cos\pi x \sin\pi y \\ 2\sin\pi x \cos\pi y \end{Bmatrix}. \tag{4.5.-2}$$

The domain is partitioned by $\mathcal{T}^h$ formed by uniform quadrilateral S-elements, each one subdivided into four triangles, with $h = 1/2^{-\ell}, \ell = 0, ..., 3$. Figure 4.6 illustrates this mesh configuration for $h = \frac{1}{2}$. The trace polynomial degrees are for $1 \leq k \leq 7$, and the internal degree is $k_b = k$.

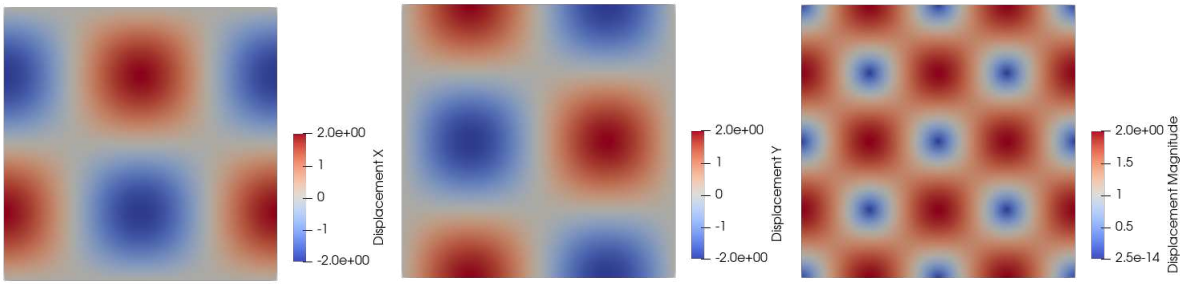

x-direction y-direction magnitude

Figure 4.14: Example 6 - Displacement u_x, u_y, and $||\underline{u}||$ for $h = 1/4$ and $k = 7$.

The motivation of this example is to verify the convergence properties of the bubble functions using high-order approximations in Elasticity problems. Optimal rates of convergence are observed in Fig. 4.15, reaching $k + 1$ for the L^2-norm and k for the energy norm. The error values are documented in Table A.19.

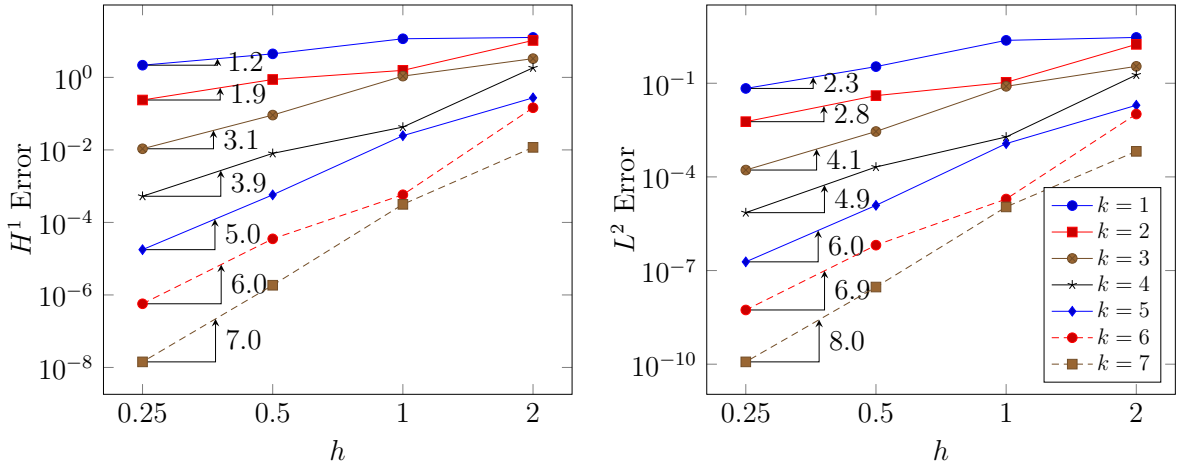

Figure 4.15: Example 6 - Energy and L^2 errors versus $h = 2/2^\ell$, $\ell = 0, ..., 3$, using the Galerkin SBFEM with bubbles in uniform partitions of quadrilateral S-elements for $k = k_b = 1, ..., 7$.

Example 7 - Elasticity problem in 3D

The last example refers to a 3D Elasticity problem in a domain $\Omega = [0, 1] \times [0, 1] \times [0, 1]$, for a Young modulus of $E = 1$ GPa, Poisson coefficient of $\nu = 0.2$, and body loads vector is given by

$$\underline{f} = \begin{Bmatrix} 3\pi(\lambda + 2\mu)\cos(\pi x)\cos(\pi y)\sin(\pi z) \\ 3\pi(\lambda + 2\mu)\cos(\pi x)\sin(\pi y)\cos(\pi z) \\ 3\pi(\lambda + 2\mu)\sin(\pi x)\cos(\pi y)\cos(\pi z) \end{Bmatrix}, \tag{4.5.-2}$$

and the analytical solution expressed by

$$\underline{u} = \begin{Bmatrix} 2\cos(\pi x)\cos(\pi y)\sin(\pi z) \\ 2\cos(\pi x)\sin(\pi y)\cos(\pi z) \\ 2\sin(\pi x)\cos(\pi y)\cos(\pi z) \end{Bmatrix}, \tag{4.5.-2}$$

and illustrated in Fig. 4.16 for a mesh refined four times, composed of tetrahedrons, with $h = 1/8$ (see Fig. 4.19) and polynomial order $k = 2$.

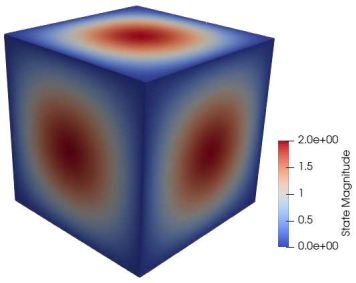

Figure 4.16: Example 7 - Post-processed solution of $||\underline{u}||$ using a partition $\mathcal{T}^h$ of hexahedral S-elements subpartitioned into regular tetrahedrons of characteristic width $h = 1/8$ (see Fig. 4.17), $k = 2$ and $k_b = 3$.

The domain is partitioned into hexagonal S-elements using two configurations for the S-elements' subpartition. First, the S-elements are subdivided into pyramids, similar to Example 2 - Poisson 3D mesh (Fig. 4.12). Further, each facet is refined only one time but instead of using pyramids, the subpartition is composed of tetrahedrons, as illustrated

in Fig. 4.17. The simulations include linear and quadratic polynomial order. The same mesh increasing the internal polynomial order by one is tested, likewise the numerical example in Example 2, where the boundary of a S-element is refined.

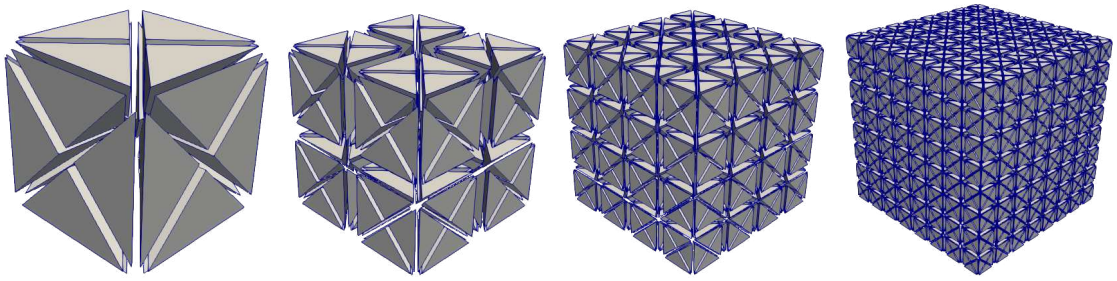

Figure 4.17: Example 7 - Partition of the 3D domain into hexahedra S-elements, subpartitioned into regular tetrahedrons for $h = 1/2^{\ell}$, where $\ell = 0, ..., 3$.

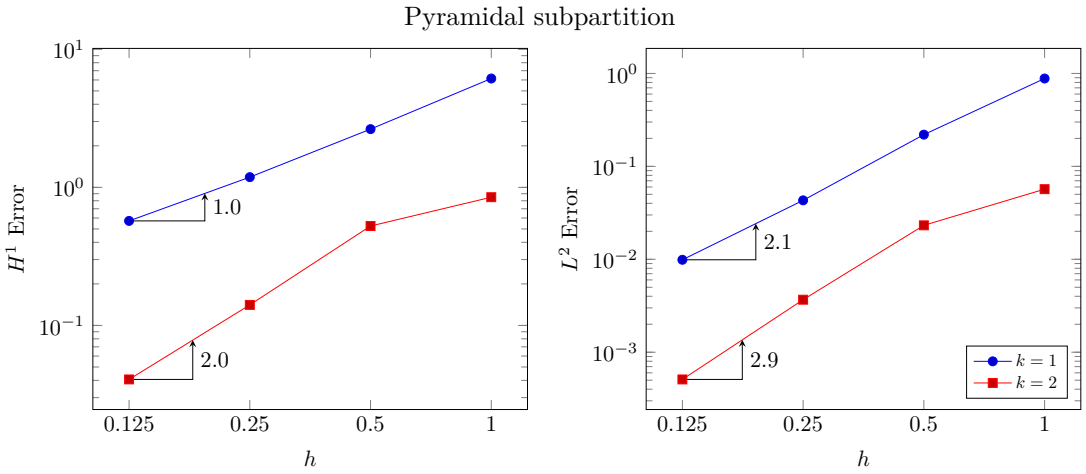

Figure 4.18: Example 7 - Energy and L^2 errors versus $h = 1/2^{\ell}$, $\ell = 0, ..., 3$ using uniform partitions of pyramids, as illustrated in Fig. 4.12, for $k = k_b = 1, 2$.

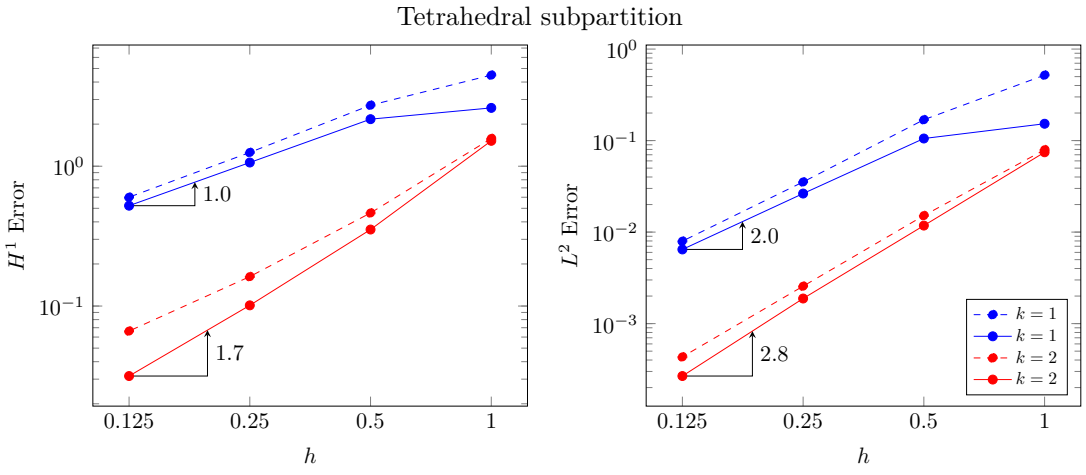

Figure 4.19: Example 7 - Energy and L^2 errors versus $h = 1/2^{\ell}$, $\ell = 0, ..., 3$ using uniform partitions of tetrahedrons, as illustrated in Fig. 4.17, for $k = 1, 2$ and $k_b = k$ (dashed lines) and $k_b = k + 1$ (solid lines).

The convergence curves for the three approximations are displayed in Fig. 4.18, for the pyramid subpartition, and in Fig 4.19, for the tetrahedral one. For the pyramidal mesh,

optimal rates of convergence were obtained, as already predicted theoretically, and verified numerically for the 3D scalar problem Example 2 - 3D Poisson problem. However, the boundary is refined, obtaining tetrahedral subpartitions for each S-element, and a loss of convergence for $k_b = k$ is observed, recovered only by increasing the internal polynomial order by one (i.e. $k_b = k + 1$). This result is similar to the obtained in the 3D Poisson experiment of refining only the boundary in Example 4. It means that for a boundary refinement Γ^S, a good alternative would be to increase the internal polynomial order k_b according to the number of refinement steps.

4.6 Conclusions

This chapter provides a new straightforward procedure to approximate non-homogeneous PDE using the SBFEM, based on the enrichment of usual SBFEM spaces with a bubble function space.

The bubble function space is constructed with the sum of the polynomial Duffy's bubble subspace $\mathcal{D}^{0,h}_{kk}(S)$ enriched with bubbles composed of non-integer eigenvalues of the SBFEM approximation and eigenvalues higher than the k. The proposed SBFEM space $\mathbb{V}^h_K$ is composed of the direct sum of the bubble-free $\mathbb{S}^h_k$ and bubble subspaces $\mathbb{B}^h_k$. Also, it is proved that $\mathbb{V}^h_k(S)$ contains the finite-dimensional Duffy's approximation subspace $\mathcal{D}^{0,h}_{kk}(S)$. Since $\mathcal{D}^{0,h}_{kk}(S)$ converges, proving the SBFEM convergence is a straightforward procedure, as presented in this chapter. Moreover, a procedure to avoid complex functions is proposed. Taking advantage of the orthogonal property of SBFEM approximations the resulting stiffness matrix in static problems have a reduced number of DOF.

Mathematical demonstrations prove the optimal rates of convergence of this procedure, and numerical experiments illustrate these proofs and elliptic non-homogeneous PDEs in 2D and 3D examples, considering Poisson and Elasticity problems. High-order simulations for 2D meshes and different mesh configurations for 3D problems are performed: refining the domain, the boundary, and both domain and boundary, using different subpartitions for the S-elements, such as triangles, tetrahedrons, and pyramids.

Chapter 5

Locally conservative SBFEM approximations

This chapter presents the multiphysics SBFEM formulation based on locally conservative approximation spaces. The mixed and hybridized mixed FEM theory, already introduced in Chapter 2, is further explored to apply it to the SBFEM concepts. The deductions are based on the early developments of the SBFEM for H^1 spaces, when the method was named Consistent Finite Element Cell method (WOLF; SONG, 1996).

First, the SBFEM coefficient matrices using H^1-compatible spaces are obtained, for a Darcy Flow, through the discretization of a FE into strips. This amounts to a different point of view of the SBFEM-H^1 formulation. The technique applied in this Chapter, known as the ballooning process, was explored by Wolf and Song (1996) but considering *infinitesimal* strips. In summary, the SBFEM-H^1 formulation can be also obtained by a ballooning process in which the strip has infinitesimal width. Exploring this fact is crucial to develop the Hybridized-Mixed formulation for the SBFEM since the $H(div)$ spaces for the SBFEM formulation are proposed by approximating the infinitesimal strips using the hybridized-mixed FEM.

The proposed formulation was implemented in NeoPZ [1] as a new feature for simulating mechanical problems using the SBFEM. Numerical tests for two-dimensional Darcy flows illustrate the optimal convergence rates for L^2 of flux and pressure of $k+1$, where k is the polynomial order. Since the scope of this thesis is two-dimensional problems and convergence results, future studies will address three-dimensional problems and complex applications. It is worth mentioning that the SBFEM can be applied in any other FE technique that allows discretizing the FE into infinitesimal strips. It means that the SBFEM can be seen as a generic technique that can be applied in other FE methods such as (Hybrid High-Order) HHO methods, Discontinuous Galerkin, and $H(curl)$, to name a few.

[1] The code is open-source and can be downloaded in <https://github.com/labmec/neopz/tree/develop>

5.1 SBFEM as a ballooning process

An intuitive approach to understanding the SBFEM is to interpret the method as a ballooning process, a technique already explored by Lowther, Rajanathan and Silvester (1978) in open boundary electric and magnetic field problems. Ballooning means dividing a finite element into several slices and performing recurrent static condensations, by condensing "interior" DOF in "exterior" DOF. This process is based on observing that the stiffness matrix of FEM does not depend on the width of the slice or even the position. For instance, in Fig. 5.1 the stiffness matrix of the finite element cell 1 is the same matrix of cell 2, even if the width is different.

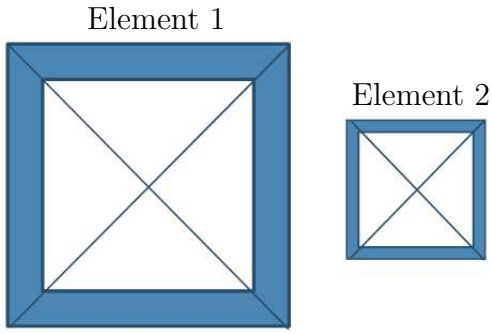

Figure 5.1: Comparison between two FE cells: The stiffness matrix of the element 1 and element 2 are equal.

In Fig. 5.2, one can see similarities between the FE cell and the Scaled Boundary FE. As highlighted by Lowther, Rajanathan and Silvester (1978), the FE cell can have an arbitrary number of facets. The authors named as star center the point inside the FE cell that can be seen by the whole facets. Such a point is similar to the scaling center definition presented in Chapter 3. Thus, the Scaled Boundary FE is a FE cell with infinitesimal width.

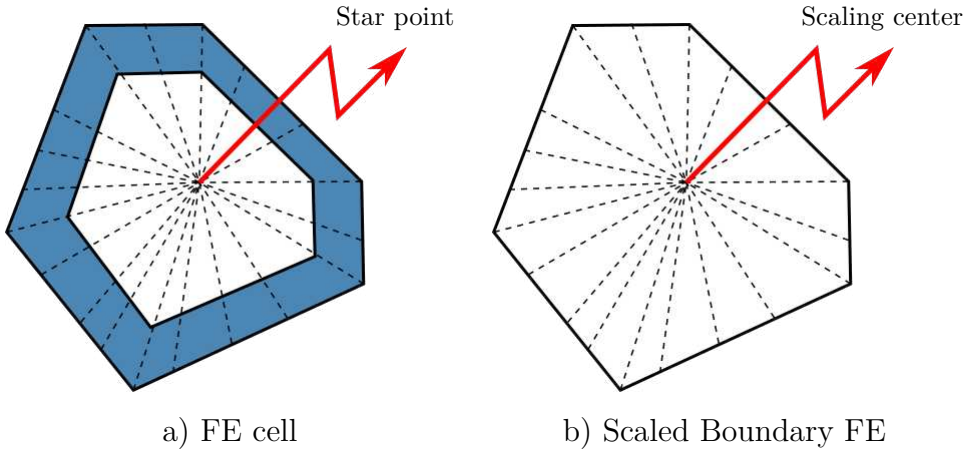

Figure 5.2: Comparison between a) FE cell as presented by Lowther and co-workers: the scaling center is named by "star point" by Lowther, Rajanathan and Silvester (1978); and b) scaled boundary FE.

Indeed, early developments of the SBFEM, when the method was known as the Infinitesimal Finite Element Cell Method, applied ballooning process concepts. To perform a

numerical simulation of semi-infinite domains, such as soil-structure interaction, Wolf and Song (1996) discretized the domain into infinitesimal finite element layers (see Fig. 5.3). The concept behind the method is that, if one considers an infinitesimal dimensionless cell, it is possible to compute the limit analytically as a function of the boundary discretization (i.e. the structure-medium interface).

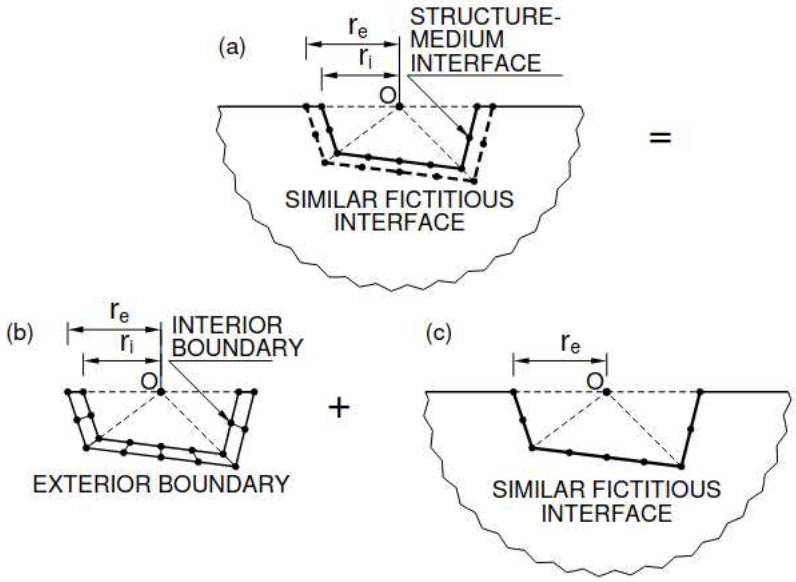

Figure 5.3: Consistent infinitesimal finite-element cell method. Image from Wolf and Song (1996)

Although Wolf and Song (1996) applied the ballooning technique in semi-infinite domains, it can be also applied to bounded domains in an analogous procedure. As can be seen in Fig. 5.4(a), the FE cell can be discretized into several layers. If the number of layers tends to infinity, the FE can be seen as a Scaled Boundary FE, as shown in Fig. 5.4. This case is equivalent to performing recurrent static condensations until the FE cell's DOF is only composed of the external ones. This point of view was the inspiration for understanding the orthogonality properties of the SBFEM approximations.

(a) SBFEM as a ballooning process

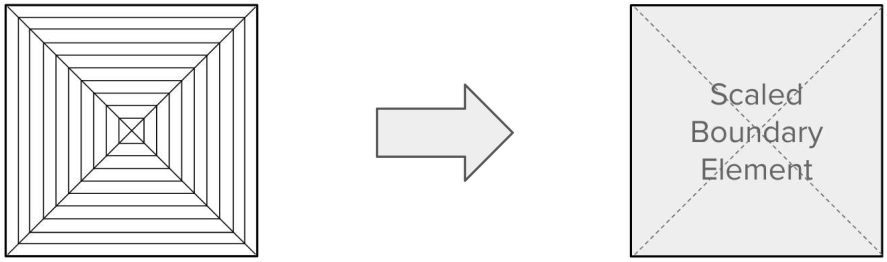

(b) Obtaining SBFEM through an infinitesimal dimensionless FE cell

Figure 5.4: SBFEM viewed as a condensation of an infinite number of infinitesimal layers: (a) SBFEM can be seen as a condensed infinite number of layers, (b) the SBFEM matrices can be obtained by performing the analytical limit of a FE cell.

To ease the computation of the stiffness matrix, similarly to the Consistent Infinitesimal FE Cell Method (WOLF; SONG, 1996), the approximation can be computed considering a fictitious interior interface for a cell with infinitesimal dimensionless width (see Fig. 5.4(b)). To obtain the SBFEM approximation, the internal approximation is written by the external one and the infinitesimal width. Thus, the limit is performed analytically. Intuitive reasoning is that the limit of an infinite number of infinitesimal layers leads to an analytical solution in the radial direction - i.e., the SBFEM can be seen as a ballooning process where the number of layers goes to the infinite. The process of obtaining the approximated solution using the Finite Element Cell method is related to computing the stiffness matrix using an infinitesimal layer, taking the analytical limit of the radial direction. This idea is first presented for classical FE H^1 formulation and then extended for a hybridized-mixed FE cell.

5.2 A Consistent Finite Element Cell Method

This section shows that it is possible to obtain the SBFEM coefficient matrices, $\underline{\underline{E}}_0$, $\underline{\underline{E}}_1$, and $\underline{\underline{E}}_2$, by computing the stiffness matrix of an infinitesimal dimensionless FE cell.

5.2.1 Geometry of a Finite Element Cell

First, let us define the geometric map for a FE cell. As shown in Fig. 5.5, the mappings $F_{Le} : \hat{L}_e \rightarrow L_e$ and $F_{Li} : \hat{L}_i \rightarrow L_i$ correspond to the geometric maps of the interior and exterior facets in each partition of S, where S is divided into subpartitions of finite element cells C. The geometric maps $F_{Li}(\hat{\eta})$ and $F_{Le}(\hat{\eta})$ corresponds to the mapping from the facets $(\hat{\xi} = -1, \hat{\eta})$ and $(\hat{\xi} = 1, \hat{\eta})$, respectively to $\underline{x}_i(-1, \hat{\eta})$ and $\underline{x}_e(1, \hat{\eta})$. The

assembling of the subpartitions leads to the finite element cell, as illustrated in Fig. 5.5. The interior facet, displayed in dashed lines in Fig. 5.5, is named by Wolf and Song (1996) as "*fictitious interface*".

Let δ be the infinitesimal dimensionless width given by

$$\delta = \frac{F_{Le}(\hat{\eta}) - F_{Li}(\hat{\eta})}{F_{Le}(\hat{\eta})}.$$

The internal geometric map $F_{Li}(\hat{\eta})$ is written as a function of the external $F_{Le}(\hat{\eta})$ and δ as,

$$F_{Li}(\hat{\eta}) = (1-\delta)F_{Le}(\hat{\eta}). \tag{5.2.0}$$

where $F_{Le}(\hat{\eta}) = F_K(\hat{\xi}=1,\hat{\eta})$, i.e. the external boundary of a S-element.

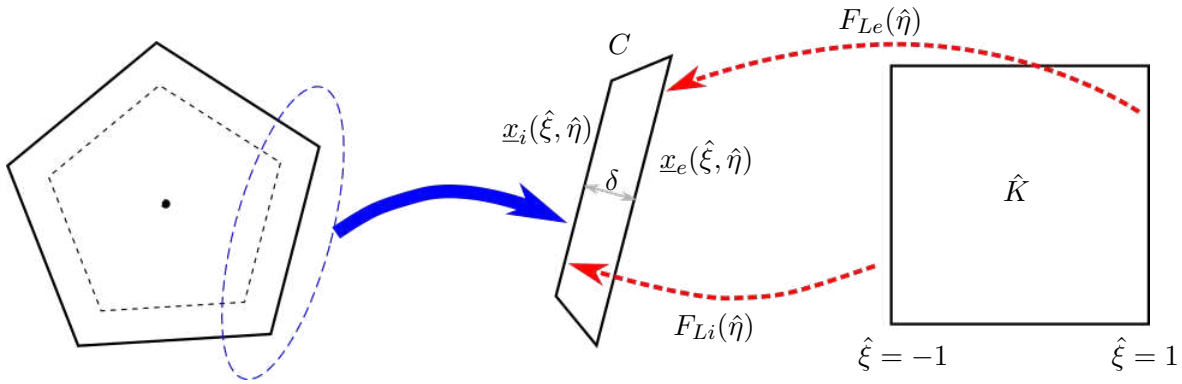

Figure 5.5: Geometric map of a FE element cell.

Using (5.2.1), the geometric map $F_C : \hat{K} \to C$ can be written as

$$\begin{aligned} F_C(\hat{\xi},\hat{\eta}) &= F_{Li}(\hat{\eta}) + \hat{\xi}\delta F_{Le}(\hat{\eta}) \\ &= \frac{1}{2}(2+\delta(\hat{\xi}-1))F_{Le}(\hat{\eta}). \end{aligned}$$

Notice that $F_C(\hat{\xi}=-1,\hat{\eta}) = (1-\delta)F_{Le}(\hat{\eta})$ and $F_C(\hat{\xi}=1,\hat{\eta}) = F_{Le}(\hat{\eta})$.

If $\underline{x} = F_C(\hat{\xi},\hat{\eta})$, the Jacobian matrix is $\underline{\underline{J}}_C = \nabla\underline{x}$. Similarly to the Chapter 3, the Jacobian matrix $\underline{\underline{J}}_C(\hat{\xi},\hat{\eta})$ of the subpartition of a FE cell C can be divided into two terms: a skeleton term, function of only $\hat{\eta}$, $\underline{\underline{J}}_K(1,\hat{\eta})$, and a term with the $\hat{\xi}$ variable $\underline{\underline{C}}_\delta(\hat{\xi})$

$$\underline{\underline{J}}_C(\hat{\xi},\hat{\eta}) = \underline{\underline{J}}_K(1,\hat{\eta})\underline{\underline{C}}_\delta(\hat{\xi}),$$

where $\underline{\underline{J}}_K(1,\hat{\eta})$ is the same Jacobian matrix defined in Chapter 3, written as

$$\underline{\underline{J}}_K(1,\eta) = \begin{bmatrix} F_L(\eta) & \nabla_\eta F_L(\eta) \end{bmatrix} \tag{5.2.-1}$$

where $\eta = \hat{\eta}$ and $F_L(\eta) = F_{L_e}(\hat{\eta})$ and $\underline{\underline{C}}_\delta(\hat{\xi})$ is a diagonal matrix given by

$$\underline{\underline{C}}_\delta = \begin{pmatrix} \frac{\delta}{2} & 0 \\ 0 & \frac{1+\delta(\hat{\xi}-1)}{2} \end{pmatrix}. \tag{5.2.-1}$$

Its inverse is written as

$$\underline{\underline{J}}_C(\hat{\xi},\hat{\eta})^{-1} = \underline{\underline{C}}_\delta(\hat{\xi})^{-1}\underline{\underline{J}}_K^{-1}(1,\hat{\eta}) \tag{5.2.-1}$$

where

$$\underline{\underline{C}}_\delta^{-1}(\hat{\xi}) = \begin{bmatrix} \frac{2}{\delta} & 0 \\ 0 & \frac{2}{2+\delta(\hat{\xi}-1)} \end{bmatrix}. \tag{5.2.-1}$$

Also, recall that, whilst scalar functions the following relationship applies

$$\phi(\underline{x}) = \hat{\phi}(\underline{\hat{x}}),\ for\ \underline{x} = F_C(\hat{x}), \tag{5.2.-1}$$

for vector-valued functions, we employ the Piola transformation $\mathbb{F}_C : \underline{q}(\underline{\hat{x}}) \rightarrow \underline{q}(\underline{x})$ as follows

$$\underline{q}(\underline{x}) = \frac{\underline{\underline{J}}_C}{|\underline{\underline{J}}_C|}\ \underline{\hat{q}}(\underline{\hat{x}}). \tag{5.2.-1}$$

5.2.2 Obtaining the SBFEM coefficient matrices using H^1 approximations

Consider as the model problem the Poisson equation with null source term as already defined in Chapter 3. Such a formulation, known also as the harmonic problem, is written in strong form as

$$\Delta u = 0,\ u \in \Omega$$
$$u|_{\partial\Omega} = u_D$$

where u_D are prescribed Dirichlet boundary conditions and $\Delta u = \nabla\cdot(\nabla u)$ is the Laplacian operator applied in u. The variational statement is: Find $u \in H^1(\Omega)$ such that

$$\int_\Omega \nabla u \cdot \nabla v\ d\Omega = 0,\ \forall\ v \in H_0^1(\Omega)$$
$$u|_{\partial\Omega} = u_D.$$

Let Ω be partitioned into FE cells of infinitesimal width, such that $\Omega = \mathcal{T}^h = \{\bar{S}\}$ where h is the characteristic size of the S-element's facets. Each cell is a conglomerate of finite element strips C mapped to the master element $\hat{K}$, $F_C : \hat{K} \rightarrow C$ using Eq. (5.2.1).

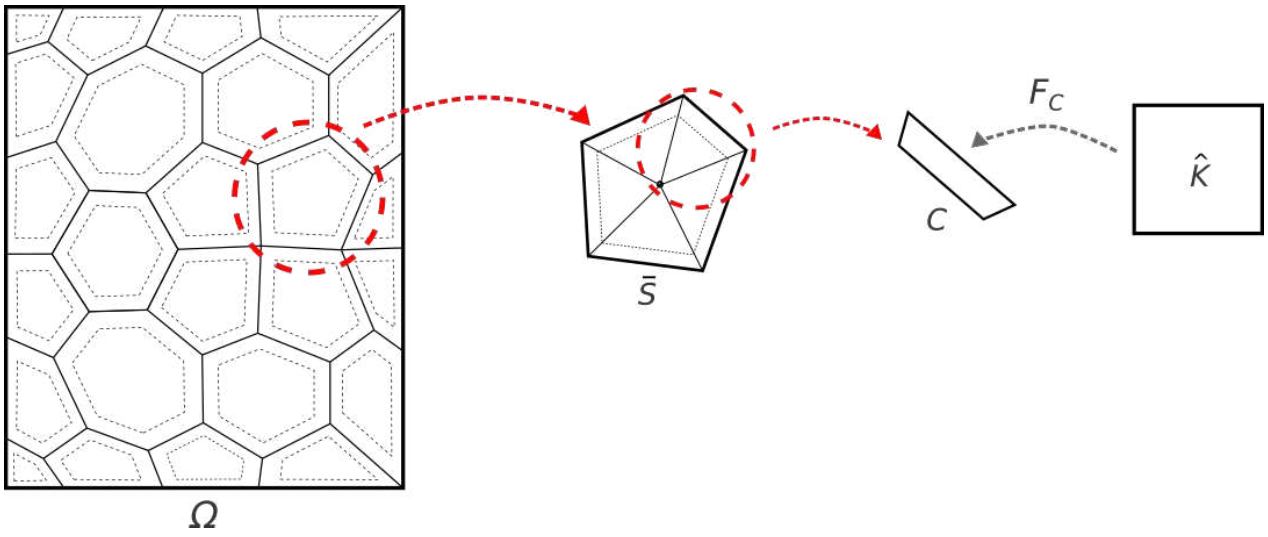

Figure 5.6: Partition of the domain $\Omega = \mathcal{T}_h = \{\bar{S}\}$ into finite element cells $\bar{S}$. Each cell $\bar{S}$ is a conglomerate of strips C.

For this discretization, a finite-dimensional subspace is defined locally as $\mathcal{V}^h(\bar{S}) \subset H^1(\Omega)$, such that $u_h = \sum_i \phi_i u_i \in \mathcal{V}^h(\bar{S})$ and $v_h = \sum_j \phi_j v_j \in \mathcal{V}^h{}_0(\bar{S}) \subset H^1_0(\Omega)$. The stiffness matrix of the FE cell is written as

$$K_{ij} = \int_\Omega \nabla\phi_i \cdot \nabla\phi_j \, d\bar{S}, \tag{5.2.-1}$$

The exterior boundary of the FE cell $\partial\bar{S}$ coincides with the S-elements' boundary ∂S. The interior boundary of $\partial\bar{S}$ is named fictitious interface. Consider $\underline{u}^e$ the nodal values of the exterior DOF and $\underline{u}^i$ the nodal values of the interior DOF (over the fictitious interface). To obtain the SBFEM coefficient matrices ($\underline{\underline{E}}_0$, $\underline{\underline{E}}_1$, $\underline{\underline{E}}_2$), we manipulate the DOF in order to write it as

- Infinitesimal average pressure, given by

$$\underline{\bar{u}} = \frac{\underline{u}^e + \underline{u}^i}{2} \tag{5.2.-1}$$

- Infinitesimal "differential pressure", resulting in

$$d\underline{\bar{u}} = \frac{1}{\hat{\xi}} \frac{u^e - u^i}{\delta} \tag{5.2.-1}$$

Notice that, when the FE cell width tends to zero ($\delta \to 0$), $\dfrac{u^e + u^i}{2} \to u|_{\partial S}$ and $\dfrac{u^e - u^i}{\delta\hat{\xi}} \to \dfrac{1}{\hat{\xi}} \dfrac{\partial u}{\partial \hat{\xi}}$.

Manipulating the DOF means that the shape functions slightly change. First, consider a space $\mathcal{V}^h = \mathbb{P}_{1,k}$, i.e. linear in $\hat{\xi}$-direction and up to order k in $\hat{\eta}$-direction. The linear approximation order is considered for $\hat{\xi}$-direction for simplicity since the width in this direction is infinitesimal, then, higher order terms are negligible. For such an arrangement, the shape functions can be grouped into two groups:

- Shape functions related to the internal DOF $\underline{u}^i$:

$$\underline{\hat{\phi}}^i = \frac{\hat{\xi} - 1}{2} \underline{\hat{N}}_k(\hat{\eta})$$

- Shape functions related to the external DOF $\underline{u}^e$:

$$\underline{\hat{\phi}}^e = \frac{\hat{\xi} + 1}{2} \underline{\hat{N}}_k(\hat{\eta})$$

The shape functions for $\underline{\bar{u}}$ and $d\underline{\bar{u}}$ are given by the sum and the difference between the two groups of shape functions $\underline{\hat{\phi}}^i$ and $\underline{\hat{\phi}}^e$ as below:

- Shape functions related to the infinitesimal differential pressure:

$$\underline{\hat{\varphi}}^i = \delta \left(\frac{\hat{\xi} - 1}{2} \underline{\hat{N}}_k(\hat{\eta}) + \frac{\hat{\xi} + 1}{2} \underline{\hat{N}}_k(\hat{\eta}) \right) = \frac{\hat{\xi}\delta}{2} \underline{\hat{N}}_k(\hat{\eta}). \tag{5.2.-1}$$

- Shape functions related to the infinitesimal average pressure:

$$\underline{\hat{\varphi}}^e = \frac{\hat{\xi}+1}{2}\underline{\hat{N}}_k(\hat{\eta}) - \frac{\hat{\xi}-1}{2}\underline{\hat{N}}_k(\hat{\eta}) = \underline{\hat{N}}_k(\hat{\eta}). \tag{5.2.-1}$$

Using the geometric map described in Section 5.2.1, the gradient $\nabla\underline{\varphi} = \underline{\underline{J}}_C^{-1}(\hat{\xi},\hat{\eta})\nabla_{\hat{\xi},\hat{\eta}}\underline{\hat{\varphi}}$ is computed for the two group of functions as

$$\nabla\underline{\varphi}^i = \underline{\underline{C}}_\delta^{-1}(\hat{\xi})\underline{\underline{J}}_K^{-T}(1,\hat{\eta})\begin{bmatrix}\frac{\delta}{2}\underline{\hat{N}}(\hat{\eta})\\ \frac{\hat{\xi}\delta}{2}\nabla_{\hat{\eta}}\underline{\hat{N}}(\hat{\eta})\end{bmatrix}$$
$$\nabla\underline{\varphi}^e = \underline{\underline{C}}_\delta^{-1}(\hat{\xi})\underline{\underline{J}}_K^{-T}(1,\hat{\eta})\begin{bmatrix}0\\ \nabla_{\hat{\eta}}\underline{\hat{N}}(\hat{\eta})\end{bmatrix}$$

From Eqs. (5.2.2) and (5.2.2) one can identify the $\underline{\underline{B}}_1$ and $\underline{\underline{B}}_2$ matrices, respectively, from Chapter 3 (see Eq. (3.2.2)), by taking the limit of $\delta \to 0$ as

$$\lim_{\delta\to 0}\nabla\underline{\varphi}^i = \underline{\underline{J}}_K^{-T}(1,\hat{\eta})\begin{bmatrix}\underline{\hat{N}}(\hat{\eta})\\ 0\end{bmatrix} = \underline{\underline{B}}_1,$$
$$\lim_{\delta\to 0}\nabla\underline{\varphi}^e = \underline{\underline{J}}_K^{-T}(1,\hat{\eta})\begin{bmatrix}0\\ \nabla_\eta\underline{\hat{N}}(\hat{\eta})\end{bmatrix} = \underline{\underline{B}}_2.$$

Thus, the local stiffness matrix of a FE cell $\bar{S}$ is the assemble of the matrices related to the strips of C

$$\begin{aligned}\underline{\underline{K}} &= \sum_l \frac{1}{\delta}\int_{C_l}\nabla\underline{\varphi}^T\nabla\underline{\varphi}\,dC_l\\ &= \frac{1}{\delta}\sum_l\int_{\hat{K}}\nabla\underline{\varphi}^T\nabla\underline{\varphi}\frac{\delta\left(2+\delta(\hat{\xi}-1)\right)}{4}|\underline{\underline{J}}_{K_l}(1,\hat{\eta})|d\hat{K}\end{aligned}$$

where $\sum_l$ represents the assemble of $\bar{S} = \mathcal{T}^{\bar{S}} = \{C_l\}$, where $l = 1, ..., n^{\bar{S}}$, $n^{\bar{S}}$ is the number of exterior facets of the $\bar{S}$ and

$$\underline{\varphi} = \left\{\underline{\varphi}^i \quad \underline{\varphi}^e\right\}.$$

and $\underline{\varphi}^i$ and $\underline{\varphi}^e$ are given by Eqs. (5.2.2) and (5.2.2) respectively. Notice that we include the factor $\dfrac{1}{\delta}$ to avoid the indeterminacy resulting from the determinant of the Jacobian $|\underline{\underline{J}}_{C_l}(\hat{\xi},\hat{\eta})| = \dfrac{\delta(2+\delta(\hat{\xi}-1))}{4}|\underline{\underline{J}}_{K_l}(1,\hat{\eta})| \to \infty$ when $\delta \to 0$.

Considering the two groups of shape functions, $\underline{\hat{\varphi}}^i$ and $\underline{\hat{\varphi}}^e$, the stiffness matrix of a FE cell is written as a block-matrix composed of

$$\underline{\underline{K}} = \begin{bmatrix}\underline{\underline{K}}^{ii} & \underline{\underline{K}}^{ie}\\ \underline{\underline{K}}^{ei} & \underline{\underline{K}}^{ee}\end{bmatrix}.$$

where

$$\underline{\underline{K}}^{ii} = \sum_l \lim_{\delta\to 0} \frac{1}{\delta} \int_{-1}^{+1}\int_{-1}^{+1} \underline{\underline{B}}_1^T \underline{\underline{B}}_1 \, |\underline{\underline{J}}_{K_l}(1,\eta)| d\eta d\xi = \int_{-1}^{+1} \sum_l \underline{\underline{E}}_{0l} \, d\hat{\xi}$$

$$\underline{\underline{K}}^{ie} = \sum_l \lim_{\delta\to 0} \frac{1}{\delta} \int_{-1}^{+1}\int_{-1}^{+1} \underline{\underline{B}}_1^T \underline{\underline{B}}_2 \, |\underline{\underline{J}}_{K_l}(1,\eta)| d\eta d\xi = \int_{-1}^{+1} \sum_l \underline{\underline{E}}_{1l}^{\ T} \, d\xi$$

$$\underline{\underline{K}}^{ei} = \sum_l \lim_{\delta\to 0} \frac{1}{\delta} \int_{-1}^{+1}\int_{-1}^{+1} \underline{\underline{B}}_2^T \underline{\underline{B}}_1 \, |\underline{\underline{J}}_{K_l}(1,\eta)| d\eta d\xi = \int_{-1}^{+1} \sum_l \underline{\underline{E}}_{1l} \, d\xi$$

$$\underline{\underline{K}}^{ee} = \sum_l \lim_{\delta\to 0} \frac{1}{\delta} \int_{-1}^{+1}\int_{-1}^{+1} \underline{\underline{B}}_2^T \underline{\underline{B}}_2 \, |\underline{\underline{J}}_{K_l}(1,\eta)| d\eta d\xi = \int_{-1}^{+1} \sum_l \underline{\underline{E}}_{2l} \, d\xi.$$

Therefore,

$$\underline{\underline{K}} = \int_{-1}^{+1} \begin{bmatrix} \underline{\underline{E}}_0 & \underline{\underline{E}}_1^{\ T} \\ \underline{\underline{E}}_1 & \underline{\underline{E}}_2 \end{bmatrix} d\xi. \tag{5.2.-1}$$

It means that the stiffness matrix of an FE cell of infinitesimal width is a block matrix composed of the SBFEM coefficient matrices. The matrices $\underline{\underline{E}}_0$, $\underline{\underline{E}}_1$, $\underline{\underline{E}}_2$ are applied to the Ricatti ODE in order to obtain the SBFEM shape functions. Such a procedure was already described in Chapter 3.

5.2.3 Obtaining SBFEM coefficient matrices using hybridized-mixed approximations

An analogous procedure to the previous section is performed to obtain the SBFEM coefficient matrices for using a locally conservative approximation. First, the hybridized-mixed approach is written for a generic S-element. Then, the case of a hybridized-mixed FE cell of infinitesimal width is analyzed in detail.

Let us rewrite the model problem (the Poisson equation) using the mixed method. The strong formulation is written as: Find $u \in L^2(\Omega)$ and $\underline{\sigma} \in H(div, \Omega)$

$$\begin{aligned} \underline{\sigma} &= \nabla u, \ in \ \Omega \\ \nabla \cdot \underline{\sigma} &= 0, \ in \ \Omega \\ u|_\Gamma &= u_D, \ in \ \partial\Omega = \Gamma. \end{aligned}$$

The variational statement, as deduced in Chapter 2, is written as: Find $\underline{\sigma} \in H(div, \Omega)$ and $u \in L^2(\Omega)$ such as

$$\begin{aligned} \int_\Omega \underline{\sigma} \cdot \underline{q} \, d\Omega - \int_\Omega u \left(\nabla \cdot \underline{q}\right) \, d\Omega &= -\int_\Gamma u_D (\underline{q} \cdot \underline{n}) \, d\Gamma, \ \forall \ \underline{q} \in H(div; \Omega) \\ -\int_\Omega (\nabla \cdot \underline{\sigma}) \ v \, d\Omega &= 0, \ \forall \ v \in L^2(\Omega) \end{aligned}$$

Consider that $\Omega = \mathcal{T}^h = \{S\}$ is partitioned into S-elements. Also, consider the finite-dimensional subspaces

$$\begin{aligned} \mathcal{Z}^h &= \left\{ v \in L^2(\Omega) \ : \ v|_{\bar{S}} \in \mathbb{P}_{1,k}(K) \right\} \\ \underline{\mathcal{Q}}^h &= \left\{ \underline{q} \in H(div; \Omega) \ : \ \underline{q}|_{\bar{S}} \in \mathbb{P}_{k+1,1}(K) \times \mathbb{P}_{k+1,1}(K) \right\} \end{aligned}$$

As already highlighted in Chapter 2, $\underline{\mathcal{Q}}^h$ has the property of continuity of the normal flux between the FE cells. It means that the continuity is imposed directly in the function space. Another approach is to enforce such continuity in the variational statement, through Lagrange multipliers.

Now, consider the skeleton mesh $\mathcal{E}_h = \bigcup_{ij} e_{ij} \bigcup \Gamma_h$ where $e_{ij} = \partial\bar{S}_i \cap \partial\bar{S}_j$, as shown in Fig. 5.7, where e_{ij} is shown in red lines and Γ_h is in blue.

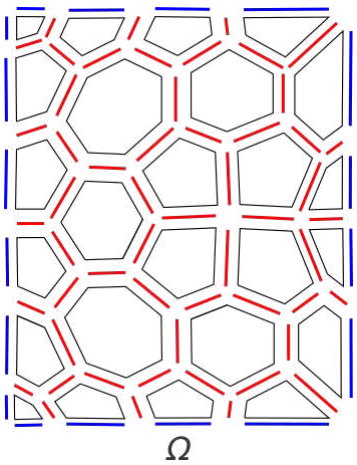

Figure 5.7: Partition of the domain into S-elements ($\mathcal{T}^h = \{S\}$) in write and skeleton mesh ($\mathcal{E}^h = \{e\}$) in red and blue.

.

The finite-dimensional subspaces for $S \in \mathcal{T}^h = \Omega$ and $e \in \mathcal{E}^h$ are given by

$$\underline{\mathcal{Z}}^h = \left\{ \underline{z}_h \in L^2(\Omega) \times L^2(\Omega),\ \underline{z}_h|_S \in\ \mathcal{D}_{k+1,k}(S) \times \mathcal{D}_{k,k+1}(S),\ \forall S \in \mathcal{T}^h \right\},$$
$$\mathcal{Z}^h = \left\{ v_h \in L^2(\Omega)\ :\ v_h|_S \in \mathbb{P}_{k,k}(S),\ \forall\ S \in \mathcal{T}^h \right\},$$
$$\mathcal{M}^h = \left\{ \mu_e \in L^2(\mathcal{E}_h)\ :\ \mu_e \in \mathbb{P}_k(e),\ \forall\ e \in \mathcal{E}^h \right\}.$$

Thus, the variational statement for the hybridized-mixed formulation is: find $(\underline{\sigma}_h,\ u_h,\ \lambda_h) \in \underline{\mathcal{Z}}^h \times \mathcal{Z}^h \times \mathcal{M}^h$ such that

$$\sum_{S\in\mathcal{T}_h} \int_S \underline{\sigma}_h \cdot \underline{q}_h\ dS - \sum_{S\in\mathcal{T}_h} \int_S u_h \left(\nabla \cdot \underline{q}_h\right)\ dS + \sum_{e\in\mathcal{E}_h} \int_e \lambda_h [\![\underline{q}_h]\!]\ de = -\int_{\Gamma_h} u_D \left(\underline{q}_h \cdot \underline{n}\right)\ d\Gamma_h$$

$$\sum_{S\in\mathcal{T}_h} \int_S v \left(\nabla \cdot \underline{\sigma}_h\right)\ dS = 0$$

$$\sum_{e\in\mathcal{E}_h} \int_e \mu_h [\![\underline{\sigma}_h]\!] de = 0.$$

where $[\![\underline{q}_{he}]\!] = \underline{q}_{he} \cdot \underline{n}_e^+ + \underline{q}_{he}^- \cdot \underline{n}_e^-$ for all $e \in \mathcal{E}_h$, and $\underline{n}_e^+ = -\underline{n}_e^-$ is the outward vector.

In matricial form, Eqs. 5.2.3 to 5.2.3 lead to

$$\underline{\underline{K}} = \begin{pmatrix} \underline{\underline{\mathbb{A}}} & -\underline{\underline{\mathbb{B}}}^T & -\underline{\underline{\mathbb{C}}}^T \\ \underline{\underline{\mathbb{B}}} & \underline{\underline{0}} & \underline{\underline{0}} \\ \underline{\underline{\mathbb{C}}} & \underline{\underline{0}} & \underline{\underline{0}} \end{pmatrix} \tag{5.2.-1}$$

where $\underline{\underline{\mathbb{A}}}$, $\underline{\underline{\mathbb{B}}}$ and $\underline{\underline{\mathbb{C}}}$ are bilinear forms as presented in Chapter 2.

Stiffness matrix for a hybridized FE cell

As well as in the H^1 case, the stiffness matrix of a hybridized FE does not depend on the scale or position. It means that, for instance, two FE cells with different positions and scales as in Fig. 5.8 have the same stiffness matrix.

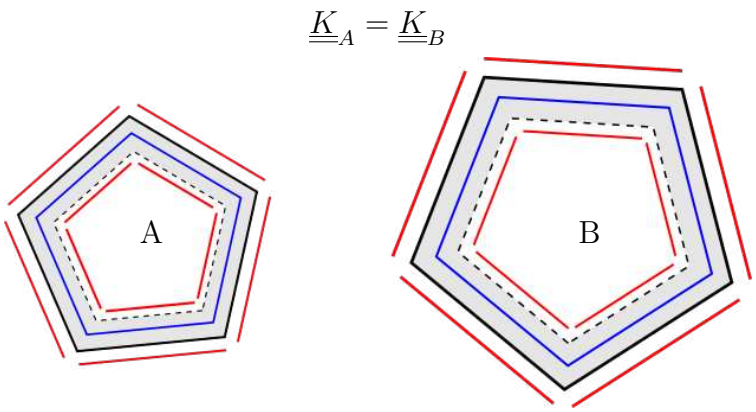

Figure 5.8: Two hybrid cells A and B with different scales and positions. The stiffness matrix of both elements is the same.

The hybrid FE cell, as shown in Fig. 5.8, is composed of $d-1$-dimensional elements for the internal pressure (shown in blue lines) and $d-1$-dimensional elements for the exterior pressure (external average pressure and differential pressure). The FE cell is described by the geometric map from a quadrilateral master element $\hat{K}$ to a deformed element C using the Eq. (5.2.1). The geometric map related to the external elements in red corresponds to the maps F_{L_i} and F_{L_e}, for the element over the fictitious interface and the exterior element relatively to ∂S, respectively. The map F_{L_e} is such that $F_{L_e} = F_C(1, \hat{\eta}) = F_K(1, \hat{\eta})$. There is also a map F_L^{int} for the geometric element associated with the internal pressure (in blue). For an infinitesimal element, i.e. the width $\delta \to 0$, $F_{L_i} = F_L^{int} = F_{L_e}$. The assembly of these geometric elements composes the hybrid FE cell.

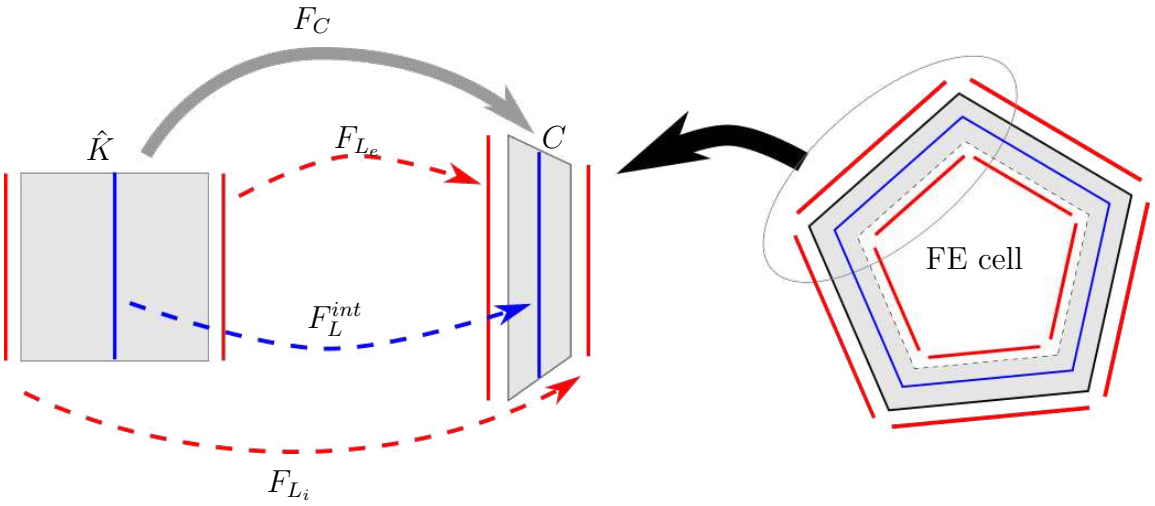

Figure 5.9: Geometric map of a hybridized FE cell.

The basis functions for the pressure approximation, either internal or external DOF, in a

hybrid infinitesimal FE cell, are $d-1$ polynomials $\hat{N}_k(\hat{\eta}) \in \mathbb{P}_k(\hat{L})$. Namely, the DOF for the pressure are:

- Internal pressure u^{int},
- Infinitesimal differential pressure (Lagrange multiplier): $\dfrac{1}{\hat{\xi}}\dfrac{u^e - u^i}{\delta}$
- Infinitesimal average pressure (Lagrange multiplier): $\dfrac{u^e + u^i}{2}$

For $\delta \to 0$

- Internal pressure $= u^{int}$,
- Infinitesimal differential pressure (Lagrange multiplier) $= \dfrac{1}{\hat{\xi}}\dfrac{du^e}{d\xi}$
- Infinitesimal average pressure (Lagrange multiplier) $= u^e$

The flux is associated with the d-dimensional element in gray. Fig. 5.10 illustrated the DOF related to the flux for a FE strip and approximation order $k = 1$. Notice that, as already mentioned in Chapter 2, instead of using the geometric transformation F_C, for vector-valued functions it is applied the Piola transformation $P_C : \hat{\underline{\psi}} \to \underline{\psi}$. Moreover, since the width is infinitesimal and it is only a part of the FE cell, the number of DOF is reduced. For instance, the internal flux in ξ-direction is negligible.

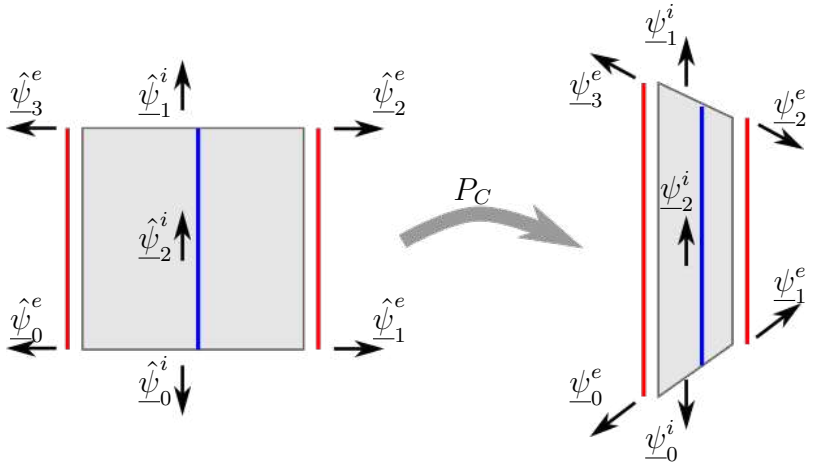

Figure 5.10: Flux components of a finite element strip mapped from the master element K to the deformed element $\hat{K}$ using the Piola transformation P_C.

The shape functions for the flux are gathered in three groups:

1. Internal flux $\underline{\sigma}_h^{int}$: $\hat{\underline{\psi}}_i^{int} = \left\{0, \hat{N}_i(\hat{\eta})\right\},\ i = 0, ..., k$
2. Exterior flux - internal facet $\underline{\sigma}_h^i$: $\hat{\underline{\psi}}_j^i = \left\{\dfrac{1-\hat{\xi}}{2}\hat{N}_j(\hat{\eta}), 0\right\},\ j = 0, ..., k$
3. Exterior flux $\underline{\sigma}_h^e$: $\hat{\underline{\psi}}_l^e = \left\{\dfrac{1+\hat{\xi}}{2}\hat{N}_l(\hat{\eta}), 0\right\},\ l = 0, ..., k$

Notice that the internal flux is an enriched space $k+1$ accordingly to the theory of the Raviart-Thomas space (ROBERTS; THOMAS, 1991).

Fig. 5.11 represents a mesh composed of quadrilateral hybrid FE cells. The d-dimensional elements in gray are the infinitesimal cells in which the flux is considered. The $d-1$-dimensional blue elements represent the internal pressure, whilst the red elements are the exterior pressure, composed of the DOF related to the Lagrange multipliers (average infinitesimal pressure and differential pressure). Lastly, the green elements are the elements related to the boundary condition. In these elements, Dirichlet values for the pressure are imposed.

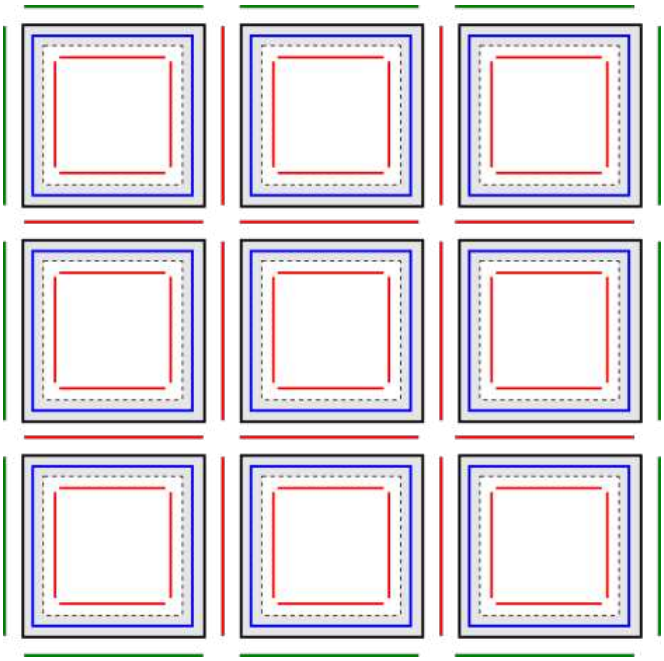

Figure 5.11: Partition of the domain Ω into quadrilateral hybrid FE cells: the skeleton mesh in red, internal elements in blue, and boundary elements in green.

Consider the partition shown in Fig. 5.11 and the finite element spaces

$$\underline{\mathcal{Z}}^h = \left\{ \underline{z}_h \in L^2(\Omega) \times L^2(\Omega),\ \underline{z}_h|_{\bar{S}} \in \mathcal{D}_{k+1}(S) \times \mathcal{D}_k(S) \right\}$$
$$\mathcal{Z}^h = \left\{ z_h \in L^2(\Omega),\ \underline{z}_h|_{\bar{S}} \in \mathcal{D}_k(S) \right\}$$

and keep the same approximation space for the Lagrange multipliers $\mathcal{M}^h$ as defined in Eq. (5.2.3).

For a hybridized-mixed FE cell of infinitesimal width, the local problem is also written as: Find $(\underline{\sigma}_h, u_h, \lambda_h) \in \underline{\mathcal{Z}}^h(\bar{S}) \times \mathcal{Z}^h(\bar{S}) \times \mathcal{M}^h(\bar{S})$

$$\begin{pmatrix} \underline{\underline{\mathbb{A}}} & -\underline{\underline{\mathbb{B}}}^T & -\underline{\underline{\mathbb{C}}}^T \\ \underline{\underline{\mathbb{B}}} & \underline{\underline{0}} & \underline{\underline{0}} \\ \underline{\underline{\mathbb{C}}} & \underline{\underline{0}} & \underline{\underline{0}} \end{pmatrix} \begin{Bmatrix} \underline{\mathcal{S}} \\ \underline{\mathcal{U}} \\ \underline{\mathcal{L}} \end{Bmatrix} = \begin{Bmatrix} \underline{0} \\ \underline{0} \\ \underline{0} \end{Bmatrix}.$$

A static condensation can be performed in order to eliminate u_h and $\underline{\sigma}_h$ from the local system, leading to a smaller local and global system of equations

$$\underline{\underline{\mathbb{E}}}\ \underline{\mathcal{L}} = \underline{0}, \tag{5.2.-1}$$

where

$$\underline{\underline{\mathbb{E}}} = \underline{\underline{\mathbb{C}}}\ \underline{\underline{\mathbb{A}}}^{-1}\left(\underline{\underline{\mathbb{A}}} - \underline{\underline{\mathbb{B}}}^{T}\left(\underline{\underline{\mathbb{B}}}\ \underline{\underline{\mathbb{A}}}^{-1}\underline{\underline{\mathbb{B}}}^{T}\right)^{-1}\underline{\underline{\mathbb{B}}}\right)\underline{\underline{\mathbb{A}}}^{-1}\underline{\underline{\mathbb{C}}}^{T} \tag{5.2.-1}$$

As already highlighted in Chapter 2, the matrix $\mathbb{E}$ has the property of being symmetric and positive definite, as well as in classical FEM, and less DOF than Mixed FEM. Moreover, since the hybridized-mixed variational statement reflects exactly the same problem as the H^1 approximation, which means that we can observe

$$\lim_{\delta\to 0}\underline{\underline{\mathbb{E}}} = \begin{pmatrix} \underline{\underline{E}}_0^{div} & \underline{\underline{E}}_1^{div^T} \\ \underline{\underline{E}}_1^{div} & \underline{\underline{E}}_2^{div} \end{pmatrix}. \tag{5.2.-1}$$

The $\underline{\underline{E}}_0^{div}$, $\underline{\underline{E}}_1^{div}$ and $\underline{\underline{E}}_2^{div}$ matrices are the SBFEM coefficient matrices from the Ricatti eigenvalue problem given by

$$\xi\underline{\underline{\mathcal{X}}}'(\xi) = -\underline{\underline{Z}}^{div}\ \underline{\underline{\mathcal{X}}}(\xi) \tag{5.2.-1}$$

where

$$\underline{\underline{Z}}^{div} = \begin{bmatrix} \left(\left[\underline{\underline{E}}_0^{div}\right]^{-1}\left[\underline{\underline{E}}_1^{div}\right]^{T} - 0.5(d-2)\underline{\underline{I}}\right) & -\left[\underline{\underline{E}}_0^{div}\right]^{-1} \\ \left(-\underline{\underline{E}}_2^{div} + \left[\underline{\underline{E}}_1^{div}\right]^{T}\left[\underline{\underline{E}}_0^{div}\right]^{-1}\underline{\underline{E}}_1^{div}\right) & \left(-\underline{\underline{E}}_1^{div}\ \left[\underline{\underline{E}}_0^{div}\right]^{-1} + 0.5(d-2)\underline{\underline{I}}\right) \end{bmatrix} \text{ and}$$

$$\underline{\underline{\mathcal{X}}}(\xi) = \begin{Bmatrix} \underline{\underline{u}}^{e}(\xi) \\ \underline{\underline{q}}(\xi) \end{Bmatrix}$$

If $\begin{bmatrix} \underline{\underline{A}}^{div} \\ \underline{\underline{A}}^{div,q} \end{bmatrix}$ are the linearly independent eigenvectors and $\underline{\lambda}^{div}$ are the respective eigenvalues,

$$\underline{\underline{\mathcal{X}}}(\xi) = \begin{bmatrix} \underline{\underline{A}} \\ \underline{\underline{A}}^{q} \end{bmatrix}\text{diag}\left(\xi^{\underline{\lambda}}\right) \tag{5.2.-1}$$

For a bounded domain, only the positive eigenvalues and the respective eigenvectors apply (see Chapter 3 for more details). Thus, the local stiffness matrix is given by

$$\underline{\underline{K}}^{S} = \underline{\underline{A}}_{+}^{div,q}\underline{\underline{A}}_{+}^{div^{-1}} \tag{5.2.-1}$$

and the local system for a hybridized-mixed S-element

$$\underline{\underline{K}}^{S}\underline{u}^{S} = \underline{0}. \tag{5.2.-1}$$

Notice that, to construct $\underline{\underline{K}}^{S}$ it was considered a quadrilateral element $-1 \leq \hat{\xi}, \hat{\eta} \leq 1$, whilst in SBFEM Ricatti equation, $0 \leq \xi \leq 1$. It means that $\hat{\xi} \neq \xi$ since ξ represents the radial variable in the SBFEM geometric map; but $\hat{\eta} = \eta$ is the parametric surface variable. To obtain $\xi = \hat{\xi}$, the geometric map of the FE cell described in Section 5.2.1. must change. If a master element $\hat{K} = [0, -1] \times [0, 1]$ is considered, $\xi = \hat{\xi}$ but multiplier factors would appear in $\underline{\underline{\mathbb{E}}}$. In summary, there are two steps:

1. Compute $\underline{\underline{\mathbb{E}}}$ of a FE cell and obtain $\underline{\underline{E}}_0^{div}$, $\underline{\underline{E}}_1^{div}$, $\underline{\underline{E}}_2^{div}$. For this step, the geometric map is Eq. (5.2.1)
2. Compute the SBFEM approximations through the Ricatti equation. For this step, the geometric map is the usual SBFEM map, described in Chapter 3.

Yet, no source term is considered in the PDE approximated using the locally conservative SBFEM formulation. To approximate non-homogeneous PDEs, the formulation in Chapter 4 must be extended for the Hybridized-Mixed approach. For the assembly of the global problem, $d-1$-dimensional boundary elements impose the boundary condition using the Dirichlet approach.

Post-processing

Since the DOF related to the flux and internal pressure are condensed into the DOF regarding the Lagrange multipliers, the global problem provides the nodal values for the average infinitesimal pressure approximation. As observed previously, when $\delta \to 0$, the average infinitesimal pressure converges to the pressure over ∂S. Consequently, the post-processing of this variable is performed similarly to the usual H^1-approximations and is given by

$$\underline{\hat{u}}^e(\xi) = \underline{\underline{A}}_+^{div} \text{diag}(\xi^{\underline{\underline{\lambda}}^{div}}) \underline{\underline{A}}_+^{-1\,div} \underline{u}^S. \tag{5.2.-1}$$

and

$$u^e(\underline{x}) = \underline{N}_k^S(\eta) \cdot \underline{\hat{u}}^e(\xi) \tag{5.2.-1}$$

Recall that the local problem in matricial reduced form is given by

$$\underline{\underline{\mathbb{E}}}\ \underline{\mathcal{L}} = \underline{0}, \tag{5.2.-1}$$

where

$$\underline{\mathcal{L}} = \begin{Bmatrix} \underline{\mathcal{L}}^i \\ \underline{\mathcal{L}}^e \end{Bmatrix} = \begin{Bmatrix} \dfrac{1}{\xi} \dfrac{d\underline{u}^e(\xi)}{d\xi} \\ \underline{u}^e(\xi) \end{Bmatrix}. \tag{5.2.-1}$$

The flux and internal pressure are obtained simply by undoing locally the static condensation, leading to

$$\begin{Bmatrix} \underline{\mathcal{S}} \\ \underline{\mathcal{U}} \end{Bmatrix} = \begin{pmatrix} \underline{\underline{\mathbb{A}}} & -\underline{\underline{\mathbb{B}}}^T \\ \underline{\underline{\mathbb{B}}} & \underline{\underline{0}} \end{pmatrix} \begin{pmatrix} -\underline{\underline{\mathbb{C}}}^T \\ \underline{\underline{0}} \end{pmatrix} \left\{ \underline{\mathcal{L}} \right\}$$

Finally, the internal product between $\underline{\mathcal{S}}(\xi)$, $\underline{\mathcal{U}}(\xi)$ and the vectorial and scalar FE space, respectively, leads to the flux and internal pressure reconstruction

$$\underline{\sigma}^h = \sum_i \mathcal{S}_i(\xi) \underline{\hat{\psi}}$$
$$\underline{u}^{int,h} = \sum_j \mathcal{U}_j(\xi) \hat{\phi}_j.$$

In the procedure shown, the approximation functions that multiply the coefficients have terms like δ, because of the geometric map, and $\hat{\xi}$. For an SBFEM approximation though, the shape functions must be based on the tensorial product between functions in a FE trace space $\hat{\alpha}(\eta) \in \Lambda_k$ and radial functions $\hat{\rho}(\xi)$. These aspects are addressed in the following topic.

5.3 Computational Implementation

The formulation shown in this chapter was implemented in NeoPZ[2], an open-source finite-element library maintained by the Computational Mechanics Laboratory. The library

[2]https://github.com/labmec/neopz/tree/develop

has already several features to simulate mechanical problems using $H(div)$-spaces, Mixed and Hybridized-Mixed formulations for the Darcy Flow, and SBFEM-H^1 approximations. Moreover, the code is based on object-oriented C++, using small blocks, parallelism, abstract classes, and templates. Such features facilitate the computational implementation of the proposed formulation.

5.3.1 Stiffness matrix computation

To implement the formulation, the volumetric integrals over the infinitesimal width were written as integrals over $d-1$-dimensional domains. The first step was to split the formulation into external and internal DOF following the procedure

$$\begin{pmatrix} \underline{\underline{\mathbb{A}}}^{int,int} & \underline{\underline{\mathbb{A}}}^{int,i} & \underline{\underline{\mathbb{A}}}^{int,e} & -\underline{\underline{\mathbb{B}}}^{ip,int} & \underline{\underline{0}} & \underline{\underline{0}} \\ \underline{\underline{\mathbb{A}}}^{i,int} & \underline{\underline{\mathbb{A}}}^{i,i} & \underline{\underline{\mathbb{A}}}^{i,e} & -\underline{\underline{\mathbb{B}}}^{ip,i} & -\underline{\underline{\mathbb{C}}}^{i,i} & \underline{\underline{0}} \\ \underline{\underline{\mathbb{A}}}^{e,int} & \underline{\underline{\mathbb{A}}}^{e,i} & \underline{\underline{\mathbb{A}}}^{e,e} & -\underline{\underline{\mathbb{B}}}^{ip,e} & \underline{\underline{0}} & -\underline{\underline{\mathbb{C}}}^{e,e} \\ \underline{\underline{\mathbb{B}}}^{ip,int} & \underline{\underline{\mathbb{B}}}^{ip,i} & \underline{\underline{\mathbb{B}}}^{ip,e} & \underline{\underline{0}} & \underline{\underline{0}} & \underline{\underline{0}} \\ \underline{\underline{0}} & \underline{\underline{\mathbb{C}}}^{i,i} & \underline{\underline{0}} & \underline{\underline{0}} & \underline{\underline{0}} & \underline{\underline{0}} \\ \underline{\underline{0}} & \underline{\underline{0}} & \underline{\underline{\mathbb{C}}}^{e,e} & \underline{\underline{0}} & \underline{\underline{0}} & \underline{\underline{0}} \end{pmatrix} \begin{Bmatrix} \underline{\mathcal{S}}^{int} \\ \underline{\mathcal{S}}^{i} \\ \underline{\mathcal{S}}^{e} \\ \underline{\mathcal{U}}^{ip} \\ \underline{\mathcal{L}}^{i} \\ \underline{\mathcal{L}}^{e} \end{Bmatrix} = \begin{Bmatrix} \underline{0} \\ \underline{0} \\ \underline{0} \\ \underline{0} \\ \underline{0} \\ \underline{0} \end{Bmatrix} \tag{5.3.0}$$

where $\underline{\mathcal{S}}^{int}$, $\underline{\mathcal{S}}^{i}$, $\underline{\mathcal{S}}^{e}$ are the DOF related to the internal flux, differential flux and external flux, respectively; $\underline{\mathcal{U}}^{ip}$ is the DOF related to the internal pressure; and $\underline{\mathcal{L}}^{i}$ and $\underline{\mathcal{L}}^{e}$ are the differential pressure and exterior pressure, respectively.

Notice that the interior pressure $\underline{\sigma}_h^{int}$ is totally decoupled from the Lagrange multiplier approximation, leading to null block matrices in $\underline{\underline{\mathbb{C}}}^{int,i}$, $\underline{\underline{\mathbb{C}}}^{int,e}$, and the respective transposed. Moreover, since there are hybrid $d-1$-dimensional elements only over the exterior facet ∂S and the interface facet, $\underline{\underline{\mathbb{C}}}^{i,e}$ and $\underline{\underline{\mathbb{C}}}^{e,i}$ are null block matrices as well.

Each block matrix was analyzed using the software Mathematica to determine boundary integrals to implement. In other words, the mathematical expression was computed symbolically by taking the limit when $\delta \to 0$ using Mathematica. So then, let us take a look at each block matrix separately.

$\mathbb{A}$ matrix

The $\underline{\underline{\mathbb{A}}}$ matrix is subdivided into nine block matrices as

$$\underline{\underline{\mathbb{A}}} = \begin{pmatrix} \underline{\underline{\mathbb{A}}}^{int,int} & \underline{\underline{\mathbb{A}}}^{int,i} & \underline{\underline{\mathbb{A}}}^{int,e} \\ \underline{\underline{\mathbb{A}}}^{i,int} & \underline{\underline{\mathbb{A}}}^{i,i} & \underline{\underline{\mathbb{A}}}^{i,e} \\ \underline{\underline{\mathbb{A}}}^{e,int} & \underline{\underline{\mathbb{A}}}^{e,i} & \underline{\underline{\mathbb{A}}}^{e,e} \end{pmatrix} \tag{5.3.0}$$

Each block matrix has the following expressions:

$$\begin{aligned} \mathbb{A}_{i,j}^{int,int} &= \lim_{\delta \to 0} \frac{1}{\delta} \int_{-1}^{+1} \int_{-1}^{+1} \underline{\hat{\psi}}_i^{int} \cdot \underline{\hat{\psi}}_j^{int} \left| \frac{\delta(2+\delta(\hat{\xi}-1))}{4} \underline{\underline{J}}_K(1,\hat{\eta}) \right| d\hat{\eta} \\ &= \int_{-1}^{+1} \underline{\hat{\psi}}_i^{int}(\hat{\eta}) \cdot \underline{\hat{\psi}}_j^{int}(\hat{\eta}) |\underline{\underline{J}}_K(1,\hat{\eta})| d\hat{\eta}, \end{aligned}$$

where $\underline{\psi}_i^{int} = \{0, \hat{N}_i(\hat{\eta})\}$, $\underline{\psi}_j^{int} = \{0, \hat{N}_j(\hat{\eta})\}$, $i, j = 0, ..., k+1$.

$$\begin{aligned}\underline{\underline{\mathbb{A}}}_{i,l}^{int,i} &= \lim_{\delta \to 0} \frac{1}{\delta} \int_{-1}^{+1} \int_{-1}^{+1} \underline{\hat{\psi}}_i^{int} \cdot \underline{\hat{\psi}}_l^{i} \left| \frac{\delta(2 + \delta(\hat{\xi} - 1))}{4} \underline{\underline{J}}_K(1, \hat{\eta}) \right| d\hat{\eta} \\ &= \underline{\underline{0}}.\end{aligned}$$

where $\underline{\psi}_l^i = \{\delta\hat{\xi}\hat{N}_j(\hat{\eta}), 0\}$, $j = 0, ..., k$. Similarly, the other block matrices with $\underline{\hat{\psi}}^i$ components are null, i.e. $\underline{\underline{\mathbb{A}}}^{i,i} = \underline{\underline{\mathbb{A}}}^{i,e} = \underline{\underline{0}}$.

$$\begin{aligned}\mathbb{A}_{i,l}^{int,e} &= \lim_{\delta \to 0} \frac{1}{\delta} \int_{-1}^{+1} \int_{-1}^{+1} \underline{\hat{\psi}}_i^{int} \cdot \underline{\hat{\psi}}_l^{e} \left| \frac{\delta(2 + \delta(\hat{\xi} - 1))}{4} \underline{\underline{J}}_K(1, \hat{\eta}) \right| d\hat{\eta} \\ &= \int_{-1}^{+1} \underline{\hat{\psi}}_i^{int}(\hat{\eta}) \cdot \underline{\hat{\psi}}_l^{e}(\hat{\eta}) \left| \underline{\underline{J}}_K(1, \hat{\eta}) \right| d\hat{\eta},\end{aligned}$$

where $\underline{\hat{\psi}}_l^e = \{\hat{N}_l(\hat{\eta}), 0\}$, $l = 0, ..., k$.

$$\begin{aligned}\mathbb{A}_{m,l}^{e,e} &= \lim_{\delta \to 0} \frac{1}{\delta} \int_{-1}^{+1} \int_{-1}^{+1} \underline{\hat{\psi}}_m^{e} \cdot \underline{\hat{\psi}}_l^{e} \left| \frac{\delta(2 + \delta(\hat{\xi} - 1))}{4} \underline{\underline{J}}_K(1, \eta) \right| d\hat{\eta} \\ &= \int_{-1}^{+1} \underline{\hat{\psi}}_m^{e}(\hat{\eta}) \cdot \underline{\hat{\psi}}_l^{e}(\hat{\eta}) \left| \underline{\underline{J}}_K(1, \hat{\eta}) \right| d\hat{\eta},\end{aligned}$$

where $\underline{\hat{\psi}}_m^e = \{\hat{N}_m(\hat{\eta}), 0\}$, $l = 0, ..., k$. Also, $\underline{\underline{\mathbb{A}}}^{e,int} = [\underline{\underline{\mathbb{A}}}^{int,e}]^T$. Thus,

$$\underline{\underline{\mathbb{A}}} = \begin{pmatrix} \underline{\underline{\mathbb{A}}}^{int,int} & \underline{\underline{0}} & \underline{\underline{\mathbb{A}}}^{int,e} \\ \underline{\underline{0}} & \underline{\underline{0}} & \underline{\underline{0}} \\ [\underline{\underline{\mathbb{A}}}^{int,e}]^T & \underline{\underline{0}} & \underline{\underline{\mathbb{A}}}^{e,e} \end{pmatrix} \tag{5.3.-4}$$

$\underline{\underline{\mathbb{B}}}$ matrix

The $\underline{\underline{\mathbb{B}}}$ matrix is subdivided into three block matrices, resulting in

$$\underline{\underline{\mathbb{B}}} = \begin{pmatrix} \underline{\underline{\mathbb{B}}}^{ip,int} & \underline{\underline{\mathbb{B}}}^{pi,i} & \underline{\underline{\mathbb{B}}}^{pi,e} \end{pmatrix} \tag{5.3.-4}$$

where the superscript ip is related to the internal pressure and the superscript int, i, and e are related to the internal flux and exterior flux in the fictitious interface and exterior ∂S.

For the $\underline{\underline{\mathbb{B}}}^{ip,int}$, the integrals are

$$\begin{aligned}\mathbb{B}_{i,j}^{ip,int} &= \lim_{\delta \to 0} \frac{1}{\delta} \int_{-1}^{+1} \int_{-1}^{+1} \left(\nabla \cdot \underline{\hat{\psi}}_i^{ip} \right) \hat{\phi}_j \left| \frac{\delta \left(2 + \delta(\hat{\xi} - 1) \right)}{4} \underline{\underline{J}}_K(1, \hat{\eta}) \right| d\hat{\eta} d\hat{\xi} \\ &= \int_{-1}^{+1} \left(\nabla \cdot \underline{\hat{\psi}}_i^{ip}(\hat{\eta}) \right) \hat{\phi}_j(\hat{\eta}) |\underline{\underline{J}}_K(1, \hat{\eta})| d\hat{\eta},\end{aligned}$$

where $\hat{\phi}_j = \hat{N}_j(\hat{\eta})$ and $\underline{\hat{\psi}}_i^{ip} = \{0, \hat{N}_i(\hat{\eta})\}$. Also,

$$\begin{aligned}\mathbb{B}_{i,j}^{ip,i} &= \lim_{\delta \to 0} \frac{1}{\delta} \int_{-1}^{+1} \int_{-1}^{+1} \left(\nabla \cdot \underline{\hat{\psi}}_i^{e} \right) \hat{\phi}_j \left| \frac{\delta \left(2 + \delta(\hat{\xi} - 1) \right)}{4} \underline{\underline{J}}_K(1, \hat{\eta}) \right| d\hat{\eta} d\hat{\xi} \\ &= \underline{\underline{0}},\end{aligned}$$

where $\underline{\hat{\psi}}_i^i = \{\delta\hat{\xi}\hat{N}_i(\hat{\eta}), 0\}$. Last,

$$\mathbb{B}_{i,j}^{ip,e} = \lim_{\delta\to 0}\frac{1}{\delta}\int_{-1}^{+1}\int_{-1}^{+1}\left(\nabla\cdot\underline{\hat{\psi}}_i^i\right)\hat{\phi}_j\ \left|\frac{\delta\left(2+\delta(\hat{\xi}-1)\right)}{4}\underline{\underline{J}}_K(1,\hat{\eta})\right|\ d\hat{\eta}d\hat{\xi}$$
$$= \int_{-1}^{+1}\hat{N}_i(\hat{\eta})\hat{\phi}_j(\hat{\eta})\ \left|\underline{\underline{J}}_K(1,\hat{\eta})\right|\ d\hat{\eta},$$

where $\underline{\hat{\psi}}_i^e = \{\hat{N}_i(\hat{\eta}), 0\}$. Thus, $\underline{\underline{\mathbb{B}}}$ matrix is written as

$$\underline{\underline{\mathbb{B}}} = \begin{pmatrix}\underline{\underline{\mathbb{B}}}^{ip,int} & \underline{\underline{0}} & \underline{\underline{\mathbb{B}}}^{ip,e}\end{pmatrix}. \tag{5.3.-4}$$

Last, $\underline{\underline{\mathbb{C}}}^{i,i}$ and $\underline{\underline{\mathbb{C}}}^{e,e}$ are already $d-1$ integrals over the skeleton mesh $\mathcal{E}^h$ given by Eq. (5.2.3).

Stiffness matrix of a hybridized-mixed Scaled Boundary FE

The local matrix for the S-element is given by

$$\begin{pmatrix}\underline{\underline{\mathbb{A}}}^{int,int} & \underline{\underline{0}} & \underline{\underline{\mathbb{A}}}^{int,e} & \underline{\underline{\mathbb{B}}}^{ip,int} & \underline{\underline{0}} & \underline{\underline{0}}\\ \underline{\underline{0}} & \underline{\underline{0}} & \underline{\underline{0}} & \underline{\underline{0}} & \underline{\underline{\mathbb{C}}}^{i,i} & \underline{\underline{0}}\\ \underline{\underline{\mathbb{A}}}^{e,int} & \underline{\underline{0}} & \underline{\underline{\mathbb{A}}}^{e,e} & \underline{\underline{\mathbb{B}}}^{pi,e} & \underline{\underline{0}} & \underline{\underline{\mathbb{C}}}^{e,e}\\ \underline{\underline{\mathbb{B}}}^{ip,int} & \underline{\underline{0}} & \underline{\underline{\mathbb{B}}}^{ip,e} & \underline{\underline{0}} & \underline{\underline{0}} & \underline{\underline{0}}\\ \underline{\underline{0}} & \underline{\underline{\mathbb{C}}}^{i,i} & \underline{\underline{0}} & \underline{\underline{0}} & \underline{\underline{0}} & \underline{\underline{0}}\\ \underline{\underline{0}} & \underline{\underline{0}} & \underline{\underline{\mathbb{C}}}^{e,e} & \underline{\underline{0}} & \underline{\underline{0}} & \underline{\underline{0}}\end{pmatrix}\begin{Bmatrix}\underline{\mathcal{S}}^{int}\\ \underline{\mathcal{S}}^{i}\\ \underline{\mathcal{S}}^{e}\\ \underline{\mathcal{U}}^{ip}\\ \underline{\mathcal{L}}^{i}\\ \underline{\mathcal{L}}^{e}\end{Bmatrix} = \begin{Bmatrix}\underline{0}\\ \underline{0}\\ \underline{0}\\ \underline{0}\\ \underline{0}\\ \underline{0}\end{Bmatrix} \tag{5.3.-4}$$

A static condensation is performed locally, condensing the DOF related to $\underline{\mathcal{S}}^{int}$, $\underline{\mathcal{S}}^{i}$, $\underline{\mathcal{S}}^{e}$ and $\underline{\mathcal{U}}^{ip}$ into $\underline{\mathcal{L}}^{i}$ and $\underline{\mathcal{L}}^{e}$,

$$\underline{\underline{\mathbb{E}}} = \begin{pmatrix}\underline{\underline{0}} & \underline{\underline{\mathbb{C}}}^{i,i} & \underline{\underline{0}}\\ \underline{\underline{0}} & \underline{\underline{0}} & \underline{\underline{\mathbb{C}}}^{e,e}\end{pmatrix}\begin{pmatrix}\underline{\underline{\mathbb{A}}}^{int,int} & \underline{\underline{0}} & \underline{\underline{\mathbb{A}}}^{int,e} & -\underline{\underline{\mathbb{B}}}^{ip,int}\\ \underline{\underline{0}} & \underline{\underline{0}} & \underline{\underline{0}} & -\underline{\underline{0}}\\ \underline{\underline{\mathbb{A}}}^{e,int} & \underline{\underline{0}} & \underline{\underline{\mathbb{A}}}^{e,e} & -\underline{\underline{\mathbb{B}}}^{pi,e}\\ \underline{\underline{\mathbb{B}}}^{ip,int} & \underline{\underline{0}} & \underline{\underline{\mathbb{B}}}^{pi,e} & \underline{\underline{0}}\end{pmatrix}^{-1}\begin{pmatrix}\underline{\underline{0}} & \underline{\underline{0}}\\ \underline{\underline{\mathbb{C}}}^{i,i} & \underline{\underline{0}}\\ \underline{\underline{0}} & \underline{\underline{\mathbb{C}}}^{e,e}\end{pmatrix} \tag{5.3.-4}$$

Recall that the condensed system is written as $\underline{\underline{\mathbb{E}}}\ \underline{\mathcal{L}} = \underline{0}$ (Eq. 5.2.3) and $\underline{\underline{\mathbb{E}}}$ is written in terms of the SBFEM coefficient matrices (Eq. (5.2.3)). Thus, the local system leads to

$$\begin{pmatrix}\underline{\underline{E}}_0^{div} & \underline{\underline{E}}_1^{div^T}\\ \underline{\underline{E}}_1^{div} & \underline{\underline{E}}_2^{div}\end{pmatrix}\begin{Bmatrix}\underline{\mathcal{L}}^i\\ \underline{\mathcal{L}}^e\end{Bmatrix} = \begin{Bmatrix}\underline{0}\\ \underline{0}\end{Bmatrix}. \tag{5.3.-4}$$

The solution for the flux and for the internal pressure is obtained by undoing the static condensation locally per S-element as

$$\begin{Bmatrix}\underline{\mathcal{S}}^{int}(\xi)\\ \underline{\mathcal{S}}^{i}(\xi)\\ \underline{\mathcal{S}}^{e}(\xi)\\ \underline{\mathcal{U}}^{ip}(\xi)\end{Bmatrix} = -\begin{pmatrix}\underline{\underline{\mathbb{A}}}^{int,int} & \underline{\underline{0}} & \underline{\underline{\mathbb{A}}}^{int,e} & \underline{\underline{\mathbb{B}}}^{ip,int}\\ \underline{\underline{0}} & \underline{\underline{0}} & \underline{\underline{0}} & \underline{\underline{0}}\\ \underline{\underline{\mathbb{A}}}^{int,int} & \underline{\underline{0}} & \underline{\underline{\mathbb{A}}}^{int,e} & \underline{\underline{\mathbb{B}}}^{int,int}\\ \underline{\underline{\mathbb{A}}}^{e,int} & \underline{\underline{0}} & \underline{\underline{\mathbb{A}}}^{e,e} & \underline{\underline{\mathbb{B}}}^{ip,e}\\ \underline{\underline{\mathbb{B}}}^{ip,int} & \underline{\underline{0}} & \underline{\underline{\mathbb{B}}}^{ip,e} & \underline{\underline{0}}\end{pmatrix}^{-1}\begin{pmatrix}\underline{\underline{0}} & \underline{\underline{0}}\\ \underline{\underline{\mathbb{C}}}^{i,i} & \underline{\underline{0}}\\ \underline{\underline{0}} & \underline{\underline{\mathbb{C}}}^{e,e}\\ \underline{\underline{0}} & \underline{\underline{0}}\end{pmatrix}\begin{Bmatrix}\underline{\mathcal{L}}^i(\xi)\\ \underline{\mathcal{L}}^e(\xi)\end{Bmatrix}. \tag{5.3.-4}$$

leading to

$$\underline{\sigma}_h(\underline{x}) = \sum_i \underline{\psi}_i^{int}(\eta)\mathcal{S}_i^{int}(\xi) + \sum_j \underline{\psi}_j^{i}(\eta)\mathcal{S}_j^{i}(\xi) + \sum_l \underline{\psi}_l^{e}(\eta)\mathcal{S}_l^{e}(\xi)$$
$$u_h^{int}(\underline{x}) = \underline{\hat{\phi}}(\eta)\cdot\underline{\mathcal{U}}^{ip}(\xi).$$

Last, since $u^e = u^i = u^{int}$ when $\delta\to 0$, $u_h^{int}(\underline{x}) = u^e(\underline{x})$ necessarily.

5.3.2 Class structure

The code follows an object-oriented philosophy using class structure to couple overlapping meshes. The classes and methods implemented can be grouped according to the tasks involved in a FE simulation:

- Geometric and Computational Meshes;
- Approximation spaces;
- Weak formulations;
- Post-processing.

The idea of implementing Hybridized SBFEM approximation in NeoPZ is to use the classes and algorithm structure already existing in NeoPZ for the FEM multiphysics simulation. An overview of the tasks involved in an SBFEM simulation using NeoPZ is summarized as follows:

1. Create a geometric mesh with the skeleton mesh **or** the volumetric elements (a classical FE mesh). From such a mesh, create Duffy's geometric elements and set a volumetric material identification (material id).
2. Create a computational SBFEM mesh for the pressure. Three material ids are related to the pressure: the skeleton material id for the skeleton mesh, composed of the external pressure; the internal pressure, and the differential pressure. The volumetric elements do not have approximation space associated since the SBFEM approximates only the boundary of ∂S and the trace approximation is extended in an analytical procedure inside Duffy's elements.
3. Create a computational SBFEM mesh for the flux.
4. Create a multiphysics computational SBFEM mesh composed of the pressure and flux meshes.
   (a) Create SBFEM multiphysics elements.
   (b) Define the DOF to be condensed.
5. Initialize the analysis, in which the SBFEM stiffness matrices are computed based on the SBFEM-$H(div)$ coefficient matrices.
   (a) For each Scaled Boundary FE, perform the static condensation and compute the eigenvalues and eigenvectors.
   (b) Compute the local SBFEM stiffness matrix using the eigenvectors.
6. Post-process error and solution visualization using Paraview for the SBFEM shape functions.
   (a) For each Scaled Boundary FE, undo the static condensation to obtain the nodal solution for the flux and the pressure.
   (b) Post-process solution for each Duffy's element.

The code insertions in NeoPZ focused on implementing classes to build the SBFEM multiphysics computational mesh, computing the stiffness matrix based on the eigenvalue

problem, and post-processing the solution for each Scaled Boundary FE. The classes implemented are described in sequence.

TPZBuildSBFemMultiphysics: The goal of this class is to implement the hybridized-mixed SBFEM mesh. For that, two steps are performed.

1. Build the geometric SBFEM mesh: In this step, Duffy's elements are created following one of the configurations
   (a) Input mesh is a geometric FE mesh (such as a usual mesh from a gmsh file): create Duffy's elements considering the geometric centroid as the scaling center, and each facet is the side L of Duffy's elements. Create the $d-1$ elements for pressure and flux.
   (b) Input mesh is a skeleton mesh: In this case, the user must also pass as input the partitions in which each skeleton element belongs and the scaling center. Based on this data, the method builds Duffy's elements and the geometric elements related to the flux.
2. Build the computational SBFEM mesh: based on the geometric mesh, the following computational elements are created:
   (a) $d-1$ computational elements for flux and pressure approximations;
   (b) Volumetric computational elements: these elements have no DOF associated due to their definition of the Scaled Boundary FE;
   (c) Multiphysics elements that couples flux and pressure approximation.

.

The $d-1$ computational pressure elements are simply L^2 elements. Since the NeoPZ does have a computational implementation for discontinuous elements, no additional code was required for the trace approximation for the pressure. However, the $H(div)$ trace space for the SBFEM is unusual since the direction of the normal vector is defined by the geometric Duffy's element, and fewer shape functions are required to compose the finite-dimensional space (see Fig. 5.10).

TPZCompElHDivSBFem: This class implements the computational element related to the SBFEM-$H(div)$ space.

TPZSBFemMultiphysicsElGroup: This class implements hybridized-mixed scaled boundary FEs and computes the SBFEM coefficient matrices, the pair of eigenvalues and eigenvectors related to the locally conservative SBFEM problem and the local stiffness matrix. Such a class is composed of:

1. $d-1$ flux, pressure, and multiphysics computational SBFEM elements;
2. SBFEM volumetric elements.

The computational volumetric elements are responsible for post-processing the SBFEM skeleton solution. In other words, these classes extend the trace approximation to the interior of Duffy's element.

TPZSBFemVolumeL2: Computational Duffy's element that performs integral computations for state variables in the L^2-space;

TPZSBFemVolumeHdiv: Computational Duffy's element that performs integral computations for variable in the SBFEM-$H(div)$ space;

TPZSBFemVolumeMultiphysics: Computational multiphysics Duffy's element that couples the TPZSBFemVolumeL2 and TPZSBFemVolumeHdiv elements.

5.4 Numerical tests

5.4.1 Example 1: 2D Polynomial Darcy Flow

The first numerical test is a polynomial Darcy Flow given by

$$\begin{aligned} \nabla \cdot \underline{\sigma} &= 0 \\ \underline{\sigma} = -K\nabla u &= -\begin{Bmatrix} 6x^5 - 60x^3y^2 + 30xy^4 \\ -30x^4y + 60x^2y^3 - 6y^5 \end{Bmatrix} \end{aligned}$$

in a 2D domain $\Omega = [-1,-1] \times [1,1]$. The analytical pressure is expressed as

$$u = -15x^4y^2 + 15x^2y^4 + x^6 - y^6. \tag{5.4.0}$$

Dirichlet boundary conditions for the pressure over $\partial\Omega$ are considered.

Two mesh configurations are tested for polynomial trace approximations $k = 1, ..., 6$, namely

- Case 1: Partition $\mathcal{T}^h = \{S\}$ composed of a single S-element. Skeleton refinement is performed. Namely, each side of ∂S is subdivided into n subintervals. The scaling center is positioned in the center $(x, y) = (0, 0)$, which means that the S-element is composed of $4n$ uniform triangles.

- Case 2: Uniform partition $\mathcal{T}^h$ composed of a dense mesh with $n \times n$ quadrilateral S-elements. Each S-element is composed of four uniforms Duffy's elements with a scaling center positioned at the element's centroid.

Both meshes are refined three times, leading to characteristic width of $h = 2^{1-\ell}$, $\ell = 0, ..., 3$. Figure 5.12 shows case 1 and 2 meshes for $\ell = 3$ and $h = 0.25$.

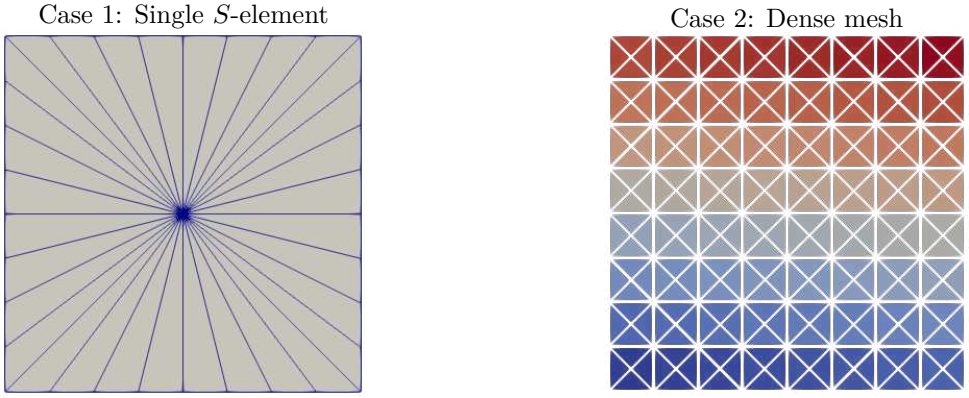

Figure 5.12: Example 1: Geometric SBFEM mesh refinement for $h = 0.25$: Case 1 - Dense mesh and Case 2 - Single S-element mesh.

The convergence solution for a single S-element refining the skeleton is shown in Fig. 5.13. Optimal rates of convergence are obtained for the flux L^2 error. Yet, the analytical solution is recovered for $k = 4$ even though the solution is a 5th-order polynomial. This fact occurs because the $H(div)$ space is enriched with $k+1$ internal functions in η-direction, which were enough to recover the analytical solution for $k = 4$. Still, in Fig. 5.13, optimal rates of convergence were obtained for the pressure approximation and the analytical solution recovered for $k = 6$. Analogous results were obtained for the dense mesh case, as shown in Fig. 5.14. For both curves, the last refinement step (i.e. characteristic size $h = 0.25$) for $k = 6$ presented small disturbances similarly to what was verified in H^1 examples in Chapters 3 and 4. Such disturbances occurs when the size of the eigenvalue problem increases, leading to an ill-conditioned matrix, pairs of eigenvalues/eigenvectors composed of complex numbers and numerical issues. Song (2018) already documented this problem and suggests using the Schur decomposition instead of the usual eigenvalue decomposition.

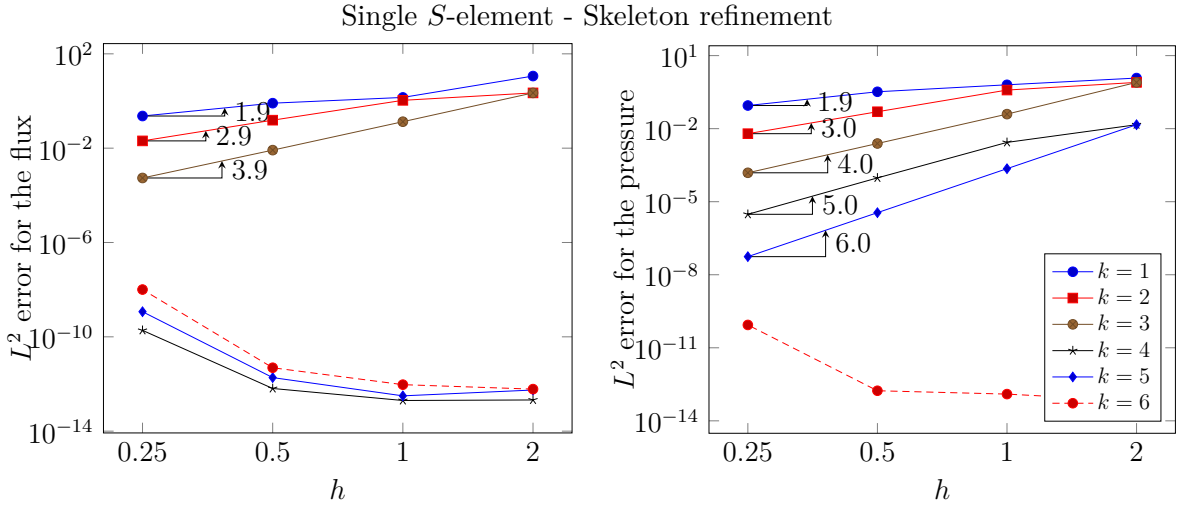

Figure 5.13: Example 1 - Case 1 - Energy and L^2 errors versus $h = 2/2^\ell$, $\ell = 0, ..., 3$, using the SBFEM in uniform skeleton partitions of a single S-elements for $k = 1, ..., 6$.

For the dense mesh configuration, similar results were obtained with similar error values, as shown in Fig. 5.14. Optimal convergence rates were obtained for the L^2 norm of the

flux and pressure. The analytical result for the flux was recovered from $k = 4$. Numerical instabilities were also found in the analytical solution of the flux. Yet, the maximum numerical magnitude order for the error was $\approx 10^{-11}$.

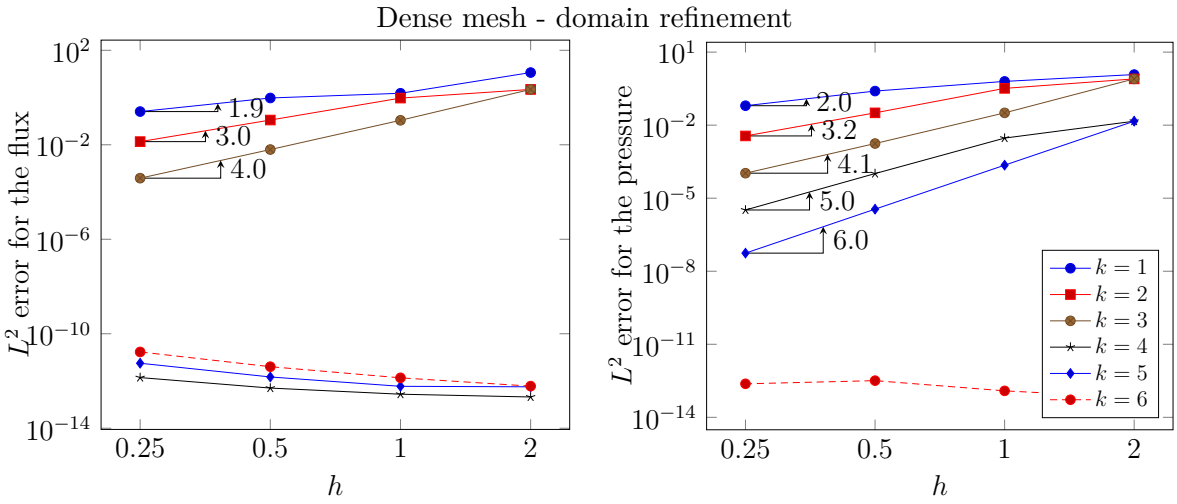

Figure 5.14: Example 1 - Case 2 - Energy and L^2 errors versus $h = 2/2^{\ell}$, $\ell = 0, ..., 3$, using the SBFEM-$H(div)$ formulation in uniform partitions of quadrilateral S-elements for $k = 1, ..., 6$.

5.4.2 Example 2: 2D Darcy Flow

The second numerical test is a two-dimensional Darcy Flow expressed as

$$\nabla \cdot \underline{\sigma} = 0,$$
$$\underline{\sigma} = -K\nabla u = \begin{Bmatrix} \exp \pi x \pi \sin \pi y \\ \exp \pi x \pi \cos \pi y \end{Bmatrix},$$

defined in a domain $\Omega = [-1, -1] \times [1, 1]$, for $K = 1$. The analytical solution for the pressure and the flux vector field is plotted in Fig. 5.15. The SBFEM approximation was based on trace approximation space from $k = 1$ to $k = 7$, using a uniform mesh of $n \times n$ S-elements where $n = 2^{-\ell+1}$, $\ell = 0, .., 3$ (see Fig. 5.12 - Dense mesh).

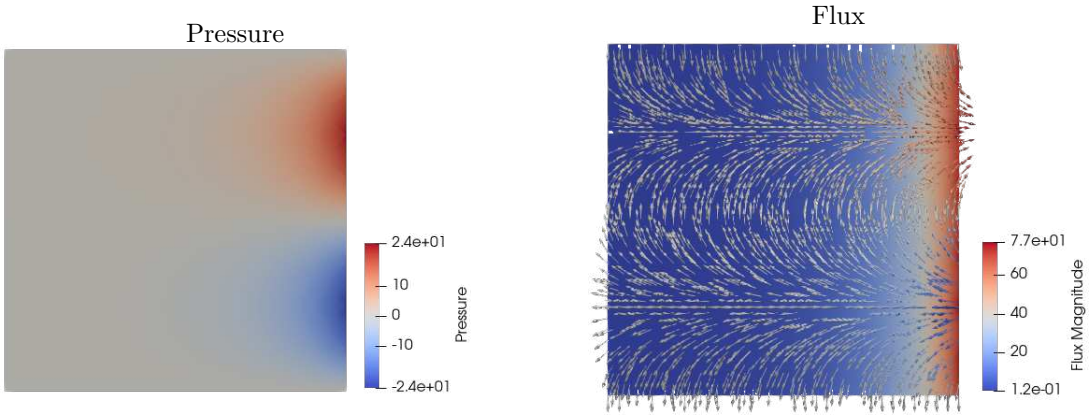

Figure 5.15: Example 2: Analytical solution for the pressure u and the flux $\underline{\sigma}$.

In this example, the SBFEM-$H(div)$ formulation developed in this chapter is compared to the SBFEM-H^1 approximation presented in Chapter 3. For that, a dense mesh of $n \times n$ elements is considered, where $n = 2^{-\ell+1}$, $\ell = 0, .., 3$ (see Fig. 5.12 - Dense mesh).

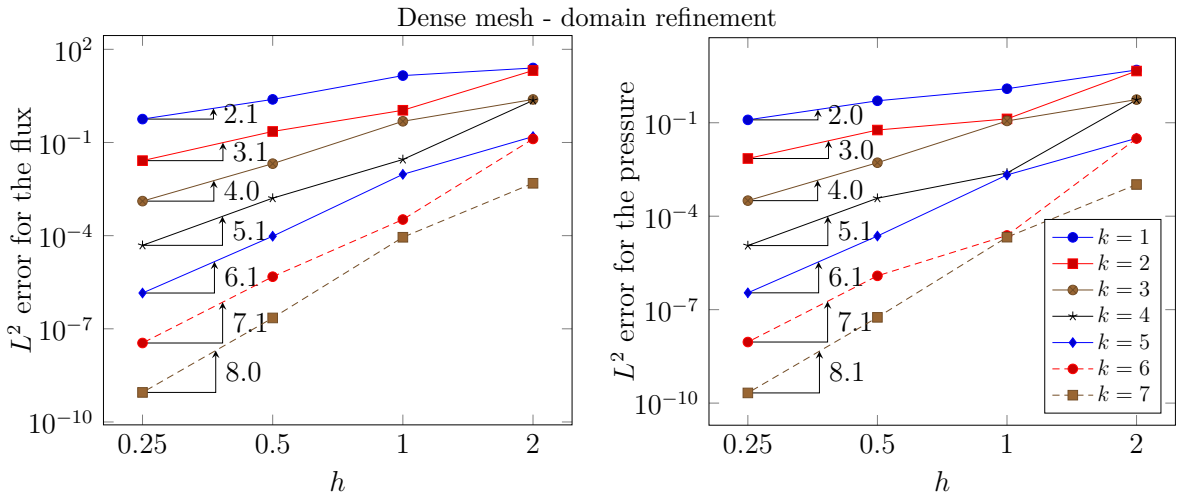

Figure 5.16: Example 2 - Energy and L^2 errors versus $h = 2/2^\ell$, $\ell = 0, ..., 3$, using the Galerkin SBFEM with bubbles in uniform partitions of quadrilateral S-elements for $k = 1, ..., 7$.

5.4.3 2D single crack

The last numerical example refers to a Darcy Flow in which the analytical solution has a square-root singularity, given by

$$\nabla \cdot \underline{\sigma} = 0,$$
$$\underline{\sigma} = -K\nabla u = \begin{Bmatrix} 2^{-3/4} r^{-1/2} \cos\theta/2 \\ -2^{-3/4} r^{-1/2} \sin\theta/2 \end{Bmatrix}$$

defined in a two-dimensional domain $\Omega = [-1, -1] \times [1, 1]$. The analytical solution for the pressure and the flux is shown in Fig. 5.18 and 5.17.

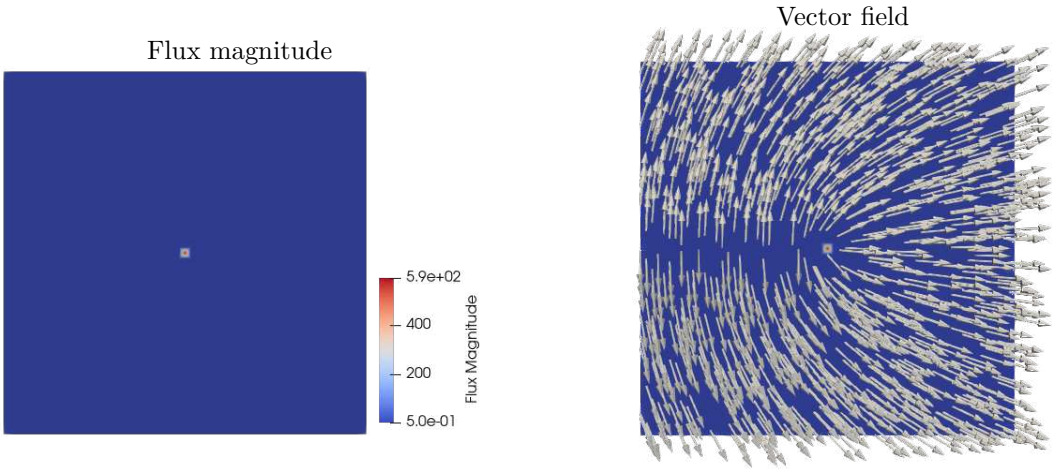

Figure 5.17: Example 2: Analytical solution for flux $\underline{\sigma}$: (a) flux magnitude, (b) vector field (only direction).

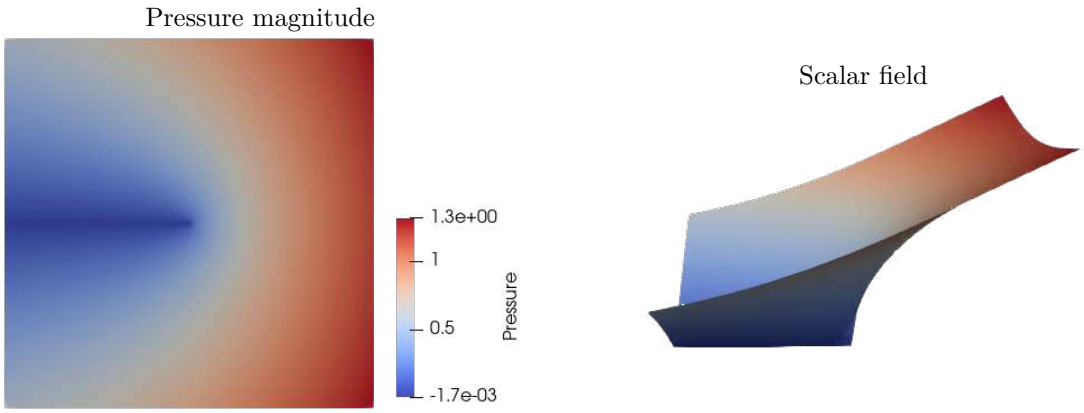

Figure 5.18: Example 2: Analytical solution for flux u: (a) pressure magnitude, (b) pressure field (only direction).

For this example, the numerical simulation is performed considering a mesh partition of a single S-element, $\mathcal{T}^h = \{S\}$ refined only at the element's skeleton. For the fracture example, the scaling center must be positioned at the crack's tip, which is located at $(0, 0)$. The most refined mesh is similar to the first example, as illustrated in Fig. 5.12 - Case 1: Single S-element. Polynomial trace approximation up to the fourth order was considered. Figure 5.19 shows that optimal convergence rates were obtained for the L^2 norm of the flux and the pressure.

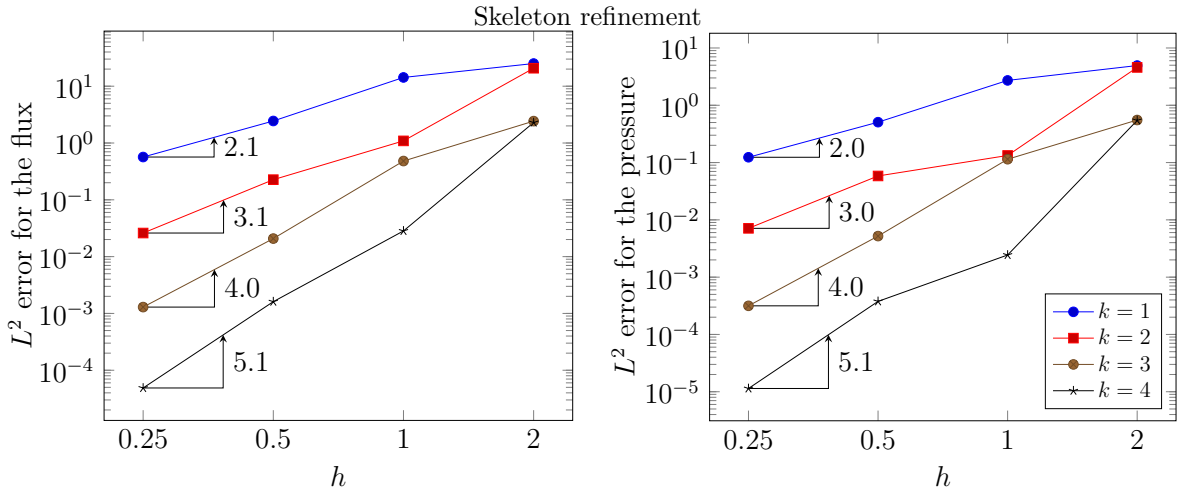

Figure 5.19: Example 3 - Energy and L^2 errors versus $h = 2/2^\ell$, $\ell = 0, 1, 2$, using a single S-element for $k = 1, ..., 4$.

5.5 Conclusions

This chapter shows that locally conservative approximations for the SBFEM can be obtained by applying the ballooning technique in a hybridized-mixed FE cell of infinitesimal width. The limit of the width tending to zero leads to an almost analytical solution in the radial component, similarly to the SBFEM for H^1 approximations. Optimal convergence rates for the L^2 norm of the flux and the pressure were obtained, considering either skeleton refinement or a dense mesh. Although simple examples were addressed in this thesis, yet, the numerical experiments prove that the formulation leads to optimal

convergence rates even for problems with square-root singularities. Although only two-dimensional examples were considered, the formulation is generic and the computational algorithm can be extended to three-dimensional problems. The major advantage is the local conservation of mass imposed directly in the approximation space.

Further studies must address the extension of the proposed formulation to more complex applications. First and more intuitive is the extension of the SBFEM-$H(div)$ computational code to three-dimensional problems. Also, a useful application is simulating a fractured porous media, such as in Discrete Fracture Networks, as already explored by Devloo et al. (2019a) and Berre et al. (2021) for two and three-dimensional problems using Mixed FEM. Finally, another application is in numerical simulations using multiscale methods, for instance, to improve the Multiscale Hybrid Mixed method (MHM-$H(div)$). Also, a posteriori error estimates can be developed using the studies of Batistela et al. (2022) and the references cited therein as the basis.

Chapter 6

Conclusion and future research

As developed over this thesis, the SBFEM can be seen from two different points of view. First, the SBFEM was presented as a type of Duffy's approximation space. Also, the SBFEM can be seen as a general ballooning technique applied in a generic star-shaped geometric element (but also using Duffy geometric maps), considering an infinite number of layers.

Chapters 3 and 4 explored the fact of SBFEM being a subspace of general Duffy's approximation space. The SBFEM approximation is based on partitions of the computational domain by polygonal/polyhedral subregions, where the shape functions approximate local Dirichlet problems with piecewise polynomial trace data. These basis functions are constructed using a semi-analytical approach, using this operator adaptation approach. By imposing a starlike scaling requirement on the subregions, the representation of local SBFEM shape functions in radial and surface directions are obtained from eigenvalues and eigenvectors solution of an ODE system, whose coefficients are determined by the element geometry and the trace polynomial spaces. Duffy's framework is the key to understanding and proving the SBFEM convergence, as explored to define a priori error estimates in Chapter 3. Yet, Duffy's approximation space was applied to construct a bubble enrichment for approximating two and three-dimensional elliptic and parabolic problems using the SBFEM, as developed in Chapter 4.

The second point of view is to understand the SBFEM as applying the ballooning technique in a FE considering an infinite number of layers. Ballooning means dividing a FE into several slices and then performing recurrent static condensations. This technique is based on observing that the stiffness matrix in the FEM does not vary according to the width of the layer or even the position. The limit of this operation tending to infinity leads to the analytical solution over the radial direction. In other words, when the limit of the infinitesimal layer width tends to zero, the approximated solution tends to be the analytical solution in the radial direction. In Chapter 5, the ballooning technique was the key to developing a hybridized-mixed SBFEM formulation.

SBFEM as Duffy's space

Using Duffy's FE theory, a priori error estimates for SBFEM's solutions of harmonic test problems was provided in Chapter 3 and a bubble enrichment was proposed to approximate the solution of non-homogeneous PDEs in Chapter 4.

The SBFEM space is a subspace of Duffy's approximations in which a gradient-orthogonality constraint is imposed. Scaled boundary functions being gradient-orthogonal to any function in Duffy's spaces vanishing at the mesh skeleton is a consequence of the function space definition. This orthogonality property is applied to provide a priori SBFEM error estimates in terms of known finite element interpolant errors of the exact solution. Similarities with virtual harmonic approximations are also explored to understand SBFEM convergence properties. Numerical experiments with 2D and 3D polytopal meshes confirm optimal SBFEM convergence rates for two test problems with smooth solutions. Attention is also paid to the approximation of a point singular solution by using SBFEM close to the singularity and finite element approximations elsewhere, revealing optimal accuracy rates of standard regular contexts.

SBFEM approximation errors come from two sources: one is due to the trace of approximated functions over the facets of ∂S, and the other is related to the deviation of the radial extensions inside S. The fact that the first source of error is the dominant one is favorable for applications for singular problems, where the singularity may be isolated, without interaction with the S-element facets. For this class of problems, the solution away from the singularity is regular. If the convergence rate is dominated by the approximation on the boundary of S, then this explains regular convergence rates even for singular problems, as illustrated by the verification simulations. Due to the method's features, and the problems with square-root singularities, the scaling center must be located at the singularity point.

This thesis also proposed a polynomial bubble enrichment based on tensorial Duffy's functions. These spaces have optimal rates for approximating two and three-dimensional non-homogeneous PDEs. The proof is based on the convergence of Duffy's polynomial approximation spaces. Since the polynomial Duffy's space is a FE approximation space that converges with optimal convergence rates and is a subspace of the SBFEM enriched space, and the first converges with optimal convergence rates, the proposed SBFEM space converges as well. Numerical examples of Poisson and Elasticity problems for two and three-dimensional domains emphasize the theoretical results. Yet, it is shown that the bubble enrichment is orthogonal in the energy norm to the SBFEM approximation for homogeneous PDEs. This fact implies a decoupled skeleton and interior approximation for static simulations. In other words, adding bubble Duffy functions to the SBFEM space does not modify the skeleton solution. Thus, the SBFEM solution already provides the best approximation for the skeleton.

SBFEM as a balooning process

The second point of view, regarding the SBFEM as a ballooning process, is suitable to extend the SBFEM formulation as a general technique applied to improve FE approximations. This strategy was applied to obtain locally conservative SBFEM approximations using a hybridized-mixed approach in Chapter 5.

First, this thesis shows that the SBFEM coefficient matrices for H^1 approximations can be obtained through an infinitesimal FE cell. The same technique was applied for a Darcy Flow described by a hybridized-mixed variational statement. Static condensation is performed to reduce the DOF and write the problem as a function of the pressure. The DOF is slightly modified to write the DOF as the infinitesimal average and differential pressure, instead of usual nodal pressure values. From the condensed stiffness matrix, the

SBFEM coefficient matrices are obtained. The flux is constructed locally per element by undoing the static condensation. Numerical examples of 2D Darcy Flows illustrate the optimal convergence rates for the L^2 norm of flux and pressure.

It is worth mentioning that the technique to obtain the SBFEM coefficient matrices using an infinitesimal FE cell can be applied to any method in which the ballooning process can be utilized. From such a point of view, the SBFEM can be seen as a general technique that can be applied in other FE formulations beyond classical FEM and hybridized-mixed FEM.

Highlights

To summarize, the novel topics addressed in this thesis were:

1. A priori error estimates for the energy norm for homogeneous PDEs;
2. A bubble enrichment for the SBFEM to approximate three-dimensional elliptic PDEs;
3. A priori error estimates for both energy and L^2 norm for non-homogeneous PDEs;
4. Locally conservative SBFEM formulations for two-dimensional Darcy Flows, based on hybridized-mixed FEM.

6.1 Future works

In this thesis, the convergence was proven only for the energy norm. Additional efforts may be dedicated to proving the optimal convergence rate for the L^2 norm. Yet, only a priori error estimates were addressed in this Chapter 3. Further studies might address a posteriori error estimates as well. Recent studies from the Computational Mechanics Laboratory derive a posteriori error estimations for enriched mixed methods (BATISTELA; SIQUEIRA; DEVLOO, 2020) for Poisson problems. Such studies may be extended to derive a general methodology, based on potential and flux reconstruction, for the SBFEM for H^1 and $H(div)$ formulation.

Lack of convergence is observed in high-order SBFEM approximations for 3D problems using bubble enrichment. This fact occurs because, in such approximations, the SBFEM eigenvalues lead to complex values and numerical instabilities. An alternative to overcome this issue for homogeneous problems is addressed by Song in (SONG, 2018). In his book, Song suggests using the Schur Decomposition instead of traditional eigenvalue decomposition to avoid complex numbers and numerical instabilities. Therefore, future work might be to apply the same decomposition for the non-homogeneous problems to recover optimal convergence rates for high-order 3D problems.

The thesis involves locally conservative approximations in two-dimensional domains and Darcy Flows only. The algorithms presented in this thesis can be also extended for three-dimensional Darcy Flows. In this case, there is no difference between two and three-dimensional mathematical formulations. The dissimilarities that arise are only from a numerical implementation point of view. Other mechanical problems can be also the focus of studies, such as Elasticity for incompressible materials and Stokes flow. Although the variational statement using hybridized-mixed FEM for these problems is widely known

in the literature, applying the scaled boundary technique in these cases might add some advantages such as optimal convergence rates for problems with point singularities, and flexible mesh generation.

Another topic of further study is to apply the SBFEM in multiscale simulations. The FE library utilized in this thesis, the NeoPZ, already has the framework to solve multiscale problems using a mixed-hybrid approach, but only for FEM. This method, known as Multiscale Hybrid Mixed (MHM) method already exists for H^1 and $H(div)$ approximations. For these cases, the S-elements in the SBFEM can be used as the macro-elements of the coarse mesh.

Finally, topics about the generalization of SBFEM can be addressed in further studies, such as constructing complete De Rham sequences. Also, since the SBFEM is can be seen as a ballooning technique, it means that it can be applied in any FE technique that allows subdividing the FE into an infinite number of slices. Such an approach allows generalizing the SBFEM and applying it together with other FE methods, such as Hybrid High Order methods (HHO).

Bibliography

ALIABADI, M. H. **The boundary element method, volume 2: applications in solids and structures**. [S.l.]: John Wiley & Sons, 2002. v. 2.

ANKIT, A. A sideface traction approach for cohesive and frictional crack growth problems using SBFEM. **Computer Methods in Applied Mechanics and Engineering**, v. 386, p. 114076, 2021.

ARBOGAST, T.; WHEELER, M. F. A characteristics-mixed finite element method for advection-dominated transport problems. **SIAM Journal on Numerical Analysis**, SIAM, v. 32, n. 2, p. 404–424, 1995.

ARNOLD, D. N. Mixed finite element methods for elliptic problems. **Computer Methods in Applied Mechanics and Engineering**, Elsevier, v. 82, n. 1-3, p. 281–300, 1990.

ARNOLD, D. N.; BREZZI, F. Mixed and nonconforming finite element methods: implementation, postprocessing and error estimates. **ESAIM: Mathematical Modelling and Numerical Analysis-Modélisation Mathématique et Analyse Numérique**, v. 19, n. 1, p. 7–32, 1985.

ASSAF, R. et al. Three-dimensional phase-field modeling of brittle fracture using an adaptive octree-based scaled boundary finite element approach. **Computer Methods in Applied Mechanics and Engineering**, Elsevier, v. 399, p. 115364, 2022.

BABUŠKA, I.; SURI, M. The h-p version of the finite element method with quasiuniform meshes. **RAIRO - Modélisation Mathématique et Analyse Numérique**, v. 21, n. 2, p. 199–238, 1987.

BATALHA, N. A. et al. Stability analysis and uncertainty modeling of vertical and inclined wellbore drilling through heterogeneous field. **Oil & Gas Science and Technology–Revue d'IFP Energies nouvelles**, EDP Sciences, v. 75, p. 14, 2020.

BATISTELA, G. A.; SIQUEIRA, D. de; DEVLOO, P. R. A posteriori error estimates for enriched mixed formulations. **Proceeding Series of the Brazilian Society of Computational and Applied Mathematics**, v. 7, n. 1, 2020.

BATISTELA, G. A. et al. A posteriori error estimator for a multiscale hybrid mixed method for darcy's flows. **International Journal for Numerical Methods in Engineering**, Wiley Online Library, 2022.

BAZYAR, M. H.; SONG, C. Analysis of transient wave scattering and its applications to site response analysis using the scaled boundary finite-element method. **Soil Dynamics and Earthquake Engineering**, Elsevier, v. 98, p. 191–205, 2017.

BELHACHMI, Z.; SAC-EPÉE, J.-M.; SOKOLOWSKI, J. Mixed finite element methods for smooth domain formulation of crack problems. **SIAM Journal on Numerical Analysis**, SIAM, v. 43, n. 3, p. 1295–1320, 2005.

BERGAMASCHI, L.; MANTICA, S.; MANZINI, G. A mixed finite element–finite volume formulation of the black-oil model. **SIAM Journal on Scientific Computing**, SIAM, v. 20, n. 3, p. 970–997, 1998.

BERGOT, M.; COHEN, G.; DURIFLÉ, M. Higher-order finite elements for hybrid meshes using new nodal pyramidal elements. **Journal of Scientific Computing**, v. 42, p. 345–381, 2010.

BERRE, I. et al. Verification benchmarks for single-phase flow in three-dimensional fractured porous media. **Advances in Water Resources**, Elsevier, v. 147, p. 103759, 2021.

BERTRAND, F.; BOFFI, D.; DIEGO, G. G de. Convergence analysis of the scaled boundary finite element method for the laplace equation. **Advances in Computational Mathematics**, Springer, v. 47, n. 3, p. 1–17, 2021.

BIRK, C.; BEHNKE, R. A modified scaled boundary finite element method for three-dimensional dynamic soil-structure interaction in layered soil. **International Journal for Numerical Methods in Engineering**, Wiley Online Library, v. 89, n. 3, p. 371–402, 2012.

BISHOP, J. A displacement-based finite element formulation for general polyhedra using harmonic shape functions. **International Journal for Numerical Methods in Engineering**, v. 97, n. 1, p. 1–31, 2014. ISSN 1097-0207.

BLYTH, M. G.; POZRIKIDIS, C. A Lobatto interpolation grid over triangle. **IMA Journal of Applied Mathematics**, v. 71, p. 153–169, 2006.

BOFFI, D.; BREZZI, F.; FORTIN, M. **Mixed Finite Element Methods and Applications**. [S.l.]: Springer, 2013. v. 44.

CARVALHO, P. G. S.; DEVLOO, P. R. B.; GOMES, S. M. On the use of divergence balanced h (div)-l2 pair of approximation spaces for divergence-free and robust simulations of stokes, coupled stokes–darcy and brinkman problems. **Mathematics and Computers in Simulation**, Elsevier, v. 170, p. 51–78, 2020.

CASTRO, D. A. et al. Hierarchical high order finite element bases for h (div) spaces based on curved meshes for two-dimensional regions or manifolds. **Journal of Computational and Applied Mathematics**, Elsevier, v. 301, p. 241–258, 2016.

CASTRO, D. A. et al. Three dimensional hierarchical mixed finite element approximations with enhanced primal variable accuracy. **Computer Methods in Applied Mechanics and Engineering**, Elsevier, v. 306, p. 479–502, 2016.

CECÍLIO, D. L. et al. An adaptive finite element model for wellbore breakout simulation. **International Journal for Numerical and Analytical Methods in Geomechanics**, Wiley Online Library, v. 43, n. 4, p. 814–828, 2019.

CHEN, K. et al. An efficient nonlinear octree SBFEM and its application to complicated geotechnical structures. **Computers and Geotechnics**, Elsevier, v. 96, p. 226–245, 2018.

CHEN, X.; BIRK, C.; SONG, C. Transient analysis of wave propagation in layered soil by using the scaled boundary finite element method. **Computers and Geotechnics**, Elsevier, v. 63, p. 1–12, 2015.

CHERNOV, A.; MASCOTTO, L. The harmonic virtual element method: stabilization and exponential convergence for the Laplace problem on polygonal domains. **IMA Journal of Numerical Analysis**, v. 39, n. 4, p. 1787–1817, 2019.

CHIDGZEY, S. R.; DEEKS, A. J. Determination of coefficients of crack tip asymptotic fields using the scaled boundary finite element method. **Engineering Fracture Mechanics**, Elsevier, v. 72, n. 13, p. 2019–2036, 2005.

CHIONG, I. **The development of a polygon based numerical technique for structural analyses: Scaled Boundary Polygons**. Thesis (Ph.D.) — School of Civil and Environmental Engineering - University of New South Wales, 2014.

CHIONG, I. et al. Scaled boundary polygons with application to fracture analysis of functionally graded materials. **International Journal for Numerical Methods in Engineering**, Wiley Online Library, v. 98, n. 8, p. 562–589, 2014.

CIARLET, P. G. **The Finite Element Method for Elliptic Problems**. [S.l.]: Siam, 2002. v. 40.

COCKBURN, B.; GOPALAKRISHNAN, J. A characterization of hybridized mixed methods for second order elliptic problems. **SIAM Journal on Numerical Analysis**, SIAM, v. 42, n. 1, p. 283–301, 2004.

COCKBURN, B.; GOPALAKRISHNAN, J.; LAZAROV, R. Unified hybridization of discontinuous galerkin, mixed, and continuous galerkin methods for second order elliptic problems. **SIAM Journal on Numerical Analysis**, SIAM, v. 47, n. 2, p. 1319–1365, 2009.

COCKBURN, B.; GOPALAKRISHNAN, J.; WANG, H. Locally conservative fluxes for the continuous galerkin method. **SIAM Journal on Numerical Analysis**, SIAM, v. 45, n. 4, p. 1742–1776, 2007.

COCKBURN, B.; LI, F.; SHU, C.-W. Locally divergence-free discontinuous galerkin methods for the maxwell equations. **Journal of Computational Physics**, Elsevier, v. 194, n. 2, p. 588–610, 2004.

COELHO, K. O.; DEVLOO, P. R.; GOMES, S. M. Error estimates for the scaled boundary finite element method. **Computer Methods in Applied Mechanics and Engineering**, Elsevier, v. 379, p. 113765, 2021.

CORREA, M. R.; MURAD, M. A. A new sequential method for three-phase immiscible flow in poroelastic media. **Journal of Computational Physics**, Elsevier, v. 373, p. 493–532, 2018.

DAI, L.; LONG, D.; WANG, L. Meso-scale modeling of concrete cracking induced by 3d corrosion expansion of helical strands. **Computers & Structures**, Elsevier, v. 254, p. 106615, 2021.

DEEKS, A. J.; CHENG, L. Potential flow around obstacles using the scaled boundary finite-element method. **International Journal for Numerical Methods in Fluids**, Wiley Online Library, v. 41, n. 7, p. 721–741, 2003.

DEEKS, A. J.; WOLF, J. P. A virtual work derivation of the scaled boundary finite-element method for elastostatics. **Computational Mechanics**, Springer, v. 28, n. 6, p. 489–504, 2002.

DEEKS, A. J.; WOLF, J. P. An h-hierarchical adaptive procedure for the scaled boundary finite-element method. **International Journal for Numerical Methods in Engineering**, Wiley Online Library, v. 54, n. 4, p. 585–605, 2002.

DEEKS, A. J.; WOLF, J. P. Stress recovery and error estimation for the scaled boundary finite-element method. **International Journal for Numerical Methods in Engineering**, Wiley Online Library, v. 54, n. 4, p. 557–583, 2002.

DEMKOWICZ, L. Polynomial Exact Sequences and Projection-Based Interpolation with Application to Maxwell Equations. In: BOFFI, D.; GASTALDI, L. (Ed.). **Mixed Finite Elements, Compatibility Conditions, and Applications, Lecture Notes in Mathematics, Vol. 1939**. [S.l.]: Springer, 2008. p. 101–158.

DEMKOWICZ, L. et al. **Computing with hp-Adaptive Finite Elements, Vol. 2**. [S.l.]: Chapman and Hall, 2007.

DEMKOWICZ, L. et al. De Rham diagram for hp finite element spaces. **Computers & Mathematics with Applications**, Elsevier, v. 39, n. 7-8, p. 29–38, 2000.

DEVLOO, P. et al. Mixed finite element approximations based on 3-D hp-adaptive curved meshes with two types of $h(div)$-conforming spaces. **International Journal for Numerical Methods in Engineering**, Wiley Online Library, v. 113, n. 7, p. 1045–1060, 2018.

DEVLOO, P. et al. On continuous, discontinuous, mixed, and primal hybrid finite element methods for second-order elliptic problems. **International Journal for Numerical Methods in Engineering**, Wiley Online Library, v. 115, n. 9, p. 1083–1107, 2018.

DEVLOO, P. et al. Multiscale hybrid-mixed finite element method for flow simulation in fractured porous media. **Computer Modeling in Engineering & Sciences**, Tech Science Press, 2019.

DEVLOO, P. R. et al. High-order composite finite element exact sequences based on tetrahedral–hexahedral–prismatic–pyramidal partitions. **Computer Methods in Applied Mechanics and Engineering**, Elsevier, v. 355, p. 952–975, 2019.

DEVLOO, P. R. et al. Two-dimensional $h(div)$-conforming finite element spaces with hp-adaptivity. In: **Numerical Mathematics and Advanced Applications ENUMATH 2015**. [S.l.]: Springer, 2016. p. 87–94.

DEVLOO, P. R. et al. Two-dimensional hp adaptive finite element spaces for mixed formulations. **Mathematics and Computers in Simulation**, Elsevier, v. 126, p. 104–122, 2016.

DEVLOO, P. R. et al. New $h(div)$-conforming multiscale hybrid-mixed methods for the elasticity problem on polygonal meshes. **ESAIM: Mathematical Modelling and Numerical Analysis**, EDP Sciences, v. 55, n. 3, p. 1005–1037, 2021.

DEVLOO, P. R. B. PZ: An object oriented environment for scientific programming. **Computer Methods in Applied Mechanics and Engineering**, Elsevier, v. 150, n. 1-4, p. 133–153, 1997.

DEVLOO, P. R. B.; BRAVO, C. M. A. A.; RYLO, E. C. Systematic and generic construction of shape functions for p-adaptive meshes of multidimensional finite elements. **Computer Methods in Applied Mechanics and Engineering**, Elsevier, v. 198, n. 21-26, p. 1716–1725, 2009.

DEVLOO, P. R. B. et al. $h(div)$ finite elements based on nonaffine meshes for 3D mixed formulations of flow problems with arbitrary high order accuracy of the divergence of the flux. **International Journal for Numerical Methods in Engineering**, Wiley Online Library, v. 121, n. 13, p. 2896–2915, 2020.

DÖLLING, S. et al. A scaled boundary finite element method model for interlaminar failure in composite laminates. **Composite Structures**, Elsevier, v. 241, p. 111865, 2020.

DUFFY, M. G. Quadrature over a pyramid or cube of integrands with a singularity at a vertex. **SIAM Journal on Numerical Analysis**, SIAM, v. 19, n. 6, p. 1260–1262, 1982.

DURAN, O. et al. A multiscale hybrid method for Darcy's problems using mixed finite element local solvers. **Computer Methods in Applied Mechanics and Engineering**, Elsevier, v. 354, p. 213–244, 2019.

DURAN, O. et al. A multiscale mixed finite element method applied to the simulation of two-phase flows. **Computer Methods in Applied Mechanics and Engineering**, Elsevier, v. 383, p. 113870, 2021.

DURAN, O. et al. An enhanced sequential fully implicit scheme for reservoir geomechanics. **Computational Geosciences**, Springer, v. 24, n. 4, p. 1557–1587, 2020.

EISENTRÄGER, J. et al. An SBFEM approach for rate-dependent inelasticity with application to image-based analysis. **International Journal of Mechanical Sciences**, Elsevier, v. 182, p. 105778, 2020.

EKEVID, T.; WIBERG, N.-E. Wave propagation related to high-speed train: a scaled boundary FE-approach for unbounded domains. **Computer Methods in Applied Mechanics and Engineering**, Elsevier, v. 191, n. 36, p. 3947–3964, 2002.

ERN, A.; GUERMOND, J.-L. **Theory and Practice of Finite Elements, Vol. 159**. [S.l.]: Springer Science & Business Media, 2013.

FARIAS, A. M. et al. Two dimensional mixed finite element approximations for elliptic problems with enhanced accuracy for the potential and flux divergence. **Computers & Mathematics with Applications**, Elsevier, v. 74, n. 12, p. 3283–3295, 2017.

FORTI, T. L. et al. A comparative numerical study of different finite element formulations for 2d model elliptic problems: Continuous and discontinuous Galerkin, mixed and hybrid methods. **Finite Elements in Analysis and Design**, Elsevier, v. 115, p. 9–20, 2016.

GEUZAINE, C.; REMACLE, J.-F. Gmsh: A 3-D finite element mesh generator with built-in pre-and post-processing facilities. **International Journal for Numerical Methods in Engineering**, Wiley Online Library, v. 79, n. 11, p. 1309–1331, 2009.

GOMES, A. T. A.; PEREIRA, W. S.; VALENTIN, F. The MHM Method for Elasticity on Polytopal Meshes. Working paper or preprint. 2020. Available from Internet: <https://hal.archives-ouvertes.fr/hal-02931170>.

GRAVENKAMP, H.; BIRK, C.; SONG, C. Simulation of elastic guided waves interacting with defects in arbitrarily long structures using the scaled boundary finite element method. **Journal of Computational Physics**, Elsevier, v. 295, p. 438–455, 2015.

GRAVENKAMP, H. et al. The computation of dispersion relations for three-dimensional elastic waveguides using the scaled boundary finite element method. **Journal of Sound and Vibration**, Elsevier, v. 332, n. 15, p. 3756–3771, 2013.

GRAVENKAMP, H.; SAPUTRA, A. A.; DUCZEK, S. High-order shape functions in the scaled boundary finite element method revisited. **Archives of Computational Methods in Engineering**, Springer, v. 28, n. 2, p. 473–494, 2021.

GRAVENKAMP, H.; SONG, C.; PRAGER, J. A numerical approach for the computation of dispersion relations for plate structures using the scaled boundary finite element method. **Journal of Sound and Vibration**, Elsevier, v. 331, n. 11, p. 2543–2557, 2012.

GRAVENKAMP, H.; SONG, C.; ZHANG, J. On mass lumping and explicit dynamics in the scaled boundary finite element method. **Computer Methods in Applied Mechanics and Engineering**, Elsevier, v. 370, p. 113274, 2020.

GUO, H. et al. A quadtree-polygon-based scaled boundary finite element method for image-based mesoscale fracture modelling in concrete. **Engineering Fracture Mechanics**, Elsevier, v. 211, p. 420–441, 2019.

GUO, H. et al. A quadtree-polygon-based scaled boundary finite element method for image-based mesoscale fracture modelling in concrete. **Engineering Fracture Mechanics**, Elsevier, v. 211, p. 420–441, 2019.

GURTIN, M. E. **An introduction to continuum mechanics**. [S.l.]: Academic press, 1982.

HE, Z. et al. Generalized multiscale approximation of a mixed finite element method with velocity elimination for Darcy flow in fractured porous media. **Computer Methods in Applied Mechanics and Engineering**, Elsevier, v. 381, p. 113846, 2021.

HERRMANN, L. R. Finite-element bending analysis for plates. **Journal of the Engineering Mechanics Division**, American Society of Civil Engineers, v. 93, n. 5, p. 13–26, 1967.

HUGHES, T. J. et al. The continuous Galerkin method is locally conservative. **Journal of Computational Physics**, Elsevier, v. 163, n. 2, p. 467–488, 2000.

IQBAL, M. et al. Development of the scaled boundary finite element method for crack propagation modeling of elastic solids subjected to coupled thermo-mechanical loads. **Computer Methods in Applied Mechanics and Engineering**, Elsevier, v. 387, p. 114106, 2021.

JIA, Y.-M. et al. The high-order completeness analysis of the scaled boundary finite element method. **Computer Methods in Applied Mechanics and Engineering**, Elsevier, v. 362, p. 112867, 2020.

JO, G.; KWAK, D. Y.; LEE, Y.-J. Locally conservative immersed finite element method for elliptic interface problems. **Journal of Scientific Computing**, Springer, v. 87, n. 2, p. 1–27, 2021.

KARNIADAKIS, G.; SHERWIN, S. **Spectral/hp Element Methods for Computational Fluid Dynamics**. [S.l.]: Oxford University Press, 1999.

LI, X.; LIU, Z.; LEWIS, R. Mixed finite element method for coupled thermo-hydro-mechanical process in poro-elasto-plastic media at large strains. **International Journal for Numerical Methods in Engineering**, Wiley Online Library, v. 64, n. 5, p. 667–708, 2005.

LIU, J. et al. Free vibration and transient dynamic response of functionally graded sandwich plates with power-law nonhomogeneity by the scaled boundary finite element method. **Computer Methods in Applied Mechanics and Engineering**, Elsevier, v. 376, p. 113665, 2021.

LIU, L. et al. Automatic three-dimensional acoustic-structure interaction analysis using the scaled boundary finite element method. **Journal of Computational Physics**, Elsevier, v. 395, p. 432–460, 2019.

LIU, L. et al. Automatic scaled boundary finite element method for three-dimensional elastoplastic analysis. **International Journal of Mechanical Sciences**, Elsevier, v. 171, p. 105374, 2020.

LOWTHER, D.; RAJANATHAN, C.; SILVESTER, P. A finite element technique for solving 2-D open boundary problems. **IEEE Transactions on Magnetics**, IEEE, v. 14, n. 5, p. 467–469, 1978.

LYNESS, J. N.; COOLS, R. **A survey of numerical cubature over triangles**. [S.l.], 1994.

MALTA, S. M.; LOULA, A. F.; GARCIA, E. L. Numerical analysis of a stabilized finite element method for tracer injection simulations. **Computer Methods in Applied Mechanics and Engineering**, Elsevier, v. 187, n. 1-2, p. 119–136, 2000.

MASUD, A.; HUGHES, T. J. R. A stabilized mixed finite element method for darcy flow. **Computer Methods in Applied Mechanics and Engineering**, Elsevier, v. 191, n. 39-40, p. 4341–4370, 2002.

MELENK, J. M.; ROJIK, C. On commuting p-version projection-based interpolation on tetrahedra. **Mathematics of Computation**, v. 89, p. 45–87, 2020.

MOUSAVI, S.; SUKUMAR, N. Generalized Duffy transformation for integrating vertex singularities. **Computational Mechanics**, Springer, v. 45, n. 2, p. 127–140, 2010.

MUÑOZ-SOLA, R. Polynomial lifting on the tetrahedron and applications to the h-p version of the finite element method in three dimensions. **SIAM Journal on Numerical Analysis**, v. 34, n. 1, p. 282–314, 1997.

NATARAJAN, S. et al. Convergence and accuracy of displacement based finite element formulations over arbitrary polygons: Laplace interpolants, strain smoothing and scaled boundary polygon formulation. **Finite Elements in Analysis and Design**, Elsevier, v. 85, p. 101–122, 2014.

NIGAM, N.; PHILLIPS, J. High-order conforming finite elements on pyramids. **IMA Journal of Numerical Analysis**, v. 32, p. 448–483, 2012.

OOI, E.; YANG, Z. Modelling multiple cohesive crack propagation using a finite element–scaled boundary finite element coupled method. **Engineering Analysis with Boundary Elements**, Elsevier, v. 33, n. 7, p. 915–929, 2009.

OOI, E.; YANG, Z. A hybrid finite element-scaled boundary finite element method for crack propagation modelling. **Computer Methods in Applied Mechanics and Engineering**, Elsevier, v. 199, n. 17-20, p. 1178–1192, 2010.

OOI, E. T.; SONG, C.; NATARAJAN, S. Construction of high-order complete scaled boundary shape functions over arbitrary polygons with bubble functions. **International Journal for Numerical Methods in Engineering**, Wiley Online Library, v. 108, n. 9, p. 1086–1120, 2016.

OOI, E. T.; SONG, C.; NATARAJAN, S. A scaled boundary finite element formulation with bubble functions for elasto-static analyses of functionally graded materials. **Computational Mechanics**, Springer, v. 60, n. 6, p. 943–967, 2017.

ORLANDINI, F. T. et al. A high-precision fem scheme for modal analysis of photonic waveguides using high-order edge elements. In: IEEE. **2019 International Conference on Optical MEMS and Nanophotonics (OMN)**. [S.l.], 2019. p. 160–161.

ORLANDINI, F. T. et al. On the implementation of high-order $H(curl;\Omega)$-conforming approximation spaces for full-wave waveguide analysis. In: OPTICAL SOCIETY OF AMERICA. **Latin America Optics and Photonics Conference**. [S.l.], 2018. p. Tu4A–22.

PFEIL, S. et al. Scaled boundary finite element method for hydrodynamic bearings in rotordynamic simulations. **International Journal of Mechanical Sciences**, Elsevier, v. 199, p. 106427, 2021.

PIAN, T. A historical note about 'hybrid elements'. **International Journal for Numerical Methods in Engineering**, Wiley Online Library, v. 12, n. 5, p. 891–892, 1978.

PIAN, T. H. Derivation of element stiffness matrices by assumed stress distributions. **AIAA journal**, v. 2, n. 7, p. 1333–1336, 1964.

PRAMOD, A. et al. Adaptive phase-field modeling of brittle fracture using the scaled boundary finite element method. **Computer Methods in Applied Mechanics and Engineering**, Elsevier, v. 355, p. 284–307, 2019.

PRAMOD, A. et al. An adaptive scaled boundary finite element method for contact analysis. **European Journal of Mechanics-A/Solids**, Elsevier, v. 86, p. 104180, 2021.

PU, S. L.; HUSSAIN, M.; LORENSEN, W. E. The collapsed cubic isoparametric element as a ingular element for crack probblems. **International Journal for Numerical Methods in Engineering**, Wiley Online Library, v. 12, n. 11, p. 1727–1742, 1978.

QUEY, R.; DAWSON, P. R.; BARBE, F. Large-scale 3D random polycrystals for the finite element method: Generation, meshing and remeshing. **Computer Methods in Applied Mechanics and Engineering**, Elsevier, v. 200, n. 17-20, p. 1729–1745, 2011.

RADU, F. A. et al. A mixed finite element discretization scheme for a concrete carbonation model with concentration-dependent porosity. **Journal of Computational and Applied Mathematics**, Elsevier, v. 246, p. 74–85, 2013.

RAJU, I. S. Calculation of strain-energy release rates with higher order and singular finite elements. **Engineering Fracture Mechanics**, Elsevier, v. 28, n. 3, p. 251–274, 1987.

REISSNER, E. On a variational theorem for finite elastic deformations. **Journal of Mathematics and Physics**, Wiley Online Library, v. 32, n. 1-4, p. 129–135, 1953.

ROBERTS, J.; THOMAS, J.-M. Mixed and hybrid methods. In: **Finite Element Methods (Part 1)**. [S.l.]: Elsevier, 1991, (Handbook of Numerical Analysis, v. 2). p. 523–639.

ROMANO, G.; ROSATI, L.; DIACO, M. Well-posedness of mixed formulations in elasticity. **ZAMM-Journal of Applied Mathematics and Mechanics/Zeitschrift für Angewandte Mathematik und Mechanik: Applied Mathematics and Mechanics**, Wiley Online Library, v. 79, n. 7, p. 435–454, 1999.

SANEI, M.; FORTI, T.; SANTOS, E. An assisted calibration of physics-based elasto-plastic models using optimization algorithms for porous rock, Part I. **Construction and Building Materials**, 2020.

SANTOS, T. D. d. et al. Implementation and performance of adaptive mesh refinement in the ice sheet system model (ISSM v4. 14). **Geoscientific Model Development**, Copernicus GmbH, v. 12, n. 1, p. 215–232, 2019.

SAPUTRA, A. A. et al. Three-dimensional image-based numerical homogenisation using octree meshes. **Computers & Structures**, Elsevier, v. 237, p. 106263, 2020.

SCHWAB, C. **p-and hp-Finite Element Methods: Theory and Applications in Solid and Fluid Mechanics**. [S.l.]: Clarendon Press Oxford, 1998.

SINGH, G.; WHEELER, M. F. Compositional flow modeling using a multi-point flux mixed finite element method. **Computational Geosciences**, Springer, v. 20, n. 3, p. 421–435, 2016.

SIQUEIRA, D. D.; DEVLOO, P. R.; GOMES, S. M. Hierarchical high order finite element approximation spaces for $h(div)$ and $h(curl)$. In: **Numerical Mathematics and Advanced Applications 2009**. [S.l.]: Springer, 2010. p. 269–276.

SIQUEIRA, D. D.; DEVLOO, P. R.; GOMES, S. M. A new procedure for the construction of hierarchical high order $h(div)$ and $h(curl)$ finite element spaces. **Journal of Computational and Applied Mathematics**, Elsevier, v. 240, p. 204–214, 2013.

SIQUEIRA, D. de et al. Mixed finite element approximations of a singular elliptic problem based on some anisotropic and hp-adaptive curved quarter-point elements. **Applied Numerical Mathematics**, Elsevier, v. 158, p. 85–102, 2020.

SOLIN, P.; SEGETH, K.; DOLEZEL, I. **Higher-order finite element methods**. [S.l.]: Chapman and Hall/CRC, 2003.

SOLIN, P.; SEGETH, K.; DOLEZEL, I. **Higher-order Finite Element Methods**. [S.l.]: CRC Press, 2003.

SONG, C. Evaluation of power-logarithmic singularities, T-stresses and higher order terms of in-plane singular stress fields at cracks and multi-material corners. **Engineering Fracture Mechanics**, Elsevier, v. 72, n. 10, p. 1498–1530, 2005.

SONG, C. Analysis of singular stress fields at multi-material corners under thermal loading. **International Journal for Numerical Methods in Engineering**, Wiley Online Library, v. 65, n. 5, p. 620–652, 2006.

SONG, C. **The Scaled Boundary Finite Element Method: Theory and Implementation**. [S.l.]: John Wiley & Sons, 2018. ISBN 9781119388487.

SONG, C.; OOI, E. T.; NATARAJAN, S. A review of the scaled boundary finite element method for two-dimensional linear elastic fracture mechanics. **Engineering Fracture Mechanics**, Elsevier, v. 187, p. 45–73, 2018.

SONG, C.; VRCELJ, Z. Evaluation of dynamic stress intensity factors and T-stress using the scaled boundary finite-element method. **Engineering Fracture Mechanics**, Elsevier, v. 75, n. 8, p. 1960–1980, 2008.

SONG, C.; WOLF, J. P. Consistent infinitesimal finite-element–cell method: out-of-plane motion. **Journal of engineering mechanics**, American Society of Civil Engineers, v. 121, n. 5, p. 613–619, 1995.

SONG, C.; WOLF, J. P. The scaled boundary finite-element method — alias consistent infinitesimal finite-element cell method—for elastodynamics. **Computer Methods in Applied Mechanics and Engineering**, Elsevier, v. 147, n. 3-4, p. 329–355, 1997.

SONG, C.; WOLF, J. P. The scaled boundary finite-element method: analytical solution in frequency domain. **Computer Methods in Applied Mechanics and Engineering**, Elsevier, v. 164, n. 1-2, p. 249–264, 1998.

SONG, C.; WOLF, J. P. Body loads in scaled boundary finite-element method. **Computer Methods in Applied Mechanics and Engineering**, Elsevier, v. 180, n. 1-2, p. 117–135, 1999.

SONG, C.; WOLF, J. P. The scaled boundary finite element method—alias consistent infinitesimal finite element cell method—for diffusion. **International Journal for Numerical Methods in Engineering**, Wiley Online Library, v. 45, n. 10, p. 1403–1431, 1999.

SONG, C.; WOLF, J. P. Semi-analytical representation of stress singularities as occurring in cracks in anisotropic multi-materials with the scaled boundary finite-element method. **Computers & Structures**, Elsevier, v. 80, n. 2, p. 183–197, 2002.

TALISCHI, C. et al. PolyMesher: a general-purpose mesh generator for polygonal elements written in Matlab. **Structural and Multidisciplinary Optimization**, Springer, v. 45, n. 3, p. 309–328, 2012.

TCHONKOVA, M.; PETERS, J.; STURE, S. A new mixed finite element method for poro-elasticity. **International Journal for Numerical and Analytical Methods in Geomechanics**, Wiley Online Library, v. 32, n. 6, p. 579–606, 2008.

TONG, P. New displacement hybrid finite element models for solid continua. **International Journal for Numerical Methods in Engineering**, Wiley Online Library, v. 2, n. 1, p. 73–83, 1970.

VEIGA, L. Beirão da et al. Basic principles of virtual element methods. **Mathematical Models and Methods in Applied Sciences**, World Scientific, v. 23, n. 01, p. 199–214, 2013.

WHEELER, J. A.; WHEELER, M. F.; YOTOV, I. Enhanced velocity mixed finite element methods for flow in multiblock domains. **Computational Geosciences**, Springer, v. 6, n. 3, p. 315–332, 2002.

WIJESINGHE, D. R. et al. Development of the scaled boundary finite element method for image-based slope stability analysis. **Computers and Geotechnics**, Elsevier, v. 143, p. 104586, 2022.

WOLF, J. P. **The Scaled Boundary Finite Element Method**. [S.l.]: John Wiley & Sons, 2003.

WOLF, J. P.; SONG, C. Consistent infinitesimal finite-element cell method: in-plane motion. **Computer Methods in Applied Mechanics and Engineering**, Elsevier, v. 123, n. 1-4, p. 355–370, 1995.

WOLF, J. P.; SONG, C. Consistent infinitesimal finite-element cell method: Three-dimensional case. Springer, p. 690–695, 1995.

WOLF, J. P.; SONG, C. **Finite-element modelling of unbounded media**. [S.l.]: Wiley Chichester, 1996.

WOLF, J. P.; SONG, C. Unit-impulse response of unbounded medium by scaled boundary finite-element method. **Computer Methods in Applied Mechanics and Engineering**, Elsevier, v. 159, n. 3-4, p. 355–367, 1998.

WOLF, J. P.; SONG, C. The scaled boundary finite-element method – a primer: derivations. **Computers & Structures**, Elsevier, v. 78, n. 1-3, p. 191–210, 2000.

WOLF, J. P.; SONG, C. The scaled boundary finite-element method – a fundamental solution-less boundary-element method. **Computer Methods in Applied Mechanics and Engineering**, Elsevier, v. 190, n. 42, p. 5551–5568, 2001.

WOLF, J. P.; SONG, C. Some cornerstones of dynamic soil–structure interaction. **Engineering Structures**, Elsevier, v. 24, n. 1, p. 13–28, 2002.

WU, Y.-L. Collapsed isoparametric element as a singular element for a crack normal to the bi-material interface. **Computers & Structures**, Elsevier, v. 47, n. 6, p. 939–943, 1993.

XU, X.; ZHANG, S. A new divergence-free interpolation operator with applications to the darcy–stokes–brinkman equations. **SIAM Journal on Scientific Computing**, SIAM, v. 32, n. 2, p. 855–874, 2010.

YA, S. et al. An open-source abaqus implementation of the scaled boundary finite element method to study interfacial problems using polyhedral meshes. **Computer Methods in Applied Mechanics and Engineering**, Elsevier, v. 381, p. 113766, 2021.

YANG, Z. Fully automatic modelling of mixed-mode crack propagation using scaled boundary finite element method. **Engineering Fracture Mechanics**, Elsevier, v. 73, n. 12, p. 1711–1731, 2006.

YANG, Z.; DEEKS, A. Fully-automatic modelling of cohesive crack growth using a finite element–scaled boundary finite element coupled method. **Engineering fracture mechanics**, Elsevier, v. 74, n. 16, p. 2547–2573, 2007.

YANG, Z.; DEEKS, A.; HAO, H. Transient dynamic fracture analysis using scaled boundary finite element method: a frequency-domain approach. **Engineering Fracture Mechanics**, Elsevier, v. 74, n. 5, p. 669–687, 2007.

ZHANG, J. et al. A massively parallel explicit solver for elasto-dynamic problems exploiting octree meshes. **Computer Methods in Applied Mechanics and Engineering**, Elsevier, v. 380, p. 113811, 2021.

ZHANG, J. et al. Discrete modeling of fiber reinforced composites using the scaled boundary finite element method. **Composite Structures**, Elsevier, v. 235, p. 111744, 2020.

ZHANG, J. et al. Adaptive analysis using scaled boundary finite element method in 3d. **Computer Methods in Applied Mechanics and Engineering**, Elsevier, v. 372, p. 113374, 2020.

ZHANG, J. et al. An asynchronous parallel explicit solver based on scaled boundary finite element method using octree meshes. **Computer Methods in Applied Mechanics and Engineering**, Elsevier, v. 401, p. 115653, 2022.

ZHANG, Z. et al. Three-dimensional damage analysis by the scaled boundary finite element method. **Computers & Structures**, Elsevier, v. 206, p. 1–17, 2018.

ZHANG, Z. et al. Nonlocal damage modelling by the scaled boundary finite element method. **Engineering Analysis with Boundary Elements**, Elsevier, v. 99, p. 29–45, 2019.

Appendix A

Tables - Convergence Results

A.1 Chapter 3 - The Scaled Boundary Finite Element Method

A.1.1 Poisson problems

Example 1 - Smooth solution in 2D - Single S-element

Table A.1: Example 1 - SBFEM errors $E^h_{L^2} = \|u - u^h\|_{L^2(\Omega)}$ and $E^h_{H^1} = |u - u^h|_{H^1(\Omega)}$ for partitions $\mathcal{T}^h = \{S\}$ of a single S-element, with the skeleton subdivided into $h = 2^{-\ell}$ scaled boundary elements using uniform and distorted subpartitions.

Uniform sub-partitions

ℓ	k=1			k=2			$k=3$		
	DOF	$E^h_{L^2}$	$E^h_{H^1}$	DOF	$E^h_{L^2}$	$E^h_{H^1}$	DOF	$E^h_{L^2}$	$E^h_{H^1}$
0	8	6.33E0	3.85E1	16	3.32E-1	3.86E0	12	2.26E-1	2.99E0
1	16	9.34E-1	1.45E1	32	1.07E-1	2.23E0	24	1.04E-2	3.11E-1
2	32	2.06E-1	6.81E0	64	1.60E-2	5.57E-1	48	6.75E-4	3.79E-2
	Rate	2.18	1.09	Rate	2.74	2.00	Rate	3.95	3.04
ℓ	$k=4$			$k=5$			$k=6$		
	DOF	$E^h_{L^2}$	$E^h_{H^1}$	DOF	$E^h_{L^2}$	$E^h_{H^1}$	DOF	$E^h_{L^2}$	$E^h_{H^1}$
0	32	5.88E-3	1.18E-1	40	3.96E-3	8.28E-2	48	6.05E-5	1.76E-3
1	64	7.09E-4	2.54E-2	80	4.72E-5	2.14E-3	96	2.34E-6	1.20E-4
2	128	2.42E-5	1.58E-3	160	7.61E-7	6.47E-5	192	1.95E-8	1.85E-6
	Rate	4.87	4.01	Rate	5.96	5.05	Rate	6.91	6.02

Distorted sub-partitions

ℓ	$k=1$			$k=2$			$k=3$		
	DOF	$E^h_{L^2}$	$E^h_{H^1}$	DOF	$E^h_{L^2}$	$E^h_{H^1}$	DOF	$E^h_{L^2}$	$E^h_{H^1}$
0	8	7.06E0	3.92E1	16	4.05E-1	4.47E0	24	2.63E-1	3.23E0
1	16	1.08E0	1.51E1	32	1.27E-1	2.49E0	48	1.24E-2	3.45E-1
2	32	2.41E-1	7.15E0	64	1.88E-2	6.24E-1	96	8.01E-4	4.25E-2
	Rate	2.16	1.08	Rate	2.76	2.00	Rate	3.95	3.02
ℓ	$k=4$			$k=5$			$k=6$		
	DOF	$E^h_{L^2}$	$E^h_{H^1}$	DOF	$E^h_{L^2}$	$E^h_{H^1}$	DOF	$E^h_{L^2}$	$E^h_{H^1}$
0	32	8.41E-3	1.61E-1	40	4.67E-3	9.42E-2	48	9.48E-5	2.55E-3
1	64	8.67E-4	2.95E-2	80	5.71E-5	2.45E-3	96	2.91E-6	1.42E-4
2	128	2.92E-5	1.83E-3	160	2.47E-5	3.63E-4	192	4.96E-6	2.81E-4
	Rate	4.89	4.01	Rate	1.21	2.76	Rate	-0.77	-0.99

Example 2 - Smooth solution in 2D - Quadrilateral and polygonal mesh refining the domain

Table A.2: Example 2 - Galerkin SBFEM errors $E^h_{L^2} = \|u - u^h\|_{L^2(\Omega)}$ and $E^h_{H^1} = |u - u^h|_{H^1(\Omega)}$ for partitions $\mathcal{T}^h$, $h = 2^{-\ell}$, with uniform quadrilateral S-elements, subdivided in uniform and distorted triangles.

Uniform quadrilateral S-elements - uniform sub-partitions

ℓ	$k=1$			$k=2$			$k=3$		
	DOF	$E^h_{L^2}$	$E^h_{H^1}$	DOF	$E^h_{L^2}$	$E^h_{H^1}$	DOF	$E^h_{L^2}$	$E^h_{H^1}$
1	25	1.80E0	1.99E1	65	1.31E-1	2.56E0	105	7.78E-3	2.28E-1
2	81	4.50E-1	9.50E0	225	1.68E-2	5.92E-1	369	4.68E-4	2.62E-2
3	289	1.13E-1	4.68E0	833	2.12E-3	1.42E-1	1377	2.95E-5	3.19E-3
4	1089	2.82E-2	2.33E0	3201	2.65E-4	3.50E-2	5313	1.86E-6	3.96E-4
	Rate	2.00	1.01	Rate	3.00	2.02	Rate	3.99	3.01
ℓ	$k=4$			$k=5$			$k=6$		
	DOF	$E^h_{L^2}$	$E^h_{H^1}$	DOF	$E^h_{L^2}$	$E^h_{H^1}$	DOF	$E^h_{L^2}$	$E^h_{H^1}$
1	145	5.87E-4	2.09E-2	185	3.89E-5	1.77E-3	225	1.96E-6	1.03E-4
2	513	1.99E-5	1.29E-3	657	6.04E-7	5.22E-5	801	1.53E-8	1.47E-6
3	1921	6.42E-7	8.14E-5	2465	9.47E-9	1.57E-6	3009	1.23E-10	2.21E-8
4	7425	2.03E-8	5.11E-6	9537	1.48E-10	4.81E-8	11649	9.46E-13	3.42E-10
	Rate	4.98	3.99	Rate	6.00	5.03	Rate	6.99	6.02

Uniform quadrilateral S-elements - distorted sub-partitions

ℓ	$k=1$			$k=2$			$k=3$		
	DOF	$E^h_{L^2}$	$E^h_{H^1}$	DOF	$E^h_{L^2}$	$E^h_{H^1}$	DOF	$E^h_{L^2}$	$E^h_{H^1}$
1	25	1.81E0	2.00E1	65	1.38E-1	2.66E0	105	9.25E-3	2.59E-1
2	81	4.51E-1	9.51E0	225	1.80E-2	6.20E-1	369	5.52E-4	3.02E-2
3	289	1.13E-1	4.68E0	833	2.26E-3	1.49E-1	1377	3.43E-5	3.66E-3
4	1089	2.81E-2	2.33E0	3201	2.83E-4	3.68E-2	5313	2.15E-6	4.51E-4
	Rate	2.00	1.07	Rate	2.94	2.10	Rate	4.07	3.10
ℓ	$k=4$			$k=5$			$k=6$		
	DOF	$E^h_{L^2}$	$E^h_{H^1}$	DOF	$E^h_{L^2}$	$E^h_{H^1}$	DOF	$E^h_{L^2}$	$E^h_{H^1}$
1	145	6.86E-4	2.36E-2	185	4.33E-5	1.94E-3	225	2.23E-6	1.15E-4
2	513	2.21E-5	1.42E-3	657	6.48E-7	5.65E-5	801	1.69E-8	1.61E-6
3	1921	6.93E-7	8.79E-5	2465	9.96E-9	1.68E-6	3009	1.32E-10	2.40E-8
4	7425	2.16E-8	5.47E-6	9537	1.57E-10	5.09E-8	11649	1.68E-12	6.55E-10
	Rate	4.96	4.06	Rate	6.06	5.10	Rate	7.04	6.16

Table A.3: Example 2 - Galerkin SBFEM errors $E^h_{L^2} = \|u - u^h\|_{L^2(\Omega)}$ and $E^h_{H^1} = |u - u^h|_{H^1(\Omega)}$ for partitions $\mathcal{T}^h$, $h = 2^{-\ell}$, with uniform quadrilateral S-elements, subdivided in polygonal S-elements with uniform sub-partitions (case 3).

Uniform polygonal S-elements - Case 3

ℓ	$k=1$			$k=2$			$k=3$		
	DOF	$E^h_{L^2}$	$E^h_{H^1}$	DOF	$E^h_{L^2}$	$E^h_{H^1}$	DOF	$E^h_{L^2}$	$E^h_{H^1}$
1	21	8.06E-1	1.23E1	45	8.77E-2	1.95E0	69	8.09E-3	2.53E-1
2	65	2.86E-1	6.66E0	145	1.55E-2	5.30E-1	225	4.98E-4	2.79E-2
3	225	1.54E-2	3.08E0	513	1.87E-3	1.22E-1	801	3.05E-5	3.24E-3
4	833	3.74E-3	1.50E0	1921	2.30E-4	2.97E-2	3009	1.92E-6	3.94E-4
	Rate	2.08	1.04	Rate	3.02	2.04	Rate	3.99	3.02
ℓ	$k=4$			$k=5$			$k=6$		
	DOF	$E^h_{L^2}$	$E^h_{H^1}$	DOF	$E^h_{L^2}$	$E^h_{H^1}$	DOF	$E^h_{L^2}$	$E^h_{H^1}$
1	93	5.49E-4	2.09E-2	117	3.59E-5	1.70E-3	141	1.78E-6	9.68E-5
2	305	1.98E-5	1.26E-3	385	5.76E-7	4.95E-5	465	1.53E-8	1.44E-6
3	1089	5.99E-7	7.40E-5	1377	8.65E-9	1.41E-6	1665	1.17E-10	2.05E-8
4	4097	1.86E-8	4.54E-6	5185	1.37E-10	4.21E-8	6273	9.03E-13	3.10E-10
	Rate	5.01	4.03	Rate	5.98	5.06	Rate	7.02	6.05

Table A.4: Example 2 - Galerkin SBFEM errors $E^h_{L^2} = \|u - u^h\|_{L^2(\Omega)}$ and $E^h_{H^1} = |u - u^h|_{H^1(\Omega)}$ for partitions $\mathcal{T}^h$, $h = 2^{-\ell}$, with irregular S-elements (Case 4) and the Galerkin FEM errors for a mesh composed the respective conglomerate triangles $\mathcal{P}^h$.

Irregular polygonal S-elements - Case 4

ℓ	$k=2$			$k=4$			$k=6$		
	DOF	$E^h_{L^2}$	$E^h_{H^1}$	DOF	$E^h_{L^2}$	$E^h_{H^1}$	DOF	$E^h_{L^2}$	$E^h_{H^1}$
1	81	8.27E-2	1.61E0	178	7.01E-4	2.02E-2	273	2.40E-6	1.00E-4
2	321	1.53E-2	5.33E-1	705	2.51E-5	1.55E-3	1089	2.54E-8	2.31E-6
3	1275	1.49E-3	1.06E-1	2805	5.35E-7	6.68E-5	4335	1.25E-10	2.26E-8
4	5099	1.61E-4	2.30E-2	11221	1.48E-8	3.56E-6	17343	1.02E-12	3.14E-10
	Rate	3.21	2.21	Rate	5.18	4.22	Rate	6.94	6.17

FE triangular conglomerate mesh

ℓ	$k=2$			$k=4$			$k=6$		
	DOF	$E^h_{L^2}$	$E^h_{H^1}$	DOF	$E^h_{L^2}$	$E^h_{H^1}$	DOF	$E^h_{L^2}$	$E^h_{H^1}$
1	177	1.62E-1	3.59E0	673	1.49E-3	5.26E-2	1489	7.07E-6	3.41E-4
2	739	2.26E-2	1.00E0	2893	4.57E-5	3.40E-3	6463	5.44E-8	5.53E-6
3	3000	2.34E-3	2.18E-1	11875	9.51E-7	1.53E-4	26626	2.38E-10	5.18E-8
4	12121	2.69E-4	5.11E-2	48233	2.72E-8	8.72E-6	108337	1.72E-12	7.33E-10
	Rate	3.10	2.08	Rate	5.07	4.09	Rate	7.04	6.08

Example 3 - Smooth solution in 3D - Single S-element

Table A.5: Example 3 - SBFEM errors $E^h_{L^2} = \|u-u^h\|_{L^2(\Omega)}$ and $E^h_{H^1} = |u-u^h|_{H^1(\Omega)}$ for $\mathcal{T}^h$ a partition composed of a 3D single S-element refined over the boundary, with $h = 2^{-\ell}$.

Uniform hexahedral S-elements

ℓ	$k=1$			$k=2$			$k=3$			$k=4$		
	DOF	$E^h_{L^2}$	$E^h_{H^1}$	DOF	$E^h_{L^2}$	$E^h_{H^1}$	DOF	$E^h_{L^2}$	$E^h_{H^1}$	DOF	$E^h_{L^2}$	$E^h_{H^1}$
0	8	8.66E-2	6.98E-1	26	8.97E-3	9.88E-2	56	2.84E-4	4.06E-3	98	1.82E-5	3.37E-4
1	26	1.94E-2	2.96E-1	98	1.25E-3	2.21E-2	218	1.76E-5	5.30E-4	386	5.83E-7	1.92E-5
2	98	4.29E-3	1.41E-1	386	1.59E-4	5.28E-3	866	1.16E-6	6.85E-5	1538	1.83E-8	1.18E-6
	Rate	2.18	1.07	Rate	2.98	2.07	Rate	3.92	2.95	Rate	4.99	4.02

Example 4 - Smooth solution in a 3D domain - Hexahedral and polytopal mesh

Table A.6: Example 4 - Galerkin SBFEM errors $E^h_{L^2} = \|u-u^h\|_{L^2(\Omega)}$ and $E^h_{H^1} = |u-u^h|_{H^1(\Omega)}$ for uniform partitions $\mathcal{T}^h$ of hexahedral (Case 1) and polyhedral (Case 2) regular S-elements, irregular polyhedral S-elements (Case 3), and the its conglomerate mesh of tetrahedral FEs, with $h = 2^{-\ell}$.

Uniform hexahedral S-elements - Case 1

ℓ	$k=1$			$k=2$			$k=3$			$k=4$		
	DOF	$E^h_{L^2}$	$E^h_{H^1}$	DOF	$E^h_{L^2}$	$E^h_{H^1}$	DOF	$E^h_{L^2}$	$E^h_{H^1}$	DOF	$E^h_{L^2}$	$E^h_{H^1}$
1	27	3.17E-2	3.85E-1	117	1.41E-3	2.40E-2	279	1.92E-5	5.22E-4	513	6.46E-7	2.09E-5
2	127	7.85E-3	1.87E-1	665	1.93E-4	6.02E-3	1685	1.25E-6	6.49E-5	3185	2.12E-8	1.31E-6
3	729	1.93E-3	9.20E-2	4401	2.48E-5	1.51E-3	11529	7.99E-8	8.07E-6	22113	6.75E-10	8.16E-8
	Rate	2.02	1.02	Rate	2.96	2.00	Rate	3.97	3.01	Rate	4.98	4.00

Uniform polyhedral S-elements - Case 2

ℓ	$k=1$			$k=2$			$k=3$			$k=4$		
	DOF	$E^h_{L^2}$	$E^h_{H^1}$	DOF	$E^h_{L^2}$	$E^h_{H^1}$	DOF	$E^h_{L^2}$	$E^h_{H^1}$	DOF	$E^h_{L^2}$	$E^h_{H^1}$
1	26	1.94E-2	2.96E-1	98	1.25E-3	2.21E-2	218	1.76E-5	5.30E-4	386	5.83E-7	1.92E-5
2	117	5.24E-3	1.42E-1	513	1.68E-4	5.34E-3	1197	1.19E-6	6.45E-5	2169	1.91E-8	1.18E-6
3	665	1.35E-3	7.00E-2	3185	2.14E-5	1.33E-3	7625	7.79E-8	7.92E-6	13985	6.08E-10	7.32E-8
	Rate	1.96	1.02	Rate	2.97	2.01	Rate	3.93	3.03	Rate	4.97	4.01

Irregular polyhedral S-elements - Case 3

ℓ	$k=1$			$k=2$			$k=3$			$k=4$		
	DOF	$E^h_{L^2}$	$E^h_{H^1}$	DOF	$E^h_{L^2}$	$E^h_{H^1}$	DOF	$E^h_{L^2}$	$E^h_{H^1}$	DOF	$E^h_{L^2}$	$E^h_{H^1}$
1	63	2.04E-2	4.56E-1	261	5.94E-4	2.04E-2	603	1.43E-5	5.85E-4	1089	2.25E-7	1.19E-5
2	595	5.24E-3	2.11E-1	2693	6.51E-5	3.95E-3	6359	6.35E-7	5.20E-5	11593	5.43E-9	5.49E-7
3	5349	1.07E-3	9.28E-2	24653	5.70E-6	7.39E-4	58425	2.72E-8	4.60E-6	106665	1.12E-10	2.34E-8
	Rate	2.17	1.12	Rate	3.30	2.00	Rate	4.26	3.28	Rate	5.25	4.27

Tetrahedral FEs - Case 3

ℓ	$k=1$			$k=2$			$k=3$			$k=4$		
	DOF	$E^h_{L^2}$	$E^h_{H^1}$	DOF	$E^h_{L^2}$	$E^h_{H^1}$	DOF	$E^h_{L^2}$	$E^h_{H^1}$	DOF	$E^h_{L^2}$	$E^h_{H^1}$
1	63	3.01E-2	7.01E-1	365	8.27E-4	2.97E-2	1099	1.93E-5	8.29E-4	386	2.78E-7	1.61E-5
2	605	8.89E-3	3.82E-1	4406	1.21E-4	7.34E-3	14330	1.24E-6	1.01E-4	2169	9.83E-9	1.04E-6
3	5500	2.01E-3	1.80E-1	43486	1.28E-5	1.58E-3	145313	6.34E-8	1.06E-5	13985	2.61E-10	5.48E-8
	Rate	2.02	1.02	Rate	2.95	2.02	Rate	3.85	2.92	Rate	4.67	3.79

Example 5 - Singular harmonic function - Single S-element

Table A.7: Errors $E^h_{L^2} = \|u-u^h\|_{L^2(\Omega)}$ and $E^h_{H^1} = |u-u^h|_{H^1(\Omega)}$, $h = 2^{-\ell}$ for the SBFEM approximation, using a single S-element, for $k = 1, .., 4$.

ℓ	$k=1$			$k=2$			$k=3$			$k=4$		
	DOF	$E^h_{L^2}$	$E^h_{H^1}$	DOF	$E^h_{L^2}$	$E^h_{H^1}$	DOF	$E^h_{L^2}$	$E^h_{H^1}$	DOF	$E^h_{L^2}$	$E^h_{H^1}$
0	5	1.29E-2	1.16E-1	9	1.31E-3	1.90E-2	13	1.86E-4	3.50E-3	17	2.65E-5	6.77E-4
1	9	2.70E-3	5.77E-2	17	1.90E-4	4.90E-3	25	1.26E-5	4.71E-4	33	9.94E-7	4.75E-5
2	17	6.46E-4	2.86E-2	33	2.48E-5	1.23E-3	49	8.09E-7	5.96E-5	65	3.25E-8	3.03E-6
3	33	1.60E-4	1.43E-2	65	3.13E-6	3.09E-4	97	5.15E-8	7.46E-6	129	1.19E-9	1.91E-7
	Rate	2.01	1.01	Rate	2.99	2.00	Rate	3.96	3.00	Rate	4.96	3.99

Example 6 - Singular harmonic function - Coupled mesh FEM/SBFEM

Table A.8: Errors $E^h_{L^2} = \|u-u^h\|_{L^2(\Omega)}$ and $E^h_{H^1} = |u-u^h|_{H^1(\Omega)}$, $h = 2^{-\ell}$, using the combined FE-SBFEM mesh, for $k = 1, ..., 4$.

ℓ	$k=1$			$k=2$			$k=3$			$k=4$		
	DOF	$E^h_{L^2}$	$E^h_{H^1}$	DOF	$E^h_{L^2}$	$E^h_{H^1}$	DOF	$E^h_{L^2}$	$E^h_{H^1}$	DOF	$E^h_{L^2}$	$E^h_{H^1}$
1	14	8.44E-4	1.11E-1	26	7.87E-4	1.94E-2	76	9.17E-5	2.82E-3	125	1.19E-5	5.25E-4
2	39	2.02E-3	5.54E-2	117	1.12E-4	4.23E-3	259	6.35E-6	3.83E-4	441	4.59E-7	3.72E-5
3	125	4.95E-4	2.73E-2	665	1.45E-5	1.06E-3	949	4.16E-7	4.87E-5	1649	1.54E-8	2.39E-6
4	441	1.23E-4	1.36E-2	4401	1.84E-6	2.66E-4	3625	2.67E-8	6.10E-6	6369	4.97E-10	1.50E-7
	Rate	2.01	1.01	Rate	2.99	2.00	Rate	3.96	3.00	Rate	4.96	3.99

A.1.2 Elasticity problems

Example 7 - Two-dimensional loaded beam

Table A.9: Example 7 - Interpolation errors $E^h_{L^2} = \|u-u^h\|_{L^2(\Omega)}$ and $E^h_{H^1} = |u-u^h|_{H^1(\Omega)}$ for uniform partitions $\mathcal{T}^h$ of a single quadrilateral S-element and of a dense mesh of quadrilateral S-elements, with $h = 2/2^{-\ell}$.

Single quadrilateral S-element

ℓ	$k=1$			$k=2$			$k=3$		
	DOF	$E^h_{L^2}$	$E^h_{H^1}$	DOF	$E^h_{L^2}$	$E^h_{H^1}$	DOF	$E^h_{L^2}$	$E^h_{H^1}$
0	8	1.16E-1	1.38E0	16	4.13E-2	4.80E-1	24	1.44E-15	1.57E-14
1	16	5.17E-2	7.89E-1	32	5.55E-3	1.07E-1	48	2.27E-15	2.84E-14
2	32	9.83E-3	3.85E-1	64	6.68E-4	2.61E-2	96	2.26E-15	5.22E-14
	Rate	2.39	1.04	Rate	3.05	2.04	Rate	-	-

Uniform dense mesh of quadrilateral S-elements

ℓ	$k=1$			$k=2$			$k=3$		
	DOF	$E^h_{L^2}$	$E^h_{H^1}$	DOF	$E^h_{L^2}$	$E^h_{H^1}$	DOF	$E^h_{L^2}$	$E^h_{H^1}$
0	8	1.16E-1	1.38E0	16	4.13E-2	4.80E-1	24	1.44E-15	1.57E-14
1	18	1.04E-1	1.06E0	42	7.46E-3	1.32E-1	66	1.00E-15	1.80E-14
2	50	2.42E-2	5.16E-1	130	1.05E-3	3.46E-2	210	8.10E-15	2.04E-14
3	162	5.88E-3	2.52E-1	450	1.35E-4	8.75E-3	738	1.83E-15	4.36E-14
	Rate	2.04	1.03	Rate	2.96	1.98	Rate	-	-

Example 8 - Three-dimensional cantilever beam

Table A.10: Example 8 - Galerkin SBFEM errors $E^h_{L^2} = \|u - u^h\|_{L^2(\Omega)}$ and $E^h_{H^1} = |u - u^h|_{H^1(\Omega)}$ for uniform partitions $\mathcal{T}^h$ of hexahedral regular S-elements, with $h = 2^{-\ell}$.

ℓ	$k=1$			$k=2$			$k=3$			$k=4$		
	DOF	$E^h_{L^2}$	$E^h_{H^1}$	DOF	$E^h_{L^2}$	$E^h_{H^1}$	DOF	$E^h_{L^2}$	$E^h_{H^1}$	DOF	$E^h_{L^2}$	$E^h_{H^1}$
0	72	3.12E-1	2.08E0	282	2.18E-2	1.71E-1	648	6.21E-4	1.08E-2	1170	1.12E-4	3.25E-3
1	297	8.84E-2	1.08E0	1455	3.07E-3	4.44E-2	3597	7.50E-5	2.83E-3	6723	2.62E-5	1.11E-3
2	1575	2.15E-2	5.31E-1	9003	4.06E-4	1.14E-2	23247	9.30E-6	6.01E-4	44307	1.96E-6	1.46E-4
3	9963	5.30E-3	2.64E-1	62547	5.15E-5	2.80E-3	165435	7.13E-7	7.06E-5	318627	9.77E-8	1.42E-5
4	70227	1.32E-3	1.32E-1	464547	6.51E-6	6.99E-4	1244403	5.22E-8	1.03E-5	2409795	2.99E-9	7.39E-7
	Rate	2.01	1.00	Rate	2.98	2.00	Rate	3.77	2.78	Rate	5.03	4.26

ℓ	$k=5$		
	DOF	$E^h_{L^2}$	$E^h_{H^1}$
0	1848	5.47E-5	1.84E-3
1	10833	1.06E-5	5.81E-4
2	72183	6.11E-7	5.89E-5
3	522123	6.63E-9	1.08E-6
	Rate	6.53	5.78

Example 9 - Lateral crack

Table A.11: Example 9 - Galerkin SBFEM errors $E^h_{L^2} = \|u - u^h\|_{L^2(\Omega)}$ and $E^h_{H^1} = |u - u^h|_{H^1(\Omega)}$ for a lateral crack approximated using only the SBFEM for a single S-element and a coupled mesh SBFEM+FEM mesh, for $h = 2^{-\ell}$.

SBFEM mesh

ℓ	$k=1$			$k=2$			$k=3$			$k=4$		
	DOF	$E^h_{L^2}$	$E^h_{H^1}$	DOF	$E^h_{L^2}$	$E^h_{H^1}$	DOF	$E^h_{L^2}$	$E^h_{H^1}$	DOF	$E^h_{L^2}$	$E^h_{H^1}$
0	18	4.24E-3	3.75E-2	34	6.06E-4	8.96E-3	50	1.13E-4	2.12E-3	66	2.00E-5	5.05E-4
1	34	9.76E-4	1.90E-2	66	8.95E-5	2.34E-3	98	8.06E-6	2.97-4	130	7.91E-7	3.77E-5
2	66	2.39E-4	9.47E-3	130	1.19E-5	5.88E-4	194	5.17E-7	3.78E-5	258	2.62E-8	2.42E-6
3	130	5.97E-5	4.73E-3	258	1.51E-5	1.47E-4	386	3.30E-8	4.74E-6	514	8.32E-10	1.52E-7
	Rate	2.00	1.00	Rate	2.98	2.00	Rate	3.97	3.00	Rate	4.98	3.99

SBFEM+FEM mesh

ℓ	$k=1$			$k=2$			$k=3$			$k=4$		
	DOF	$E^h_{L^2}$	$E^h_{H^1}$	DOF	$E^h_{L^2}$	$E^h_{H^1}$	DOF	$E^h_{L^2}$	$E^h_{H^1}$	DOF	$E^h_{L^2}$	$E^h_{H^1}$
1	52	2.60E-3	3.38E-2	150	3.41E-4	7.18E-3	296	4.98E-5	1.63E-3	490	8.57E-6	3.77E-4
2	150	7.17E-4	1.70E-2	490	4.54E-5	1.89E-3	1022	3.57E-6	2.28E-4	1746	3.31E-7	2.82E-5
3	490	1.86E-4	8.46E-2	1746	5.73E-6	4.77E-4	3770	2.29E-7	2.92E-5	6562	1.07E-8	1.83E-6
	Rate	1.95	1.00	Rate	2.99	1.99	Rate	3.96	2.97	Rate	4.95	3.95

A.2 Chapter 4 - A bubble function approach to approximate non-homogeneous PDE with the SBFEM

A.2.1 Poisson problems

Example 1: Two-dimensional single element

Table A.12: Example 1 - SBFEM errors $E^h_{L^2} = \|u-u^h\|_{L^2(\Omega)}$ and $E^h_{H^1} = |u-u^h|_{H^1(\Omega)}$ for $h = 2/2^\ell,\ \ell = 0,...,3$, using only polynomial bubbles of internal order $k_b = 5$ and trace approximation $k = 1,...,5$.

Polynomial bubbles - $k_b = 5$

ℓ	$k=1$			$k=2$			$k=3$		
	DOF	$E^h_{L^2}$	$E^h_{H^1}$	DOF	$E^h_{L^2}$	$E^h_{H^1}$	DOF	$E^h_{L^2}$	$E^h_{H^1}$
0	4	5.69E-1	2.48E0	8	2.56E-1	1.69E0	12	4.78E-2	4.66E-1
1	8	2.66E-1	1.85E0	16	7.95E-2	7.70E-1	24	1.66E-2	2.22E-1
2	16	9.25E-2	1.19E0	32	1.43E-2	2.75E-1	48	6.03E-3	1.27E-1
3	32	2.46E-2	6.76E-1	64	6.16E-3	1.41E-1	96	5.91E-3	1.30E-1
	Rate	1.91	0.82	Rate	1.22	0.96	Rate	-	-

ℓ	$k=4$			$k=5$		
	DOF	$E^h_{L^2}$	$E^h_{H^1}$	DOF	$E^h_{L^2}$	$E^h_{H^1}$
0	16	4.73E-2	4.43E-1	20	5.38E-3	1.06E-1
1	32	6.09E-3	1.22E-1	40	6.09E-3	1.28E-1
2	64	5.96E-3	1.30E0-1	80	5.89E-3	1.31E-1
3	128	5.88E-3	1.31E-1	160	5.88E-3	1.31E-1
	Rate	-	-	Rate	-	-

Table A.13: Example 1 - SBFEM errors $E^h_{L^2} = \|u-u^h\|_{L^2(\Omega)}$ and $E^h_{H^1} = |u-u^h|_{H^1(\Omega)}$ for $h = 2/2^n,\ n = 0,...,3$, using only polynomial bubbles of internal order $k_b = 6$ and trace approximation $k = 1,...,5$.

Polynomial bubbles - $k_b = 6$

ℓ	$k=1$			$k=2$			$k=3$		
	DOF	$E^h_{L^2}$	$E^h_{H^1}$	DOF	$E^h_{L^2}$	$E^h_{H^1}$	DOF	$E^h_{L^2}$	$E^h_{H^1}$
0	4	5.69E-1	2.48E0	8	2.56E-1	1.69E0	12	4.78E-2	4.66E-1
1	8	2.66E-1	1.85E0	16	7.94E-2	7.70E-1	24	1.60E-2	2.08E-1
2	16	9.25E-2	1.19E0	32	1.34E-2	2.62E-1	48	2.61E-3	6.41E-2
3	32	2.46E-2	6.72E-1	64	3.01E-3	9.02E-2	96	2.48E-3	6.58E-2
	Rate	1.91	0.82	Rate	2.15	1.54	Rate	-	-

ℓ	$k=4$			$k=5$		
	DOF	$E^h_{L^2}$	$E^h_{H^1}$	DOF	$E^h_{L^2}$	$E^h_{H^1}$
0	16	4.71E-2	4.40E-1	20	1.59E-3	3.69E-2
1	32	2.69E-3	5.65E-2	40	2.53E-3	6.22E-2
2	64	2.51E-3	6.50E0-2	80	2.47E-3	6.65E-2
3	128	2.46E-3	6.67E-2	160	2.45E-3	6.68E-2
	Rate	-	-	Rate	-	-

Note: The number of equations do not change with the increment of the internal polynomial order due to the local static condensation of the internal DOF per element.

Table A.14: Example 1 - SBFEM errors $E^h_{L^2} = \|u-u^h\|_{L^2(\Omega)}$ and $E^h_{H^1} = |u-u^h|_{H^1(\Omega)}$ for $h = 2/2^n$, $n = 0, ..., 3$, using the SBFEM bubbles of internal order $k_b = 4, 5, 6$ and trace approximation $k = 1, ..., 5$.

SBFEM bubble space up to $k_b = 4$

ℓ	$k=1$			$k=2$			$k=3$		
	DOF	$E^h_{L^2}$	$E^h_{H^1}$	DOF	$E^h_{L^2}$	$E^h_{H^1}$	DOF	$E^h_{L^2}$	$E^h_{H^1}$
0	4	5.69E-1	2.48E0	8	2.56E-1	1.69E0	12	4.77E-2	4.66E-1
1	8	2.66E-1	1.85E0	16	7.94E-2	7.71E-1	24	1.62E-2	2.10E-1
2	16	9.24E-2	1.19E0	32	1.36E-2	2.64E-1	48	3.02E-3	4.84E-2
3	32	2.41E-2	6.72E-1	64	3.40E-3	8.03E-2	96	2.83E-3	3.78E-2
	Rate	1.94	0.82	Rate	2.00	1.72	Rate	0.09	0.36

ℓ	$k=4$			$k=5$		
	DOF	$E^h_{L^2}$	$E^h_{H^1}$	DOF	$E^h_{L^2}$	$E^h_{H^1}$
0	16	4.71E-2	4.42E-1	20	2.84E-3	3.77E-2
1	32	3.23E-3	4.52E-2	40	2.583E-3	3.76E-2
2	64	2.83E-3	3.77E-2	80	2.83E-3	3.76E-2
3	128	2.83E-3	3.76E-2	160	2.83E-3	3.76E-2
	Rate	-	-	Rate	-	-

SBFEM bubble space up to $k_b = 5$

ℓ	$k=1$			$k=2$			$k=3$		
	DOF	$E^h_{L^2}$	$E^h_{H^1}$	DOF	$E^h_{L^2}$	$E^h_{H^1}$	DOF	$E^h_{L^2}$	$E^h_{H^1}$
0	4	5.69E-1	2.48E0	8	2.56E-1	1.69E0	12	4.78E-2	4.66E-1
1	8	2.66E-1	1.85E0	16	7.94E-2	7.70E-1	24	1.59E-2	2.07E-1
2	16	9.24E-2	1.19E0	32	1.33E-2	2.61E-1	48	1.03E-3	3.04E-2
3	32	2.41E-2	6.73E-1	64	1.87E-3	7.10E-2	96	6.74E-5	3.93E-3
	Rate	1.94	0.82	Rate	2.83	1.88	Rate	3.93	2.95

ℓ	$k=4$			$k=5$		
	DOF	$E^h_{L^2}$	$E^h_{H^1}$	DOF	$E^h_{L^2}$	$E^h_{H^1}$
0	16	4.70E-2	4.40E-1	20	7.54E-12	1.88E-11
1	32	1.50E-3	2.51E-2	40	7.53E-12	1.98E-11
2	64	4.72E-5	1.55E-3	80	7.78E-6	2.65E-4
3	128	1.53E-6	9.80E-5	160	1.80E-7	1.12E-5
	Rate	4.95	3.98	Rate	-	-

SBFEM bubble space up to $k_b = 6$

ℓ	$k=1$			$k=2$			$k=3$		
	DOF	$E^h_{L^2}$	$E^h_{H^1}$	DOF	$E^h_{L^2}$	$E^h_{H^1}$	DOF	$E^h_{L^2}$	$E^h_{H^1}$
0	4	5.69E-1	2.48E0	8	2.56E-1	1.69E0	12	4.77E-2	4.66E-1
1	8	2.66E-1	1.85E0	16	7.94E-2	7.70E-1	24	1.59E-2	2.07E-1
2	16	9.25E-2	1.19E0	32	1.33E-2	2.61E-1	48	1.03E-3	3.04E-2
3	32	2.40E-2	6.72E-1	64	1.87E-3	7.10E-2	96	6.74E-5	3.93E-3
	Rate	1.95	0.82	Rate	2.83	1.88	Rate	3.93	2.95

ℓ	$k=4$			$k=5$		
	DOF	$E^h_{L^2}$	$E^h_{H^1}$	DOF	$E^h_{L^2}$	$E^h_{H^1}$
0	16	4.70E-2	4.40E-1	20	7.71E-12	3.76E-11
1	32	1.50E-3	2.51E-2	40	7.68E-12	3.91E-11
2	64	4.71E-5	1.54E-3	80	3.70E-6	1.41E-4
3	128	1.50E-6	9.71E-5	160	1.24E-7	8.16E-6
	Rate	4.97	3.99	Rate	-	-

Example 2: Two-dimensional domain refinement

Table A.15: Example 2 - SBFEM errors $E^h_{L^2} = \|u-u^h\|_{L^2(\Omega)}$ and $E^h_{H^1} = |u-u^h|_{H^1(\Omega)}$ for $h = 2/2^\ell$, $\ell = 0, ..., 4$, using Duffy polynomial space and SBFEM bubble space enriching the SBFEM bubble-free space considering internal polynomial order equal to the trace polynomial order, i.e. $k = k_b = 1, ..., 5$.

SBFEM bubble-free space enriched with Duffy polynomial bubbles

ℓ	$k=1$			$k=2$			$k=3$		
	DOF	$E^h_{L^2}$	$E^h_{H^1}$	DOF	$E^h_{L^2}$	$E^h_{H^1}$	DOF	$E^h_{L^2}$	$E^h_{H^1}$
0	4	1.25E0	4.51E0	8	3.28E-1	2.26E0	12	5.50E-2	6.60E-1
1	9	6.14E-1	3.24E0	21	1.19E-1	1.22E0	33	2.13E-2	3.42E-1
2	25	2.36E-1	2.13E0	65	2.43E-2	5.47E-1	105	2.26E-3	1.04E-1
3	81	6.75E-2	1.17E0	225	4.71E-3	2.44E-1	369	4.45E-4	4.37E-2
4	289	1.74E-2	5.94E-1	833	1.03E-3	1.17E-1	1377	1.07E-4	2.09E-2
	Rate	1.96	0.98	Rate	2.19	1.06	Rate	2.06	1.06

ℓ	$k=4$			$k=5$		
	DOF	$E^h_{L^2}$	$E^h_{H^1}$	DOF	$E^h_{L^2}$	$E^h_{H^1}$
0	16	4.82E-2	4.72E-1	20	5.38E-3	1.06E-1
1	45	3.34E-3	9.61E-2	57	9.20E-4	3.58E-2
2	145	5.60E-4	3.48E-2	185	1.64E-4	1.28E-2
3	513	1.18E-4	1.47E-2	657	3.35E-5	5.20E-3
4	1921	2.77E-5	6.92E-3	2465	7.77E-6	2.42E-3
	Rate	2.09	1.09	Rate	2.11	1.10

SBFEM bubble-free space enriched with SBFEM bubbles

ℓ	$k=1$			$k=2$			$k=3$		
	DOF	$E^h_{L^2}$	$E^h_{H^1}$	DOF	$E^h_{L^2}$	$E^h_{H^1}$	DOF	$E^h_{L^2}$	$E^h_{H^1}$
0	4	1.25E0	4.51E0	8	3.35E-1	2.25E0	12	5.97E-2	5.82E-1
1	9	6.14E-1	3.24E0	21	1.17E-1	1.16E0	33	2.04E-2	2.67E-1
2	25	2.36E-1	2.13E0	65	2.15E-2	3.82E-1	105	1.38E-3	3.66E-2
3	81	6.75E-2	1.17E0	225	3.07E-3	1.04E-1	369	8.72E-5	4.61E-3
4	289	1.74E-2	5.94E-1	833	4.01E-4	2.68E-2	1377	5.42E-6	5.74E-4
	Rate	1.96	0.98	Rate	2.94	1.96	Rate	4.01	3.01

ℓ	$k=4$			$k=5$		
	DOF	$E^h_{L^2}$	$E^h_{H^1}$	DOF	$E^h_{L^2}$	$E^h_{H^1}$
0	16	4.71E-2	4.42E-1	20	7.54E-12	1.88E-11
1	45	1.70E-3	2.82E-2	57	7.54E-12	1.99E-11
2	145	5.56E-5	1.78E-3	185	7.54E-12	2.10E-11
3	513	1.76E-6	1.12E-4	657	7.54E-12	2.23E-11
4	1921	5.54E-8	6.98E-6	2465	7.54E-12	2.35E-11
	Rate	4.99	4.00	Rate	-	-

Example 3: A heat flow

Table A.16: Example 3 - SBFEM errors $E^h_{L^2} = \|u-u^h\|_{L^2(\Omega)}$ and $E^h_{H^1} = |u-u^h|_{H^1(\Omega)}$ for $h = 2/2^n,\ n = 0, ..., 3$, using Duffy polynomial space and SBFEM bubble space enriching the SBFEM bubble-free space considering internal polynomial order equal to the trace polynomial order, i.e. $k = k_b = 1, ..., 3$.

SBFEM bubble-free space

ℓ	$k=1$			$k=2$			$k=3$		
	DOF	$E^h_{L^2}$	$E^h_{H^1}$	DOF	$E^h_{L^2}$	$E^h_{H^1}$	DOF	$E^h_{L^2}$	$E^h_{H^1}$
0	4	5.17E-5	2.30E-4	8	5.17E-5	2.30E-4	12	5.17E-5	2.30E-4
1	9	5.17E-5	2.30E-4	21	5.17E-5	2.30E-4	33	5.17E-5	2.30E-4
2	25	4.67E-5	2.08E-4	65	4.31E-5	1.92E-4	105	4.30E-5	1.92E-4
3	81	2.23E-5	1.04E-4	225	1.92E-5	9.05E-5	369	1.92E-5	9.03E-5
	Rate	1.07	1.00	Rate	1.17	1.09	Rate	1.16	1.09

SBFEM bubble-free space enriched with Duffy's polynomial bubble space

ℓ	$k=1$			$k=2$			$k=3$		
	DOF	$E^h_{L^2}$	$E^h_{H^1}$	DOF	$E^h_{L^2}$	$E^h_{H^1}$	DOF	$E^h_{L^2}$	$E^h_{H^1}$
0	4	1.25E0	2.16E-4	8	2.22E-5	5.07E-5	12	9.16E-6	8.07E-5
1	9	1.04E-5	9.76E-5	21	4.05E-6	5.30E-5	33	2.70E-7	4.87E-6
2	25	5.94E-6	7.01E-5	65	9.35E-7	2.17E-5	105	1.21E-7	4.91E-6
3	81	1.14E-6	3.14E-5	833	1.91E-7	9.91E-6	369	2.05E-8	1.90E-6
	Rate	2.38	1.16	Rate	2.29	1.13	Rate	2.56	1.37

SBFEM bubble-free space enriched with the SBFEM bubble space

ℓ	$k=1$			$k=2$			$k=3$		
	DOF	$E^h_{L^2}$	$E^h_{H^1}$	DOF	$E^h_{L^2}$	$E^h_{H^1}$	DOF	$E^h_{L^2}$	$E^h_{H^1}$
0	4	5.07E-5	2.16E-4	8	2.22E-5	1.44E-4	12	5.59E-6	5.27E-5
1	9	1.04E-5	9.76E-5	21	1.79E-6	2.75E-5	33	2.70E-7	4.87E-6
2	25	5.94E-6	7.01E-5	65	6.62E-7	1.27E-5	105	5.09E-8	1.42E-6
3	81	1.14E-6	3.14E-5	225	9.52E-8	3.40E-6	369	3.00E-9	1.73E-7
	Rate	2.38	1.16	Rate	2.78	1.90	Rate	4.09	3.04

Example 4: Three-dimensional single element

Table A.17: Example 4 - SBFEM errors $E^h_{L^2} = \|u - u^h\|_{L^2(\Omega)}$ and $E^h_{H^1} = |u - u^h|_{H^1(\Omega)}$ for a partition composed of 3D single S-element, refining the skeleton, with $h = 2/2^n,\ n = 0, 1, 2$, using SBFEM bubble space enriching the SBFEM bubble-free space for $k = k_b = 1, ..., 3$ and $k_b = k + \ell$.

Bubble approximation: $k_b = k$

ℓ	$k=1$			$k=2$			$k=3$		
	DOF	$E^h_{L^2}$	$E^h_{H^1}$	DOF	$E^h_{L^2}$	$E^h_{H^1}$	DOF	$E^h_{L^2}$	$E^h_{H^1}$
0	24	6.66E-1	2.43E0	78	4.03E-2	3.14E-1	168	2.49E-2	1.91E-1
1	78	1.93E-1	1.24E0	294	3.20E-2	2.83E-1	654	1.73E-3	2.36E-2
2	294	5.93E-2	5.82E-1	1158	2.88E-2	2.52E-1	2598	1.24E-3	1.55E-2
	Rate	1.70	1.09	Rate	0.15	0.17	Rate	0.48	0.61

Bubble approximation: $k_b = k + \ell$

ℓ	$k=1$			$k=2$			$k=3$		
	DOF	$E^h_{L^2}$	$E^h_{H^1}$	DOF	$E^h_{L^2}$	$E^h_{H^1}$	DOF	$E^h_{L^2}$	$E^h_{H^1}$
0	27	6.66E-1	2.43E0	78	4.03E-2	3.14E-1	168	2.49E-2	1.91E-1
1	78	1.34E-1	1.04E0	294	1.12E-2	1.32E-1	254	1.37E-3	2.09E-2
2	294	2.67E-2	4.75E-1	1158	1.90E-3	3.58E-2	2598	7.57E-5	2.17E-3
	Rate	2.33	1.13	Rate	2.56	1.88	Rate	4.18	3.27

Example 5: Three-dimensional uniform refinement by hexahedral S-elements

Table A.18: Example 2 - Errors $E^h_{L^2} = \|u - u^h\|_{L^2(\Omega)}$ and $E^h_{H^1} = |u - u^h|_{H^1(\Omega)}$, for $h = 2/2^\ell,\ \ell = 0, ..., 3$, using the Galerkin SBFEM approximation for uniform meshes of hexahedral S-elements (see Fig. 4.12).

ℓ	$k=1$			$k=2$			$k=3$		
	DOF	$E^h_{L^2}$	$E^h_{H^1}$	DOF	$E^h_{L^2}$	$E^h_{H^1}$	DOF	$E^h_{L^2}$	$E^h_{H^1}$
0	24	6.663E-1	2.433E0	60	4.032E-2	3.144E-1	96	2.493E-2	1.911E-1
1	81	1.925E-1	1.238E0	243	2.097E-2	1.996E-1	405	1.770E-3	2.516E-2
2	375	4.309E-2	5.796E-1	1275	3.236E-3	5.324E-2	2175	1.115E-4	3.099E-3
3	2187	1.038E-2	2.837E-1	8019	4.342E-4	1.361E-2	13851	7.032E-6	3.827E-4
	Rate	2.05	1.03	Rate	2.90	1.97	Rate	3.99	3.02

A.2.2 Elasticity

Example 6 - Elasticity problem in 2D

Table A.19: Example 6 - Errors $E^h_{L^2} = \|u - u^h\|_{L^2(\Omega)}$ and $E^h_{H^1} = |u - u^h|_{H^1(\Omega)}$, for $h = 2/2^\ell,\ \ell = 0, ..., 3$ and $k = k_b = 1, ..., 7$, using the Galerkin SBFEM with bubbles in an uniform partition of quadrilateral S-elements.

ℓ	k=1			k=2			k=3			k=4		
	DOF	$E^h_{L^2}$	$E^h_{H^1}$	DOF	$E^h_{L^2}$	$E^h_{H^1}$	DOF	$E^h_{L^2}$	$E^h_{H^1}$	DOF	$E^h_{L^2}$	$E^h_{H^1}$
0	8	2.94E0	1.26E1	16	1.76E0	1.05E1	24	3.48E-1	3.29E0	32	1.85E-1	1.84E0
1	18	2.37E0	1.16E1	42	1.07E-1	1.56E0	66	7.96E-2	1.08E0	90	1.90E-3	4.26E-2
2	50	3.41E-1	4.46E1	130	4.01E-2	8.75E-1	210	2.85E-3	9.13E-2	290	2.08E-4	8.02E-3
3	162	6.82E-2	2.17E0	450	5.88E-3	2.38E-1	738	1.66E-4	1.08E-2	1026	7.16E-6	5.27E-4
	Rate	2.32	1.19	Rate	2.77	1.93	Rate	4.10	3.07	Rate	3.94	4.86

ℓ	k=5			k=6			k=7		
	DOF	$E^h_{L^2}$	$E^h_{H^1}$	DOF	$E^h_{L^2}$	$E^h_{H^1}$	DOF	$E^h_{L^2}$	$E^h_{H^1}$
0	40	1.97E-2	2.73E-1	48	1.03E-2	1.45E-1	56	6.59E-4	1.18E-2
1	114	1.17E-3	2.47E-2	138	1.96E-5	5.80E-4	162	1.09E-5	3.15E-4
2	370	1.23E-5	5.76E-4	450	6.50E-7	3.53E-5	530	2.97E-8	1.85E-6
3	1314	1.90E-7	1.78E-5	1602	5.46E-9	5.71E-7	1890	1.19E-10	1.43E-8
	Rate	6.01	5.02	Rate	5.95	6.90	Rate	7.96	7.03

Example 7 - Elasticity problem in 3D

Table A.20: Example 6 - Errors $E^h_{L^2} = \|u - u^h\|_{L^2(\Omega)}$ and $E^h_{H^1} = |u - u^h|_{H^1(\Omega)}$, for $h = 2/2^\ell,\ \ell = 0, ..., 3$ and $k = k_b = 1, ..., 7$, using the Galerkin SBFEM with bubbles in an uniform partition of quadrilateral S-elements.

Tetrahedral subpartition

ℓ	$k = k_b = 1$			$k = k_b = 2$			$k = 1$ and $k_b = 2$			$k = 2$ and $k_b = 3$		
	DOF	$E^h_{L^2}$	$E^h_{H^1}$	DOF	$E^h_{L^2}$	$E^h_{H^1}$	DOF	$E^h_{L^2}$	$E^h_{H^1}$	DOF	$E^h_{L^2}$	$E^h_{H^1}$
0	12	5.19E-1	4.48E0	40	7.94E-2	1.58E0	84	1.53E-1	2.61E0	114	7.45E-2	1.52E0
1	34	1.69E-1	2.73E0	138	1.52E-2	4.63E-1	306	1.05E-1	2.17E0	538	1.18E-2	3.53E-1
2	114	3.53E-2	1.26E0	514	2.56E-3	1.62E-1	1170	2.64E-2	1.06E0	2082	1.88E-3	1.01E-1
3	418	7.96E-3	6.01E-1	1986	4.33E-4	6.63E-2	4578	6.46E-3	5.22E-1	8194	2.67E-4	3.16E-2
	Rate	2.32	1.19	Rate	2.77	1.93	Rate	4.10	3.07	Rate	3.94	4.86

Hexahedral subpartition

ℓ	$k = k_b = 1$			$k = k_b = 2$		
	DOF	$E^h_{L^2}$	$E^h_{H^1}$	DOF	$E^h_{L^2}$	$E^h_{H^1}$
0	220	8.82E-1	6.15E0	312	5.68E-2	8.49E-1
1	834	2.20E-1	2.64E0	1194	2.32E-2	5.25E-1
2	3250	4.31E-2	1.19E0	4674	3.68E-3	1.41E-1
3	12834	9.88E-3	5.72E-1	18498	5.10E-4	4.06E-2
	Rate	6.01	5.02	Rate	5.95	6.90

A.3 Chapter 5 - Locally conservative SBFEM approximation

Example 1: 2D Polynomial Darcy Flow

Table A.21: Example 3 - L^2 errors for the flux and the pressure, using the Galerkin SBFEM a single S-element with skeleton refinement, for $h = 2/2^\ell,\ \ell = 0, ..., 3$ and $k = 1, ..., 6$.

ℓ	$k=1$			$k=2$			$k=3$		
	DOF	$E^H_{L^2}$ - u	$E^H_{L^2}$ - $\underline{\sigma}$	DOF	$E^H_{L^2}$ - u	$E^H_{L^2}$ - $\underline{\sigma}$	DOF	$E^H_{L^2}$ - u	$E^H_{L^2}$ - $\underline{\sigma}$
1	8	1.196E0	1.142E1	12	7.931E-1	2.205E0	16	7.931E-1	2.205E0
2	24	6.261E-1	1.515E0	36	3.238E-1	9.477E-1	48	3.191E-2	1.086E-1
3	80	2.510E-1	9.575E-1	120	3.201E-2	1.115E-1	160	1.757E-3	6.282E-3
4	288	6.291E-2	2.546E-1	432	3.606E-3	1.360E-2	576	1.064E-4	3.857E-4
	Rate	2.00	1.91	Rate	3.15	3.04	Rate	4.045	4.03

ℓ	$k=4$			$k=5$			$k=6$		
	DOF	$E^H_{L^2}$ - u	$E^H_{L^2}$ - $\underline{\sigma}$	DOF	$E^H_{L^2}$ - u	$E^H_{L^2}$ - $\underline{\sigma}$	DOF	$E^H_{L^2}$ - u	$E^H_{L^2}$ - $\underline{\sigma}$
1	20	1.452E-2	1.993E-13	24	1.452E-2	5.504E-13	28	6.507E-14	6.161E-13
2	60	2.940E-3	2.777E-13	72	2.269E-4	5.775E-13	84	1.645E-13	1.349E-12
3	200	1.025E-4	5.016E-13	240	3.545E-6	1.755E-12	280	2.967E-13	3.951E-12
4	720	3.279E-6	1.396E-12	864	5.540E-8	5.654E-12	1008	2.589E-13	1.697E-11
	Rate	4.97	-	Rate	6.00	-	Rate	-	-

Example 2: 2D Darcy Flow

Table A.22: Example 3 - L^2 errors for the flux and the pressure, using the Galerkin SBFEM a single S-element with skeleton refinement, for $h = 2/2^\ell,\ \ell = 0, ..., 3$ and $k = 1, ..., 7$.

ℓ	$k=1$			$k=2$			$k=3$			$k=4$		
	DOF	$E^H_{L^2}$ - u	$E^H_{L^2}$ - $\underline{\sigma}$	DOF	$E^H_{L^2}$ - u	$E^H_{L^2}$ - $\underline{\sigma}$	DOF	$E^H_{L^2}$ - u	$E^H_{L^2}$ - $\underline{\sigma}$	DOF	$E^H_{L^2}$ - u	$E^H_{L^2}$ - $\underline{\sigma}$
1	8	4.935E0	2.505E1	12	4.576E0	2.073E1	16	5.530E-1	2.428E0	20	5.440E-1	2.292E0
2	24	2.716E0	1.426E1	36	1.330E-1	1.090E0	48	1.143E-1	4.814E-1	60	2.436E-3	2.833E-2
3	80	5.068E-1	2.441E0	120	5.837E-2	2.262E-1	160	5.207E-3	2.078E-2	200	3.775E-4	1.611E-3
4	288	1.237E-1	5.664E-1	432	7.112E-3	2.602E-2	576	3.158E-4	1.293E-3	720	1.140E-5	4.874E-5
	Rate	2.03	2.11	Rate	3.04	3.12	Rate	4.04	4.01	Rate	5.05	5.05

ℓ	$k=5$			$k=6$			$k=7$		
	DOF	$E^H_{L^2}$ - u	$E^H_{L^2}$ - $\underline{\sigma}$	DOF	$E^H_{L^2}$ - u	$E^H_{L^2}$ - $\underline{\sigma}$	DOF	$E^H_{L^2}$ - u	$E^H_{L^2}$ - $\underline{\sigma}$
1	24	3.168E-2	1.549E-1	28	3.111E-2	1.305E-1	32	1.041E-3	4.858E-3
2	72	2.109E-3	9.411E-3	84	2.410E-5	3.302E-4	96	2.121E-5	8.873E-5
3	240	2.306E-5	9.582E-5	280	1.217E-6	4.764E-6	320	5.661E-8	2.238E-7
4	864	3.468E-7	1.420E-6	1008	9.132E-9	3.490E-8	1152	2.123E-10	8.943E-10
	Rate	6.06	6.08	Rate	7.06	7.09	Rate	8.06	7.97

Example 3: 2D single crack

Table A.23: Example 3 - L^2 errors for the flux and the pressure, using the Galerkin SBFEM a single S-element with skeleton refinement, for $h = 2/2^\ell,\ \ell = 0, ..., 3$ and $k = 1, ..., 4$.

ℓ	$k=1$			$k=2$			$k=3$			$k=4$		
	DOF	$E^H_{L^2}$ - u	$E^H_{L^2}$ - $\underline{\sigma}$	DOF	$E^H_{L^2}$ - u	$E^H_{L^2}$ - $\underline{\sigma}$	DOF	$E^H_{L^2}$ - u	$E^H_{L^2}$ - $\underline{\sigma}$	DOF	$E^H_{L^2}$ - u	$E^H_{L^2}$ - $\underline{\sigma}$
1	32	4.935E0	2.505E1	48	4.576E0	2.073E1	64	5.530E-1	2.428E0	80	5.440E-1	2.292E0
2	64	2.716E0	1.426E1	96	1.330E-1	1.090E0	128	1.143E-1	4.814E-1	160	2.436E-3	2.833E-2
3	128	5.068E-1	2.441E0	192	5.837E-2	2.262E-1	256	5.207E-3	2.078E-2	320	3.775E-4	1.611E-3
4	256	1.237E-1	5.664E-1	384	7.112E-3	2.602E-2	512	3.158E-4	1.293E-3	640	1.140E-5	4.874E-5
	Rate	2.03	2.11	Rate	3.04	3.12	Rate	4.04	4.01	Rate	5.05	5.05